Diffractive dissociation of protons in 7 TeV collisions at the ATLAS detector.

Timothy Alexander David Martin

Thesis submitted for the degree of
Doctor of Philosophy

Particle Physics Group,
School of Physics and Astronomy,
University of Birmingham.

December 21, 2012

ABSTRACT

A data sample with integrated luminosity 7.1 μb^{-1} of pp collisions was collected with a minimum bias trigger at $\sqrt{s} = 7$ TeV using the ATLAS detector at the Large Hadron Collider. It is analysed to identify large pseudorapidity gaps. The inelastic cross section is presented differentially in $\Delta\eta^F$, the largest continuous region of pseudorapidity which extends from the edge of the detector at $\eta = \pm 4.9$ and which contains no final state particles above a threshold $p_{\text{T}}^{\text{cut}}$. The measurement is presented in the region $0 < \Delta\eta^F < 8$ for $200 < p_{\text{T}}^{\text{cut}} < 800$ MeV. Diffractive topologies are isolated at large gap sizes. The distribution is interpreted using triple Regge models of diffractive scattering, and the dependence of the inelastic cross section on the kinematics of diffraction is studied and compared with other LHC measurements.

DECLARATION OF AUTHORS CONTRIBUTION

The design, construction and continued successful operation of the LHC, along with the detectors which adorn it is due to the dedication of many thousand scientists, engineers and technicians over a period of many years. Having been fortunate to have the opportunity to work in the ATLAS collaboration during the beginning of this new exploration in high energy physics research, I have made contributions in different areas of the experiment which will be detailed in this thesis.

The scope of this document encompasses an overview of the whole LHC project along with ATLAS specifics. Particular focus and detail is given to areas in which I have contributed directly. These include the ATLAS trigger systems, specifically the Level 1 Calorimeter Trigger (L1Calo) and the minimum bias trigger.

My official service position was maintenance and development of the Detector Control Systems for L1Calo and other L1 trigger systems. An overview of technical work is separated from the main document in Appendix A. My involvement with the minimum bias trigger group came from being based at CERN and working on a minimum bias analysis during the first data taking campaign at a 900 GeV centre of mass energy in 2009. I continued to work with this group throughout my PhD.

The diffractive physics analysis presented in this thesis was for the large part performed jointly with colleagues from Fyzikální ústav in Prague. The speed and quality of the analysis was greatly increased through collaboration and through maintaining two independent code bases. In addition to the main physics results, many cross checks and control distributions were produced. Some of these controls were produced by only one group or the other and analysis plots included in the narative of this document which was performed solely by Prague is cited to the joint internal documentation of the analysis, [1].

ACKNOWLEDGEMENTS

I am grateful to everyone who has helped and inspired me throughout my education.

I would like to thank Mari Baker both for being a fantastic maths and physics teacher during my A-levels and for introducing me to the LHC.

I am thankful to the whole of the Birmingham group, to Pete and John for being such enthusiastic tutors during my undergraduate, to all my fellow post-grad students for the numerous interesting discussions we've had over the years and to Paul for guiding me through all the steps needed to make a physics measurement.

At CERN, I am grateful to the level one calorimeter trigger and minimum bias communities, both for being comprised of such friendly and enthusiastic people and for being pleasures to work with.

I give my thanks to my loved ones for the support given whilst preparing this document.

Finally, I would like to thank the STFC for funding my studentship.

Dedicated to the memory of my father.

Discere gratiā discendī

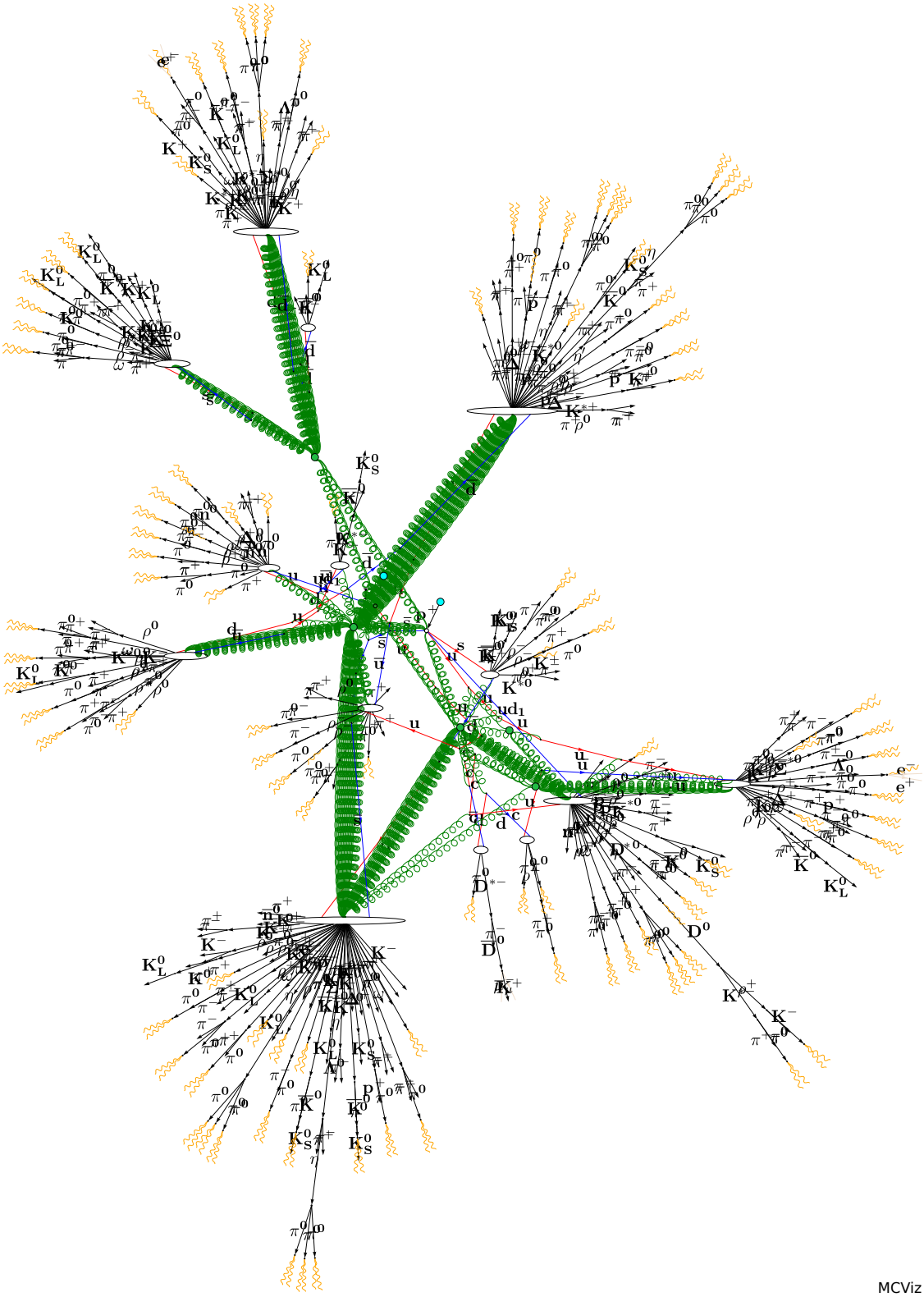

MCViz

Contents

List of Tables

List of Figures

DEFINITIONS OF ACRONYMS

ADC Analogue-to-Digital Converter

ALFA Absolute Luminosity for ATLAS
Tracking detector located in Roman Pots at ±240 m from the nominal interaction point in ATLAS. Designed to calibrate the ATLAS luminosity measurement using the low t Coulomb interaction region.

ALICE A Large Ion Collider Experiment
One of the four principal LHC detectors, specialising in heavy ion collisions.

AOD Analysis Object Data

ATLAS A Toroidal LHC ApparatuS
A large general purpose detector installed on the LHC.

ASIC Application Specific Integrated Circuit

BC Bunch Crossing
Occurs every 25 ns (40 MHz); the nominal LHC bunch separation.

BCM Beam Condition Monitors
Diamond scintillator detector surrounding the beam pipe at small radius. The BCM monitors the radiation environment and will issue a request to dump the beam should the activity levels become dangerously high for the ATLAS inner detector.

BCID Bunch-Crossing Identifier
Numeric ID given to 3564 of the RF-buckets in the LHC. 2808 of which contain particles under the nominal fill scheme. May refer either to the ID or to the process of associating interaction data with the correct ID.

BPTX Beam Pickup Detector
Part of the LHC beam instrumentation. Fast electrostatic pickup rings which detect the current induced by a passing proton bunch at ±175 m from ATLAS. Utilised as a trigger input during initial data taking.

BS Byte Stream

CAF CERN Analysis Facility

CAN Controller Area Network

CD Central Diffractive
$pp \to pXp$.

CDF The Collider Detector at Fermilab

CERN European Organisation for Nuclear Research

CMM Common Merger Module
Part of L1Calo, responsible for collating trigger objects for transmission to the CTP.

CMS Compact Muon Solenoid
One of the four principal detectors on the LHC ring with similar physics goals to ATLAS.

CMT Configuration Management Tool
Package manager used with ATLAS software.

CNI Coulomb-Nuclear-Interference

COMPASS COmmon Muon Proton Apparatus for Structure and Spectroscopy

CP Charge-Parity
Combined charge and parity symmetry operations, the symmetry between matter and anti-matter.

CPM Cluster Processor Module
Part of L1Calo, locates e/γ and τ/hadron objects.

CR Colour Reconnection

CSC Cathode Strip Chamber

CTP Central Trigger Processor
Receives input from the L1 trigger systems and forms the L1 trigger decision.

CU Control Unit
Branch of the DCS FSM. Operationally identical to a LU, a CU may additionally be partitioned.

D3PD Derived 3rd level Physics Data

DAOD Derived Analysis Object Data

DAQ Data AcQuisition

DCS Detector Control Systems

DD Double Diffractive
$pp \to XY$ where the X system is defined to be the dissociation with larger invariant mass.

DDC DCS-DAQ-Communication

DESD Derived Event Summary Data

DFM Data Flow Manager
Part of the Event Builder Network, manages the building of complete events which have been accepted by L2.

DIGI Detector simulation analogue digitisation file

DL Donnachie and Landshoff
Regge Pomeron flux parametrisation with supercritical Pomeron trajectory implemented in the PYTHIA8 MC.

DoF Degrees of Freedom
Statistical measure of how many data points and free fit parameters there are when minimising a function to data.

DPD Derived Physics Data

DPDF Diffractive Parton Density Function
Structure function for the Pomeron.

DSS Detector Safety System

DT Drift Tube

DU Device Unit
Leaf of the DCS FSM encapsulating a hardware unit.

EBN Event Building Network
The network of systems involved in receiving data fragments for the ROS and building full events from them.

ECal Electromagnetic Calorimeter

EF Event Filter
The third and final level of the ATLAS trigger.

EFP Event Farm Processor
A PC forming part of the Event Farm, it analyses fully built events and decides which ones to save to permanent storage.

EM Electromagnetic

ESD Event Summary Data

EVNT Event File
File format for storing MC event records.

FADC Flash Analogue-to-Digital Converter

FCal Forward Calorimeter

FIR Finite Impulse Response
Part of the L1Calo PPM, digital filter which performs BCID.

FPGA Field Programmable Gate Array
Re-programmable integrated circuit.

FSM Finite State Machine

GCS Global Control Station
Top level of the DCS operational hierarchy.

GPD General Purpose Detector
Term for particle detectors which are designed to record data applicable to many types of physics analysis.

H1 Particle detector at the HERA accelerator.

HCal Hadronic Calorimeter

HEC Hadronic Endcap Calorimeter

HERA Hadron-Electron Ring Accelerator
Proton - electron (and positron) collider at $\sqrt{s} = 318$ GeV. Responsible for measurement of many hadronic structure functions through deep inelastic scattering of protons with a probe lepton.

HITS Detector simulation hits file

HLT High Level Trigger
Comprising L2 and the EF.

HV High Voltage

ID Inner Detector
The tracking regions of ATLAS within the solenoid magnet at $|\eta| < 2.5$. Comprised of Pixel, the SCT and TRT.

IP Interaction Point
The nominal interaction point at the origin of the ATLAS coordinate system.

ISR Intersecting Storage Rings
Worlds first hadron collider. Running at CERN from 1971, it collided protons at up to $\sqrt{s} = 62$ GeV.

JCOP Joint ContrOls Project

JEM Jet Energy processor Module
Part of L1Calo, locates jets and calculates scalar-E_{T} and $E_{\mathrm{T}}^{\mathrm{miss}}$.

L1 Level 1
First level of the ATLAS trigger.

L1A Level 1 Accept
Signal issued by the CTP when an event is triggered at L1.

L1Calo Level 1 Calorimeter Trigger

L1Muon Level 1 Muon Trigger

L2 Level 2
Second level of the ATLAS trigger.

L2N Level 2 Network
Dedicated LAN used by the L2 trigger.

L2PU Level 2 Processing Unit

L2SV Level 2 Supervisor
Manages data flow through the L2 trigger, assigns events to a L2PU.

LAN Local Area Network

LAr Liquid Argon Calorimeter

LCS Local Control Station
Lower level of the DCS operational hierarchy.

LEIR Low Energy Ion Ring
Formerly the Low Energy Antiproton Ring, the LEIR now bunches and accelerates lead ions from the PS for use in the LHC.

LEP Large Electron-Positron collider

LHC Large Hadron Collider
Superconducting collider occupying the 27 km ring at CERN.

LHCb LHC – Beauty
One of the four principal LHC detectors. Specialising in b-quark physics and CP-violation.

LHCf LHC – Forward
Experiment located temporarily in the TAN on one side of ATLAS. Ultra forward energy flow is used to simulate cosmic ray interactions.

LO Leading Order
First order expansion in perturbation theory.

LU Logical Unit
Branch of the DCS FSM abstracting a physical collection of hardware.

LUCID LUminosity measurement using Čerenkov Integrating Detector
Gaseous particle counter which provides the main instantaneous luminosity measurement for ATLAS.

LUT Look-up Table

MBTS Minimum Bias Trigger Scintillator
Array of sensitive scintillator counters located on either side of the ATLAS detector. Used to trigger on inelastic proton-proton interactions with minimum bias.

MC Monte Carlo
Method of simulating high energy interactions by randomly sampling distributions.

MDT Muon Drift Tube

MIP Minimum Ionising Particle
A particle whose energy loss through ionisation, $-dE/dx$ from the Bethe-Bloche equation, is minimum over a range of applicable momenta.

MoEDAL Monopole and Exotics Detector At the LHC

MPI Multi-Parton Interactions

ND Non-Diffractive
$pp \to X$.

NIM Nuclear Instrumentation Module
Standardised electrical and mechanical specification for electronic modules used in high energy physics.

NLO Next-to-Leading Order
Perturbative expansion to second order.

N^{3}LO Next-to-Next-to-Next-to-Leading Order
Perturbative expansion to fourth order.

NTD Nuclear Track Detector

PC Personal Computer

PDF Parton Density Function

PIX Pixel Detector

PMT Photo-Multiplier Tube
Converts incident light to an amplified electric signal.

POOL Pool Of persistent Objects for LHC

PPM PreProcessor Module
Part of L1Calo, digitises calorimeter information and performs BCID.

PS Proton Synchrotron
Particle accelerator at CERN used to accelerate protons to 26 GeV. Injects into the SPS.

PSB Proton Synchrotron Booster

PVSS ProzessVisualisierungs und Steuerungs-System

QCD Quantum Chromodynamics

RAW Byte Stream data format

RDO Raw Data
Object oriented MC equivalent to RAW files.

RF Radio Frequency
The range 3 kHz - 3 GHz of the EM spectrum.

RICH Ring Imaging Čerenkov Detector

RMS Root Mean Square

ROB Read-Out Buffer
Part of the ROS, hold event fragments to be utilised by the L2 trigger.

ROD Read-Out Driver
Sub detector specific drivers which construct and transmit a data fragment upon the receipt of a L1A.

RoI Region of Interest
(η, ϕ) coordinate and object threshold identified at L1 for use in the HLT.

RoIB Region of Interest Builder
Crate responsible for the construction of RoIs which are supplied to the L2SV.

ROOT ROOT Data Analysis Framework

ROS Read-Out System
Comprising of the subsystems used to perform detector readout and supply data fragments to the L2 trigger and EBN.

RPC Resistive Plate Chamber

SCADA Supervisory Control And Data Acquisition

SCS Subdetector Control Station
Middle level of the DCS operational hierarchy.

SCT Semi-Conductor Tracker
Silicon strip based tracking detector.

SD Single Diffractive
$pp \to pX$ or $pp \to Xp$.

SFI Sub-Farm Input
System of computers which build whole events in memory which were accepted by the L2 trigger.

SFO Sub-Farm Output
Transfers triggered events from the Event Builder Network for permanent, off-line storage.

SLHC Super-LHC

SM Standard Model

SPS Super Proton Synchrotron
Particle accelerator at CERN used to accelerate protons to 450 GeV. Injects into the LHC.

SSC Superconducting Super Collider
Cancelled project to build a 40 TeV particle accelerator in the USA.

TAG Tag Data
Per-event meta data for use in pre selection of a physics data sample.

TAN Target Absorber of Neutrals
Copper absorber which fills the ATLAS forward aperture for neutral particles with $|\eta| > 8.3$.

TDAQ Trigger and Data AcQuisition

TDR Technical Design Report

TGC Thin Gap Chamber

TOTEM TOTal cross section, Elastic scattering and diffraction dissociation Measurement at the LHC
Detector associated with the CMS experiment which measures the total cross section through elastic scattering.

TPC Time Projection Chamber

TRT Transition Radiation Tracker
Straw tube based tracking detector.

TTC Trigger Timing and Control
Receives and distributes the 40 MHz clock signal generated by the RF accelerator station on the LHC ring.

UA4 Experiment at on the SPS, measuring elastic scattering in the Coulomb interference region of $p\bar{p}$ collisions.

UE Underlying Event
All additional interactions between the partons of two colliding protons except for the hard scale interaction of interest.

vdM van der Meer
Beam optics method of determining the absolute luminosity from by scanning the beams through each other.

VEV Vacuum Expectation Value

WA91 West Area 91
CERN SPS experiment to search for gluonic states.

ZDC Zero Degree Calorimeter
Ultra forward calorimeter for neutral particles at $|\eta| > 8.3$. Primarily used to detect spectator neutrons in heavy ion collisions.

CHAPTER 1

NON-TECHNICAL SUMMARY

> In the beginning there was nothing, which exploded.
> *Terry Pratchett*

1.1 THE EARLY UNIVERSE

The universe we live in is a little under 14 billion years old, and we explore the majority of it with various types of telescopes. To explore the universe with a telescope is to observe it, and come to understand it, using the ancient light which has travelled through space to our planet. Light itself is pretty fast, a beam of light could race around the equator in a tenth of a second. The universe however is also pretty big. When you look at the moon - you don't see the moon as it is *now*; rather you see it as it *was* a second ago. It takes the light from the Sun, bouncing off the Moon, a full second to travel the distance to your eye. Likewise the light shining

down from the Sun shows us not the Sun now, but the Sun as it was eight minutes ago. The further away you look in space, the further back you look in time and this trick works almost all the way back to the beginning of the universe, at which point our telescopes observe the Cosmic Microwave Background, Figure 1.1. This is

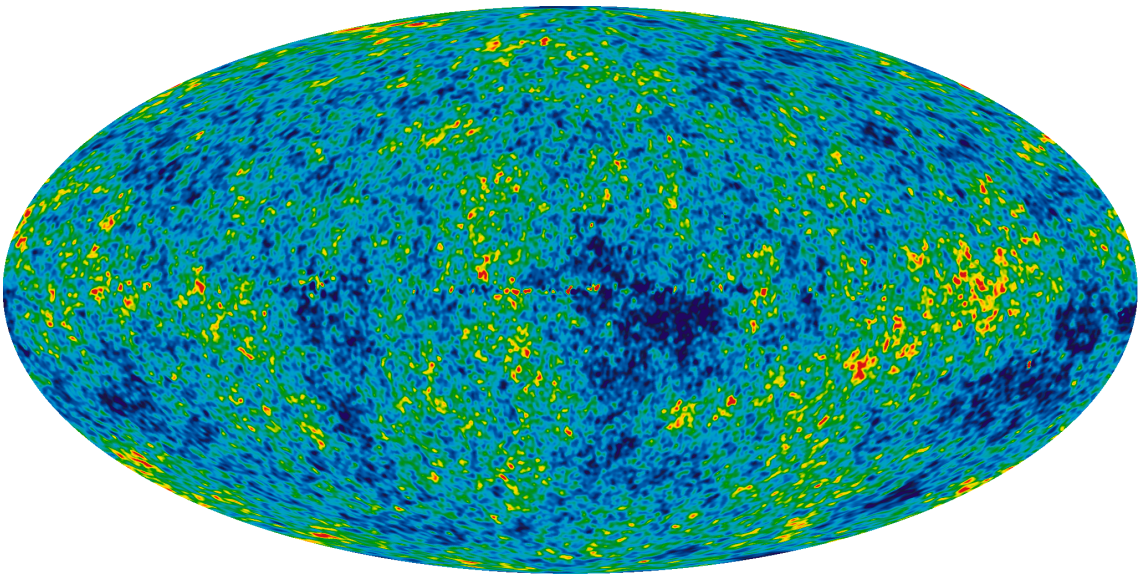

Figure 1.1: The Cosmic Microwave Background: Plot of the whole sky showing the last remnant of the 'fireball' that was the early universe. The different colours depict the very small variations in the temperature across different regions in the early universe. Image credit: NASA / WMAP Science Team.

the point at which the 'fireball' which filled the universe for the first three hundred thousands years of its existence died out. It was the moment at which the whole universe became transparent to the passage of light. The remnant heat from the early universe is still all around us today, but the universe has cooled so much that we now only experience it as static on an untuned radio. As the very early universe was opaque, telescopes cannot peer further back and exploring the first moments of the infant universe requires another approach.

1.2 STUDYING THE MOMENT AFTER INCEPTION

The Large Hadron Collider (LHC) is a tool whose purpose, in some sense, is the exploration of the early universe. It is a piece of machinery which allows us to focus a large amount of energy into a tiny volume of space, repeatedly, and at the centre of giant detectors such as ATLAS which record images of the miniature explosions. By focusing such large amounts of energy in such a small space, we recreate the conditions and, importantly, we probe the *laws of physics* which were at play when the universe had been in existence for only ten billionths of a second. Through studying how the elementary constituents of nature interact with each other during this early epoch, we advance the total sum of human knowledge and can test out theoretical hypotheses which relate to the laws of nature.

The LHC achieves these large energy concentrations in what some might call a rather crude manner; by smashing particles together at high speed. Tiny, sub-atomic particles of matter are collected in their billions into bunches whose dimensions are roughly the same as a pencil lead. These bunches are accelerated to extreme high speeds, gaining huge energy, and are circulated around an underground circular tunnel outside Geneva which is similar in size to the circle line in the London Underground.

The particles used in the LHC are protons and ionised atoms. Protons, as illustrated in Figure 1.2, are positively charged and are found at the centre of all atoms. They are also unimaginably small. If a proton were to be blown up to the size of a speck of dust, then proportionally the speck of dust would have been blown up to the size of the Earth. Protons are used due to their abundance and because they do not radiate much of their energy away when bent around the LHC ring using magnets. The other prime candidate, electrons, are much lighter than protons and would radiate far too much to be used at such high energies in the LHC tunnel.

Unlike electrons however, protons are not fundamental particles. They are composite objects which are made up of three principal *quarks*, held in place by the continuous

interactions of a soup of countless *gluons*, which interact strongly with the quarks and prevent them from escaping the proton. This tends to make interactions in the LHC more complicated than at previous particle colliders such as the Large Electron-Positron collider (LEP) in the 80s and 90s, which did use electrons.

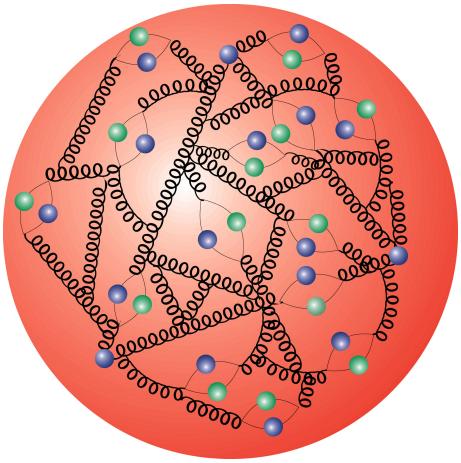

Figure 1.2: Simplified illustration of the complex object that is the proton. The three principal quarks (blue balls) are entwined with gluons (looped lines), many of which also create more, short lived, pairs of quarks and anti-quarks (blue and green ball pairs). Image credit: DESY, Hamburg.

1.3 WHEN PROTONS INTERACT

When two high energy protons collide at the LHC, many things can happen, some of them more common than others. All of them are interesting.

Particle physics is above all a game of statistics; it's all down to the odds. If you wished to place a bet on the creation of a rare, primordial *top quark* from a single collision then a bookmaker would give you odds of one hundred million to one. A recently discovered Higgs boson? Five billion to one. You are 350 times more likely to win the National Lottery jackpot than successfully bet that a single interaction between two protons in the LHC will produce a Higgs particle. The LHC does not, however, just collide a single pair of protons, once. Under normal conditions it collides around one hundred million pairs a second in the ATLAS detector, for periods

of many hours on end. Sophisticated electronics discussed later in Section 5 are used to pick out the rarest of interactions. Only around 200 of the one hundred million collisions per second are saved to disk for analysis, the rest are discarded.

This thesis is not however about these rare processes. It is instead about a much more commonplace proton interaction referred to as *inelastic diffraction*. Inelastic means that the mass of the particles before and after the collision is not conserved[1] and diffractive in that it is analogous to the way light diffracts through a pin hole as in Figure 1.3.

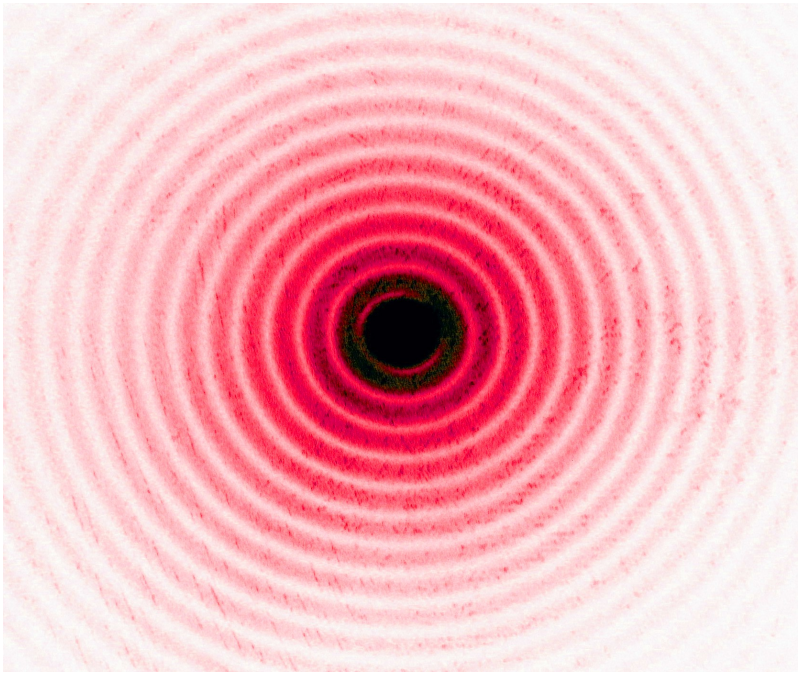

Figure 1.3: Circular diffraction pattern obtained by shining a laser light through a small circular aperture [2].

The odds on a pair of protons interacting diffractively is large, around one in four. Therefore a large number of such events were recorded by the ATLAS detector in the very first few hours of collisions. The physics of diffraction is poorly understood as it does not fit within the standard mathematical frameworks used to describe the rare particle interactions that were just discussed. This framework requires the strength

[1] As $E = mc^2$, some of the proton's energy in *inelastic* interactions is converted into mass, creating more particles.

of the forces in play to be small so that they can be included in the equation as a small perturbation to a problem of known solution. Diffraction happens so often as it is a low energy interaction of at least two gluons, and due to the peculiar and counter-intuitive way gluons interact, their interactions are strongest at low energies.

Without a full understanding of the underlying mechanisms, *phenomenological* models were developed in the 1960s by Regge, Froissart, Pomerančuk, Gribov and others. These models describe diffractive interactions using the mathematics of scattering theory, but make no attempt to explain the underlying mechanics. We find from these equations that there is a strong correlation in the angles of the outgoing particles produced in diffractive interactions, which is not present in other common but non-diffractive interaction.

By selecting events in which a large gap is present in the detector, devoid of all particles, we create a collection of diffractive events which are subsequently studied. Using this sample we measure present the probabilities of different gap sizes and examine the data to extract a key quantity from the underlying Regge theory. Such an event is displayed in Figure 1.4.

This knowledge helps us to improve our models of diffraction, which are in turn used to apply corrections to other rarer types of physics which occur side-by-side with diffractive interactions. A working knowledge of ultra high energy diffractive scattering is also key for astro-particle physicists, some of whom study energetic collisions of cosmic ray particles with our upper atmosphere. These interactions, some of which are over fourteen million times more powerful than anything achieved at the LHC, have a strong dependence on diffractive theory.

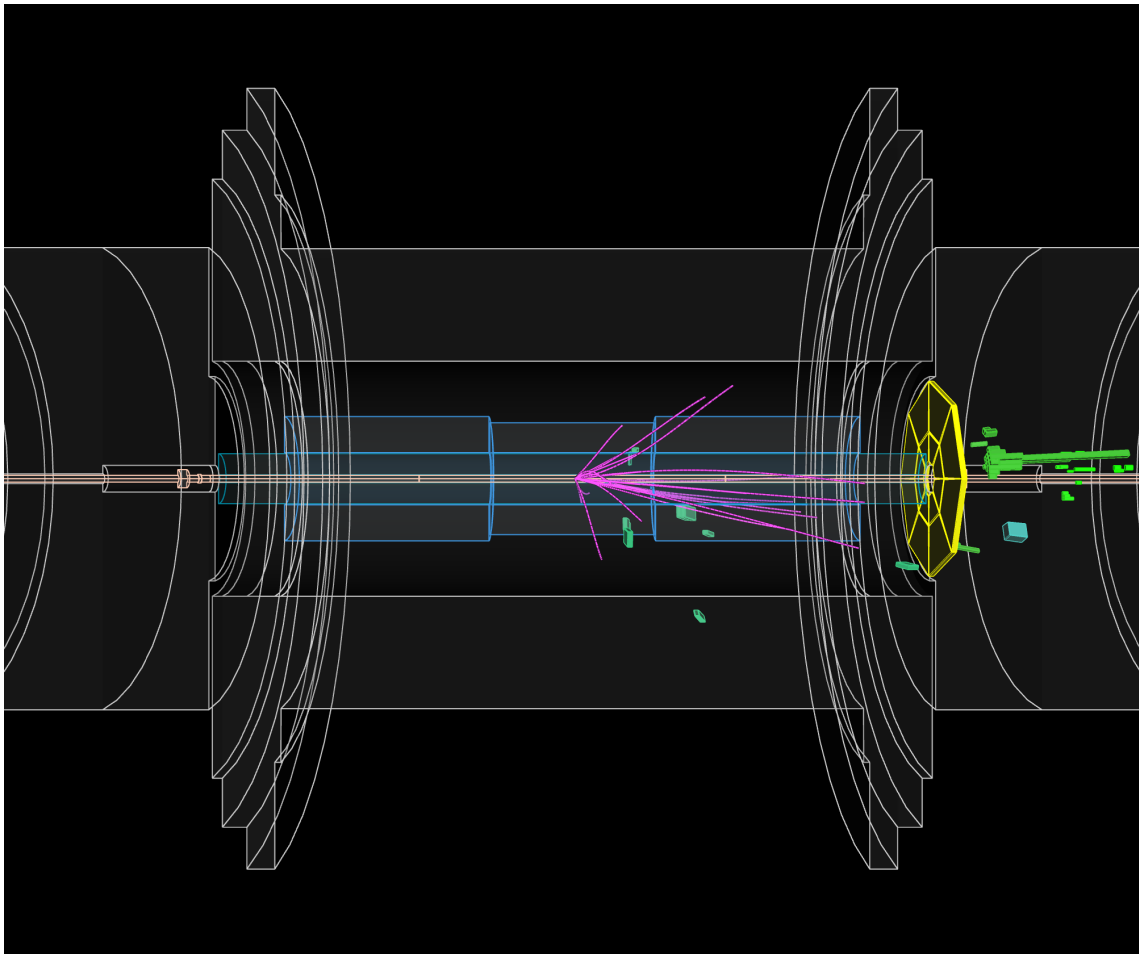

Figure 1.4: Visualisation of a candidate diffractive interaction from early ATLAS data, viewed from the side of the detector. The protons come in from left and right and collide at the midpoint. Trajectories of electrically charged particles are displayed as pink lines, these are curved as the particles bend in the ATLAS magnetic field. Energy deposits from charged and neutral particles are shown as blue and green cubes. The yellow disk is extremely sensitive to detecting charged particles and informs the rest of the detector when an interaction has occurred. Notice how all of the particles are travelling in one direction, toward the right hand side of ATLAS, and leaving a large empty gap with no particles present. This is the property of diffractive interactions exploited in the analysis.

CHAPTER 2

INTRODUCTION

The A Toroidal LHC ApparatuS (ATLAS) detector and the LHC have both performed exceptionally during their first years of operation. This culminated in July 2012 with the observation by ATLAS of a neutral boson, compatible with the Standard Model (SM) Higgs boson, with a mass[1] of $126.0 \pm 0.4(\text{stat}) \pm 0.4(\text{sys})$ GeV at a local significance of 5.9 standard deviations [3]. The observation was independently corroborated by the Compact Muon Solenoid (CMS) collaboration [4]. A large fraction of the data used in the discovery was taken during the 2012 *pp* campaign at a center of mass energy $\sqrt{s} = 8$ TeV. During this period, the LHC provided a record peak instantaneous luminosity for a hadron collider of $7.73 \times 10^{33}\text{cm}^{-2}\text{s}^{-1}$. A consequence of such beam intensity is that the number of proton-proton interactions per beam-crossing is large. When averaged over the whole run, the peak number of events per bunch-crossing at this luminosity was 37. These additional soft-scale interactions are known as *pile-up* and form a background from which hard-scale interactions,

[1] Unless explicitly stated otherwise, natural units are assumed such that $c = \hbar = 1$.

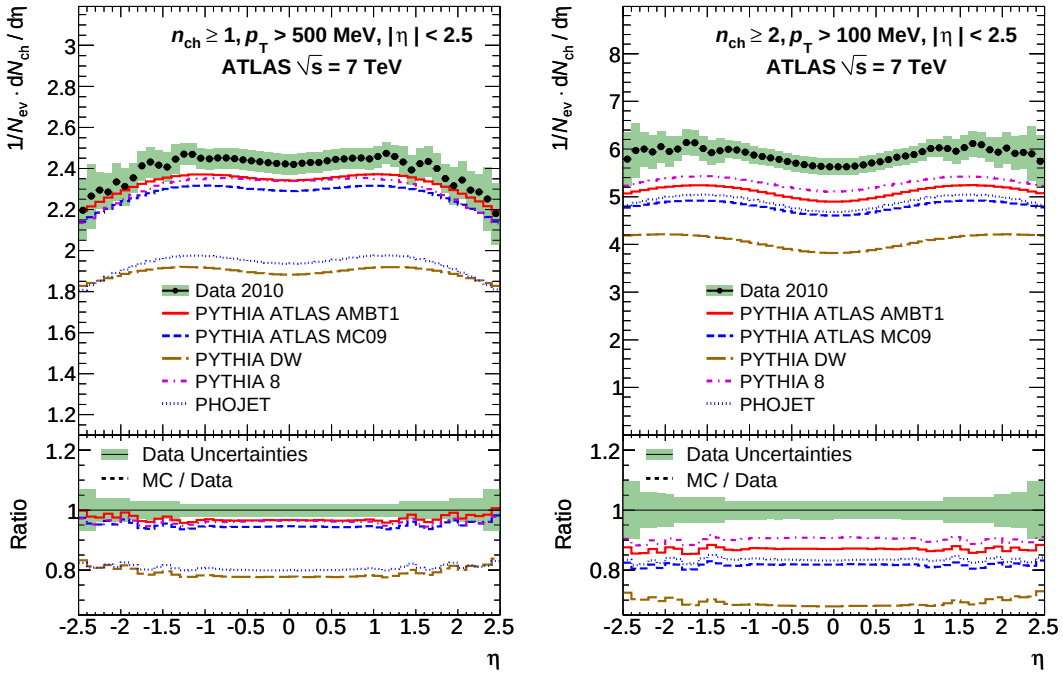

(a) (b)

Figure 2.1: Single-event normalised charged particle multiplicity as a function of η from early $\sqrt{s} = 7$ TeV data. For events with a number of charged particles $N_{\mathrm{Ch}} \geq 1$ with $p_{\mathrm{T}} > 500$ MeV in (a) and $N_{\mathrm{Ch}} \geq 2$ with $p_{\mathrm{T}} > 100$ MeV in (b). The data are compared to a variety of MC models and tunes. Taken from [5].

such as scalar boson production, must be separated. As pile-up arises from multiple independent interactions, the physics of a high pile-up environment is inferred from studies of isolated soft interactions.

In March 2010, the counter rotating proton beams in the LHC were for the first time steered into coincidence at $\sqrt{s} = 7$ TeV. As the LHC was just starting its high-energy commissioning phase, the instantaneous luminosity was small ($10^{27}\mathrm{cm}^{-2}\mathrm{s}^{-1}$). This resulted in an interaction probability per beam-crossing of 0.1%. With such conditions, only a tiny fraction of events contained more than one proton-proton interaction in a single bunch-crossing and the properties of the inelastic interactions which form the bulk of the proton-proton cross section were studied in detail.

One such early measurement performed by the collaboration [5] was of the average

multiplicity of charged particles, differential in pseudorapidity[2] as shown for two different selection criteria in Figure 2.1. It is observed that the average flux of charged particles is significantly underestimated in data when compared with various MC models. Furthermore, the agreement worsens in Figure 2.1(b) when the event selection is relaxed to include particles with lower transverse momentum, p_{T}.

This is further illustrated in Figure 2.2 where the average multiplicity is plotted differentially in p_{T} for the relaxed selection. Here the excess is clearly observed to be due to an underestimation of charged particles, in all considered models, by up to a factor two, in the range $100 < p_{\mathrm{T}} < 400$ MeV. The diffractive interactions explored in this thesis tend to be highly peripheral and are large contributors to the dynamics at the low end of the p_{T} spectrum. They are also some of the most poorly investigated due to ambiguity in their definition and in the practical techniques used to isolate them.

2.1 DOCUMENT STRUCTURE

This work opens with an overview of the CERN laboratory and the LHC in Chapter 3. The ATLAS detector is summarised in Chapter 4 with additional depth provided on the trigger system in Chapter 5, computing in Chapter 6. Technical work on the Detector Control Systems (DCS) is described in Appendix A.

Scattering theory and Regge phenomenology are introduced in Chapter 7 with MC techniques following in Chapter 8. The remainder of the document from Chapter 9 onwards describes the search for large rapidity gaps in minimum bias events and presents the results along with their interpretation.

[2]In the ATLAS coordinate system, the z-axis points in the direction of the anti-clockwise beam viewed from above. Polar angles θ and transverse momenta p_{T} are measured with respect to this axis. The pseudorapidity $\eta = -\ln\tan(\theta/2)$ is a good approximation to the rapidity of a particle whose mass is negligible compared with its energy and is used here, relative to the nominal $z = 0$ point at the centre of the apparatus, to describe regions of the detector. The hemisphere at positive pseudorapidity is denoted the A side of the detector while the hemisphere at negative pseudorapidity is denoted the C side of the detector.

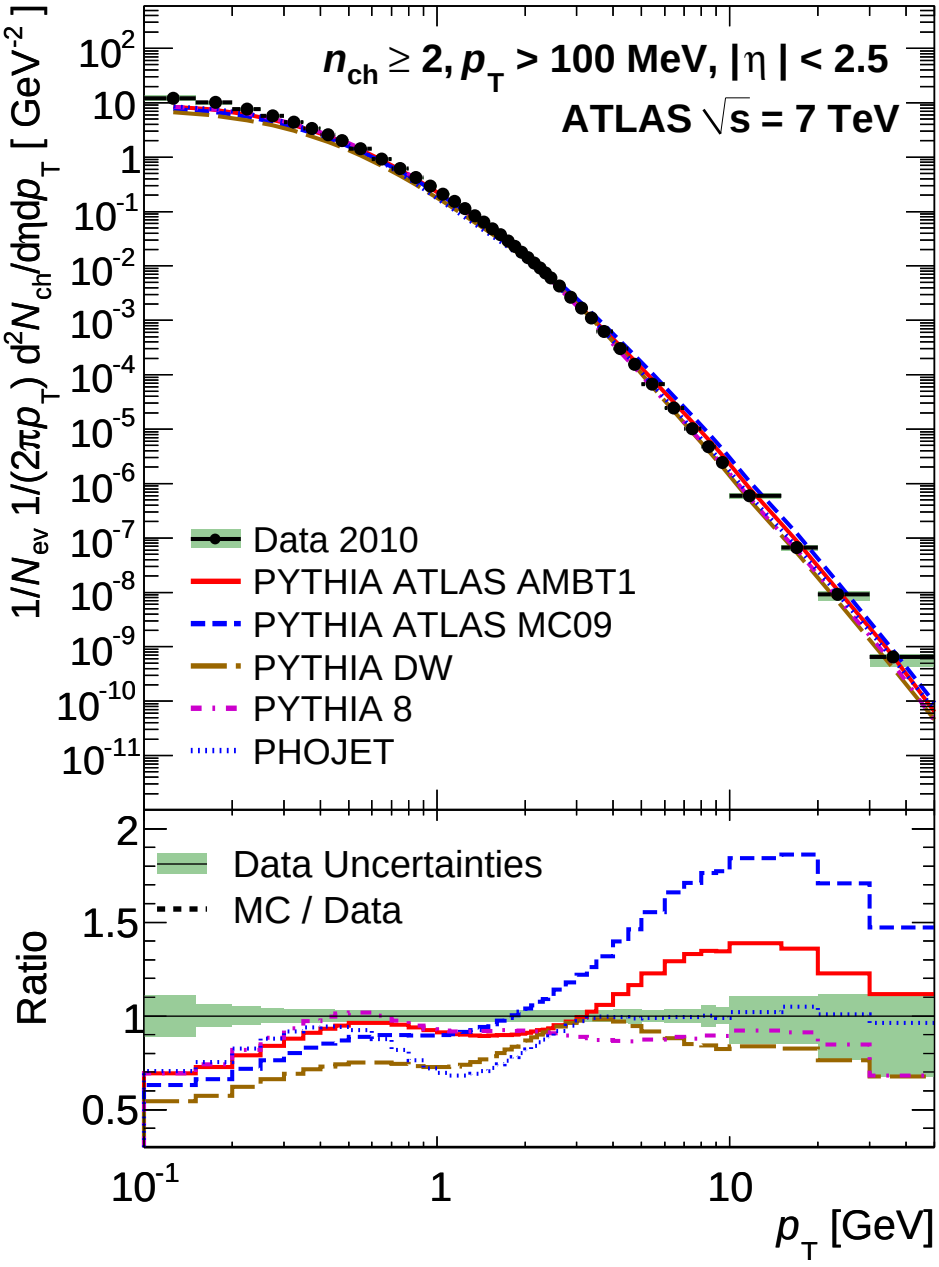

Figure 2.2: Single-event normalised charged particle multiplicity as a function of p_{T}, for events with $N_{\mathrm{Ch}} \geq 2$ with $p_{\mathrm{T}} > 100$ MeV. The data are compared with a variety of MC models and tunes. Taken from [5].

CHAPTER 3

THE CERN COMPLEX

The European Organisation for Nuclear Research (CERN), from its French name *Conseil Européen pour la Recherche Nucléaire* is an international organisation founded in September 1954 and has since played a pivotal role in the advancement of fundamental physics. These include the discovery of the field particles of the weak interaction, the W and Z in 1983 [6] and the first manufacture of anti-hydrogen atoms in 1995 [7] to name but two.

CERN employs approximately 2400 full-time employees with around 10000 visiting users from academic institutes around the world. Located on the Franco-Swiss border, the main complex is shown in Figure 3.1.

Many historic experiments have been performed at CERN with many continuing to run to the present day, making full use of the various particle species, energies and intensities available from different parts of the accelerator complex. The full chain of accelerators is shown in Figure 3.2. The following sections will focus on how proton

Figure 3.1: Aerial photograph of the countryside next to lake Geneva. The path of thee underground CERN accelerator rings are superimposed, in order of increasing size the Proton Synchrotron, Super Proton Synchrotron and Large Hadron Collider. ©CERN.

and ion beams are delivered to the current flagship LHC project.

3.1 LINEAR ACCELERATORS

CERN currently has two operational linear accelerators with a third under construction to supply the increased current which will be necessary for future Super-LHC (SLHC) upgrades.

Operational since 1978, Linac-2 supplies a 1 Hz pulsed beam of protons at up to 180 mA and energy 50 MeV with 70% availability on average. The protons are collated and bunched in the four vertically stacked rings of the 100 m diameter Proton Synchrotron Booster (PSB) [9] and accelerated up to 1.69 GeV for injection into the Proton Synchrotron (PS).

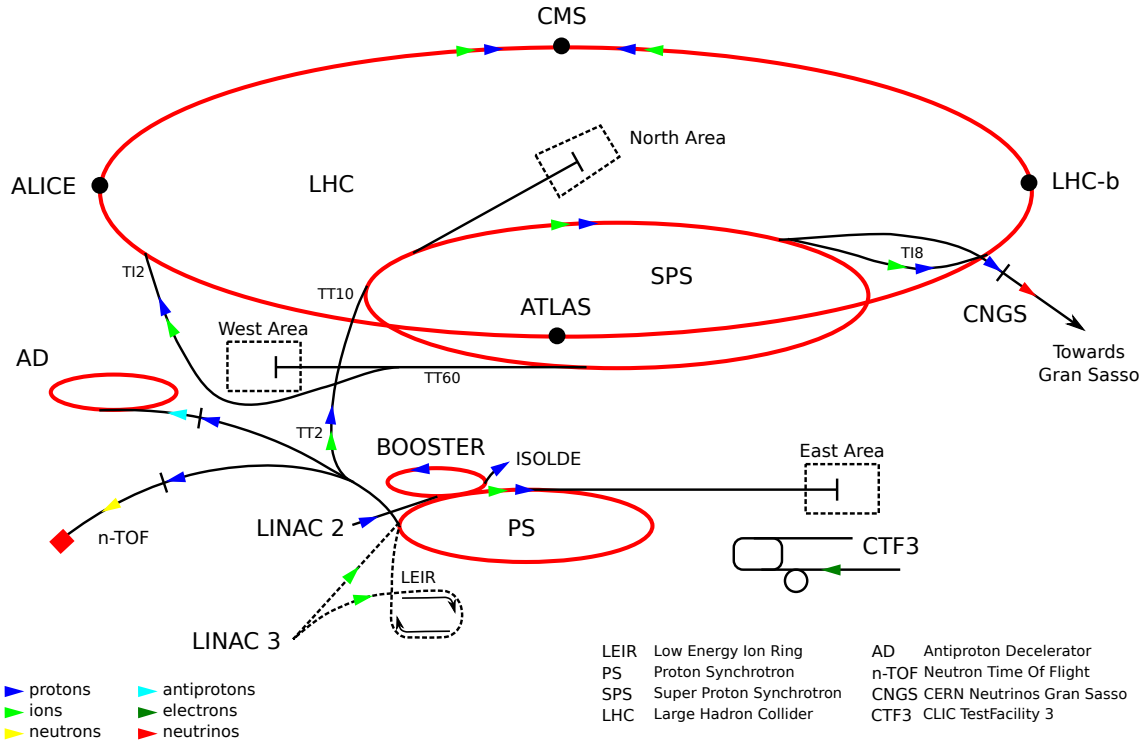

Figure 3.2: The CERN accelerator complex, listing major accelerator systems and detectors. Derived from [8].

Linac-3 has been in operation since 1994 and supplies partially ionised lead atoms for use in the LHC via the Low Energy Ion Ring (LEIR) which was re-purposed for this task in 2006 [10].

3.2 PROTON AND SUPER PROTON SYNCHROTRONS

The PS has been operational since 1959. The 200 m diameter accelerator now operates at up to 26 GeV and injects into the Super Proton Synchrotron (SPS). For heavy ion runs, lead ions are fully ionised to $^{208}Pb^{82+}$ via a 1 mm aluminium foil in the PS-SPS transfer line.

Like the PS, the SPS operates with room-temperature magnets. 774 dipoles bend the particle beam around the 2196 m diameter ring. The SPS accelerates and injects protons into the LHC at 450 GeV.

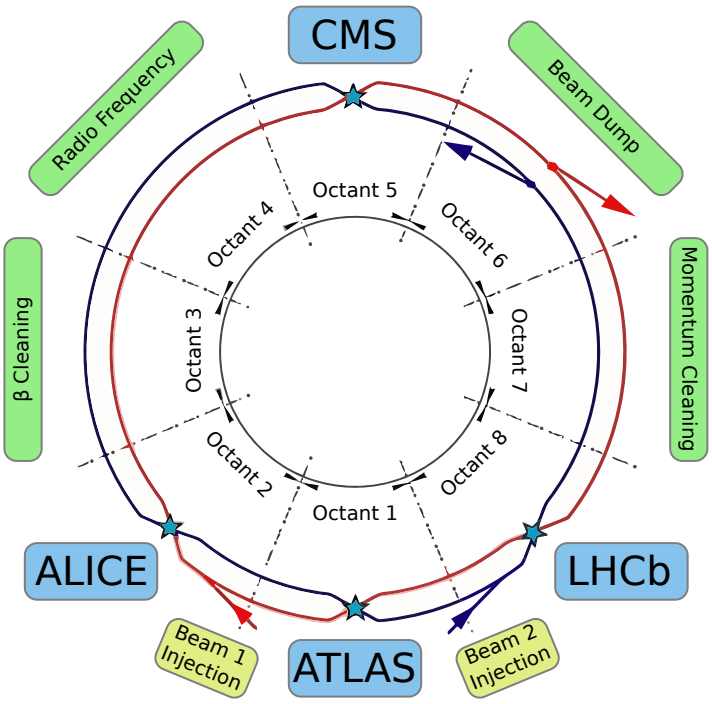

Figure 3.3: LHC Schematic showing apparatus installed in each of the eight segments. Derived from [11].

3.3 LARGE HADRON COLLIDER

The LHC is a 8490 m diameter ring accelerator and collider. It is octagonal in shape with eight straight sections and eight curved sections. A schematic of the ring is presented in Figure 3.3. In total there are over 6600 superconducting magnets installed, including 1232 dipole magnets which are used to bend the beam around the curved sections and 392 arc-quadrupole focusing magnets. The remaining magnets are primarily used for orbit correction and during beam injection and dump.

Each LHC dipole is 14.3 m long, operates at a cryogenic liquid helium temperature of 1.9 K and can sustain a current of 11.9 kA generating a 8.3 T field in the niobium-titanium type II superconducting windings. So as to minimise interactions between the beam and any residual gas, the pressure in the beam pipe is kept very low at

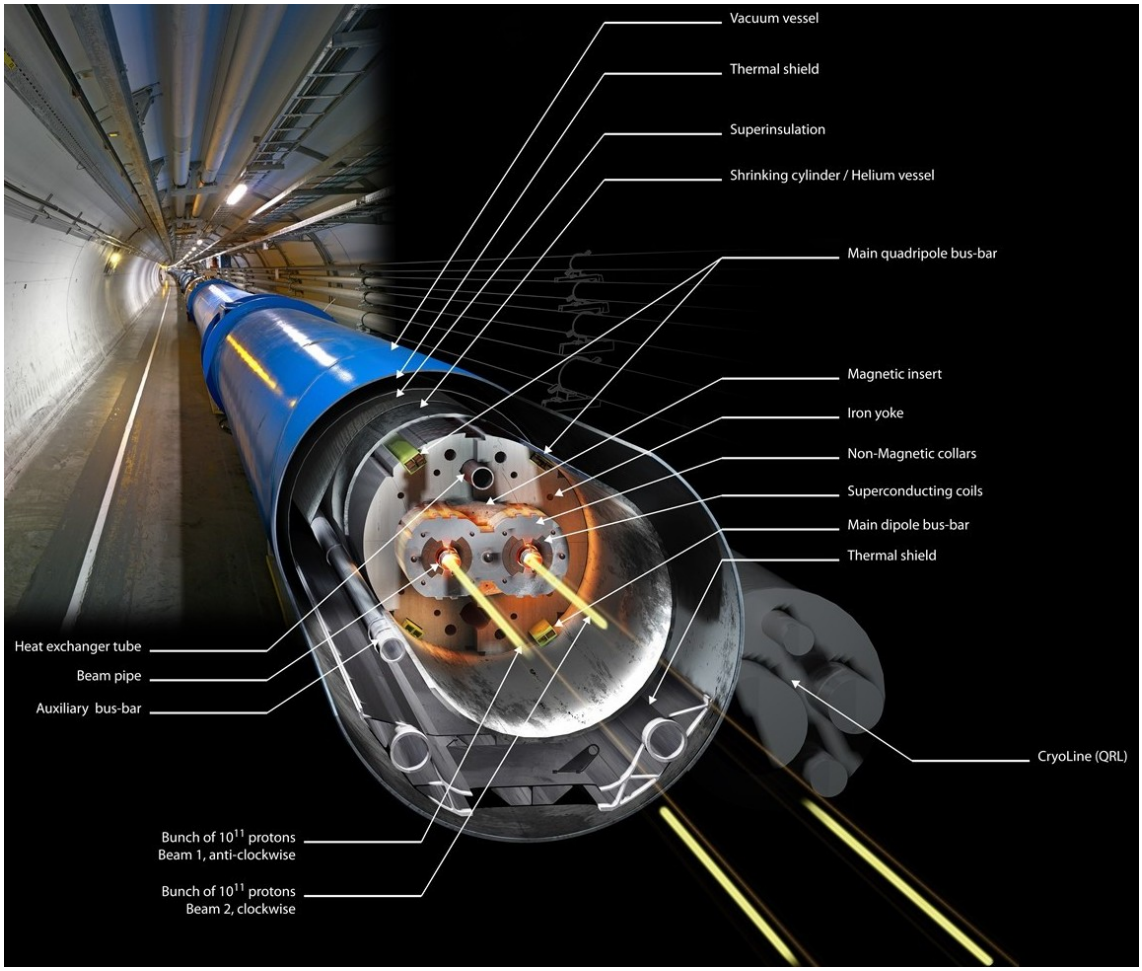

Figure 3.4: Annotated cut away schematic of the LHC beam line. ©CERN.

1.3×10^{-8} Pa. In addition, the surrounding insulation vacuum for the cryogenic magnets occupies a total of 9000 m^3, all of which is evacuated to a pressure of 1.3×10^{-4} Pa. An illustration of a cross section of a dipole magnet is presented in Figure 3.4.

The LHC is 26659 m in circumference with a cavity Radio Frequency (RF) of just over 400 MHz. Dividing the circumference by the frequency gives the harmonic number of the ring, 35640. This segmentation defines the 35640 RF buckets spaced around the ring. The point at the centre of each RF bucket is synchronous with the applied RF field. Particles within a bucket envelope experience longitudinal focusing and undergo synchrotron oscillations around this bunch centroid. The elliptical bucket acceptance at the LHC is 7.91 eVs [12]. The RF systems are located at Point-4 on

the ring. The LHC uses a total of eight 2 MV superconducting RF cavities per beam, leading to an acceleration gradient of 485 keV/turn during the 20 minute ramping phase [11].

From the PS onward, particles are grouped into bunches. In the LHC, one in ten RF buckets are assigned a Bunch-Crossing Identifier (BCID) and may hold a particle bunch. Filling the LHC occurs in stages due to the differing circumferences of the preceding accelerators. Due to the time required to ramp the kicker magnets when injecting from the PS to the SPS, only 72 of the total of 84 BCIDs in the PS are filled, with 12 left empty. This run of 72 continuous filled bunches is referred to as a *bunch train*. In the SPS, three injections of 72 bunches from the PS are accumulated with eight empty bunches kept free between the first–second and second–third fills (short gaps) and 38 empty bunches reserved after the third fill (long gap). This SPS 'fill' occupies approximately 30% of the SPS ring. Three fills of the SPS are injected into the LHC with the final one differing in that another bunch train is added from the PS and the long gap is increased by one to 39 bunches. This pattern of $3+3+4=10$ bunch trains is repeated two more times to give 30 bunch trains and finished with another three fills from the SPS to give a total of 39. The pattern is terminated with 119 empty bunches which form the *abort gap*. This 25 ns fill pattern[1] is illustrated in Figure 3.5. Many other fill patterns are also used, such as ones in which bunches in each train are separated by 50 ns.

The clockwise rotating beam is injected between Point-1 and Point-2, while the anti-clockwise beam is injected between Point-1 and Point-8. To receive the 450 GeV beam from the SPS, four 54 kV injection kicker magnets per beam must each reach a field strength of 0.3 Tm with a rise time of only 0.9 μs and hold this field during a flat top of up to 7.86 μs with $\pm 0.5\%$ tolerance [13].

For extraction, beam dumps are located at Point-6. Here at least 14 of the 15 kicker magnets per beam are required to each ramp to 0.43 Tm during the abort gap of

[1]More precisely the bunch separation is 24.95 ns. Rounded numbers are used to due to the limited depth of this discussion of the machine operation.

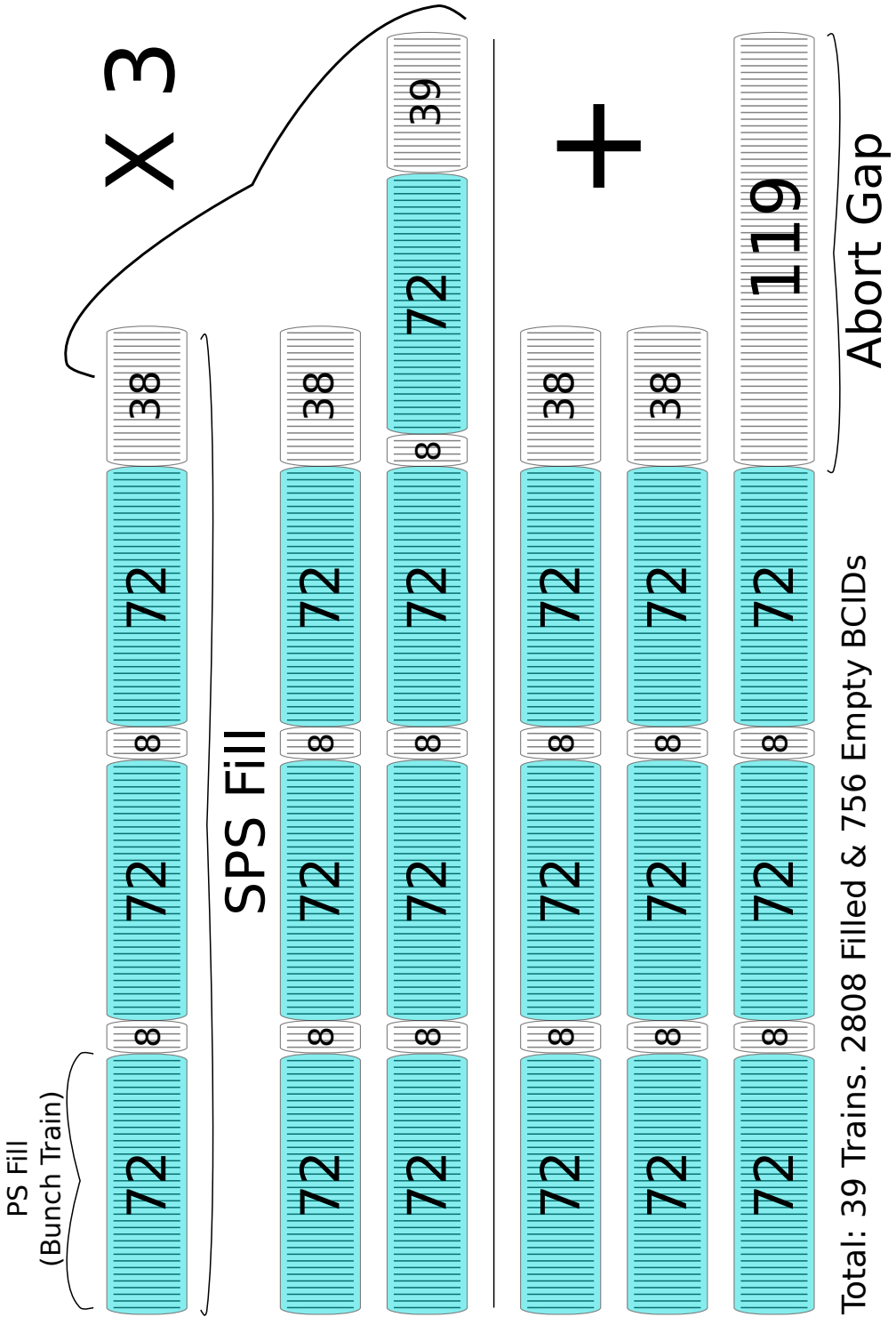

Figure 3.5: Illustration of the LHC 25 ns bunch pattern. The top pattern is of nine bunch trains from three fills of the SPS with an additional bunch train on the end of the third fill. This pattern is executed three times. Nine more bunch trains are then added in three more SPS fills before the abort gap. Overall the 3564 BCIDs are divided into 39 bunch trains comprising 2808 filled and 756 empty bunches.

3 μs and hold the field for an entire revolution, 90 μs [14]. The tunnels to the beam dumps are 600 m long. Dilution magnets are used to sweep the beam into an 'e' shape, which reaches a circumference of 1.2 m, and to increase the Root Mean Square (RMS) spread of the beam from 0.3 mm to 1.6 mm in both planes. The dumps themselves are water cooled carbon cylinders in a stainless steel jacket. They are 7.7 m long and 0.7 m in diameter with 900 tonnes of surrounding shielding. Carbon is used due to its low density and high melting point, the dumps are expected to function after future LHC luminosity upgrades so they must absorb a beam energy of up to 428 MJ. Upon dump, the cylinders will experience a maximum heat loading of 1250 °C.

Beam cleaning occurs at two points on the ring. Betatron[2] cleaning occurs at Point-3, where primary and secondary collimators are placed at 6σ and 7σ from the beam envelope respectively. At Point-7 the beam is cleaned of off-axis particles with a single horizontal primary collimator followed by three vertical secondary collimators. The view down a collimator is shown in Figure 3.6.

3.4 THE ALICE DETECTOR

A Large Ion Collider Experiment (ALICE) [15] is an LHC experiment installed at Point-2. Its primary physics goal is to study in detail the collisions of lead nuclei at 2.76 TeV per nucleon. In such collisions the strongly interacting matter of the nucleus can thermalise into a plasma in which the quarks and gluons are de-confined. ALICE also studies and has published papers on pp interactions [16]. Heavy ion collisions produce very large particle multiplicities with a $\mathrm{dN_{Ch}/d}\eta$ evaluated at $\eta = 0$ of around 1600. Six layers of silicon tracking are installed around the beam line before a large Time Projection Chamber (TPC) covering $|\eta| < 0.9$. This TPC provides the detector with excellent momentum reconstruction and particle identification for $0.1 < p_{\mathrm{T}} < 10$ GeV. The performance is limited, however, by the drift time of

[2]Particle oscillations transverse to the equilibrium orbit in the direction of motion.

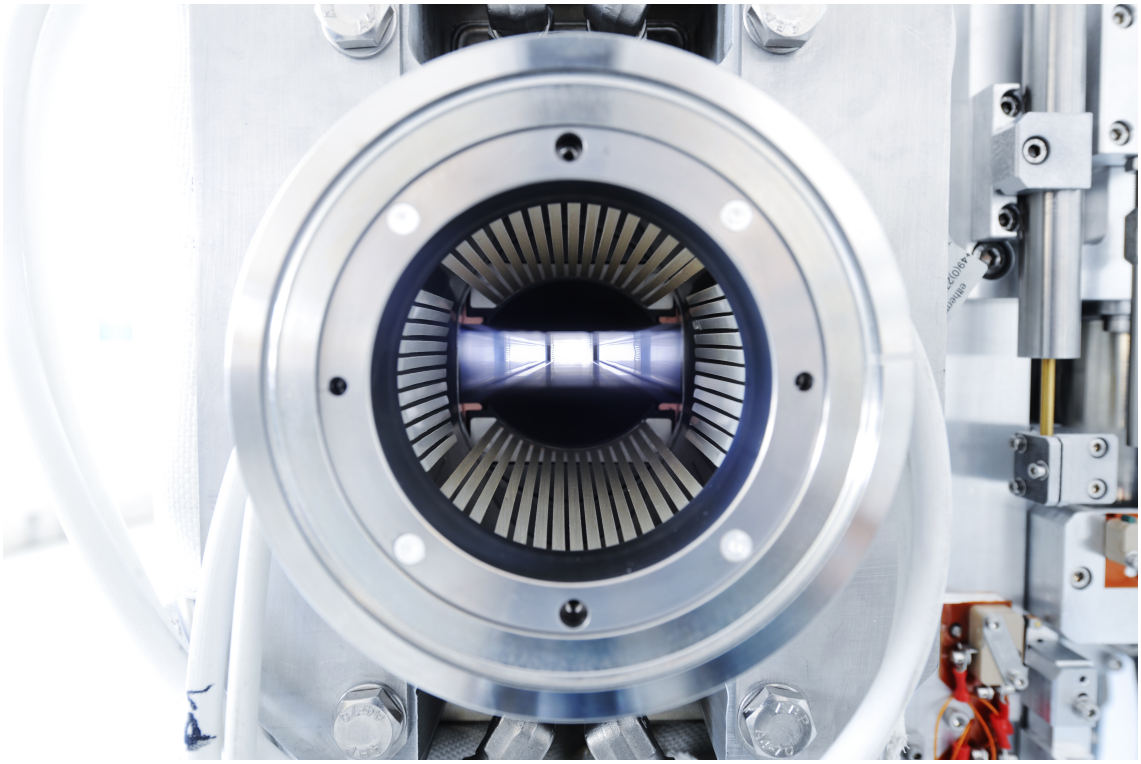

Figure 3.6: Photograph of an LHC collimator. ©CERN.

electrons in the inner volume of 100 μs and hence ALICE de-focus the beams when the LHC is running at high luminosity so as to reduce the interaction rate in the detector.

ALICE is additionally equipped with a Ring Imaging Čerenkov Detector (RICH) for high momentum pion/kaon particle identification, a muon spectrometer for studying the decay of J/ψ and mesons, a partial azimuthal acceptance Electromagnetic (EM) calorimeter and forward multiplicity detectors which also act as timing and centrality triggers.

3.5 THE CMS DETECTOR

The CMS [17] detector is a small volume, high density General Purpose Detector (GPD) with a mass of 12.5 kTonne. It is located at Point-5 of the LHC. The physics

program is comparable to that of ATLAS. At the centre of CMS is a large silicon tracking volume, extending radially out to 1.1 m with up to 14 tracking layers. This is followed by an Electromagnetic Calorimeter (ECal) made of lead tungstate crystals with up to $28.5X_0$ (See Section 4.3.1 for a discussion of X_0 in ATLAS) in the barrel and a Hadronic Calorimeter (HCal) consisting of brass and steel absorbers with plastic scintillator and quartz fibre readout.

The entirety of the calorimetric and silicon tracking systems are contained within a 6 m diameter superconducting solenoid, generating a 3.8 T field at 18 kA. The return yoke for the solenoid is a surrounding iron superstructure which is instrumented with muon detectors.

3.6 THE LHCb DETECTOR

LHC – Beauty (LHCb) [18] differs from the other principle detectors in that it is a forward spectrometer which only tracks particles produced in one direction along the beam axis. To accommodate the detector, the interaction point is displaced by 11.25 m from the nominal centre of the detector cavern. LHCb studies with great precision the decay of b and $\bar{b}$ hadrons to investigate Charge-Parity (CP) symmetry violation in the beauty sector.

Reconstruction of secondary decay vertices is key in studying b-hadron decays. LHCb uses a novel vertex detector which is moved in situ to just 7 mm from the beam, once beam stability has been confirmed by LHC operation. Moving away from the interaction point along the beam axis, LHCb is equipped with a low-momentum RICH and silicon strip tracker at 2–3 m, a dipole bending magnet at 5 m, straw tube tracking at 7 m followed by a secondary high-momentum RICH at 10 m. This is followed by an ECal, HCal and muon stations.

3.7 THE LHCf EXPERIMENT

LHC – Forward (LHCf) [19] is located ±140 m from the ATLAS Interaction Point (IP). When installed in the beam line, it sits upstream of the ATLAS Zero Degree Calorimeter (ZDC) in the copper Target Absorber of Neutrals (TAN). The two arms are similar in design, each containing a 54 X_0 deep ECal allowing for the reconstruction of forward photons up to multi-TeV energies.

LHCf reconstructs the two-photon π^0 invariant mass peak in the ultra-forward region at $\eta > 8.7$. This gives constraints on MC models used to simulate ultra-high-energy cosmic-ray showers [20].

3.8 THE TOTEM EXPERIMENT

TOTal cross section, Elastic scattering and diffraction dissociation Measurement at the LHC (TOTEM) is installed downstream of the CMS detector [21]. It measures elastic pp scattering in the regime $10^{-3} \lesssim |t| \lesssim 10$ GeV^2 where t is the square of the four-momentum transfer. This allows for a luminosity independent measure of the total cross section when combined with the forward inelastic pp rate, it also studies diffractive topologies. TOTEM includes telescopes sensitive to charged particles in the intervals $3.1 < |\eta| < 4.7$ and $5.3 < |\eta| < 6.5$, which are interfaced with the CMS trigger.

The measurement of elastic and diffractive scattering pp cross sections is performed with two sets of silicon detectors housed in Roman pots at 147 m and 220 m, which can measure protons scattered at 5–10 μrad. This requires special run conditions such that the beam divergence is small at the IP compared to the scattering angle. This is achieved using special optics with small emittance and a very large[3] β^* of 1.5 km, such that the beams are as close to plane-parallel with each other as is feasible.

[3]The betatron function at the IP.

Results from TOTEM are discussed later in Section 11.5.

3.9 THE MoEDAL EXPERIMENT

The Monopole and Exotics Detector At the LHC (MoEDAL) [22] detector is installed around the LHCb interaction point. It is designed to search for highly ionising stable or quasi-stable particles with low relativistic β, a characteristic of some exotic theoretical particles such as magnetic monopoles and dyons [23].

Detectors such as ATLAS conventionally assume that the particles they detect are travelling close to the speed of light. With the short trigger window at the LHC of only 25 ns, this implies that a reconstructed particle in the ATLAS central muon chambers will only be associated with the correct bunch crossing ID if its $\beta \gtrsim 0.5$. An additional problem with measuring such particles is that they may be fully absorbed within the detector. To prevent signal saturation, a large dynamic range is required in the electronics measuring energy loss, as magnetic monopoles (in particular) are predicted to have a significantly larger $\mathrm{d}E/\mathrm{d}x$ than electrically charged particles.

MoEDAL detects highly ionising particles using layers of Nuclear Track Detectors (NTDs) in a trigger-less manner. The NTD is etched with equally sized, collinear pits when traversed by highly ionising particles as in Figure 3.7. After the detector has been exposed to around 6 fb^{-1} of integrated luminosity, the NTD will be analysed with optical scanners to identify any pits which are characteristic of highly ionising, massive particles.

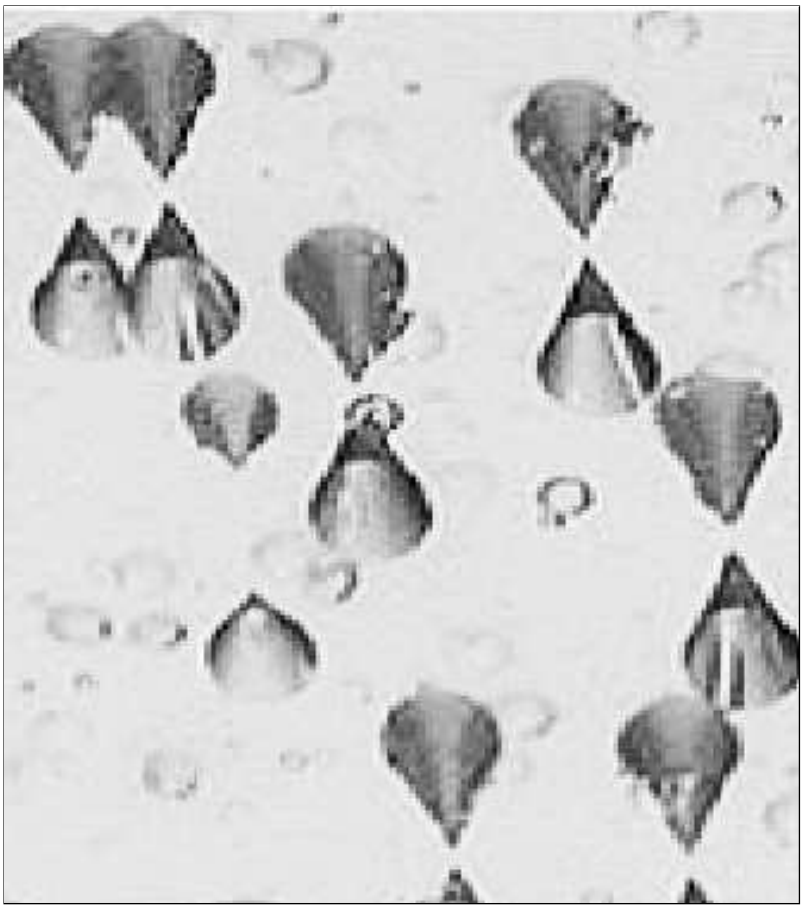

Figure 3.7: Etched biconal (equal area entry and exit) pits in a CR39 NTD. Taken from [22].

CHAPTER 4

THE ATLAS DETECTOR

A Toroidal LHC ApparatuS (ATLAS) (Figure 4.1) is by volume the largest detector installed on the LHC ring. It is forward-backward symmetric and covers almost the entire 4π solid angle. The layout of the central 'barrel' detector forms a leek-like structure with concentric rings of detector layers wrapping around the beam line. The barrel is sandwiched between two endcap regions, where detector layers are fanned perpendicular to the beam line. The following chapter describes the individual sub detectors in more detail. It is based strongly on the ATLAS Technical Design Report (TDR) [24].

4.1 ATLAS MAGNETIC SYSTEM

Large volumes of intense magnetic flux density are required to generate Lorentz forces sufficient to bend the trajectory of high p_{T} charged particles as they traverse

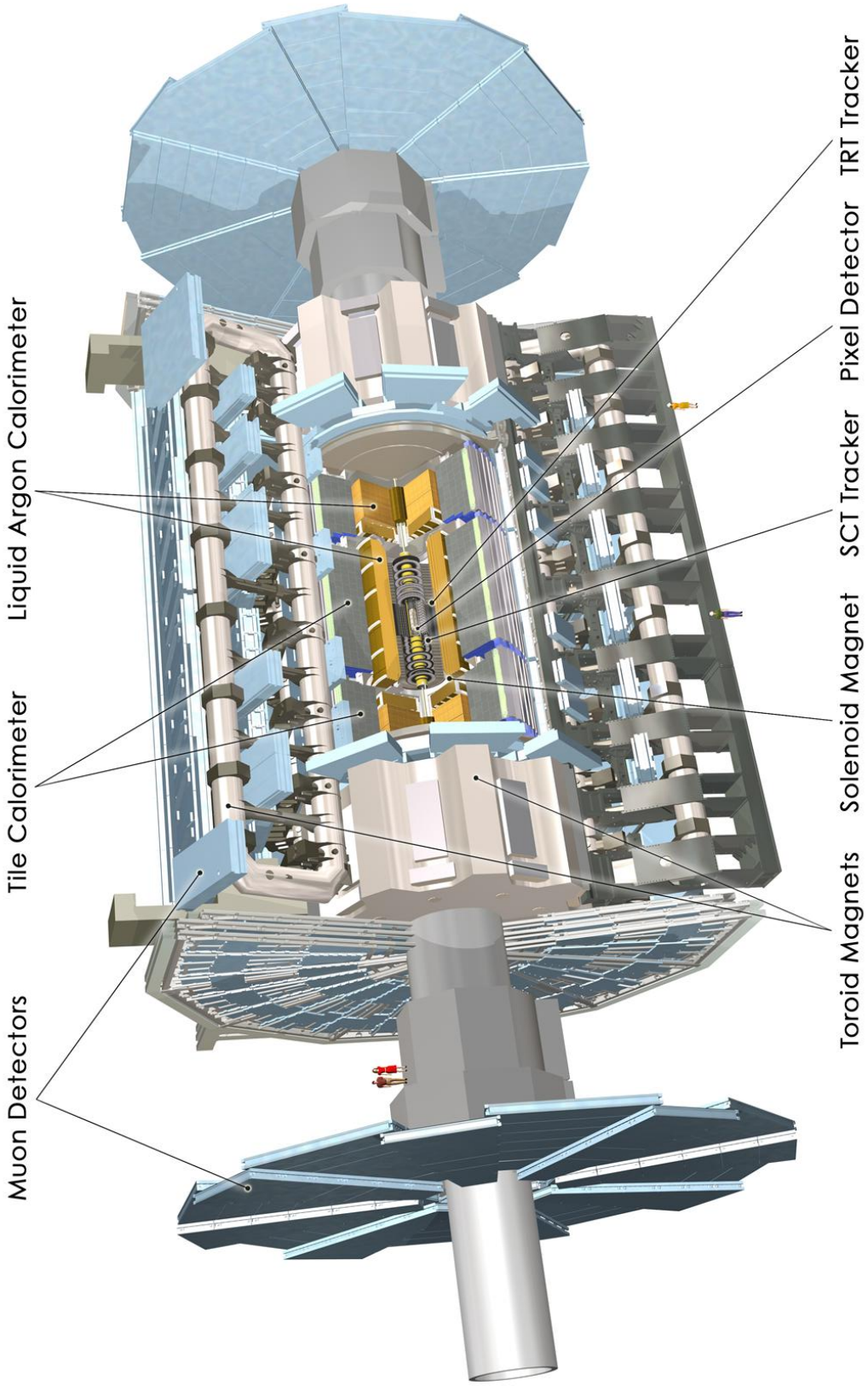

Figure 4.1: Cut-out of the ATLAS detector. The detector is approximately 25 m high, 44 m long and weighs 7000 tonnes. ©CERN.

the detector and hence allow for the reconstruction of their momenta. ATLAS has a complicated magnetic field map, generated by three sets of toroidal magnets and one solenoid.

The solenoid magnet bathes the inner detector in a 2 T axial field when at the nominal current of 7.7 kA in the windings. As the solenoid is placed closer to the beam line than the calorimeters, it must be as thin and light as possible so as to not adversely affect the energy measurements. Located at a radius of 2.46 m, the solenoid is only 10 cm thick and contributes only 0.66 X_0 (see Section 4.3.1). The material budget is minimised by the solenoid sharing a vacuum vessel with the Liquid Argon Calorimeter (LAr). The magnetic flux returns via the steel of the hadronic calorimeter and its support structure.

The three other magnet systems produce a toroidal field which circulates around the outside of the detector, giving a secondary measurement of the momentum of muons which traverse muon chambers located in and around the toroids. The barrel toroid is formed of eight giant 'race-track' coils, supported by eight inner and outer rings of struts, which form much of the mechanical support of ATLAS. When operational, the toroid stores 1.1 GJ of energy and generates a field of up to 2.5 T in the bore. Two endcap toroids generate the field in the forward area. They are supported on movable rails and are removed when the detector is being serviced. The eight coils are contained in a single cold mass, bolted together for rigidity. Figure 4.2 shows one of the endcap toroids during transport to the experimental pit.

4.2 ATLAS INNER DETECTOR

The subdetectors of the inner tracking detector, the Inner Detector (ID) in Figure 4.3, are the closest to the interaction point. The remit of the ID is to provide robust tracking in the high radiation environment produced at LHC luminosities. The tracking systems must provide sufficient resolution to resolve the secondary

Figure 4.2: The ATLAS A side endcap toroid magnet en route to installation. ©CERN.

decay vertices associated with relatively long lived states such as b-hadrons. The ID provides tracking at $|\eta| < 2.5$ with additional electron identification capacity for $|\eta| < 2$ and 0.5 GeV $< p_{\mathrm{T}} <$ 150 GeV. Charged particles down to a p_{T} of 100 MeV are reconstructed in the innermost layers.

4.2.1 PIXEL DETECTOR AND SEMICONDUCTOR TRACKER

The Pixel Detector (PIX) is the innermost tracking detector and as such must be highly resistant to radiation damage. The sensor boards are 250 μm n-type wafers, highly oxygenated to increase radiation tolerance and with pixel readout on the n^+-implanted side. A double sided process was chosen as the n-type bulk effectively becomes p-type after severe irradiation, but the n^+ implant still allows the detector to operate with a good charge collection efficiency even after this type-inversion.

ATLAS contains 1744 PIX boards in three layers. Each layer houses 47232 individual pixels of nominal size 50 $\times$ 400 μm with intrinsic accuracy of 10 μm in $R - \phi$ and

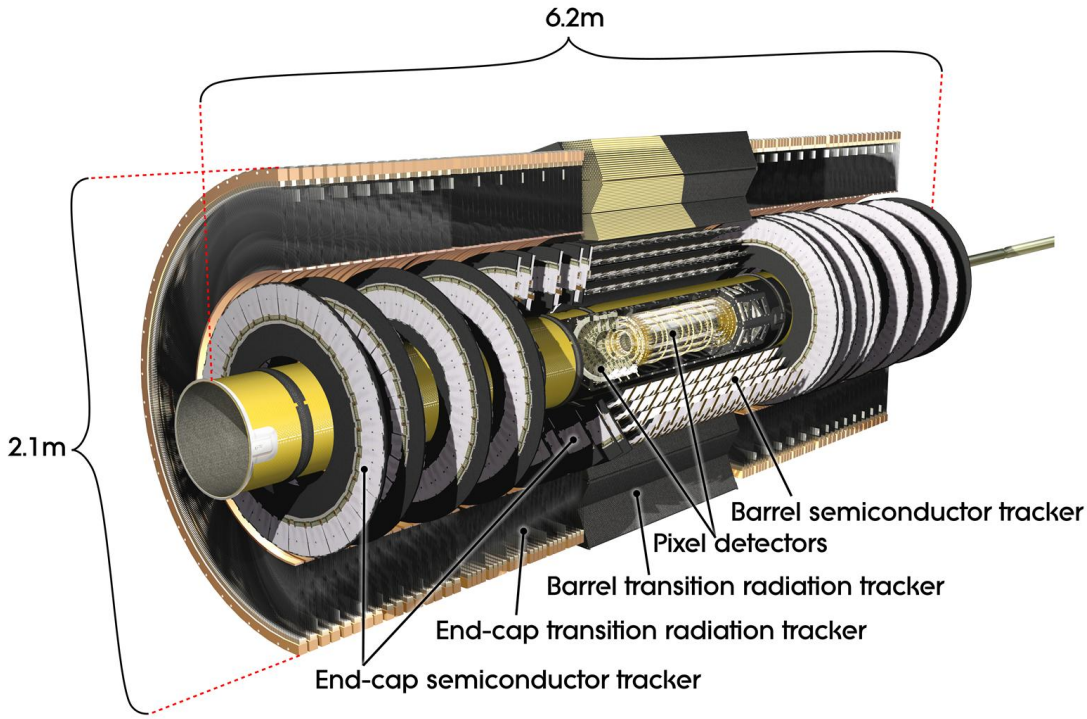

Figure 4.3: Diagram of the ID with subdetectors labelled. ©CERN.

11 μm in z.

The initial bias voltage is 150 V. However this is expected to rise to up to 600 V to maintain a good charge collection efficiency after ten years of operation.

The Semi-Conductor Tracker (SCT) immediately follows the PIX detector. There are 15912 sensor boards installed in ATLAS using a more traditional single p-in-n process for cost reasons. Each SCT barrel sensor consists of two arrays of 768 strip sensors, sandwiched back-to-back with a stereo angle of 20 μrad to give limited information on the point of impact along the strip. The active strips are each of dimension 120 mm by 80 μm, yielding a hit resolution of 17 μm in $R-\phi$ and 580 μm in z (from the stereo). There are three layers of sensors in the barrel and nine in each endcap. The initial bias voltage is 150 V, ultimately expected to rise to 350 V with cumulative irradiation damage equivalent to a 1 MeV neutron fluence of 2×10^{24} cm^{-2}.

4.2.2 TRANSITION RADIATION TRACKER

The Transition Radiation Tracker (TRT) detector is installed after the SCT. It is instrumented with polyimide drift tubes of 4 mm diameter and length 1.44 (0.37) m in the barrel (endcaps). The straws are filled with a 70% Xe, 27% CO_2 and 3% O_2 mixture and each contains a gold plated tungsten anode wire kept at ground. The tubes form the cathodes of the system and are operated at -1530 V. There are 52544 straw tubes in the barrel and a charged particle with $p_T > 0.5$ GeV and $|\eta| < 2.0$ will typically traverse at least 36, with each straw providing 0.15 mm hit position accuracy.

Transition radiation photons are emitted by particles moving between materials of different dielectric constant. These are absorbed by the Xe gas, resulting in a larger signal amplitude than from Minimum Ionising Particles (MIPs). Only electrons have sufficient Lorentz factor, due to their low mass, to produce significant amounts of transition radiation. The TRT front end electronics has separate high-pass and low-pass filters to distinguish between tracking signals and transition radiation. For an electron with $p_T > 2$ GeV, typically seven to ten high-threshold hits are expected.

4.3 ATLAS CALORIMETER SYSTEMS

Calorimeters are installed at ATLAS to absorb electrons, photons and hadrons created in the interaction, measuring their energy in the process. All calorimetric systems installed at ATLAS are of sampling type, where regions of an active sampling medium are alternated with a dense absorber material which promotes and sustains cascading particle showers.

The main ATLAS calorimeters cover the range $|\eta| < 4.9$, utilising a variety of techniques to satisfy the different physics requirements and cope with the varying radiation environment over this large η range. In the central barrel region where there

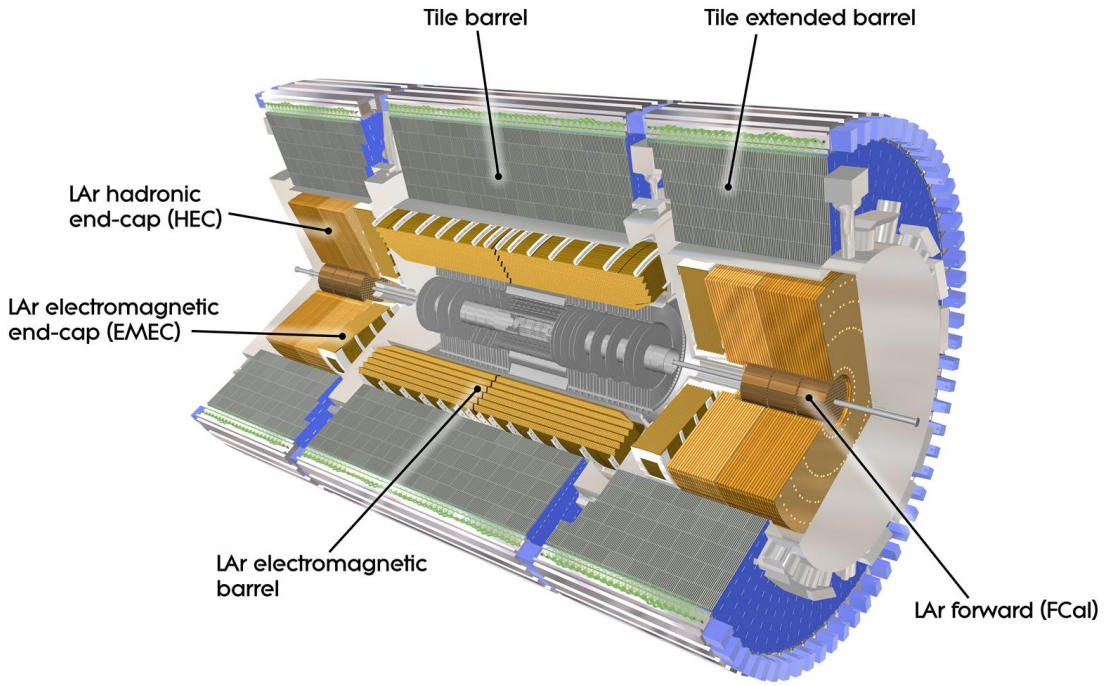

Figure 4.4: Cut away of the ATLAS calorimeter systems. ©CERN.

is overlap with the inner detector, the calorimeters are finely segmented to provide maximum granularity and perform precision measurements of electrons and photons. The rest of the calorimeter is of coarser granularity and satisfies the needs of jet reconstruction and $E_{\mathrm{T}}^{\mathrm{miss}}$ measurements. An overview of the layout of the calorimeters around the ID is shown in Figure 4.4.

4.3.1 ELECTROMAGNETIC CALORIMETRY

The ECal measures the energy of incident electrons and photons. It is LAr-based (Liquid Argon) and consists of three separate modules, the barrel and two endcaps. The detector utilises lead absorbers as its showering medium. The space between the lead sheets is bathed in liquid argon, which forms the active medium and is read out by layers of conductive copper sheets. Liquid argon was chosen for its intrinsic radiation hardness and its stability of response over time. The calorimeter shares a

cryostat with the inner detector solenoid to minimise the amount of inactive material inside the calorimeter and an additional pre-sampler is placed before the solenoid in the region $|\eta| < 1.8$. Both of these measures improve the calorimeter resolution. To provide full hermetic coverage, the calorimeter has a so-called accordion geometry allowing gap-less and symmetric ϕ coverage.

An EM shower is formed when a high energy electron or photon interacts with the dense absorber material in the calorimeter. High energy electrons primarily radiate bremsstrahlung photons, while photons pair-produce into e^+e^-. The characteristic length scale of the interactions is the radiation length, X_0. One X_0 corresponds to $\frac{7}{9}$ of the mean free path of pair production by a high energy photon and the mean distance over which a high energy electron will reduce in energy by a factor e. The number of particles in the shower hence doubles approximately every radiation length. The shower dies away when the mean energy per particle drops below the critical energy for the absorber, E_c, after which, interactions with the calorimeter are primarily through ionisation and Compton scattering. The depth of the shower peak is given by

$$X = X_0 \frac{\ln(E_0/E_c)}{\ln 2}, \tag{4.1}$$

where E_0 is the energy of the initial particle and E_c for lead is 7.43 MeV [25]. The ECal at ATLAS is 22 X_0 deep, which is sufficient to contain all kinematically accessible showers. The transverse width of the shower is characterised by the Molière radius $R_M = X_0 E_s/E_c$, where the scale energy $E_s = \sqrt{4\pi/\alpha} m_e c^2 = 21.2$ MeV [26]. On average, 90% of a shower is contained within a cylinder of radius R_M.

4.3.2 HADRONIC AND FORWARD CALORIMETRY

The HCal calorimeters lie immediately outside of the ECal envelope. ATLAS uses both LAr and steel-scintillator Tile calorimeters in its hadronic system. Hadronic showers are not as collimated as their electromagnetic counterparts. A shower typically consists of an electromagnetic core surrounded by a wider hadronic shower, which

is mediated by nuclear excitation and spallation.

For hadronic showers, the counterpart to the radiation length is the nuclear interaction length, λ_I. This is the length scale which is appropriate for hadronic cascades such that particles reduce in energy by a factor of e per interaction length.

The Tile calorimeter barrel covers $|\eta| < 1.0$ with two extended barrels covering $0.8 < |\eta| < 1.7$. It is another sampling calorimeter, which utilises steel as its absorber and scintillating tiles as the active medium. The total thickness of the calorimeter is 9.7 λ_I.

LAr is also used as the sampling material in the Hadronic Endcap Calorimeter (HEC) due to its radiation hardness, but with copper rather than stainless steel as the absorber. At very high η, a LAr Forward Calorimeter (FCal) is installed in each endcap cryostat. This is a small, high density component which sits in a region with significant energy fluxes from forward particles. It is approximately 10 λ_I deep, consisting of one copper module optimised for EM showers and two tungsten modules for hadronic interactions.

4.3.3 CALORIMETER ENERGY RESOLOUTION

The generic form of energy resolution for a sampling calorimeter is

$$\frac{\sigma_E}{E} = \frac{a}{E} \oplus \frac{b}{\sqrt{E}} \oplus c. \tag{4.2}$$

Here a is the noise term, which is dependent on electronic noise in the detector and pile-up from multiple simultaneous collisions. It is dominant at low energies, < 10 GeV. b is the sampling term and relates to the choice of absorber and active material, plus the thickness of the layers. The sampling term is most important at intermediate energies ≈ 100 GeV. c is the constant term, which relates to the depth of the calorimeter (and hence any leakage out of its rear) and any inhomogeneity from cracks and dead regions. It dominates at high energy. In test beam data, the

ATLAS FCal was shown to perform with $a = (145.5 \pm 1.6)$ GeV, $b = (24.5 \pm 0.84)\sqrt{\text{GeV}}$ and $c = (3.76 \pm 0.06)\%$, exceeding the design goals of the calorimeter [27].

4.3.4 ZERO DEGREE CALORIMETERS

Two ZDCs are installed at ATLAS, ± 140 m from the interaction point where the beam pipe splits from being a single tube through ATLAS to an individual tube for each beam. Two beam pipes are required such that the counter rotating proton beams can continue to be bent in the correct direction. The ZDC sits in slots inside the TAN which is a large block of inert copper shielding. The ZDC detects highly forward ($\infty > |\eta| > 8.3$) neutral particles produced in the interaction. The detector occupies an important region of phase space for heavy ion PbPb collisions where it provides a measure of the centrality[1] of each collision from the detection of forward spectator neutrons[2]. The ZDC is used as the primary trigger of low-centrality events during heavy ion campaigns. For *pp* collisions, the ZDC enhances the acceptance of ATLAS for minimum bias physics and also provides a minimum bias trigger input into the Central Trigger.

When fully installed, each ZDC consists of 1 electromagnetic module 29 X_0 thick, followed by 3 hadronic modules of 1.14 λ_I each. The EM modules consist of 11 tungsten plates transverse to the beam into which are embedded a matrix of 8x12 quartz rods of 1 mm diameter. These lie parallel to the beam and are bent upward at 90° from the back of the tungsten plates to be read out by multi-anode Photo-Multiplier Tubes (PMTs). This gives the position of particles impacting the ZDC.

The EM modules of the ZDC share their slot in the TAN with the LHCf experiment and were not installed during early running. The ZDC is temporarily removed from the beam line during high luminosity *pp* running to minimize radiation damage to the detector.

[1] The elliptical cross sectional overlap of the colliding nuclei.

[2] Neutrons outside the interaction ellipse which are liberated from the nucleus after the interaction.

4.4 ATLAS MUON SPECTROMETERS

High energy muons have a mean decay length of many kilometres in the laboratory frame and are MIPs over a large range of momenta. The muon spectrometer is located outside the calorimeters, where it gives a secondary measurement of the muon momentum based on magnetic deflection in the large air-core volume of the toroidal magnet system. The toroidal field created by the barrel and two endcap toroids is designed to be orthogonal to the flight direction for most muon trajectories. The toroids are instrumented with separate triggering and precision tracking chambers. Three layers of detectors are installed around the barrel as well as in the endcaps, where the detectors are arranged as three planes perpendicular to the beam pipe.

In the barrel, Muon Drift Tubes (MDTs) are used for precision tracking whilst in the endcap Cathode Strip Chambers (CSCs) are used. The MDTs consist of straw tube chambers of 30 mm diameter. Their position resolution is 80 μm. The MDTs upper counting rate of 150 Hz cm^{-2} is exceeded for nominal LHC collisions rates at $|\eta| > 2$, which corresponds to the first layer of the endcaps. Here CSC multi-wire proportional chambers are utilised. Each CSC module consists of four planes, each containing parallel anode wires, with the centre-most wire pointing in the radial direction. Cathode strips are segmented perpendicular and parallel to the wires, with position measurements interpreted from charge induction on neighbouring strips. The CSC has a position resolution of 60 μm in the bending plane and 5 mm in the non-bending direction.

For the fast muon trigger, limited tracking information is transmitted within the fixed 2.5 μs Level 1 (L1) latency whilst also identifying the correct BCID of the muon. The Resistive Plate Chamber (RPC) detector is used for this purpose in the barrel. The RPC operates with two resistive plates separated by 2 mm using insulating spacers which are charged to generate a field of 4.9 kV mm^{-1} in the gas mixture across the gap. This allows for charge avalanches to flow to the anode along ionisation tracks. At the nominal 9.8 kV operational voltage, a signal width

of around 5 ns is generated by an incident MIP.

In the endcaps, the Thin Gap Chambers (TGCs) are used to provide the fast trigger signal and to provide a second measure of the azimuthal coordinate of the muon to complement the MDT. The TGCs are multi wire proportional chambers with a wire-cathode distance of 1.4 mm being shorter than the wire-wire distance of 1.8 mm. Combined with a highly quenching gas mixture, the detector runs in quasi-saturated mode (possessing a gain of 3×10^5 from the gas, relatively low compared to previous TGC implementation). The short drift distances lead to a fast response with 99% of signals arriving within 25 ns. More information on the ATLAS muon trigger is presented in Section 5.2.2.

4.5 LUCID DETECTOR

LUminosity measurement using Čerenkov Integrating Detector (LUCID) provides ATLAS with on-line monitoring of the instantaneous luminosity. It consists of 1.5 m long tubes of 15 mm diameter filled with C_4F_{10} gas, resulting in a Čerenkov threshold of 10 MeV for electrons and 2.8 GeV for pions. There are 20 tubes per side at $\pm$ 17 m from the interaction point, where they surround the beam pipe at a radius of 10 cm ($|\eta| \approx 5.8$). Čerenkov light is read out by a PMT at the end of each tube. The benefit of a Čerenkov detector is that it is possible to determine the number of particles passing through a tube by measurement of the pulse height.

The instantaneous luminosity is measured in situ from the rate of inelastic pp collisions as sampled by LUCID in the forward region, under the principle that the number of particles detected is proportional to the number of inelastic interactions. The calibration and determination of the absolute uncertainty on the luminosity measurement were performed via dedicated van der Meer (vdM) beam scans [28]. During a vdM scan the beams are stepped through each other in both x and y. The fits to the Gaussian beam profiles allow for the absolute luminosity to be derived

from the beam optics via the equation

$$\mathcal{L} = \frac{n_b f_r n_1 n_2}{2\pi \Sigma_x \Sigma_y}. \tag{4.3}$$

Here the luminosity $\mathcal{L}$ is a function of the number of bunches n_b, the revolution frequency f_r, the numbers of protons per bunch in each beam n_1, n_2 and the widths of the Gaussian beam profiles Σ_x, Σ_y [29].

LUCID also provides an input into the Central Trigger Processor (CTP), allowing it to trigger a subset of events for further off-line analysis.

CHAPTER 5

TRIGGERING AND DATA ACQUISITION

The interaction cross sections for many physics signatures of particular interest at $\sqrt{s} = 7$ and 14 TeV have the tendency of being extremely small, picobarns and smaller are not uncommon figures. The cancelled Superconducting Super Collider (SSC) project in Texas, USA would have enhanced the cross section of these rare processes by colliding at a significantly larger energy, $\sqrt{s} = 40$ TeV. The LHC project, however, took an alternate approach and exchanged high collision energy with high collision intensity. The LHC has a design instantaneous luminosity, $\mathcal{L} = 10^{34}$ cm^{-2}s^{-1}, which is an order of magnitude larger than planned for the SSC.

The onus falls on the detectors installed around the LHC to operate at this collision rate and efficiently filter and store 'interesting' events in challenging environments. This chapter will explore the mechanisms by which events are triggered by the detector and will follow the real-time data path the ATLAS data take until they are written to disk for permanent storage.

Particular focus will be given to areas on which I have worked, Level 1 Calorimeter Trigger (L1Calo) and the minimum bias trigger.

5.1 ATLAS TRIGGER ARCHITECTURE

The Trigger and Data AcQuisition (TDAQ) architecture is responsible for selecting events from the detector that are deemed to be of interest. At nominal design conditions, proton bunches cross in ATLAS every 25 ns[1] with upward of 30 [30] interactions per crossing. Multiplied by an average event size of 1.5 Mb, this gives a data rate of 1.5 Pb s^{-1}. The trigger must reduce this flood of commonplace interactions to a trickle of rare processes and stay within the allowed transfer rate to hard disk of $300 - 600$ Mb s^{-1}. This reduction of rate by a factor 10^5 is achieved using a three tier trigger system comprising L1 followed by Level 2 (L2) and finally the Event Filter (EF). EF triggers are seeded off of L2 triggers whilst L2 triggers seed off of L1 and the trigger operates *step wise* processing. This means that events are rejected as soon as they no longer meet any of the requirements of the current trigger menu. Figure 5.1 contains a flow diagram of the trigger.

5.2 FIRST LEVEL TRIGGER

The L1 trigger performs fast, coarse, analysis of every event within a fixed latency of 2.5 μs. This latency budget comes from the front-end electronics in the detector, which operate a 100 bunch crossing digital pipeline memory. The pipelines are used to buffer the full data from each event while the L1 decision is calculated. If the event is to be kept, the front-end electronics are signalled to retrieve and transmit the event data from the pipeline.

[1]It should be emphasised that 25 ns at the speed of light equates to only 7.5 m, so when one pair of bunches are colliding, the next pair are already at the innermost muon station and are just about to traverse the calorimeter systems.

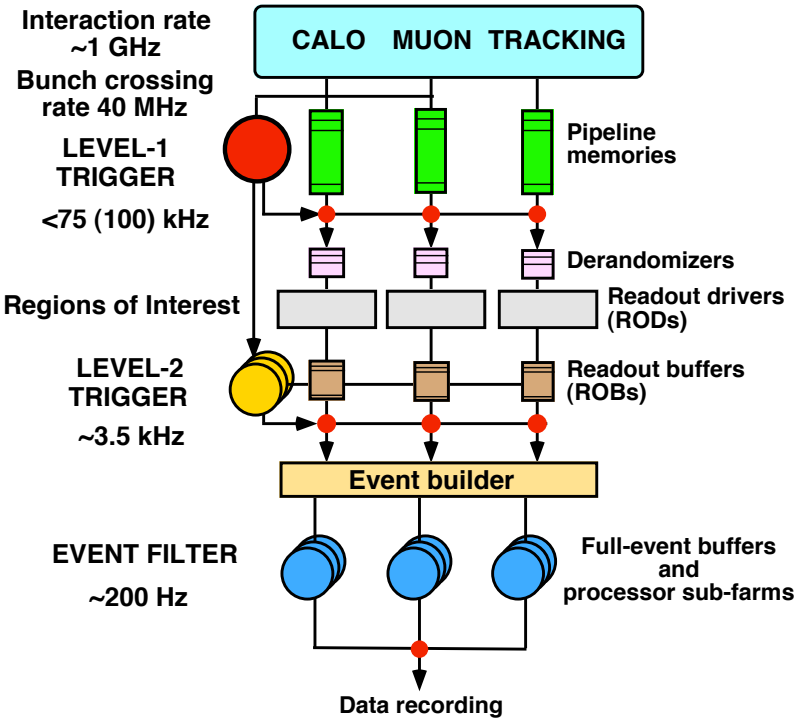

Figure 5.1: Schematic overview of the ATLAS trigger systems. Taken from [31].

The CTP decides which events to keep. It issues a Level 1 Accept (L1A) whenever an event has met sufficient criteria to pass its selection. The CTP bases its decision on internal logic and external subsystems, the primary contributors being the Level 1 Calorimeter Trigger (L1Calo) and the Level 1 Muon Trigger (L1Muon). These L1 systems and additional minimum bias infrastructure with input to the CTP are described below.

5.2.1 LEVEL ONE CALORIMETER TRIGGER

L1Calo utilises fast pattern recognition to locate local energy maxima in the calorimeter subsystems. It is described in detail in the ATLAS L1 trigger TDR [31].

L1Calo is implemented entirely in hardware, making heavy use of algorithms programmed into Application Specific Integrated Circuits (ASICs) and Field Programmable Gate Arrays (FPGAs). Analogue data from the calorimeter sub-systems are summed using dedicated on-detector electronics to form trigger towers. There are 7168 such

towers with a typical granularity of 0.1×0.1 in $\eta - \phi$.

The data are digitised in Analogue-to-Digital Converters (ADCs) within PreProcessor Modules (PPMs) at the bunch crossing rate of 40 MHz and digital signal processing is applied. As the pulse width from the calorimeters is significantly longer than a bunch crossing, a Finite Impulse Response (FIR) filter is used to perform BCID. A Look-up Table (LUT) is then used to apply noise suppression and pedestal subtraction, resulting in an 8-bit output value corresponding to approximately $E_{\mathrm{T}} \approx 1$ GeV per count. This digitised energy acts as the input to the Cluster Processor Modules (CPMs) and (after some additional summing of 2×2 trigger towers into jet elements) the Jet Energy processor Modules (JEMs). A schematic overview of L1Calo is presented in Figure 5.2

5.2.1.1 CLUSTER PROCESSORS

The CPMs identify local energy maxima utilising a *sliding window* algorithm illustrated in Figure 5.3. The input from the PPMs to the CPMs is a 2 dimensional array of trigger towers in η and ϕ, each with an E_{T} value from the EM and hadronic layers. The sliding window is 4×4 trigger towers in size, equating to 16 towers from both the EM and hadronic calorimeter layers (32 total). This search window is sequentially shifted such that every tower occupies each of the 16 positions in the window once per event. Local energy maxima are identified and *declustering* is applied to resolve ambiguity which may arise as a consequence of overlapping window arrangements.

The search operation is parallelised using many CPMs, each responsible for a small section of the trigger tower array. The CPMs are contained within four crates, each of which looks at data from $\frac{\pi}{2}$ of the azimuth. Each crate contains 14 CPMs with individual modules scanning their sliding windows over a (4×16) region of trigger towers; though this requires data from a (7×19) region to cover all possible window arrangements. When energy values for trigger towers close to boundaries are needed by CPMs from more than one crate, the data are duplicated at the output of the

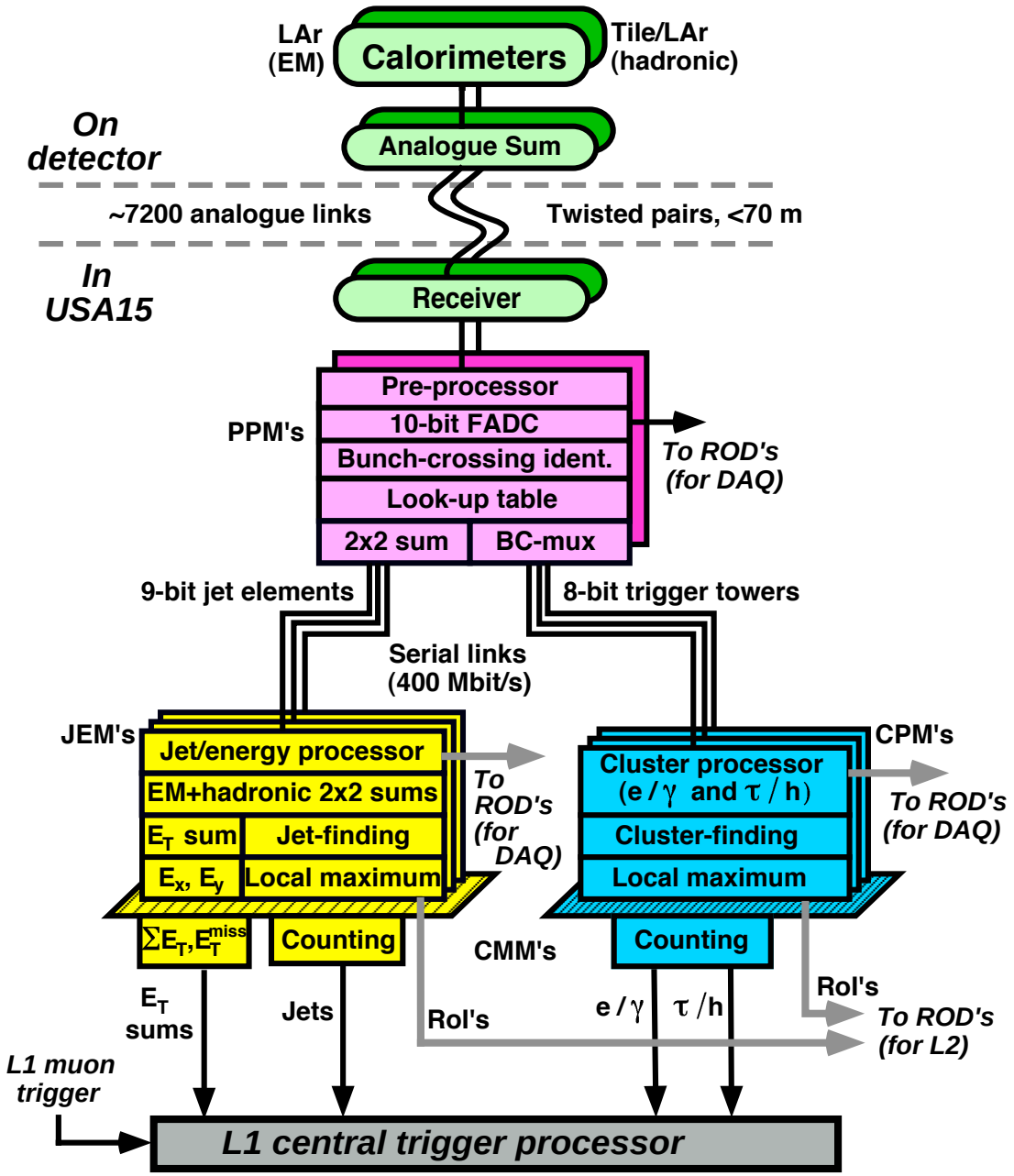

Figure 5.2: Architecture of the L1Calo system. The black data paths represent the real-time data flow while the grey data paths represent additional output to be utilised by the High Level Trigger and to be recorded by the readout systems. Taken from [31].

PPM and fed separately to two crates.

Data are also shared between the modules within a crate over a custom backplane. This data duplication is referred to as the *fan out* and amounts to a fundamental design limitation on the complexity of the system given the amount of programmable logic which was commercially available on ASIC chips at the time of construction.

5.2.1.2 JET/ENERGY PROCESSORS

The input to the JEMs is a coarser array of jet elements with 9-bit E_{T} resolution (range $\approx 0-512$ GeV). A jet element is a sum over (2×2) trigger towers and is the base processing element in the JEMs. The choice of jet finding algorithm is flexible and dependent on a number of criteria, including the amount of pile-up and the E_{T} scale of interest. The size of the sliding window is set per threshold to (2×2), (3×3) or (4×4) jet elements as required to fulfil the current physics goals.

There are 32 JEMs, split between two crates. The sliding window algorithm is implemented on FPGAs rather than ASICs as the number of required modules did not justify the cost of ASIC development. Fan-out of the jet elements follows a similar strategy to that discussed for the CPMs

The secondary function of the JEMs is to calculate the global sums of scalar $\sum|\vec{E_{\mathrm{T}}}|$ and $|\sum\vec{E_{\mathrm{T}}}|$, hereafter $E_{\mathrm{T}}^{\mathrm{miss}}$. For scalar-$E_{\mathrm{T}}$, the E_{T} values of all the jet elements including the FCal are summed. For the $E_{\mathrm{T}}^{\mathrm{miss}}$ sum, LUTs are used to multiply by $\cos(\phi)$ and $\sin(\phi)$ to form $\vec{E}_x$ and $\vec{E}_y$. A third LUT then converts these to $E_{\mathrm{T}}^{\mathrm{miss}}$.

5.2.1.3 L1CALO OUTPUT

The results of the sliding window algorithms are collated by Common Merger Modules (CMMs) which count multiplicities for different object types above E_{T} thresholds. For the cluster processors, multiplicities are formed for electron/photon and for

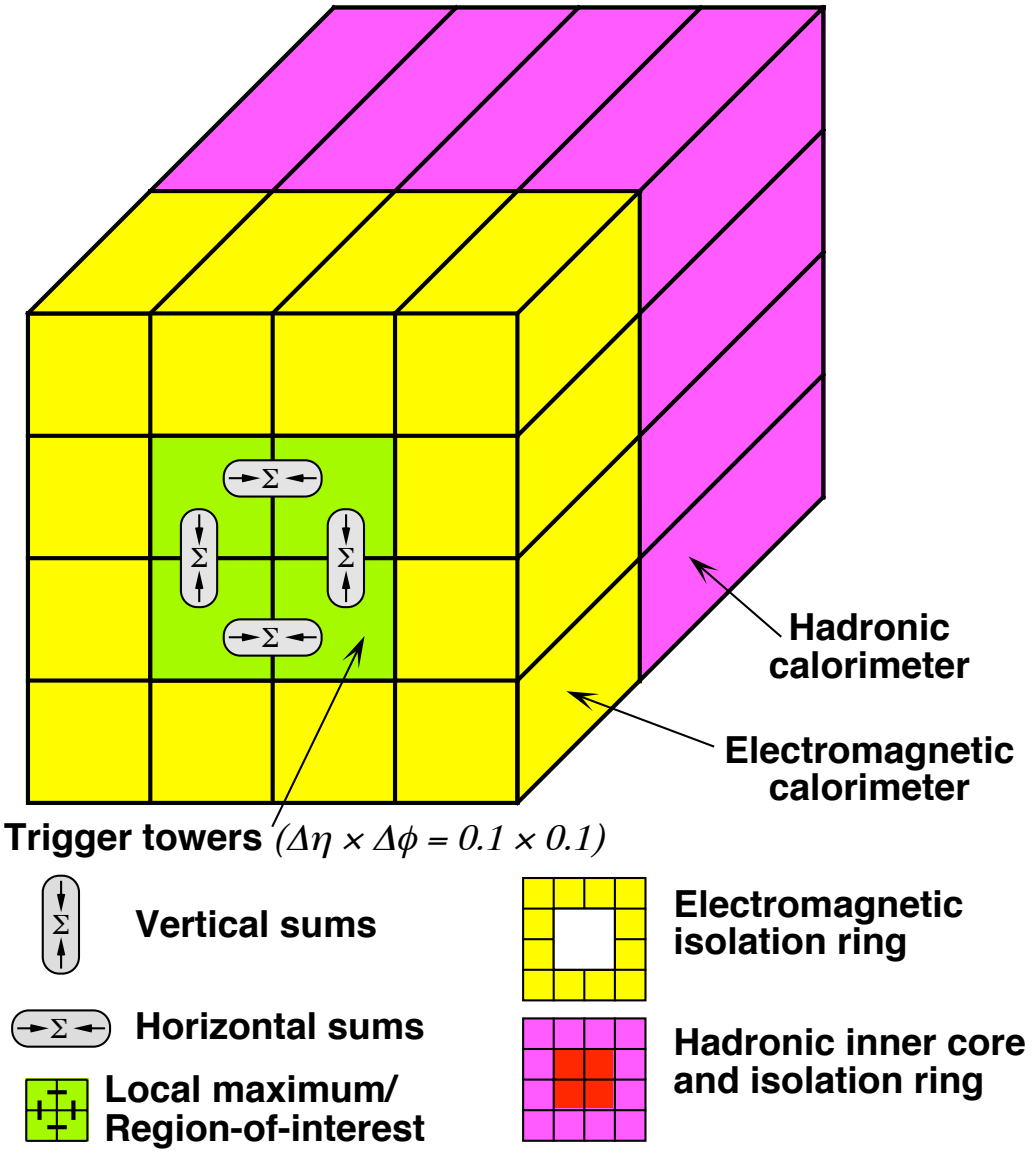

Figure 5.3: Sliding window electron/photon and tau/hadron algorithm. The windows location on the trigger tower array is permuted such that each tower lies once in each of the 16 positions. Local maxima of energy are identified. Taken from [31].

tau/hadron objects, with each discriminated against eight E_{T} thresholds. The difference between the two cases is that for tau/hadron objects, energy is summed in both the EM and hadronic calorimeters while for electron/photon objects only the EM information is used. There is also the possibility to define electron/photon objects as *isolated* by applying an energy veto in the EM ring surrounding the local maximum and in the hadronic layer behind.

For the jet/energy processors, eight different jet object threshold are again used, each having the option of utilising a different window size. These 24 multiplicities of object and threshold are each stored as a 3-bit integer, hence taking the range 0 – 7, and transmitted to the CTP. An example signature, `EM20`, corresponds to a 20 GeV EM object. The global event value $E_{\mathrm{T}}^{\mathrm{miss}}$ has eight thresholds while scalar-E_{T} has four. These are transmitted to the CTP as a 12-bit bitmap. All of the above occurs in parallel at the 40 MHz bunch-crossing rate. The data rate to the CTP from L1Calo is therefore 3.36 Gbit s^{-1}.

5.2.2 LEVEL ONE MUON TRIGGER

L1 Muon utilises two fast trigger technologies, the RPC in the barrel and the TGC in the endcaps (Section 4.4 for details). The geometry is such that most muons will traverse three tracking stations, each with sufficient timing resolution to identify the correct bunch crossing. The hardware which implements the algorithms is partly located on the detector and partly in the service cavern. Muons are located by searching in a road extrapolated from seed hits. The size of the road is dependent on the p_{T} of the muon. The coincidence logic allows for three low p_{T} thresholds ($\approx$ 6–9 GeV) and three high p_{T} thresholds ($\approx$ 9–35 GeV). These are combined into one set of six muon threshold multiplicities, which is transmitted to the CTP.

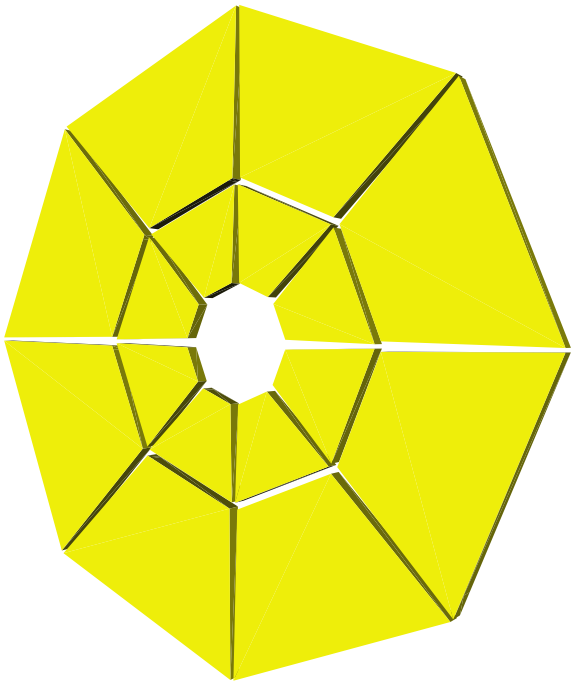

Figure 5.4: Layout of the 16 counters making up one side of the MBTS detector. The beam pipe runs through the gap in the middle.

5.2.3 LEVEL ONE MINIMUM BIAS TRIGGER

Trigger inputs are supplied from various sub detectors which are sensitive to inelastic proton interactions and can hence be used for minimum bias studies [32].

The Minimum Bias Trigger Scintillator (MBTS) is a sensitive detector designed to trigger on low momentum charged particles from inelastic proton interactions with the minimum possible bias. It consists of 2 cm thick polystyrene scintillator counters located $\pm$ 3.56 m away from the nominal IP in z. Each side is divided into two rings, with the inner and outer segments covering the pseudorapidity ranges $2.82 < |\eta| < 3.84$ and $2.09 < |\eta| < 2.82$, respectively. Each ring is further subdivided azimuthally into eight equal sized counters; giving a total of 16 counters per side as visualised in Figure 5.4.

The light yield from the MBTS is read out via PMTs along wavelength shifting fibres. Standardised Nuclear Instrumentation Module (NIM) [33] electronics are used to amplify and discriminate the signal. The MBTS signals are input into the CTP which

calculates L1 trigger items based on the multiplicity of counters above threshold on either side of the detector and triggers the event if certain criteria are met as described in more detail in Section 5.2.4.

The MBTS can supply up to 32 inputs, one for each counter. However this configuration was primarily used during MBTS commissioning as it takes up a lot of CTP inputs, of which there is a finite supply. The input was therefore changed to the summation of counters above threshold on the A and C sides of the detector, i.e. two inputs.

Additional inputs are present from LUCID, the Beam Condition Monitors (BCM), the Beam Pickup Detector (BPTX) and the ZDC which together form a range of triggers sensitive to soft proton interactions which span different regions of the solid angle with varying sensitivity.

5.2.4 CENTRAL TRIGGER PROCESSOR

The CTP accepts the above mentioned *trigger inputs* and provides some additional internal inputs. There are two random trigger inputs, referred to as `RD0` (high rate) and `RD1` (low rate). In addition there are two prescale clocks and eight bunch group triggers. Bunch groups are a novel concept developed by ATLAS, each item in the L1 trigger menu is combined with an appropriate bunch groups such that the menu remains independent from the specifics of the LHC fill pattern. Details of the eight bunch groups are given in Table 5.1, see Section 3.3 for details on the bunch structure.

The L1 *trigger menu* is comprised of up to a hardware limit of 256 *trigger items*, each of which is a logical combination of one or more *trigger inputs*. Each *trigger item* also possesses a priority and a prescale factor. The priority is either *high* or *low* and affects the dead-time as discussed below in Section 5.2.6, while the prescale factor is used to suppress and control the rate of common signatures in a manner

Table 5.1: Description of the eight bunch groups and their uses. A bunch group is a non-exclusive collection of BCIDs derived for a given run from the LHC fill pattern. They are combined with the trigger menu.

ID	Name	Description
BGRP_0	BCRVeto	Every BCID except for the reserved bunches which form the abort gap, used by the LHC to safely dump the beams.
BGRP_1	Filled	Physics bunch group, BCIDs with two colliding bunches.
BGRP_2	CalReq	Long gap, empty bunches. Used for laser calibration.
BGRP_3	Empty	Empty BCIDs for cosmics, noise and background studies. No overlap with BGRP_7
BGRP_4	IsolatedUnpaired	Unpaired (exactly one bunch, in either beam) BCIDs with separation of at least three bunch crossings from any other bunch.
BGRP_5	NonIsolatedUnpaired	Unpaired BCIDs which do not satisfy BGRP_4.
BGRP_6	EmptyAfterPaired	Empty BCIDs immediately following a filled bunch.
BGRP_7	AllUnpaired	The union of BGRP_3 and BGRP_4, for noise and background studies.

which is adjusted to match the instantaneous luminosity.

If one or more item passes the trigger logic, dead-time, and prescale requirements, then a Level 1 Accept (L1A) signal is broadcast to all sub-detectors. The L1A is received by sub-detector-specific Read-Out Drivers (RODs) which interface with their front-end electronics. Each ROD gathers a data fragment for the event from its associated digital pipeline memory and transmits this optically to its corresponding Read-Out Buffer (ROB).

The L1 trigger reduces the data rate from the bunch crossing rate of 40 MHz down to around 75 kHz. 120 GB s^{-1} of data fragments from events triggered by the CTP are transferred into the Read-Out System (ROS) from where they are accessible to the High Level Trigger (HLT). The L1 trigger operates at a latency of 20.6 μs with an additional 4.4 μs available redundancy at the front-end digital pipelines. Table 5.2 lists the latency of the L1 subsystems.

5.2.5 REGIONS OF INTEREST

Upon issue of an L1A, higher granularity information is requested from the RODs contained within the L1Calo and L1Muon subsystems. The geometric coordinates of the trigger objects which pass thresholds in both systems are transferred to the Region of Interest Builder (RoIB). A Region of Interest (RoI) specifies an (η, ϕ) coordinate along with the corresponding L1 threshold which was passed. These are sent directly to the Level 2 Supervisor (L2SV) discussed in Section 5.3.

The CTP also acts as a ROD, transmitting information about several bunch crossings which is used to monitor the system.

Table 5.2: Table of latencies in the L1 systems measured in bunch-crossings of 25 ns with additional breakdown for the L1Calo system. This is a massively parallelised operation, which is factored into the total latencies being shorter than the sum of their individual components. The overall calorimeter trigger latency of 56.1 BC is from the latencies sums for the cables, JEM preprocessor and sum E_{T} calculation.

	Latency Contribution (BC)	
Muon Trigger	**54.0**	
Calorimeter Trigger	**56.1**	
Cables to PPMs		20.6
Preprocessor for CPMs (e/γ, τ/h)		15.0
Preprocessor for JEMs (jets,E_{T})		17.0
Electron/photon hunting		14.0
Tau/hadron hunting		14.0
Jet hunting		18.0
$E_{\mathrm{T}}^{\mathrm{miss}}$ calculation		18.5
Scalar E_{T} calculation		18.5
CTP	**4.0**	
Trigger Timing and Control (TTC)	**3.1**	
Fibres to front-end electronics	**16.0**	
Receivers for front-end electronics	**3.0**	
Total Latency for L1A to reach all RODs	**82.2**	
Digital Pipeline Length	**100**	

5.2.6 DEADTIME

Dead-time is the time during which the detector is unable to read out a new event due to being busy handling a previous one. There are two types of dead-time generated by the CTP, referred to as simple and complex. Simple dead-time is a minimum period of four bunch crossings immediately following an L1A during which the ROS is busy transferring an event from the detector to the ROBs. During this time, no additional L1As are issued.

Complex dead-time is the consequence of a limit which is applied to the number of L1As issued by the CTP within a short time frame, so as to not overload the ROBs. The CTP achieves this by implementing a 'leaky bucket' algorithm. Each L1A causes an event to be placed in an hypothetical bucket and events leak from the bucket at a fixed rate. Dead-time occurs when the algorithm vetoes new triggers, this happens if the bucket has grown sufficiently full. There are two such complex vetoes which are activated at different thresholds and therefore allow separate limitations on low-priority and high-priority L1 trigger items to be defined.

5.3 SECOND LEVEL TRIGGER & EVENT BUILDING

The L2 trigger is managed by the Level 2 Supervisor (L2SV). New events are assigned as they arrive to a free Level 2 Processing Unit (L2PU) for processing. Event fragments are collated and L2 algorithms are executed on the L2PUs in software. The L2PUs generally requests fragments topologically associated with the RoIs in the event. These are transferred over the dedicated Level 2 Network (L2N) with more fragments available on request, depending on the design and complexity of the algorithm. On average, a decision is reached within 40 μs. Events which do not pass at least one L2 algorithm chain are rejected and their data fragments removed from the ROB.

Events which do pass L2 processing are communicated to the Data Flow Manager (DFM) via the L2SV, this signals that the event is to be fully built. The DFM controls data flow in the Event Building Network (EBN), which is connected to the L2N via a network switch. A Sub-Farm Input (SFI) is assigned to build each event accepted by L2. It collects all of the data fragments for the event from the ROBs and holds the fully built event in memory.

The L2 trigger results in a factor of 25 reduction in event rate, reaching an output of around 3 kHz.

5.3.1 EVENT FILTER

The EF is the final stage of trigger processing. Fully built events from a SFI are sent to a free Event Farm Processor (EFP) where information on the whole event is available. Similarly to at L2, the EF algorithms in general only process in the vicinity of the RoIs for each event but have access to finer alignment and calibration constants, along with a more detailed model of the detector.

It takes 4 seconds on average for an EFP to process an event. If the event passes at least one trigger chain then information from the EF is appended to the event and a signal is sent to transfer the event to the Sub-Farm Output (SFO). Events are accepted by the EF and saved permanently at an average rate of the order 200 Hz, the limiting factor being the output bandwidth with each built event amounting to around 1.5 Mb of data.

5.3.2 STREAMING

Events passing the EF are assigned to one ore more inclusive *streams*. Streaming allows for physics events with similar characteristics (such as muons, EM objects) to be grouped together for the purpose of later simplifying physics analysis, at

the expense of some data duplication. Calibration streams are also defined, which generally only contain data relevant to the operation of specific sub detectors and are integrated into the detector operation. The express stream is an additional physics stream which contains a representative mix of physics events being taken by the trigger menu. The express stream writes out at approximately 10 Hz and is used to both calibrate the run offline and to assess the data quality.

Data are grouped into runs and luminosity blocks. A run will typically coincide with an LHC fill and will last up to 12 hours, which is approximately the lifetime of the beam in the machine. More than one run may be taken during a fill if data taking has to stop temporarily due to a hardware or software fault. The luminosity block normally changes every two minutes throughout the run. Alternatively a new luminosity block is forced to start upon the modification of detector conditions during a run such as changing the trigger menu or recovering a tripped ROD. The integrated luminosity is calculated for each luminosity block.

CHAPTER 6

ATLAS COMPUTING

From disk to analysis, a complete software framework is required to manipulate the recorded data and apply corrections. Finally extracting physics results from the data.

ATLAS utilises a globally distributed computing framework to store, process and analyse data produced by the detector and MC simulations. Due to the unprecedented amount of data produced by the experiment and associated simulation campaigns, it is impractical for institutes or even entire countries in most cases to hold and process local copies of the data. Rather, a distributed LHC computing grid [34] is used to provide a top-down computing infrastructure originating from CERN which utilises storage and computational capacity on a global scale.

Data distribution and processing occurs over multiple tiers of computing centres, Tier-0 is located in the CERN computing centre and is where the data are streamed to from all LHC experiments. Data from ATLAS is reconstructed initially at Tier-0.

The *express* stream (see Section 5.3.2) is reconstructed first, during the so-called 36–hour calibration loop. The reconstructed data of the *express* stream is sent to the CERN Analysis Facility (CAF), where calibration constants for the run are derived and data quality is checked with monitoring histograms. Examples of calibration procedures are the locating of the beam spot[1] and the identification of any dead channels from hardware malfunctions during the run. These calibration constants are updated in a 'conditions' database. The *bulk* of the data for the run, consisting of all other physics streams, is reconstructed at Tier-0 after this calibration loop.

Tier-1 sites are generally located, one per participating country, at national institutes. They connect to Tier-0 at CERN via dedicated 10 Gb s^{-1} links. Tier-1 sites hold partial or full replicas of the ATLAS dataset and contribute significant computational power to the data processing infrastructure, such as the re-reconstruction of data and MC events with newer software caches.

The third level, Tier-2 sites are hosted mainly at universities and other technical institutes which are involved with CERN. Tier-2 sites hold a sub-set of ATLAS data and MC, with focus on the data formats used by physicists to perform their analyses. These sites run the majority of end-user jobs. The load is balanced automatically such that more popular data sets are replicated to more Tier-2 sites.

Under the ATLAS computing model, authorised ATLAS physicists can submit physics analyses to run over any part of the data set. The analysis code is transmitted to a remote site where the data are located. Once the analysis job has completed, the output of the analysis is copied back to the user.

6.1 ATLAS SOFTWARE FRAMEWORK

The ATLAS software framework is named ATHENA [35], it has been built upon an existing framework called Gaudi. Individual software packages are written in C++

[1] The luminous volume from which the majority of interactions originate.

and Python and the package structure is managed by the Configuration Management Tool (CMT). Packages with similar scope and inter-dependence with each other are grouped into projects, for example `AtlasTrigger` and `AtlasReconstruction`.

6.2 EVENT STORE

Different file types are defined for data which have received differing amounts of post-processing after leaving the detector. A schematic illustration of how the data are processed on the different tiers of the LHC grid is presented in Figure 6.1. The formats are briefly described below.

RAW: The RAW, otherwise know as Byte Stream (BS), data are the output of the TDAQ systems. As such the size of RAW output remains fixed and does not depend on luminosity. RAW is the input to the prompt event reconstruction at Tier-0 and is replicated to Tier-1 sites.

ESD: Event Summary Data (ESD) files contain the output of the ATLAS reconstruction algorithms, but also retain the detector hit information which forms the input to the reconstruction. As such, it is possible to re-reconstruct ESD files when required, due for example to modified parameters or a more recent software cache. This also makes them the largest file format and their size increases with luminosity due to the increased complexity in the reconstructed output of events with high pile-up. An ESD has a typical size of 2 Mb per event and utilises the Pool Of persistent Objects for LHC (POOL) ROOT Data Analysis Framework [36] format. They are replicated to Tier-1 sites in addition to the RAW files.

AOD: The Analysis Object Data (AOD) format is a sub-set of the ESD, containing only the final reconstructed, abstracted quantities which are used in the majority of physics analyses. As a result they are around an order of magnitude smaller than their equivalent ESDs but retain the same object-oriented POOL ROOT structure. AODs are largely replicated to Tier-2 sites for user analysis.

Derived Files: The derived DESD and DAOD data formats have undergone a selection process and therefore no longer correspond one-to-one with their respective RAW files. The selection processes, some or all of which may be employed are: *Slimming* - removal of parts of an object which are not needed, for example the error matrices of a reconstructed track, *Thinning* - removal of whole objects from a container, such as all calorimeter clusters not in the vicinity of reconstructed jets, *Trimming* - removal of whole containers, such as the entire calorimeter cluster container and *Skimming* - removal of whole events. These selection criteria are carefully controlled by physics analysis groups so as to construct datasets which are the most applicable as inputs to their analyses.

TAG: Tag Data (TAG) files contain simple meta-data on each event, such as the multiplicities of reconstructed objects. This is stored in a ROOT ntuple and imported into a database to allow quick querying of the number of events available for a given selection.

Flat Ntuples: Also known as Derived 3$^{\text{rd}}$ level Physics Data (D3PD) (D1PDs and D2PDs are deprecated). Many different layouts of flat[2] ntuples exist, targeting one or a set of analyses. They are typically generated by physicists for their analysis or by physics groups. Ntuples are constructed from regular or derived AODs, ESDs or from other ntuples. Their flat structure renders them easy and fast to process, making them a favoured input format for physics analysis.

Additional formats are also required for the production and manipulation of simulated data.

EVNT: EVNT files hold the 4-vectors and production/decay vertices of particles from the different event generators, used to simulate physics processes.

HITS and DIGI: Events are simulated in a virtual representation of the ATLAS detector using the Geant4 program which outputs analogue energy deposits in the active regions of the detector. Once the event has been fully simulated these are digitised.

[2]Branches of primitives and C++ vectors, rather than complex objects.

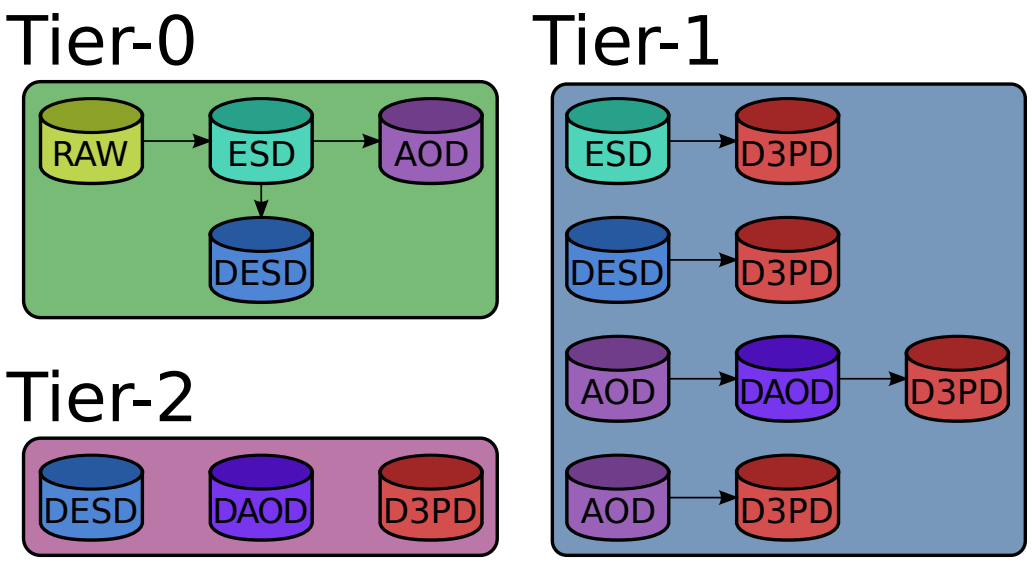

Figure 6.1: Schematic illustration of some of the common ATLAS data formats used on the LHC computing grid and their production chain.

RDO: RDO is the MC equivalent of the RAW data format. It differs from RAW data in that RDO files store data in an object-oriented basis. ATLAS reconstruction runs over either RAW or RDO files to produce identical output[3], from which point data and simulation uses the same framework.

[3]With MC reconstruction additionally retaining generator level information.

CHAPTER 7

STRONG INTERACTIONS AND DIFFRACTION

7.1 THE STANDARD MODEL OF PARTICLE PHYSICS

The Standard Model (SM) describes the the fundamental forces[1] acting between the elementary particles of nature. The SM is a SU(3) × SU(2) × U(1) symmetry group. The EM, strong and weak interactions are mediated by the exchange of gauge bosons with integer spin. The field particles of the weak interaction are the $W^{\pm}$ and the Z^0, the field particle of the EM interaction is the γ and the field particles of the strong interaction are the gluons. A non-zero Vacuum Expectation Value (VEV) of a scalar Higgs field allows for the massive W and Z bosons whilst preserving the gauge invariance of the theory [37].

Matter particles are fermions of half-integer spin. They are grouped into three families, the leptons e, μ and τ along with their electrically neutral neutrinos ν_e,

[1] With the notable exception of gravity.

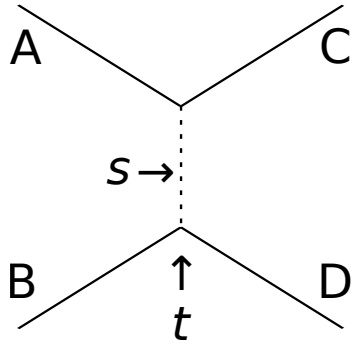

Figure 7.1: Mandlestam variables for a generalised scattering process.

ν_μ and ν_τ. There is one pair of quarks per generation, (ud), (cs) and (tb). Unlike the leptons, these additionally interact with the strong force. Each fermion has an anti-matter counterpart and each quark possesses one of three independent colour quantum numbers.

7.2 STRONG INTERACTIONS

For the generalised scattering interaction $AB \rightarrow CD$, the Mandlestam variables s and t are defined

$$s = (A + B)^2 = (C + D)^2 \approx 2A \cdot B \approx 2C \cdot D \tag{7.1}$$

$$t = (A - C)^2 = (B - D)^2 \approx -2A \cdot C \approx -2B \cdot D. \tag{7.2}$$

Here A, B, C and D are the 4-vectors of the incoming and outgoing particles. The approximations are valid in the high energy limit such that particle mass may be neglected. s equals the square of the centre of mass energy of the interaction and t equals the squared 4-momentum transfer (a negative quantity). The interaction is illustrated in Figure 7.1.

Quantum Chromodynamics (QCD) is encapsulated in the SU(3) symmetry group of the SM. The generators of this group, the Gell-Mann matrices, result in eight (3^2-1)

orthogonal coloured gluons (combinations of the R, G, B, $\overline{R}$, $\overline{G}$ and $\overline{B}$ colour fields). The ninth combination is a colour singlet and hence must be excluded. Gluons, being themselves coloured, self-interact. As a consequence, a possible model for the QCD potential between two quarks is

$$V(r) = kr - \frac{\alpha_s}{r}. \tag{7.3}$$

Here k is a constant and α_s is the coupling strength of the strong interaction. Potential energy in the colour field increases linearly with the separation of quarks, r, until it is energetically favourable to pair-produce a $q\bar{q}$ pair.

α_s is additionally dependent on the square of the four-momentum transfer in the interaction, Q^2. This sets the characteristic length scale resolved by the interactions. It was shown that one can not simply assume a uniformly constant coupling due to logarithmic divergences in loop diagrams which implies a dependence on the energy scale, Q^2. The strength of α_s decreases with Q^2, leading to the behaviour of asymptotic freedom of quarks at infinite energy [38]. This can qualitatively be thought of in terms of an anti-screening effect of virtual gluons at low energy, which arises from their self-interaction and more than cancels the screening effect of virtual quark loops.

The evolution is described to first order in the regime $Q^2 \gg \Lambda^2_{\mathrm{QCD}}$ by the beta-function

$$\alpha_s(Q^2) \approx \frac{1}{\beta_0 \ln(Q^2/\Lambda^2_{\mathrm{QCD}})} \tag{7.4}$$

where β_0 is a negative constant related to the number of quark flavours and $\Lambda_{\mathrm{QCD}} \approx 200$ MeV is a scale characteristic of the confinement transition. From this arises the concept of confinement of quarks in colour-singlet states at low energies, where this perturbative approach becomes invalid. Experimental data on α_s are plotted for energy scales up to 200 GeV in Figure 7.2

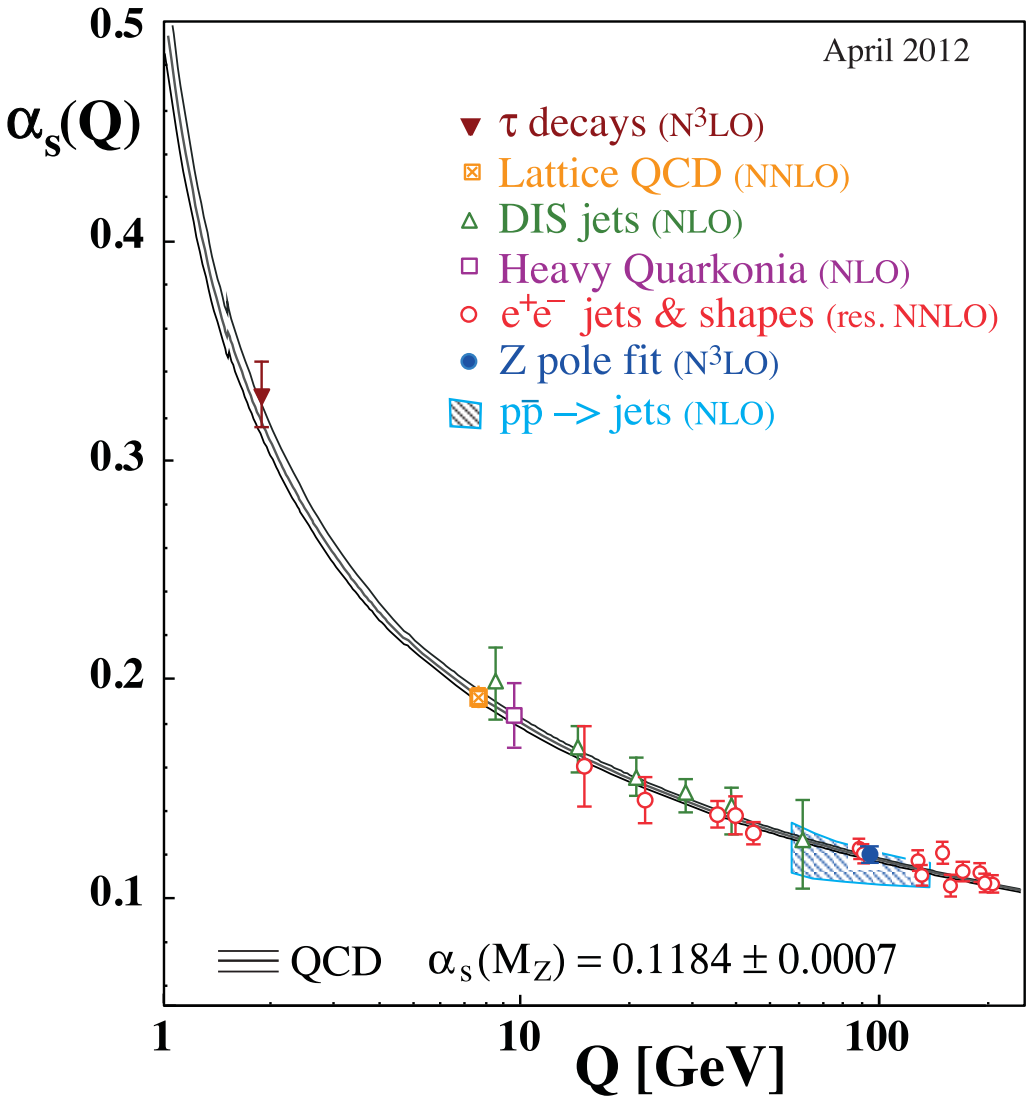

Figure 7.2: Strength of α_s as a function of energy scale, Q. Data from various experiments are presented with their α_s extraction using between second (NLO) and fourth order (N³LO) perturbative expansions. Taken from [25].

7.3 REGGE SCATTERING THEORY AND THE POMERON

Under a naïve modelling of the growth with s of the total proton-proton cross section (σ^{pp}_{Tot}) based only on hadron exchange, the cross section is dominated at high s by highly excited hadrons with large integer or half integer spin, J.

$$\sigma^{pp}_{\text{Tot}}(s) \propto s^{J} \tag{7.5}$$

Such a rise violates the Froissart-Martin bound [39][40] which stipulates that the total cross section should not rise faster than $\ln^2 s$.

In the formalism of the Regge theory of non-relativistic potential scattering [41], angular momentum is not quantized but is instead treated as a continuous complex quantity $\alpha(t)$. Observable resonances in the s channel occur at real values of $\alpha(t)$ such that $\Re[\alpha(t)]$ is integer or half integer. Unstable hadrons additionally have an imaginary component of $\alpha(t)$, proportional to their Breit-Wigner decay widths [42]. The amplitudes of these exchanges are approximated by

$$\mathcal{A}(J,t) = \frac{\beta(t)}{J - \alpha(t)} \tag{7.6}$$

where the β function describes the coupling of these *Regge poles* to external particles. Sets of resonances with increasing J but otherwise identical quantum numbers are considered to have a unified influence in the form of a *Regge trajectory*, which is parameterised by the linear equation

$$\alpha(t) = \alpha(0) + \alpha'(t). \tag{7.7}$$

The Regge trajectories whose lowest-lying s-channel resonances are with the ρ, f_2, ω and a_2 mesons together form the generalised quasi-degenerate leading meson Regge trajectory, often referred to as the Reggeon, $\mathbb{R}$. The real component of this is visualised in a Chew-Frautschi plot of J–M^2 space, where M^2 is the mass squared of the resonance, as plotted in Figure 7.3 assuming analytic continuation from the

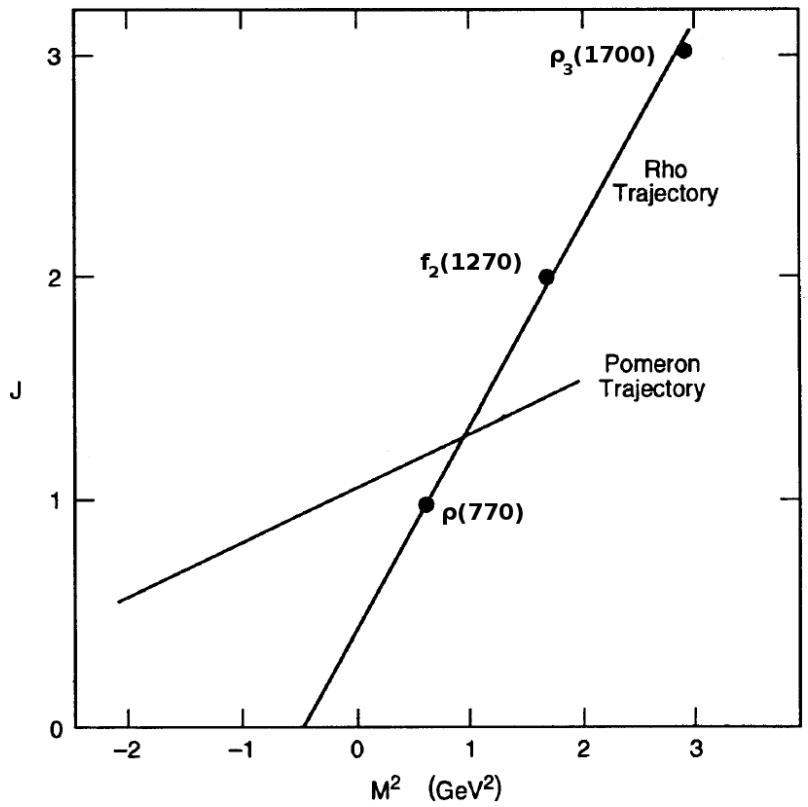

Figure 7.3: Chew-Frautschi plot of M^2 versus the real part of the complex angular momentum $\alpha(t)$. Plotted are the Pomeron trajectory (see text) and the ρ trajectory, which is quasi-degenerate with other low mass meson trajectories and is referred to in this document as the Reggeon ($\mathbb{R}$) trajectory. Derived from [43].

s to the t-channel.

It follows that the dependence of a t-channel process on the whole *set* of resonances has an s dependence at fixed t given by the corresponding Regge trajectory extended from M^2 (positive, time-like) to t (negative, space-like) [41]. This prevents the severe growth in the cross section from the contributions of large J states at large s. The trajectory parameterised by the $\mathbb{R}$ is measured experimentally to intercept at $\alpha_{\mathbb{R}}(0) \simeq 0.55$ with slope $\alpha'_{\mathbb{R}} \simeq 1$ GeV^{-2}.

In order to successfully describe the high energy rise of experimental cross section data, it was necessary to introduce a trajectory with the quantum numbers of the vacuum, $J^{PC} = 0^{++}$, in addition to these non-singlet exchanges. This trajectory was dubbed the Pomeron, $\mathbb{P}$, after I. Ya. Pomerančuk. The simplest strongly interacting

state which could lie on this trajectory in the s channel region is two gluons in a 'glueball' configuration. Some experimental hints of glueballs have been observed such as a $J^{PC} = 2^{++}$ excitation with $M \approx 1.9$ GeV by the WA91 collaboration [44]. The $X(1900)$ is observed to decay to $\pi^+\pi^-\pi^+\pi^-$ and to be isolated in phase space from other particles, both characteristics of the singlet glueball. Other studies of low-mass, centrally produced hadronic systems are being performed by the COmmon Muon Proton Apparatus for Structure and Spectroscopy (COMPASS) experiment [45].

Having vacuum quantum numbers, the Pomeron may mediate elastic scattering and it must couple equally to both particles and anti-particles to satisfy Pomerančuk's theorem that for hadrons A and B, the cross section [46]

$$\sigma(AB) \underset{s\to\infty}{\longrightarrow} \sigma(\bar{A}B). \tag{7.8}$$

7.4 THE TOTAL CROSS SECTION

The optical theorem [47] relates the total cross section to the imaginary amplitude T_{El} of the forward elastic cross section σ_{El} in the limit $t \to 0$. Regge theory predicts [41][48]

$$\frac{\mathrm{d}\sigma_{\text{El}}}{\mathrm{d}t} \propto s^{2\alpha(t)-2} \tag{7.9}$$

for fixed t. Thus, in the limits $s \to \infty$ and $t/s \to 0$

$$\sigma_{\text{Tot}}^{pp\to pp} \sim \frac{1}{s}\Im(T_{\text{El}}^{pp\to pp})\bigg|_{t=0} \sim s^{\alpha(0)-1}. \tag{7.10}$$

Experimental data for the total hadronic cross section for pp and $p\bar{p}$ are presented in Figure 7.4. The contribution to the total cross section from the $\mathbb{R}$ trajectory scales like $s^{-0.55}$ from (7.10). This is compatible with experimental data up to the maximum CERN Intersecting Storage Rings (ISR) energy of $\sqrt{s} = 63$ GeV [49],

however as s increases, the cross section is observed to slowly rise. A purely $\mathbb{R}$ description with $\alpha_{\mathbb{R}} \sim 0.55$ is unable to model this, but the rise is introduced through a $\mathbb{P}$ term with a super-critical[2] intercept (ϵ). The ($t < 0$) part of the $\mathbb{P}$ trajectory is measured experimentally and the intercept can also be extracted from fits to total cross section data. Such a fit performed by Donnachie and Landshoff [49] found $\alpha_{\mathbb{P}}(0) = 1.0808$ and the slope is determined to be around 1/4 that of the $\mathbb{R}$ slope, $\alpha'_{\mathbb{P}} \simeq 0.25$ GeV^{-2}.

This model of the total pp cross section as the sum of $\mathbb{R}$ and $\mathbb{P}$ contributions is compatible with experimental data which have been taken up to $\sqrt{s} = 57$ TeV [50]. The supercritical $\mathbb{P}$ contribution rises faster than the Froissart-Martin bound of $\ln^2 s$ and hence if left unchecked will eventually violate unitarity. However other effects such as Multi-Parton Interactions (MPI) are expected to become non-negligible at asymptotic energies, which act to control this rise by slowly lowering the effective $\mathbb{P}$ intercept [49]. The elastic and inelastic components of the total cross section are explored in Section 7.6.

7.5 INELASTIC DIFFRACTION

In addition to the elastic Pomeron contribution to the total cross section $pp \to pp$, inelastic diffraction occurs, due to the composite nature of hadrons. Good and Walker [54] first showed that partial attenuation of the proton wave function in a peripheral collision would lead to a configuration in which the outgoing particle is excited out of its ground state. Here the proton (or, each proton) will dissociate into a larger mass system with proton quantum numbers.

When one proton dissociates, the invariant mass of the diffractively dissociated system is labelled M_X. When both protons dissociate, the systems are labelled M_X and M_Y such that $M_X > M_Y$.

[2] An intercept $\alpha(0) > 1$ such that $\epsilon = \alpha(0) - 1$ is positive.

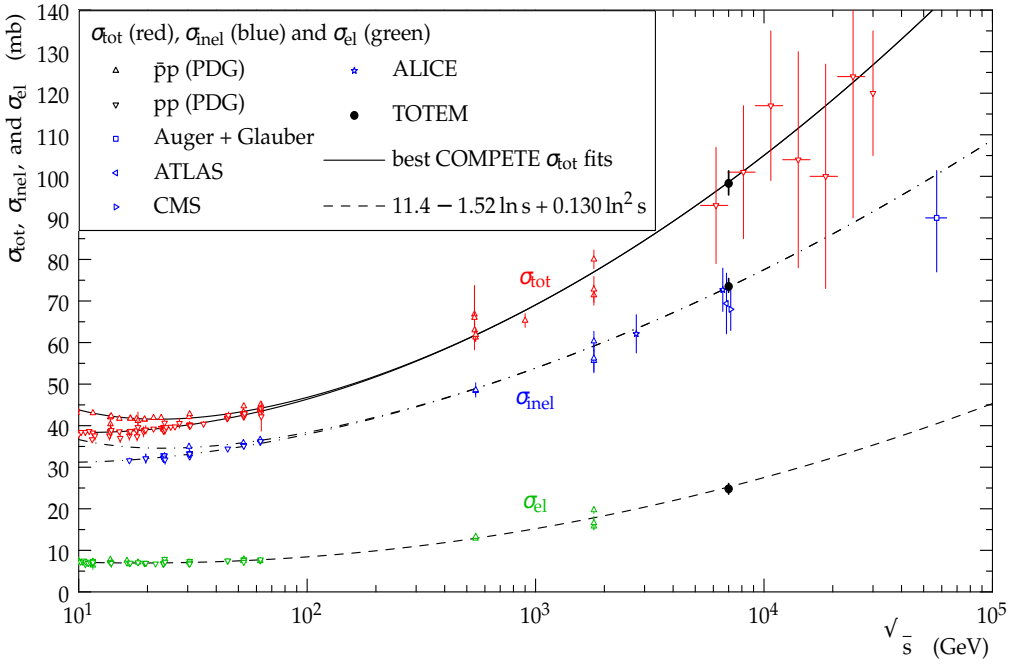

Figure 7.4: σ_{Tot} plus its elastic and inelastic constituents for pp and $p\bar{p}$ data along with a best fit parametrisations taken from TOTEM [51]. Pre-LHC and LHC data from ATLAS [52] and ALICE [53] are shown along with cosmic ray air-shower data up to $\sqrt{s} = 57$ TeV (from the Pierre Auger Observatory, [50]).

The fractional longitudinal momentum loss of the proton

$$\xi_X = M_X^2/s \tag{7.11}$$

is a convenient kinematic variable with which to classify these events. This is related in the $|t| \to 0$ limit to the Feynman variable $x_F \simeq \xi_X - 1$, corresponding to the ratio of the longitudinal momentum of the proton after the interaction to before the interaction, $x_F = p_z(p')/p_z(p)$. To assess the possible range of diffractive masses, M_X, at $\sqrt{s} = 7$ TeV, one can consider two limiting cases. High mass diffraction is ultimately limited by the coherence condition [55] $\xi_X < (M_p R)^{-1}$, where M_p is the proton mass and R is the interaction length. Assuming the Pion mass can be used to characterise this range, $R = M_\pi^{-1}$, gives an approximate upper bound of $\log_{10}(\xi_X) \lesssim -0.8$ or $M_X \lesssim 2.8$ TeV. The low mass limit is the first excitation which preserves the proton quantum numbers, $p \to p + \pi^0$. Diffractive dissociation at $\sqrt{s} = 7$ TeV hence must have $\log_{10}(\xi_X) \geq -7.6$ or $M_X \geq 1.1$ GeV.

7.6 DISSECTION OF THE TOTAL CROSS SECTION

The bulk of proton interactions at LHC energies may be subdivided, somewhat ambiguously, into different classifications. In elastic interactions, the protons are scattered through very small angles, < 10 μrad, such that they can only be detected with sensitive equipment located in the beam pipes. Ultimately TOTEM and Absolute Luminosity for ATLAS (ALFA) [56] aim to measure the Coulomb-Nuclear-Interference (CNI) region of pp elastic scattering at $|t| \sim 0.00065$ GeV^2. In this regime the cross section is calculable to high precision using Next-to-Leading Order (NLO) perturbative theory. However, experimentally probing this region requires a β^* of around 1 km which has yet to be achieved. TOTEM has so far measured the $|t|$ slope down to 0.02 GeV^2 at a β^* of 90 m (this regime is still dominated by strong interactions) and obtains its measure of the total elastic scattering cross section at $\sqrt{s} = 7$ TeV ($\sigma_{\mathrm{El}} = 24.8 \pm 0.2(\mathrm{stat}) \pm 1.2(\mathrm{syst})$ mb) via extrapolation to the optical point at $|t| = 0$ [51].

Inelastic collisions make up the remainder of the pp interaction cross section. So called Non-Diffractive (ND) inelastic interactions primarily occur through the exchange of a colour octet at relatively small impact parameter. Due to the partonic nature of the proton, multiple parton interactions are also commonplace. The colour exchange results in the correlated dissociation of both protons, combined with gluon radiation. The final state therefore consists in general of a high multiplicity of particles filling the entire η interval between the protons.

Spanning the continuum between elastic and totally inelastic collisions are the diffractive dissociation interactions. Here a singlet-state is exchanged between the protons. This may be an electroweak process but is dominated by Pomeron exchange at hadron colliders [57]. The diffractive excitations considered are the Single Diffractive (SD) process $pp \rightarrow pX$ plus $pp \rightarrow Xp$, in which there is a rapidity gap between the X system and the scattered proton. The Double Diffractive (DD) process $pp \rightarrow XY$ contains a rapidity gap between the X and Y systems and in the

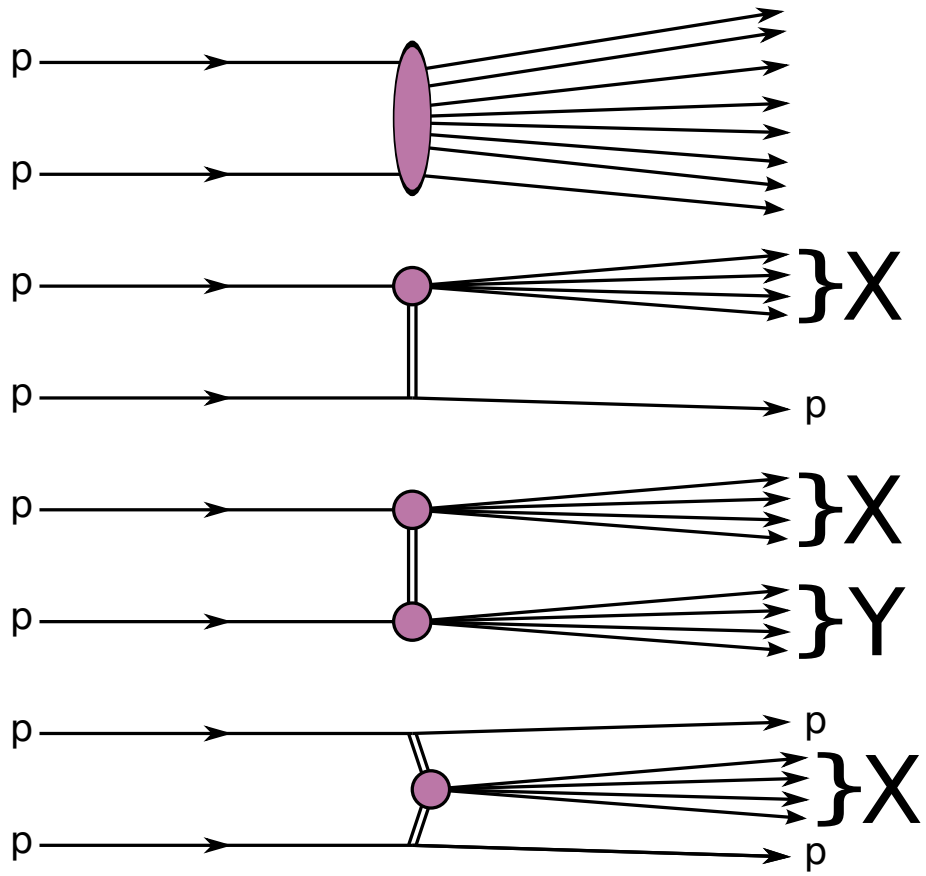

Figure 7.5: Schematic illustrations of event topologies. From top to bottom: Non-Diffractive, Single Diffractive, Double Diffractive, Central Diffractive. Shaded areas represent hadronisation of dissociated systems. The vertical direction corresponds to rapidity.

Central Diffractive (CD) process $pp \to pXp$, two rapidity gaps are produced between the system X and either scattered proton. CD, also known as double-Pomeron exchange, is a higher order process whose cross section is suppressed with respect to SD by around a factor of ten at high energies [58]. These processes are illustrated in Figure 7.5.

7.7 THE TRIPLE REGGE MODEL

The role of the Pomeron in inelastic single diffraction comes from consideration of Mueller's generalisation of the optical theorem [59] to the three body elastic

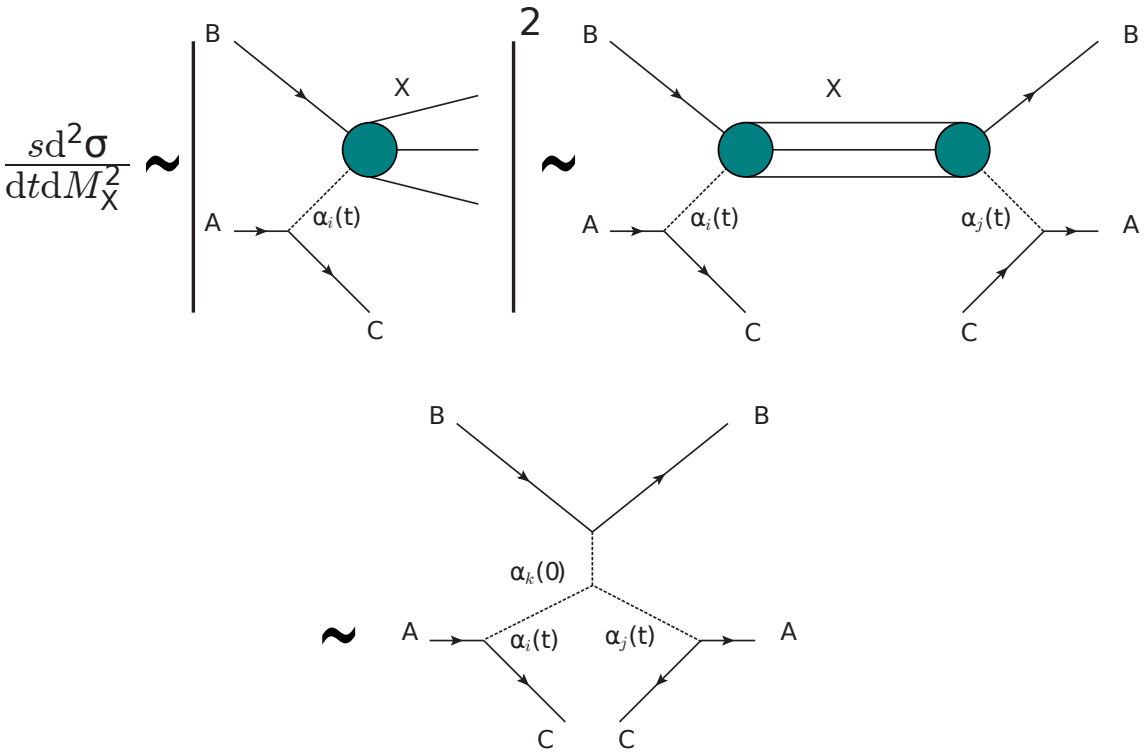

Figure 7.6: Illustration of the application of Mueller's generalisation of the optical theorem to represent the inclusive inelastic interaction $AB \to CX$ as a triple Regge amplitude.

scattering $AB\overline{C} \to AB\overline{C}$ via an unphysical decay amplitude $AB\overline{C} \to X$ as illustrated in Figure 7.6. This so called triple Regge amplitude is valid in the limit that $s \gg M_X^2 \gg t$. Such a limit is applicable to soft diffraction at LHC energy scales. In single diffraction, the Regge trajectories i and j from the rightmost diagram in Figure 7.6 must be Pomerons. The total amplitude is the sum over all Regge trajectories with the triple Pomeron, $\mathbb{P}_i\mathbb{P}_j\mathbb{P}_k$ term dominating, and with a poorly established but probably non-negligible contribution from the $\mathbb{P}_i\mathbb{P}_j\mathbb{R}_k$ term at low ξ_X from its comparatively steeper slope. The triple Pomeron differential cross section under Regge theory [60][61] reduces to

$$\frac{\mathrm{d}^2\sigma_{\mathrm{SD}}(s)}{\mathrm{d}M_X^2\mathrm{d}t} \simeq K(t)s^{2\alpha_{\mathbb{P}}(0)+2\alpha'_{\mathbb{P}}t-2}\left(\frac{1}{M_X^2}\right)^{\alpha_{\mathbb{P}}(0)+2\alpha'_{\mathbb{P}}t} \tag{7.12}$$

where $K(t)$ comprises numerical constants and couplings which are shown explicitly in Section 8.1.2, $\alpha_{\mathbb{P}}(0)$ is the Pomeron intercept and $\alpha'_{\mathbb{P}}$ is the Pomeron slope. The

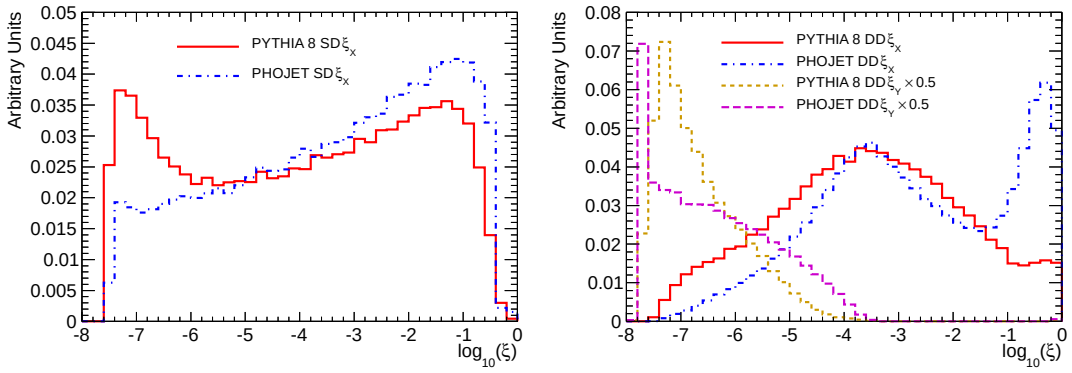

(a) (b)

Figure 7.7: PYTHIA8 and PHOJET MC cross sections as a function of the logarithm of ξ for SD (a) and DD (b). The ξ_Y distributions on plot (b) are scaled by 0.5 for display purposes.

DD expression is formulated in a similar manner [62].

For the small t, peripheral interactions which dominate, $\mathrm{d}\sigma/\mathrm{d}M_X^2$ is roughly proportional to $1/M_X^2$ and it follows that $\mathrm{d}\sigma/\mathrm{d}\log(M_X^2)$ is roughly constant. The cross section in $\log(\xi_X)$ is not exactly flat due to the intercept of the Pomeron trajectory not being exactly one, along with other factors which are discussed in Section 8.1.2. The SD and DD cross sections from two MC models are plotted as a function of ξ in Figure 7.7

7.8 KINEMATICS OF DIFFRACTIVE DISSOCIATION

From the definition of the rapidity of a particle with energy E and longitudinal momentum p_z,

$$y = \frac{1}{2}\ln\left(\frac{E+p_z}{E-p_z}\right) \tag{7.13}$$

it follows that the pseudorapidity of a diffractively produced, un-decayed particle of mass M_X is well approximated by

$$\eta_{M_X} = \ln\left(\frac{\sqrt{s}}{M_X}\right). \tag{7.14}$$

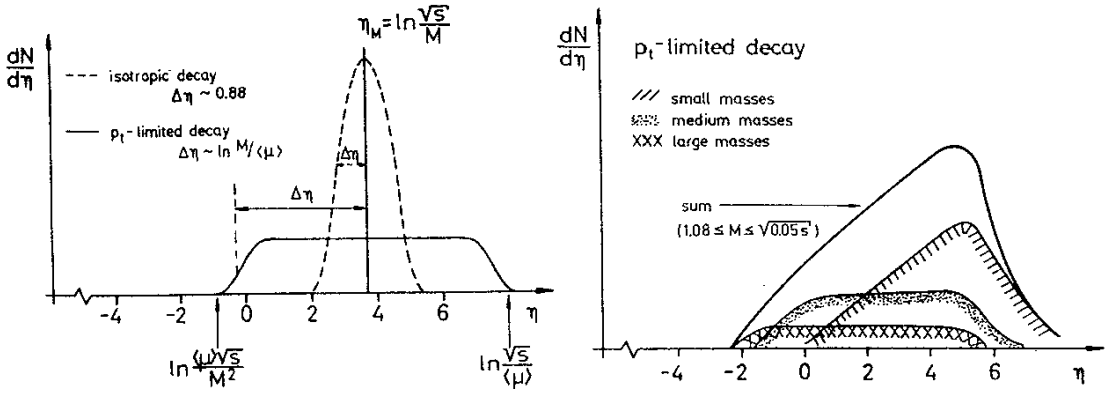

Figure 7.8: Comparison of the final state particle distribution for the 'fireball' (isotropic) and multiperipheral (p_{T} limited) decay models. Also shown is how the shape of the dissociated system changes with increasing M_X under the multiperipheral model. This illustration was designed for S$p\bar{p}$S energies [55]. The only significant change to the model at LHC energies is the larger kinematically available phase-space.

Different decay models of M_X have been considered historically, such as the 'fireball' model in which the system X is decayed isotropically in its rest frame. It is then boosted to the laboratory frame, resulting in a roughly Gaussian decay profile whose width is independent of M_X. The data, however strongly prefer a multiperipheral decay model [55]. This produces a flat pseudorapidity distribution of particle production over many units of pseudorapidity for large diffractive masses. The width of the distribution in multiperipheral models grows with increasing diffractive mass. It is given by

$$\Delta\eta(\mathrm{HWHM}) \simeq \ln\left(\frac{M_X}{<\mu>}\right). \tag{7.15}$$

Here $\mu = \sqrt{p_{\mathrm{T}}^2 + m^2}$ is the transverse mass of the final state particles, predominately pions. HWHM denotes the Half-Width-Half-Maximum. For symmetric distributions, this is the distance travelled from η_{M_X} in either direction until the particle density, $\frac{\mathrm{d}N}{\mathrm{d}\eta}$, falls to one half of its value at η_{M_X}. This is illustrated in Figure 7.8. It follows that the diffractive system occupies the approximate pseudorapidity interval

$$\text{from} \qquad \eta = \ln\left(\frac{<\mu>\sqrt{s}}{M_X^2}\right) \qquad \text{to} \qquad \eta = \ln\left(\frac{\sqrt{s}}{<\mu>}\right). \tag{7.16}$$

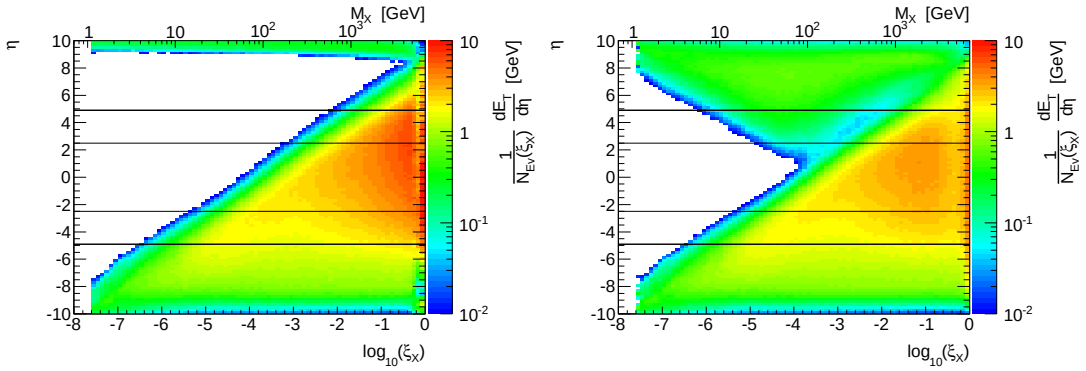

(a) (b)

Figure 7.9: Single diffractive (a) and double diffractive (b) transverse energy density as a function of ξ_X from the PYTHIA8 MC generator. The distributions are normalised to a single event in columns of ξ_X. The X system is forced to have originated from the proton travelling in the $-z$ direction. Thin and thick black lines mark the fiducial acceptance of the ATLAS ID and calorimeter systems, respectively.

This is illustrated at $\sqrt{s} = 7$ TeV in Figure 7.9, where the event-averaged transverse energy density of final state particles is plotted as a function of $\log_{10}(\xi_X)$ for SD and DD events from a MC simulation. It is observed that for a given value of ξ_X, the transverse energy density remains relatively flat over the decay width of the diffractive mass.

7.8.1 DIFFRACTIVE MASS VERSUS RAPIDITY GAP CORRELATION

The mass of a dissociated system may be inferred from the distribution of final state particles in the diffractive system. In Figure 7.10, the pseudorapidity of the final state particle from the system X which is closest in η to the scattered proton in an SD MC, η_{Max}, is plotted. This particle defines the edge of the M_X system. The resultant scatter plot is fitted in slices of ξ_X to a Gaussian distribution. It is observed that these Gaussians have width $\sigma \sim 1$ unit of pseudorapidity. This is a consequence of smearing during the hadronisation phase of MC generation.

A linear fit is taken through the means of the Gaussians to parametrise the relationship, yielding $\log_{10}(\xi_X) = (0.44 \pm 0.05)\eta_{\text{Max}} - (3.74 \pm 0.14)$. It is noted that

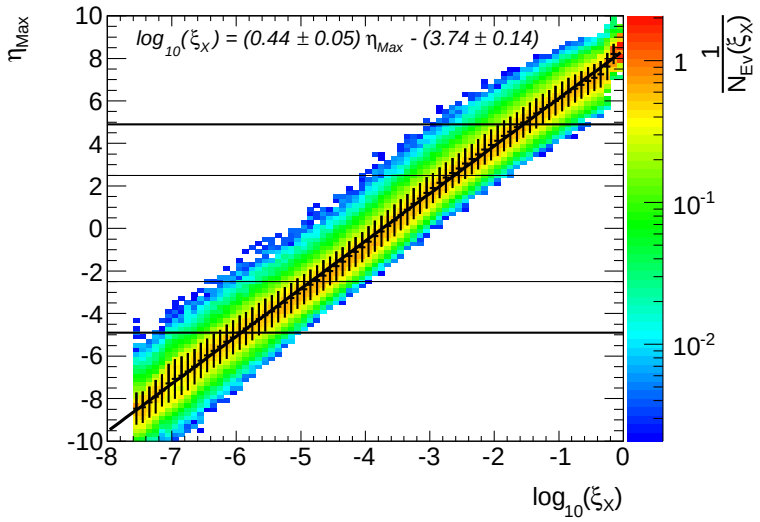

Figure 7.10: Correlation between ξ_X and η_{Max} with a fitted linear trend line. SD events simulated with the PYTHIA8 MC are used. Error bars denote the widths of Gaussian fits to slices in ξ_X of the distribution. The thick and thin horizontal lines indicate the limits of the acceptance of the ATLAS calorimeter and inner detector, respectively.

due to the $|\eta| \leq 4.9$ coverage of the ATLAS calorimeter systems, η_{Max} is experimentally measurable in a range corresponding to four orders of magnitude in ξ_X: $-6 < \log_{10}(\xi_X) < -2$.

7.8.2 GENERATOR LEVEL DIFFRACTIVE MASS RECONSTRUCTION

Two methods of reconstructing the M_X and M_Y values from an MC event record were considered. These are referred to as the *lineage* and $\Delta\eta$ methods. Using the lineage method, the decay chain of each final state particle is traced back through the event record vertex tree to the originating proton. When all final state particles have been associated with the $+z$ or $-z$ proton, the invariant masses of the two systems are calculated and identified as M_X and M_Y. This method is guaranteed to reconstruct the masses intended by the MC author, but requires access to the full vertexing information from the event and, for some generators, details of how the diffractive interaction is coded in the event record.

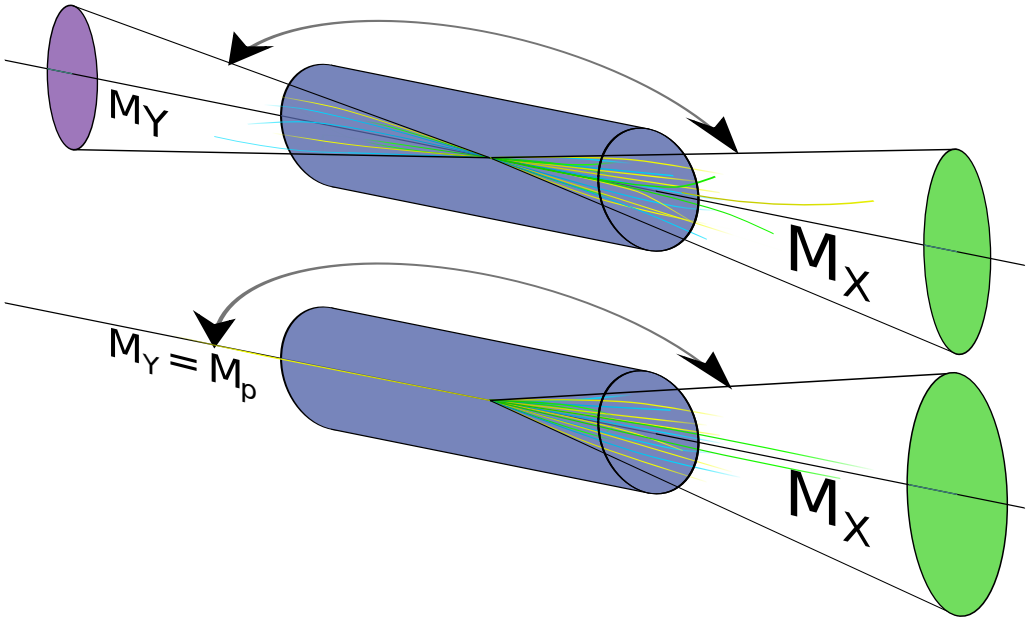

Figure 7.11: $\Delta\eta$ method of reconstructing M_X and M_Y from the largest pseudorapidity gap between any two neighbouring final state particles illustrated for DD (top) and SD (bottom) dissociation.

In the $\Delta\eta$ method, every final state particle is ordered in pseudorapidity and the largest pseudorapidity interval between any neighbouring particles, $\Delta\eta$, is identified. The event is divided in two about this division and the invariant mass is calculated for particles falling on the $+z$ side of the divide and separately the $-z$ side. These two invariant masses are then identified as M_X and M_Y as in Figure 7.11. This method is advantageous in that it is generator-agnostic and only requires knowledge of the final state, not the lineage used by the MC in the simulation. However the method is only fully valid while the separation of the two systems is greater than the mean separation of particles from hadronisation. This is not satisfied for very large systems, as is observed in the comparison of M_X as reconstructed by the two methods in Figure 7.12. The misassignment of the gap in a small fraction of events is shown to smear the kinematic reconstruction in approximately 10% of events with $\xi_X > 10^{-3}$.

Due to its practical advantages, the $\Delta\eta$ method is used to reconstruct kinematic *hadron level*[3] quantities. The main measurement presented in this document re-

[3]The *hadron level* is discussed in Section 9.3.

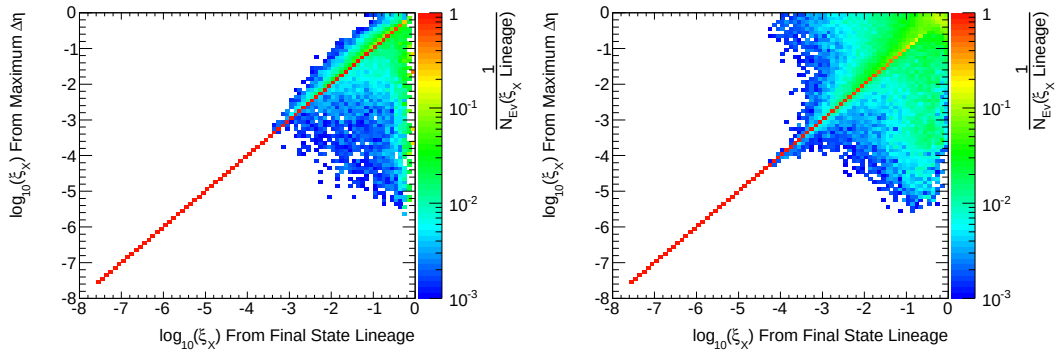

(a) (b)

Figure 7.12: Comparison of ξ_X calculated with the pseudorapidity gap and lineage methods (see text) for SD (a) and DD (b) topologies from the PYTHIA8 MC. Normalised to unity in columns of ξ_X (lineage) for display purposes.

mains independent of event kinematics, however this technique is used to derive the correction factors in Section 11.5, when ξ_X based corrections are applied to data. This is a suitable approach as this method only deviates from the lineage method when the particles forming the M_X system already span almost the full ATLAS fiducial acceptance.

7.8.3 ATLAS ACCEPTANCE FOR DOUBLE DIFFRACTION

DD events with $\xi_Y \lesssim 10^{-6}$ are indistinguishable from SD events in ATLAS, since the Y system is produced entirely outside the acceptance of the calorimeters at $|\eta| > 4.9$. Without additional input, such as forward proton tagging, these events can not be distinguished from the SD topology. In the PYTHIA8 model, 71% of the DD cross section satisfies this criteria, as shown in Figure 7.13. This degeneracy fundamentally limits the efficacy of using the MC to separate out the SD and DD components of the cross section.

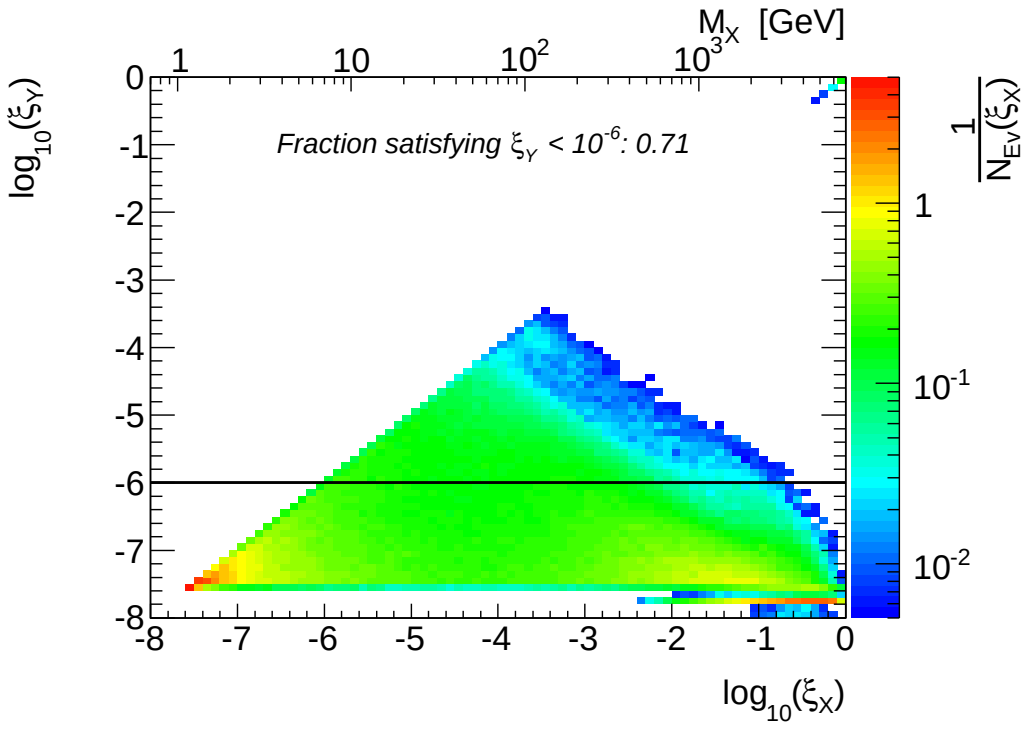

Figure 7.13: Kinematic plane of ξ_X vs. ξ_Y for DD events with PYTHIA8. The black line is drawn at $\xi_Y = 10^{-6}$. Events whose ξ_Y is smaller than this are experimentally indistinguishable from the SD event topology.

CHAPTER 8

MONTE CARLO SIMULATION

Three different MC models of soft, strong interaction physics are considered for use in correcting the data and for comparison with the corrected data, PYTHIA6, PYTHIA8 and PHOJET. These are described in this section along with HERWIG++ whose non-diffractive underlying event tune is also compared with the data. The tunes of PYTHIA used in the analysis are detailed in [63].

8.1 THE PYTHIA MONTE CARLO MODELS

8.1.1 PYTHIA CROSS SECTIONS

The PYTHIA [64] simulation process begins with the modelling of the total cross section for the chosen centre of mass energy, $\sqrt{s}$. A Donnachie and Landshoff [65] parametrisation is used where the contributions from the Pomeron and Reggeon

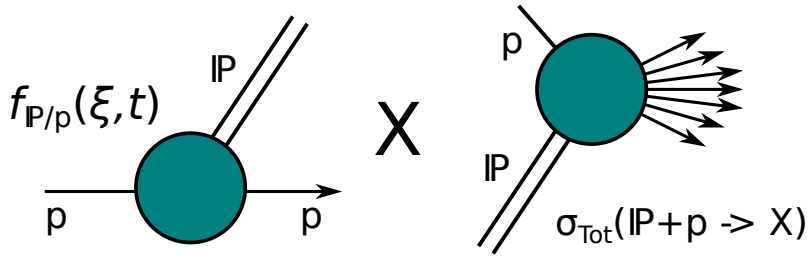

Figure 8.1: Subdivision of diffractive modelling in the PYTHIA MC into a *Pomeron flux* multiplied by a total $\mathbb{P} + p \to X$ cross section.

trajectories are summed:

$$\sigma_{\mathrm{Tot}}^{pp}(s) = X^{pp} s^{\epsilon} + Y^{pp} s^{-\eta}. \tag{8.1}$$

The s dependence from the Pomeron ($\epsilon = 0.0808$) and Reggeon ($\eta = 0.5425$) are determined by the trajectory intercept and are both expected to be universal effective quantities, while $X^{pp} = 21.70$ mb and $Y^{pp} = 56.08$ mb are coefficients specific to pp interactions. The total cross section is subdivided into the components

$$\sigma_{\mathrm{Tot}}^{pp}(s) = \sigma_{\mathrm{El}}^{pp}(s) + \sigma_{\mathrm{ND}}^{pp}(s) + \sigma_{\mathrm{SD}}^{pp}(s) + \sigma_{\mathrm{DD}}^{pp}(s). \tag{8.2}$$

Here $\sigma_{\mathrm{El}}^{pp}$ is the cross section for elastic scattering, DD denotes double proton diffractive dissociation, SD denotes single proton diffractive dissociation taking into account that either proton may dissociate and ND denotes inelastic non-diffractive.

Parametrisations for the cross section of the elastic, SD and DD contributions are quantified separately, with the ND cross section taken to be the remainder $\sigma_{\mathrm{ND}}^{pp} = \sigma_{\mathrm{Tot}}^{pp} - \sigma_{\mathrm{El}}^{pp} - \sigma_{\mathrm{SD}}^{pp} - \sigma_{\mathrm{DD}}^{pp}$. The form factor of the elastic cross section is (through use of the optical theorem as in Section 7.4) taken as a parametrisation of an exponential slope.

8.1.2 DIFFRACTION IN PYTHIA

PYTHIA6 and PYTHIA8 share much of the same formalism when modelling diffractive events, PYTHIA8 extends the model present in PYTHIA6 to improve the treatment of hard diffraction, making it more applicable to the LHC environment and introduces a user-choice of cross section parametrisation.

In both versions of PYTHIA, diffraction is modelled as a combination of a Pomeron flux from one of the incident protons with a Pomeron-proton interaction cross section as depicted in Figure 8.1.

The parametrisations of the SD and DD contributions to the cross section take the form

$$\begin{aligned}\frac{\mathrm{d}^2\sigma_{\mathrm{SD}}(s)}{\mathrm{d}t\mathrm{d}M_X^2} &= \frac{g_{3\mathbb{P}}}{8\pi}\beta_{\mathbb{P}/p}^3\,\frac{1}{M_X^2}\,e^{B_{\mathrm{SD}}(M_X^2,s)t}\,F_{\mathrm{SD}}(M_X^2,s),\\ \frac{\mathrm{d}^3\sigma_{\mathrm{DD}}(s)}{\mathrm{d}t\mathrm{d}M_X^2\mathrm{d}M_Y^2} &= \frac{g_{3\mathbb{P}}^2}{16\pi}\beta_{\mathbb{P}/p}^2\,\frac{1}{M_X^2M_Y^2}\,e^{B_{\mathrm{DD}}(M_X^2,M_Y^2,s)t}\,F_{\mathrm{DD}}(M_X^2,M_Y^2,s).\end{aligned} \tag{8.3}$$

Here the triple-Pomeron coupling factor is experimentally measured to be $g_{3\mathbb{P}} \approx 0.318\ \mathrm{mb}^{\frac{1}{2}}$ [66] and the proton-Pomeron coupling term $\beta_{\mathbb{P}/p}$ relates to the Pomeron term X^{pp} from (8.1). The simple $\frac{1}{M_X^2}\left(\frac{1}{M_X^2M_Y^2}\right)$ SD(DD) behaviour is modified in the default Schuler and Sjöstand Pomeron flux parametrisation with the inclusion of both an additional mass dependence in the exponential slope, B, and an ad-hoc 'fudge factor' F. This F factor is included to control the behaviour of the cross section in regions of phase space where the approximations required for the triple Regge description, $|t| \ll M_X^2 \ll s$ are no longer valid. For SD, these are

$$B_{\mathrm{SD}}\left(M_X^2,s\right) = 2b_p + 2\alpha'\ln\left(\frac{s}{M_X^2}\right) \tag{8.4}$$

$$F_{\mathrm{SD}}\left(M_X^2,s\right) = \left(1-\frac{M_X^2}{s}\right)\left(1+\frac{c_{\mathrm{res}}M_{\mathrm{res}}^2}{M_{\mathrm{res}}^2+M_X^2}\right). \tag{8.5}$$

And for DD,

$$B_{\mathrm{DD}}\left(M_X^2, M_Y^2, s\right) = 2\alpha' \ln\left(e^4 + \frac{s s_0}{M_X^2 M_Y^2}\right) \tag{8.6}$$

$$F_{\mathrm{DD}}\left(M_X^2, M_Y^2, s\right) = \left(1 - \frac{\left(M_X + M_Y\right)^2}{s}\right)\left(\frac{s M_p^2}{s M_p^2 + M_X^2 M_Y^2}\right) \times \left(1 + \frac{c_{\mathrm{res}} M_{\mathrm{res}}^2}{M_{\mathrm{res}}^2 + M_X^2}\right)\left(1 + \frac{c_{\mathrm{res}} M_{\mathrm{res}}^2}{M_{\mathrm{res}}^2 + M_Y^2}\right). \tag{8.7}$$

$\alpha' = 0.25$ GeV^{-2} is identified as the slope of the Pomeron trajectory with typical hadronic scale factor $s_0 = 1/\alpha' = 4$ GeV^2, the intercept of the Pomeron trajectory is taken to be unity $\alpha_{\mathbb{P}}(0) = 1$. The factor of e^4 in B_{DD} controls the behaviour at large M_X^2 and M_Y^2 while the b_p term protects B_{SD} from shrinking too small at large M_X^2. The Schuler and Sjöstand parametrisation contains a separate t slope for double diffractive dissociation.

The first term in F_{SD} and F_{DD} kills the cross section as ξ_X or $\xi_Y \to 1$ (as a reminder, $\xi_X = \frac{M_X^2}{s}$, similarly for ξ_Y). At this kinematic limit diffractive and non-diffractive event topologies are indistinguishable. The second factor in F_{DD} with dependence on the proton mass, M_p, acts to suppress the cross section for mass combinations which result in the two dissociated systems overlapping in rapidity space. The remaining factor in both F_{SD} and F_{DD} enhances the cross section for the low-mass region where resonant diffractive excitation of bound states is observed. Reasonable agreement with data is obtained for values $c_{\mathrm{res}} = 2$, $M_{\mathrm{res}} = 2$ GeV [66].

When simulating a diffractive process, the values of t, M_X (and M_Y for DD) are chosen by PYTHIA with probability distributions derived from equations (8.3)-(8.7). The decay mechanism of the dissociated systems M_X (and M_Y for DD) is chosen as a function of their mass.

For very low mass systems, $M_X < M_p + 1$ GeV, the system is decayed isotropically into a two body system. For higher masses, PYTHIA6 decays all systems via a string with the quantum numbers of the proton. This is stretched between a quark and the remaining di-quark system, or from a quark to a gluon then back to the di-quark

in a hairpin configuration. The final state hadrons are distributed in a longitudinal phase space with limited transverse momentum as described in [55].

Starting from PYTHIA8.130; a third, partonic treatment of the dissociated systems is introduced [67]. This method is selected with gradually increasing probability for dissociated masses larger than 10 GeV. By default, the H1 2006 Fit B Leading Order (LO) Q^2-dependent Diffractive Parton Density Function (DPDF) parametrisation is used from [68]. The LO fit is used as PYTHIA is a leading order generator. These DPDFs at NLO are presented in Figure 8.2. The dissociation is then modelled as a Pomeron-proton interaction at $\sqrt{s_{\text{Effective}}} = M_X, M_Y$. Under this formalism, the full standard machinery in PYTHIA for Multi-Parton Interactions (MPI), parton showers and hadronisation (as discussed in Section 8.1.4) is used in the Pomeron-proton $2 \rightarrow 2$ partonic interaction. Figure 8.3 shows the reconstructed track p_{T} spectrum for MC and data with a diffractive enhanced selection. Starting from PYTHIA8.130; a third, partonic treatment of the dissociated systems is introduced [67]. This method is selected with gradually increasing probability for dissociated masses larger than 10 GeV. By default, the H1 2006 Fit B LO Q^2-dependent DPDF parametrisation is used from [68]. The LO fit is used as PYTHIA is a leading order generator. These DPDFs at NLO are presented in Figure 8.2. The dissociation is then modelled as a Pomeron-proton interaction at $\sqrt{s_{\text{Effective}}} = M_X, M_Y$. Under this formalism, the full standard machinery in PYTHIA for Multi-Parton Interactions (MPI), parton showers and hadronisation (as discussed in Section 8.1.4) is used in the Pomeron-proton $2 \rightarrow 2$ partonic interaction. Figure 8.3 shows the reconstructed track p_{T} spectrum for MC and data with a diffractive enhanced selection. PYTHIA6 is shown to produce a significantly softer charged particle p_{T} distribution than PYTHIA8, which utilises this improved model. The data are observed to be in good agreement with the PYTHIA8 prediction.

Examples of the three dissociation models discussed above are presented for PYTHIA8 single diffractive dissociation events in Figure 8.4. Following from the discussion in Section 7.8, the pseudorapidity versus p_{T} distributions of the final state particles in

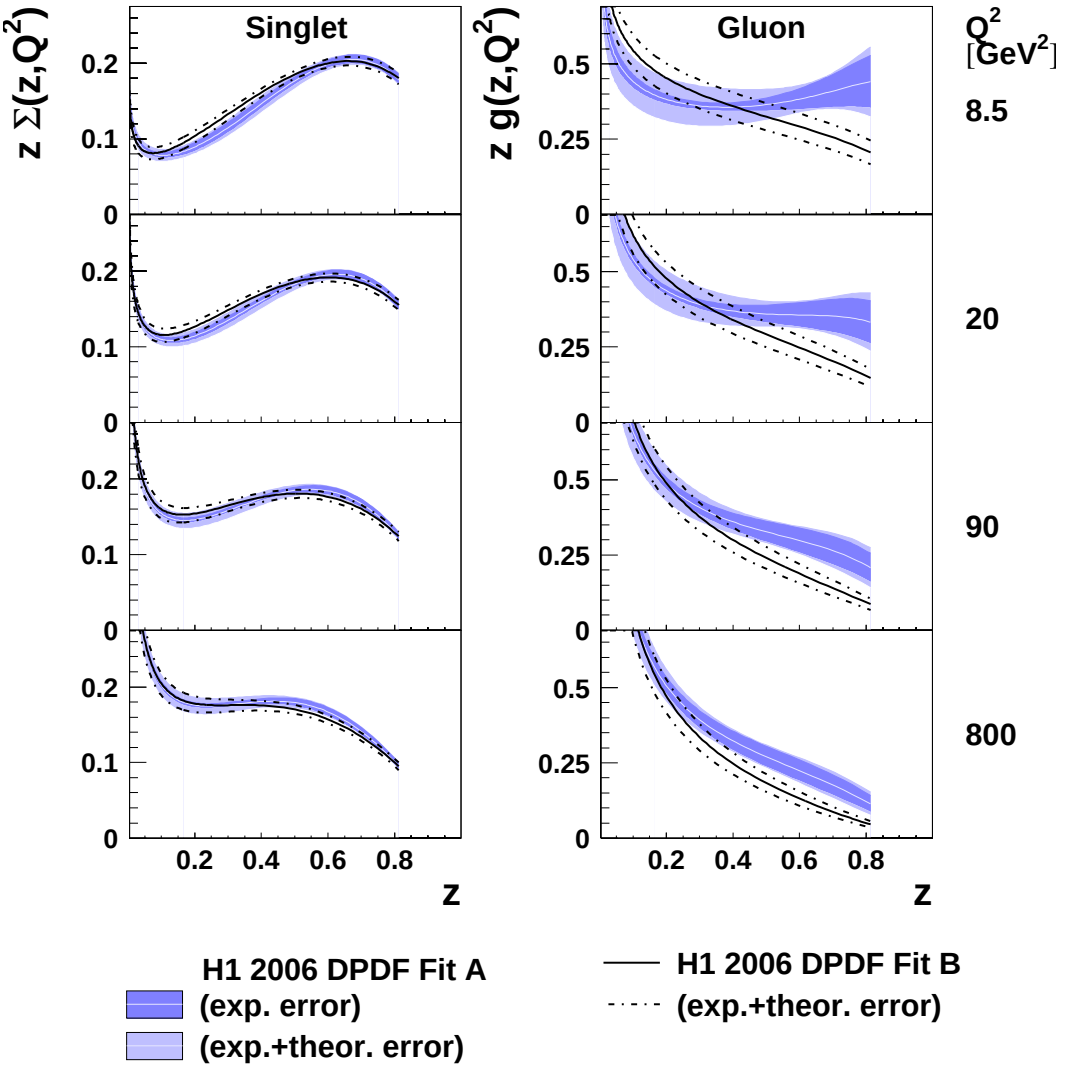

Figure 8.2: NLO quark singlet and gluon distributions for the H1 2006 DPDF Fit A and Fit B. The LO version of Fit B is used in this study. It is similar to the NLO version presented here. The DPDFs show the colour singlet and gluon contributions to the Pomeron as a function of the longitudinal momentum fraction of the struck parton, z, for four values of four-momentum transfer squared, Q^2. For fit A, a light coloured line marks the central result with inner and outer error bands corresponding to experimental and experiment al plus theoretical uncertainty respectively. For fir B the solid line corresponds to the central value with the total uncertainty shown as a dashed line. Taken from [68].

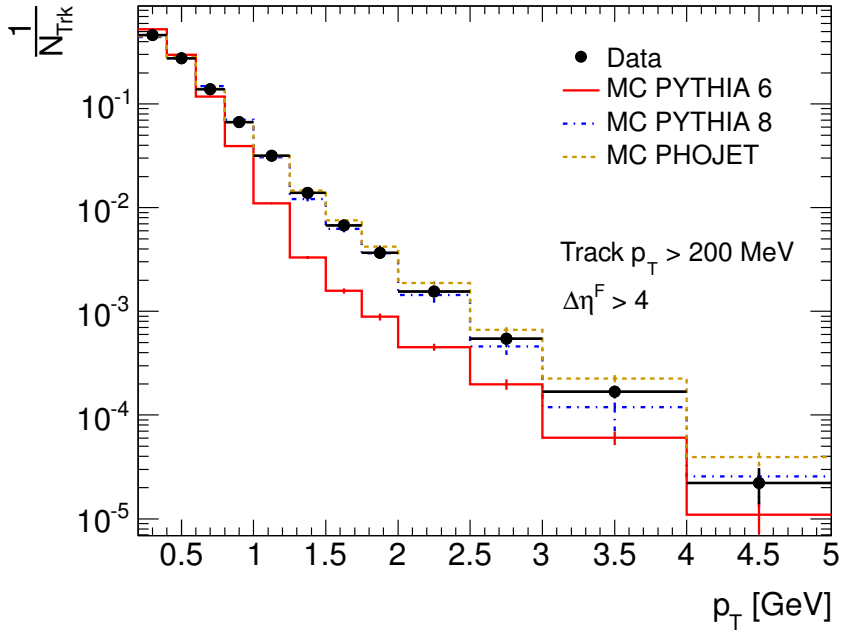

Figure 8.3: Track p_{T} spectrum for tracks with $p_{\mathrm{T}} > 200$ MeV in reconstructed MC and data for a diffractive enhanced selection $\Delta\eta^F > 4$ (see Section 10.1 for details), each distribution normalised to unit area. Errors are statistical.

the example events are also presented in Figure 8.5(a)-(c).

8.1.3 ALTERNATE POMERON FLUXES IN PYTHIA8

PYTHIA8 includes three alternative Pomeron flux parametrisations in addition to the Schuler and Sjöstand flux described in Section 8.1.2.

The Bruni and Ingelman flux parametrisation [70], (8.8), also has a Pomeron intercept of unity, though it models the t slope as the sum of two exponentials. A Pomeron-proton cross section of 2.3 mb leads to a total integrated SD cross section in agreement with UA4 [71],

$$\frac{\mathrm{d}^2\sigma_{\mathrm{SD}}}{\mathrm{d}t\mathrm{d}\xi_X} \propto \frac{1}{\xi_X}\left[6.38e^{8t} + 0.424e^{3t}\right]\frac{1}{2.3}. \tag{8.8}$$

In the Berger et al. Streng parametrisation [72][73] (8.9), numeric values for the

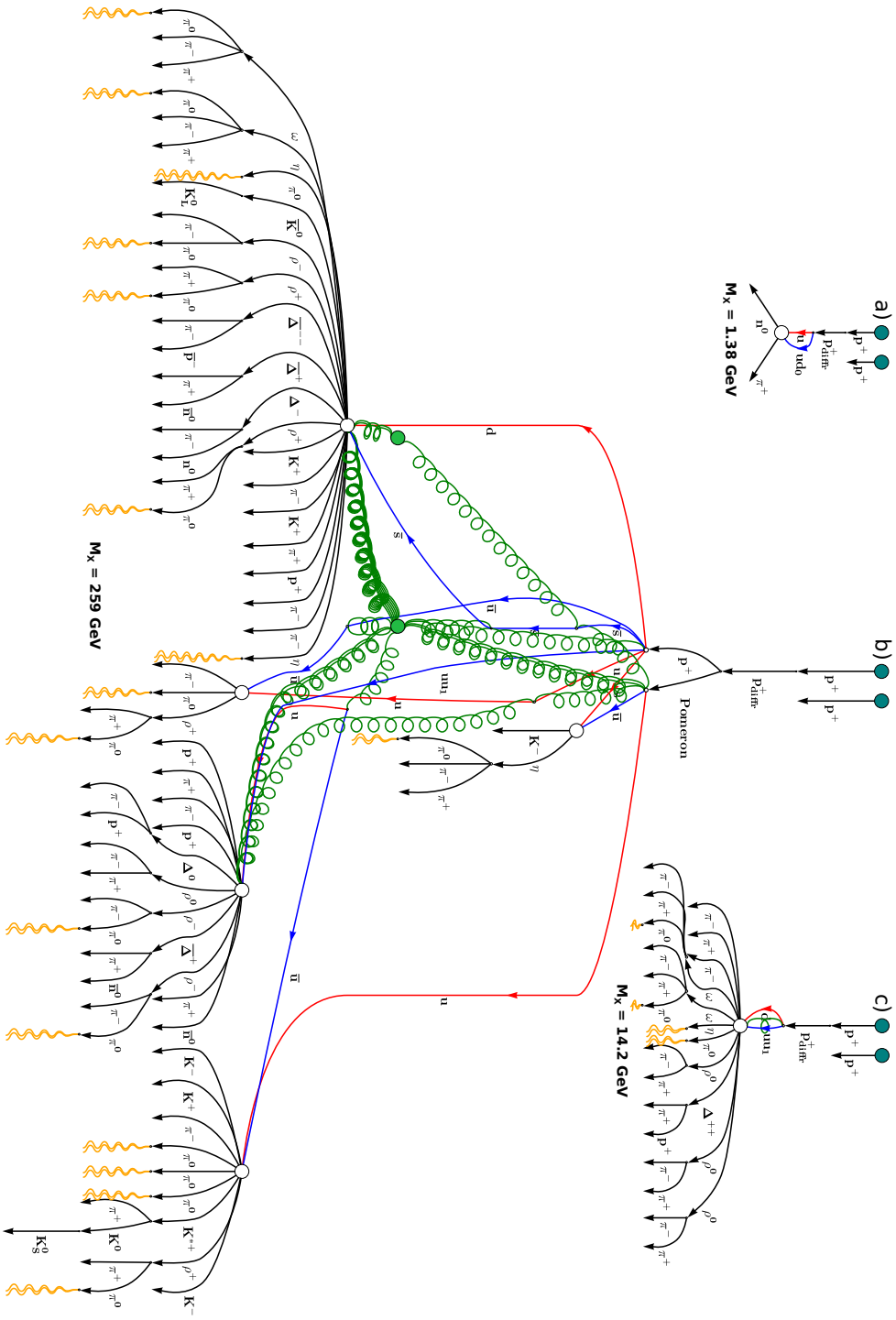

Figure 8.4: Examples of the three diffractive dissociation schemes from events generated at different masses. Ultra-low mass isotropic two body decay (a), high mass partonic treatment with DPDFs from HERA (b) and low mass, hairpin string fragmentation (c). In all cases the full PYTHIA particle flow chain is shown from the initial state proton to the final state *hadron level*. The figures were made with MCViz [69].

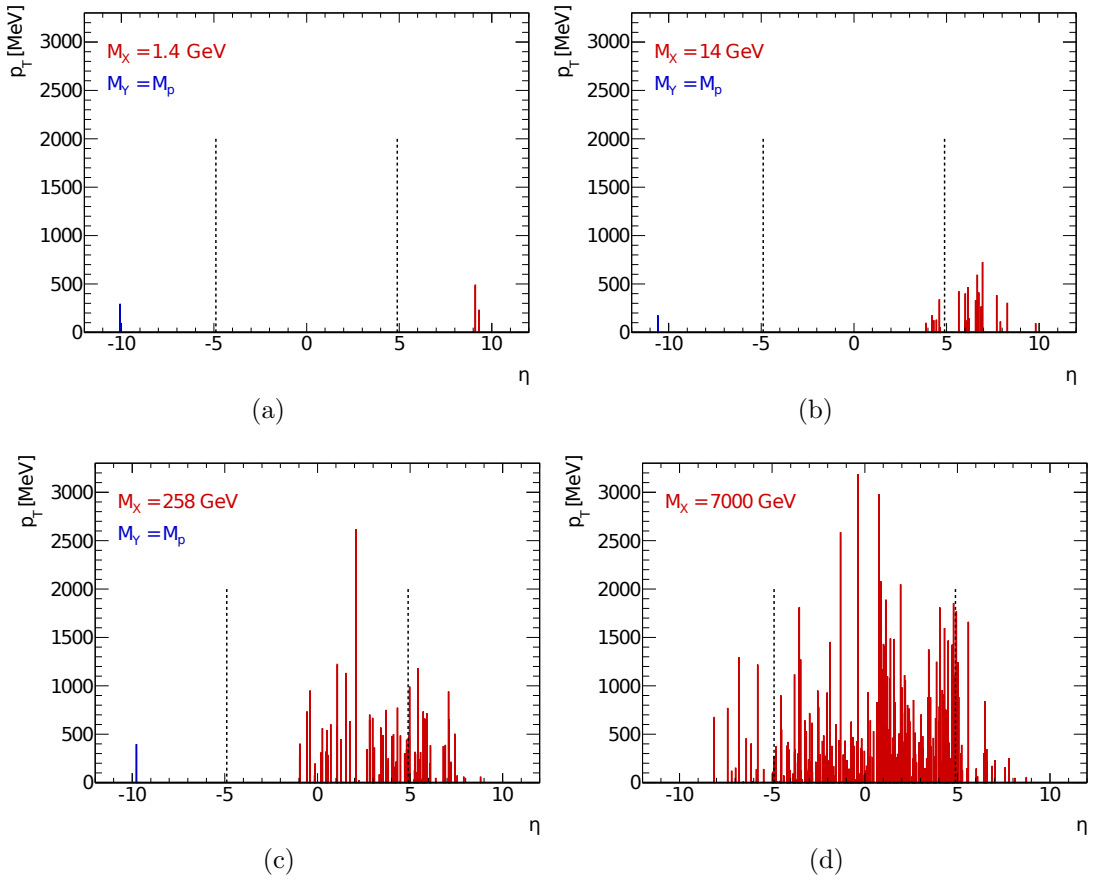

Figure 8.5: Histograms of the final state particle p_{T} as a function of η for PYTHIA events. Corresponding to the events with different diffractive masses in Figure 8.4 (a)-(c). And the inelastic non-diffractive event from the preamble on Page vi (d). Each bar corresponds to a single *hadron level* particle (see Section 9.3) with the height denoting its transverse momentum. The acceptance of the ATLAS detector is denoted by dashed lines.

parameters are taken from the RAPGAP MC [74] manual, including a supercritical Pomeron, which enhances the flux for low mass states. The diffractive slope is exponential in t with an additional mass dependence,

$$\frac{\mathrm{d}^2\sigma_{\mathrm{SD}}}{\mathrm{d}t\mathrm{d}\xi_X} \propto \frac{\beta^2_{\mathbb{P}/p}}{16\pi}\,\xi_X^{1-2\alpha_{\mathbb{P}}(t)} e^{-b_0 t}. \tag{8.9}$$

Here $\alpha_{\mathbb{P}}(t)$ is again the Pomeron trajectory with slope $\alpha' = 0.25$ GeV^2 and intercept $\alpha(0) = 1.085$. The slope parameter b_0 takes the value 4.7 GeV^{-2} and the Pomeron-proton coupling is $\beta_{\mathbb{P}/p}(0) = 58.74$ GeV^{-2}.

For the Donnachie and Landshoff parametrisation [65], the mass dependence and Pomeron trajectory of the Berger et al. Streng model are kept, but the exponential t dependence is replaced by a power law according to (8.10).

$$\frac{\mathrm{d}^2\sigma_{\mathrm{SD}}}{\mathrm{d}t\mathrm{d}\xi_X} \propto \frac{9\delta^2}{4\pi^2}\xi_X^{1-2\alpha_{\mathbb{P}}(t)} \left[\frac{4M_p^2 - 2.8t}{4M_p^2 - t}\frac{1}{(1-t/0.7)^2}\right]^2. \tag{8.10}$$

Here the parameter $\delta^2 = 3.26$ GeV^{-2} and M_p is the proton mass.

The M_X dependences resulting from these Pomeron flux models are illustrated in Figure 8.6.

8.1.4 NON-DIFFRACTIVE EVENTS IN PYTHIA

PYTHIA simulates ND interactions with LO perturbative $2 \to 2$ partonic scatters. The differential cross section is divergent at small p_{T}, with the expression proportional to $\frac{\mathrm{d}p_{\mathrm{T}}^2}{p_{\mathrm{T}}^4}$ This divergence is renormalised phenomenologically after the introduction of a lower cut[1] of $p_{T\mathrm{min}}$. Colour screening is introduced, with $1/p_{T\mathrm{min}}$ being used for a colour-screening-distance. Beyond this distance, partons no longer resolve one another's colour charges and effectively decouple. Similarly, a parton saturation simulation is introduced as a function of parton momentum fraction x to explicitly

[1]The cut-off is not sharp. A sum of contributions at different, fixed $p_{T\mathrm{min}}$ values are used.

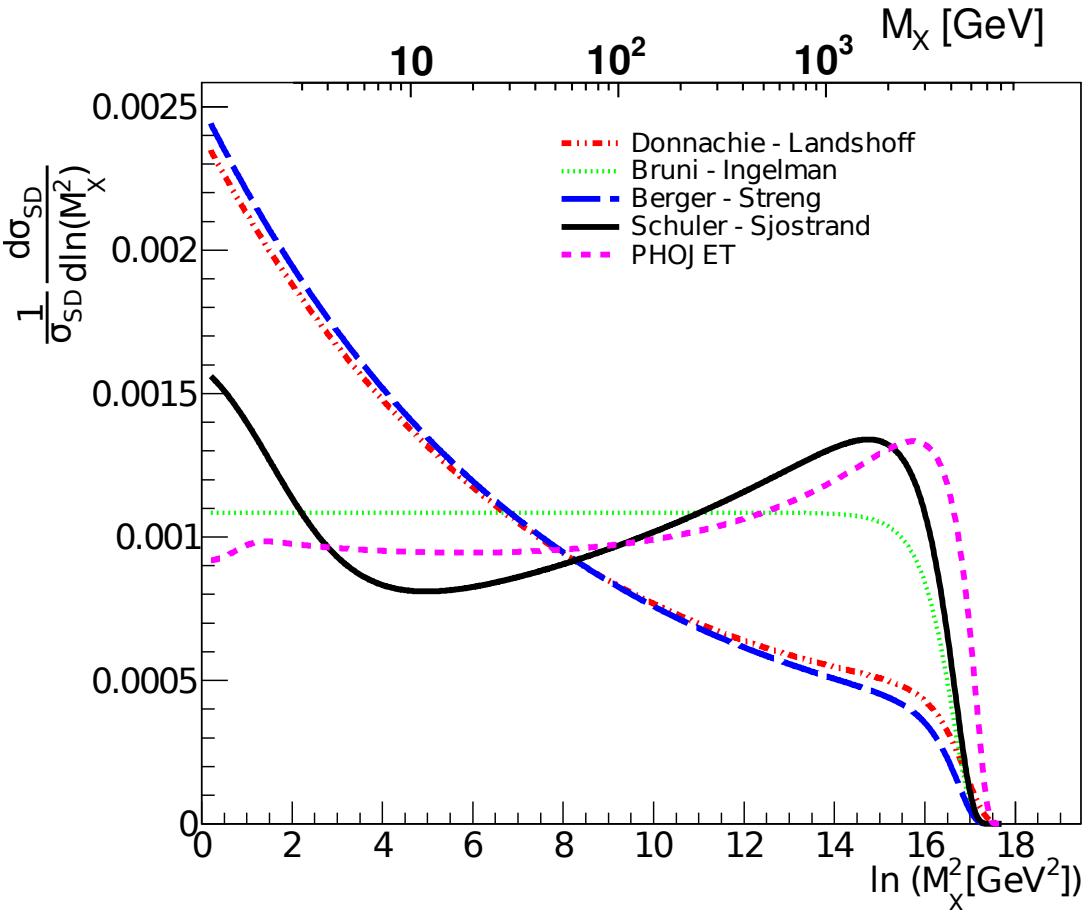

Figure 8.6: Logarithmic comparison of the M_X distributions from different Pomeron flux factors available in PYTHIA8 and PHOJET. Normalised to unit area. Modified version of figure from [75].

reduce the growth of parton densities. Combined, these factors have the effect of controlling the divergence of the cross section at high energies and small x values.

Even with the above regularisation, the basic PYTHIA ND cross section still exceeds the experimentally measured total cross section. This is however under the assumption of a single interaction per event, whereas many are possible. MPI, the multiplicity of soft scatters in the event is dependent on the impact parameter, b, of the protons. The average matter distribution of the protons in PYTHIA is modelled by a spherically symmetric double-Gaussian distribution [76]. The number of independent interactions in the overlap volume of the protons is determined by a Poisson distribution. MPI allows the interaction cross section to grow whilst remaining consistent with the total cross section and preserves the concept of KNO scaling [77]. This states that the distributions of charged particles in inelastic interactions, when normalised to the mean number of charged particles, are not a function of s and are re-scalable at different energies. Data from the ISR and beyond are made compatible with KNO scaling via the inclusion of MPI.

An event only containing soft interactions is classified Non Diffractive. For events with a hard scale, the MPI which is not part of the hard interaction is classified as the Underlying Event (UE).

8.2 PHOJET MONTE CARLO

Diffraction in PHOJET [78][79] is implemented using a $\mathbb{PPP}$ model. For SD,

$$\frac{\mathrm{d}^2\sigma_{\mathrm{SD}}(s)}{\mathrm{d}t\mathrm{d}M_X^2} = \frac{g_{3\mathbb{P}}}{8\pi}\beta_{\mathbb{P}/p}^3\left(\frac{s}{s_0}\right)^{2\Delta_{\mathbb{P}}}\left(\frac{s_0}{M_X^2}\right)^{\alpha_{\mathbb{P}}(0)} e^{2B_{\mathbb{P}}(M_X^2,s)t}, \tag{8.11}$$

with a similar expression for DD. The parameter labels here are the same as in Section 8.1.2. The diffractive slope, $B_{\mathbb{P}}$, is parameterised by a single exponential

with mass dependent slope,

$$2B_{\mathbb{P}}(M_X^2, s) = 2b_p + 2\alpha' \ln\left(2 + \frac{ss_0}{2M_p^4 + 2M_p^2 M_X^2}\right). \tag{8.12}$$

The Pomeron intercept in PHOJET is taken to be $\alpha_{\mathbb{P}}(0) = 1.08$. This slope leads to a smooth transition between elastic scattering and diffractive excitations.

To account for the modifications to the low-mass cross section from resonant exchange, the mass distribution is multiplied by a factor $f(M_D)$ where

$$f(M_D) = \begin{cases} \frac{(M_{X,\min}^2 + M_\Delta^2)(M_X^2 - M_{X,\min}^2)}{M_X^2 M_\Delta^2} & : M_X^2 \leq M_{X,\min}^2 + M_\Delta^2 \\ 1 & : M_X^2 > M_{X,\min}^2 + M_\Delta^2 \end{cases} \tag{8.13}$$

Here $M_\Delta^2 = 1.1$ GeV^2 and the minimum allowed diffractive mass in the model $M_{X,\min} = M_p + M_\Delta$, M_p is the proton mass.

The dissociated system is modelled using a Dual Parton Model [80][81] in which the effects of a soft and hard Pomeron are combined. AGK [82] cutting rules are used to transition from the Regge formalism to lowest order QCD for events with $|t| > 3$ GeV^2. Diffractive partonic interactions use DPDFs from HERA [83][84] and string fragmentation is handled by JETSET as in PYTHIA [85].

PHOJET additionally implements the CD process of double Pomeron exchange at the level of 1.7% of the total inelastic cross section.

8.3 HERWIG++ MONTE CARLO

The HERWIG++ MC has the capacity to simulate ND minimum-bias events via the application of the generator's UE model with the hard scatter matrix element set to the identity matrix . A Donnachie-Landshoff based model is used separately [86] to calculate a value of 81 mb for the total cross section.

Similarly to PYTHIA, HERWIG++ contains an UE model in which multiple scatters are treated as being independent of each other. For fixed impact parameter this results in a Poisson distribution for both soft and semi-hard scatters. The probability of a particular scattering multiplicity is given by

$$P_{h,n}(b,s) = \frac{\mu_{\mathrm{QCD}}(b,s)^h}{h!}\frac{\mu_{\mathrm{soft}}(b,s)^n}{n!}\exp\left(-\mu_{\mathrm{QCD}}(b,s) - \mu_{\mathrm{soft}}(b,s)\right), \tag{8.14}$$

where $P_{h,n}(b,s)$ is the probability of having exactly h semi-hard processes and n soft scatters, determined by mean values $\mu_{\mathrm{QCD}}(b,s)^h$ and $\mu_{\mathrm{soft}}(b,s)^n$ respectively. The probability depends on both the impact parameter b and the centre of mass energy squared s. The two regimes are divided about a point $p_{\mathrm{T}}^{\mathrm{cut}} = 3.36$ GeV such that semi-hard processes produce objects with $p_{\mathrm{T}} > p_{\mathrm{T}}^{\mathrm{cut}}$ while soft processes produce objects with $p_{\mathrm{T}} < p_{\mathrm{T}}^{\mathrm{cut}}$. In the rare cases that $h = 0$ and $n = 0$, a pseudo-DD topology is produced from the dissociation remnants of the beam protons.

HERWIG++ uses a cluster hadronisation model. Partons from the parton shower are combined into colour singlet pairs called clusters, which are akin to excited hadronic states. These clusters are continuously split until they have the required mass to decay into hadrons. In recent releases, a Colour Reconnection (CR) mechanism reconnects partons between cluster pairs to improve the modelling of the charged particle multiplicity distribution in pp collisions [87].

8.4 TUNING OF MONTE CARLO CROSS SECTIONS

The cross sections for the SD and DD processes in PYTHIA and PHOJET vary considerably once integrated over ξ_X, ξ_Y and t. The diffractive cross section in PYTHIA8 is further enhanced over PYTHIA6 with a corresponding reduction of the ND cross section, based upon the preliminary ATLAS result [88].

For use in correcting the data, the relative contributions to the total cross section from the different sub-processes are tuned from experimental data.

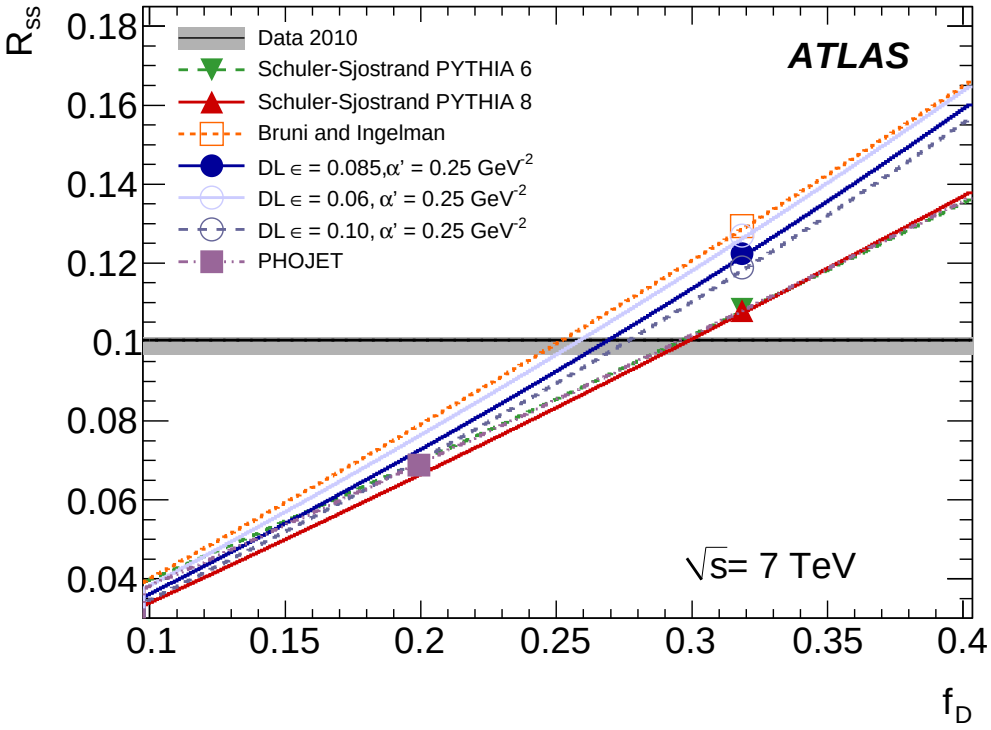

Figure 8.7: Fraction of exclusively single sided MBTS events, R_{SS}, in data and in MC as a function of f_D. The coloured symbols indicate the default MC f_D values, whilst the lines indicate the sensitivity to R_{SS} as f_D is varied from these defaults (while the generator default ratio of f_{SD} to f_{DD} is fixed). Taken from [52], see text for further explanation.

The overall fraction of diffraction (SD and DD) in the models, f_D, is tuned in a model dependent manner using the ATLAS result [52]. The variable R_{SS} is defined as the fraction of all MBTS triggered events with two or more counters above threshold on one side of the detector and exactly zero counters on the other. This single-sided event fraction is measured from ATLAS minimum bias data to be $R_{\mathrm{SS}} = [10.02 \pm 0.03(\mathrm{stat.})^{+0.10}_{-0.40}(\mathrm{syst.})]\%$. The sensitivity to f_D of R_{SS} is presented for various MC models in Figure 8.7. For each MC, f_D is tuned such that the R_{SS} value matches the result from data. This tune is sensitive to the MC diffraction dynamics so different results are obtained for each MC. Values of $f_D \approx 30\%$ are determined for the default versions of the MCs considered. However, the sensitivity of R_{SS} to the Pomeron intercept $\alpha_{\mathbb{P}}(0)$ and the flux modelling results, for example in $f_D \approx 25\%$ for PYTHIA8 with the Bruni and Ingelman flux.

The default f_{SD} and f_{DD} values in PYTHIA and PHOJET do not take into account data from the Tevatron. Measurements of $p\bar{p}$ interactions at 1.8 TeV from The Collider Detector at Fermilab (CDF) are used to constrain the SD and DD contributions in this analysis. Although the diffractive component of the cross section is expected to grow with the increased centre of mass energy, the ratio of single to double diffraction is not predicted by Regge theory to vary strongly with $\sqrt{s}$ as seen in the differences in their form factors from (8.3). The CDF measurements of the SD [89] and DD [62] cross sections are extrapolated via MC to the full kinematic range. In addition, the measurement of the CD cross section [58] is used with PHOJET.

For the SD process, the Tevatron cross section is measured to be 9.46 ± 0.44 mb for event satisfying $1.4\ \mathrm{GeV}^2 < M_X^2 < 0.15s$ [89]. For DD, a cross section of $4.43 \pm 0.02(\mathrm{stat}) \pm 1.18(\mathrm{syst})$ mb is measured for events with $\Delta\eta_0 > 3$, where $\Delta\eta_0$ is the size of the pseudorapidity gap which spans central rapidity [62]. After correcting for the acceptances of these requirements, relative to the full SD and DD cross sections according to each MC model; PYTHIA is constrained by the data to lie in the range $0.29 < \sigma_{\mathrm{DD}}/\sigma_{\mathrm{SD}} < 0.68$ and PHOJET in the range $0.44 < \sigma_{\mathrm{DD}}/\sigma_{\mathrm{SD}} < 0.94$. The fraction of CD in the PHOJET generator is compatible with the measured ratio $\sigma_{\mathrm{CD}}/\sigma_{\mathrm{SD}} = 0.093$ [58] and is hence not modified in the nominal tune, rather it is simply scaled in proportion to f_{SD}. The nominal tuned values are taken at the centre of the above bounds. The MC default and tuned nominal cross sections are listed in Table 8.1.

Table 8.1: Default and tuned MC cross sections at $\sqrt{s} = 7$ TeV

Process	PYTHIA6	PYTHIA8	PHOJET
Default σ_{ND} (mb)	48.5	50.9	61.6
Default σ_{SD} (mb)	13.7	12.4	10.7
Default σ_{DD} (mb)	9.2	8.1	3.9
Default σ_{CD} (mb)	0.0	0.0	1.3
Default f_{ND} (%)	67.9	71.3	79.4
Default f_{SD} (%)	19.2	17.3	13.8
Default f_{DD} (%)	12.9	11.4	5.1
Default f_{CD} (%)	0.0	0.0	1.7
Tuned f_{ND} (%)	70.0	70.2	70.2
Tuned f_{SD} (%)	20.7	20.6	16.1
Tuned f_{DD} (%)	9.3	9.2	11.2
Tuned f_{CD} (%)	0.0	0.0	2.5

8.4.1 MONTE CARLO TUNES

The specific MC versions used to correct the data were PYTHIA6.4.21 with the tune `AMBT1` performed by ATLAS [90], PYTHIA8.145 with the author tune `4C` [63] and PHOJET12.1.35 [79] with hadronisation and fragmentation handled in PYTHIA6.1.15. Updated versions PYTHIA8.145 with `4C` and PYTHIA6.4.25 with `AMBT2B` [63] are used when comparing tunes with the corrected data.

Details about these tunes may be found in their respective documents.

8.5 MONTE CARLO STATISTICS

The statistics of the MC samples used in the analysis are listed in Table 8.2. The cross section-normalised MC statistics are 1.7 – 2.6 times those of the data sample for the ND topology. For the diffractive regions, the MC statistics are a factor of 2.4 – 6.0 times larger than data.

Table 8.2: MC Statistics. Non-round numbers are due to events lost throughout the distributed analysis and data preparation campaigns.

	ND	SD	DD	CD
PYTHIA8	750000	499991	315990	-
PYTHIA6	674951	499992	473994	-
PHOJET	499965	199998	199994	99999

CHAPTER 9

EVENT SELECTION AND CUTS

9.1 DATA SAMPLE

The data for this analysis were collected during the first physics fill of the LHC at $\sqrt{s} = 7$ TeV. With the beam orbit declared stable by the LHC accelerator group, ATLAS was permitted to ramp the high-voltage biases of the sensitive silicon based tracking detectors to operational voltage. The first data at $\sqrt{s} = 7$ TeV with stable beams and a fully operational detector were then collected between 13:24 and 16:38 on March 30$^{\text{th}}$ 2010. A data sample of 422776 minimum bias events was recorded corresponding to an integrated luminosity of $7.1 \pm 0.2\ \mu\text{b}^{-1}$ at a maximum instantaneous luminosity of $1.1 \times 10^{27}\text{cm}^{-2}\text{s}^{-1}$.

The conditions present in the accelerator and detector were excellent for minimum bias physics. Only two proton bunches were injected into each beam; one pair colliding at both ATLAS and CMS and the other unpaired (to ATLAS) bunches colliding

in ALICE and LHCb. Beams were therefore brought into coincidence within ATLAS once every 89 μs, with a minimum gap of 22 μs between the traversal of each of the two unpaired bunches. In addition, the space-charge in each bunch was kept low at around 10^{10} protons per bunch. This resulted in a maximum number of interactions per bunch-crossing $\mu = 0.005$. Such low rates allowed for beam and collision-induced radiation levels in the detector cavern to naturally dissipate in the time between interactions.

9.1.1 TRIGGERING ON MINIMUM BIAS EVENTS

During early, low luminosity running, the ATLAS minimum bias trigger strategy was centred around the MBTS detector as described in Section 5.2.3. In the L1 trigger, MBTS items follow the nomenclature L1_MBTS_X or L1_MBTS_X_Y. In the former case, X denotes the total number of counters above threshold (summed over the A and C sides of the detector) required to fire the trigger; and in the latter case X and Y denote the multiplicity of counters on the A and C sides of the detector, respectively, required to trigger the event. Trigger items which require a larger multiplicity of counters are more biased to events with greater levels of particle production, and items which require a logical-AND of counters on both sides of the detector are more biased to events with particle production over a large range or pseudorapidities.

The loosest trigger item, L1_MBTS_1, requires only one of the 32 MBTS counters to be above threshold. Although this is most susceptible to erroneous triggers from beam induced backgrounds, the collision rate was low enough during the first few periods of data taking that all triggered events were recorded to tape. More stringent MBTS requirements were then applied during off-line selection.

9.1.2 EFFICIENCY OF THE MBTS

The efficiency of the MBTS is studied in [91] and [92]. Over the ID – MBTS overlap region ($2.09 < |\eta| < 2.5$), the trajectories of charged particles with $p_{\mathrm{T}} > 200$ MeV are extrapolated from the ID to the MBTS. The extrapolation is based on the reconstructed track parameters and incorporates material effects along with the effects of the magnetic field. For each counter in each event, the number of tracks extrapolated to the counter is recorded. For the innermost counters, with no overlap with the ID, the FCal overlap is utilised ($3.1 < |\eta| < 3.8$). Cells with $E > 1$ GeV are considered to be above the noise level in both MC and data. These are extrapolated back to the MBTS. The HEC overlap ($2.5 < |\eta| < 3.2$) is utilised similarly as a cross-check.

A counter is said to be *tagged* if it is associated with exactly one extrapolated track or calorimeter cell. By assuming the electronic noise distribution to be a Gaussian centred on zero, the efficiency of the MBTS, ϵ_{MBTS}, is defined to be the number of tagged counters with charge $Q_{\mathrm{c}} > 0.15$ pC divided by the total number of tagged counters, less twice the number of tagged counters with $Q_{\mathrm{c}} < 0.0$ pC. This statistically subtracts any noise fluctuations.

$$\epsilon_{\mathrm{MBTS}} = \frac{N_{\mathrm{Tag}}^{Q_{\mathrm{c}}>0.15}}{N_{\mathrm{Tag}} - \left[2 \times N_{\mathrm{Tag}}^{Q_{\mathrm{c}}<0.0}\right]}. \tag{9.1}$$

Here N_{Tag} is the number of tagged MBTS counters and $N_{\mathrm{Tag}}^{Q_{\mathrm{c}}}$ is the number of tagged counters satisfying the specified charge collection requirement (> 0.15 or < 0.0 pC). Although not guaranteeing a single-particle response, a good approximation is obtained by this method of requiring exactly one associated track or cell, as the mean flux per counter solid-angle per event containing charged particles with $p_{\mathrm{T}} > 100$ MeV is smaller than 0.5, as measured in [5].

The charge threshold of 0.15 pC is chosen to be well above the Gaussian electronic noise peak which has width $\sigma \approx 0.02$ pC.

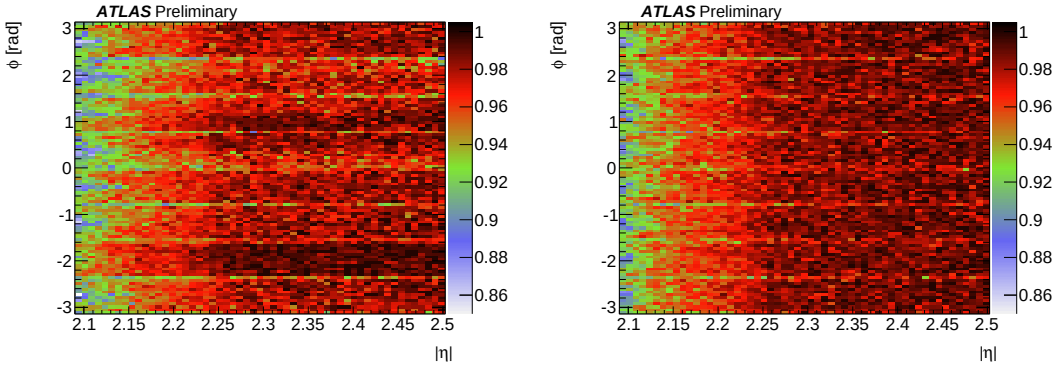

(a) (b)

Figure 9.1: Two dimensional $\eta - \phi$ map of the efficiency of MBTS counters in data (a) and MC (b) using the methods based on extrapolated tracks. Taken from [91].

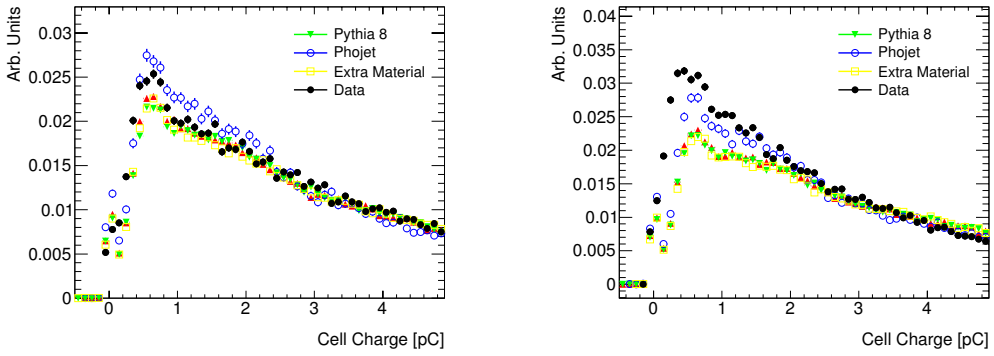

(a) (b)

Figure 9.2: Charge collection distributions for two representative MBTS counters in data and for various MC models. (a) shows a counter with relatively good agreement and (b) a counter with poor agreement. Taken from [92].

In Figure 9.1, the two-dimensional hit map of the efficiency of A side counters is presented in data (a) and MC (b) from reconstructed tracks. The overall agreement is very good. The loss of efficiency at low η is consistent with expectation based on the track extrapolation uncertainty and the loss of efficiency in ϕ at the counter edges is visible as an 8-fold symmetry. The charge collected per counter is also compared for two example counters in Figure 9.2. The counter in (a) shows a good agreement while for the counter in (b), the raw agreement is poorer. This poor modelling is corrected for in the following section.

9.1.3 OFF-LINE MBTS SELECTION PROCESS

Data are collected with the L1_MBTS_1 trigger. The simulated MBTS response in the MC is adjusted to match the conditions off-line.

Off-line, two MBTS counters are required rather than one. This improves the beam background suppression discussed in Section 9.1.4. Data events are therefore required to contain two or more counters with charge deposition > 0.15 pC.

The thresholds in MC are tuned using the results of the study described in [91][92]. Overall it was shown that the MBTS response was 1% higher in MC than in data. The MC thresholds applied are calculated separately in four detector regions; A side inner, A side outer, C side inner and C side outer counters, such that the average MC response in the region matches that of the data.

There was one MBTS counter which was not functioning due to a fault in its low voltage power supply. This counter is not explicitly disabled in MC but its effect is corrected for via the large MC threshold calculated for its detector regions.

In addition, a systematic study of the stability of the physics result with respect to the MBTS counter thresholds was performed by varying the threshold of all counters in each region in MC to match the counter in data from the same region whose response was farthest from the mean. This is utilised in the systematic uncertainties described in Section 10.3.1. Table 9.1 tabulates the nominal and systematically shifted thresholds used in data and MC.

9.1.4 TREATMENT OF BACKGROUNDS AND PILE-UP

Event types classified as *backgrounds* for this analysis include beam backgrounds which sub-categorise as *beam gas*, where an inelastic interaction occur between the beam and residual gas molecules within the beam pipe in ATLAS and *beam halo*, where ATLAS is traversed by muons (typically) created in beam gas interactions

Table 9.1: MBTS counter threshold values applied off-line to data and both nominal MC and MC systematically shifted to describe the farthest outlier in the data [92].

	Data Threshold [pC]	**MC Nominal Threshold [pC]**	**MC Systematic Threshold [pC]**
A Side Outer	0.15	0.28	0.18
A Side Inner	0.15	0.32	0.50
C Side Outer	0.15	0.26	0.38
C Side Inner	0.15	0.38	0.60

outside of the experimental cavern.

These events topologies tend to create particles which traverse the detector parallel to the beam pipe at small radii. Track finding algorithms work by default under the hypothesis that tracks originate from the IP. Therefore a signature of such beam backgrounds is a large number of space-points in the Pixel detector which are not associated to any reconstructed track.

In Figure 9.3, the multiplicity of unassociated Pixel space points is plotted in data for paired and unpaired bunches[1]. In each case the events are required to pass the off-line trigger requirement.

The two samples are normalised in the tail with > 1000 unassociated space-points. 235 events in the unpaired sample are above this multiplicity and the normalisation factor is calculated to be 1.17. Scaling the whole unpaired sample up by this factor leads to an estimate of the total background contamination of 0.22%. This is subtracted from the physics sample statistically as described in Section 10.3.2.

Studies showed that if the off-line trigger requirement was reduced to one MBTS counter, this background contribution increases by a factor of 10.

Another complicated event type for this analysis is *pile-up* which occurs when multiple inelastic proton-proton interactions take place in a single bunch-crossing. As this

[1]Bunch groups 1 and 7, respectively from Table 5.1. Paired denotes a bunch in each beam in ATLAS and hence the possibility of a beam-beam collision whereas unpaired denotes a bunch in only one beam, which is used to cleanly sample beam backgrounds.

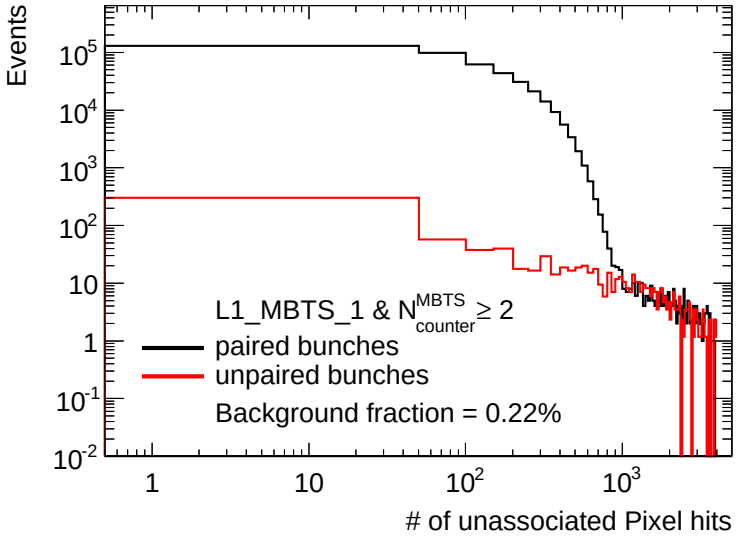

Figure 9.3: Comparison of number of unassociated space-points in paired and (normalised) unpaired bunches with all MBTS requirements. Taken from [1].

analysis uses calorimeters which lie outside of the tracking volume, it is not possible for all energy depositions to be associated with a reconstructed vertex, which is the standard method of decomposing pile-up events. Indeed, no vertexing requirements are made at all.

Through application of Poisson statistics on the interaction rate stated in Section 9.1, the probability of more than one interaction occurring in a bunch-crossing is of order 2.5×10^{-3}. This is consistent with the 402 events in the data sample containing at least two reconstructed primary vertices[2]. These events are excluded from further study.

No correction is applied for pile-up events with fewer than two reconstructed primary vertices as this contributions is further suppressed with respect to the two-or-more primary vertex case. In addition, no reduction is made to the integrated luminosity of the sample to account for the events rejected as pile-up as the correction is small with respect to the luminosity uncertainty, which is a factor of 34 larger.

[2]Here we consider good quality reconstructed vertices, with four or more associated tracks.

9.2 DEFINITION OF RECONSTRUCTED QUANTITIES

Raw electronic signals from the detector are subjected to algorithms which output calibrated *objects*. The algorithms are designed to provide a strong correlation between these objects and the underlying particles, whose interactions with the active detector volumes are responsible for their formation.

Once all cuts and selection criteria explained in this section have been applied, the selected tracks, topological calorimeter clusters and MC particles are all used as input to the analysis.

9.2.1 TRACKING SELECTION

Tracks are reconstructed from silicon space-points and TRT hits recorded in the active region of the ID. The inside-out tracking algorithms used by ATLAS are seeded by hits in the inner silicon tracker. A search window around the seed at larger radii is defined, whose size is dependent on the smallest p_{T} to be reconstructed by the algorithm. Hits within the window are assessed with Kalman filtering [93] and, if accepted, are added to the track candidate. Ambiguity resolution is then performed by assessing the quality of ambiguous solutions and favouring fully reconstructed tracks over smaller track segments [94].

The efficiency of the reconstruction of charged particles was studied in [5], Figure 9.4 shows that the efficiency is determined to be $\approx 60\%$ for charged particles with p_{T} = 200 MeV.

A modified version of the physics track selection from [5] is used to account for the lack of a vertex requirement in this analysis. The track selection is presented in Table 9.2

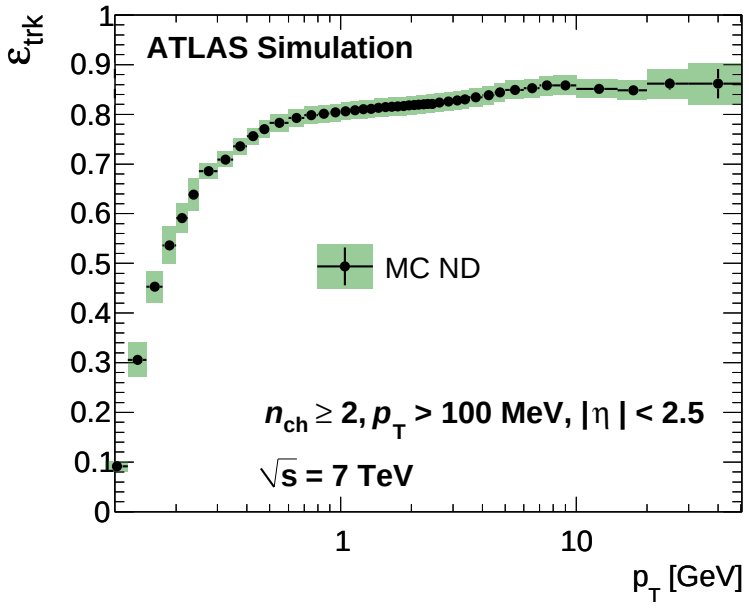

Figure 9.4: Efficiency of reconstruction of charged particle tracks as a function of p_{T} derived from ND MC. This applies to tracks with $|\eta| < 2.5$ and events with two or more tracks associated to the beam spot. Taken from [5].

Table 9.2: Selection cuts applied to reconstructed tracks. The BLayer is defined as the first tracking layer in the Pixel detector, d_0^{PV} and d_0^{BS} are the transverse impact parameters with respect to the primary vertex and beam spot, respectively, and z_0^{PV} is the longitudinal impact parameter with respect to the primary vertex.

Cut	**Value**	**Prerequisite**
$\lvert\eta\rvert$	< 2.5	
p_{T}	> 100 MeV	
N BLayer Hits	> 0	*Only if expected for trajectory*
N Pixel Hits	> 1	
N SCT Hits	> 2	*For* $p_{\mathrm{T}} > 100$ MeV
	> 4	*For* $p_{\mathrm{T}} > 200$ MeV
	> 6	*For* $p_{\mathrm{T}} > 300$ MeV
$\lvert d_0^{\mathrm{PV}}\rvert$	< 1.5 mm	*Only if primary vertex found*
$z_0^{\mathrm{PV}} \cdot \sin(\theta)$	< 1.5 mm	*Only if primary vertex found*
$\lvert d_0^{\mathrm{BS}}\rvert$	< 1.8 mm	*Only if no primary vertex found*

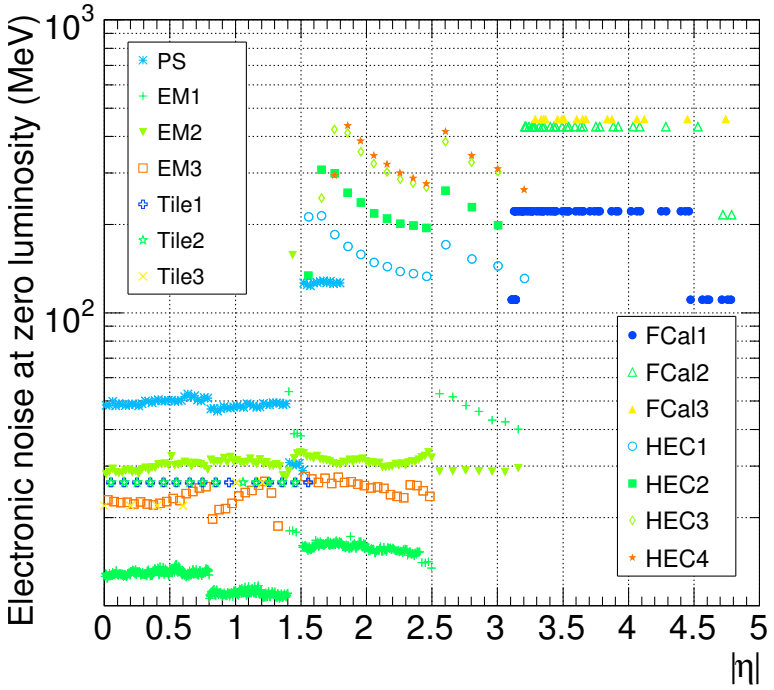

Figure 9.5: Per-cell RMS electronic noise in the calorimeters as a function of $|\eta|$. Taken from [95].

9.2.2 CALORIMETER SELECTION

The ATLAS calorimeter systems span 9.8 units of pseudorapidity, utilising multiple technologies and cell granularities, and occupying regions with greatly differing energy flux. In Figure 9.5, the per-cell RMS electronic noise in MeV is plotted for all calorimeters as a function of $|\eta|$.

The treatment of cells in the calorimeter as a whole is unified by using the cell energy significance, $S = E/\sigma_{\text{Noise}}$, where E is the pedestal-subtracted energy deposition (such that the mean of the noise peak lies at zero) and σ_{Noise} is the RMS of the electronic noise in the cell. Figure 9.6 shows the S distributions for the principal calorimeter technologies. The pedestal subtracted energy results in a Gaussian noise distribution centred on zero for the LAr based calorimeter technologies while the tile calorimeter exhibits a double-Gaussian noise profile, observed in the broadening of the noise distribution in Figure 9.6(d), when compared to the other systems. Overall,

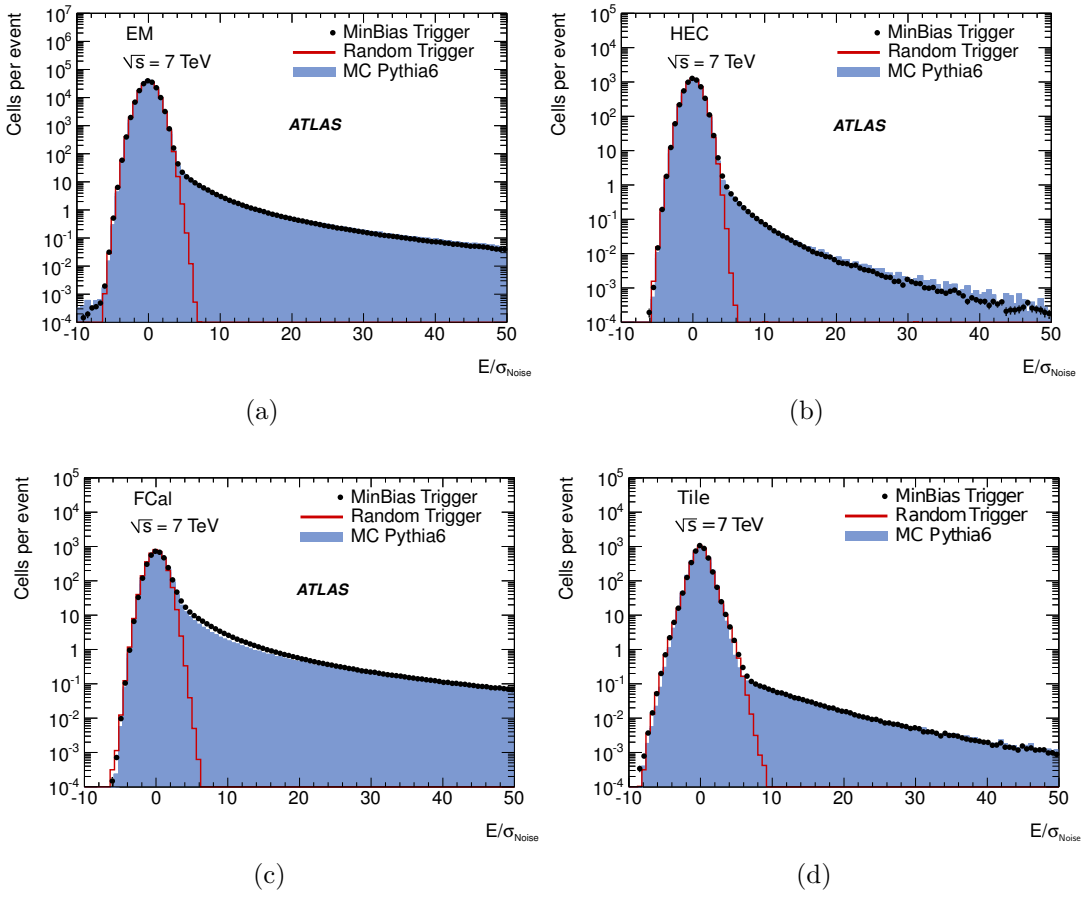

Figure 9.6: Calorimeter energy significance distributions in the EM barrel (a), the HEC (b), the forward calorimeters (c) and the Tile calorimeter (d) (see text for details). The red curve corresponds to data taken with a random trigger in combination with a veto on other minimum bias triggers including MBTS. This sample therefore represents the pure noise contribution. The filled histogram and data points are L1_MBTS_1 selected events in MC and data. The contribution from physics is visible in the positive tail. Taken from [1].

a good agreement between MC and data is observed over more than five orders of magnitude in the long positive tails, associated with real physics events. Areas where disagreement is observed are primarily expected to be due to deficiencies in the PYTHIA6 model. The agreement of the noise distribution at negative energy between the random sample and the minimum bias physics sample is excellent up to around five standard deviations.

Energy depositions in the calorimeter are collated via a topological clustering algorithm [95], the default parameters of which are listed in Table 9.3. Clusters are

Table 9.3: Parameters for the default hadronic '420' (from the choice of parameters) topological clustering algorithm.

Parameter	**Absolute Significance** $\|\boldsymbol{E}\|/\boldsymbol{\sigma}_{\mathbf{Noise}}$
t_{Seed}	4
$t_{\text{Neighbour}}$	2
t_{Cell}	0

seeded from cells with absolute significance $|S| > t_{\text{Seed}}$. The absolute significance is used so that on average, the positive and negative tails of the noise distribution will cancel each other out when the clusters are used in subsequent combinations[3].

For each seed cell, all neighbour cells are queried. Neighbours are determined in three dimensions including adjacent layers and adjacent calorimeter systems, the number of neighbours varies with position, though a typical cell has ten neighbours. The neighbour cells are included in the proton-cluster should they have $|S| > t_{\text{Neighbour}}$ and proton-clusters are merged where multiple seeds share a neighbour above threshold.

The procedure is iterated. At the beginning of each iteration, all neighbour cells become new seed cells. The process stops when no additional neighbour cells satisfy $|S| > t_{\text{Neighbour}}$.

As a final step; all neighbour cells on the perimeter of the proton-clusters with $|S| > t_{\text{Cell}}$ are added to form the final topological clusters. This step ensures that the tail of the shower is retained and provides additional sensitivity to low energy depositions. Since in the default configuration $t_{\text{Cell}} = 0$, all perimeter cells are included.

With 187616 cells in the ATLAS calorimeter systems, Poisson statistics dictate that with $t_{\text{Seed}} = 4$, there will be on average 12 clusters per event produced by noise fluctuations, half of which will be from positive energy seeds. The distribution of these

[3]As input to anti-k_t jet finding algorithms for example.

noise clusters follows the density of cells in the calorimeter, and thus peaks in the barrel region as inferred from Figure 9.7(a). This is problematic as contamination from noise severely reduces the efficiency of reconstructing large rapidity gaps. Further requirements are therefore made to suppress these topological clusters produced by noise fluctuations.

9.2.2.1 CALORIMETER NOISE SUPPRESSION

A statistical technique is used to apply a more stringent noise suppression than that of the default clustering algorithm. An energy significance cut $S_{\text{th}}(\eta)$ is determined as a function of pseudorapidity based on the density of calorimeter cells. The cut is defined by dividing the calorimeter systems spanning $|\eta| < 4.9$ into 98 regions of $\Delta\eta = 0.1$ and integrating the positive contribution of the Gaussian tail to obtain a constant P_{Noise} in (9.2) for each η region,

$$P_{\text{Noise}}/N = \int_{S_{\text{th}}}^{\infty} e^{-S^2/2} \mathrm{d}S. \tag{9.2}$$

Here S is energy significance, N is the number of cells from the LAr detectors in the detector region[4], P_{Noise} is the desired noise probability and S_{th} is the deduced cut value.

P_{Noise} is optimised to the value 1.4×10^{-4} by minimising the subsequent resolution of reconstructed rapidity gap sizes with respect to gaps at the hadron level in MC. As there are 98 regions, this corresponds to a global noise fluctuation probability of 1.4% per event. The $S_{\text{th}}(\eta)$ distribution which results in this probability along with the total number of calorimeter cells per region are plotted in Figure 9.7. The smallest cut is at the edge of the detector, $S_{\text{th}}(4.9) = 4.8$ while at central rapidity the cell density increases considerably and the threshold correspondingly rises to $S_{\text{th}}(0.0) = 5.8$.

[4]While the LAr systems exhibit a Gaussian noise profile, the electronic noise in the tile calorimeters is a double-Gaussian, as seen in Figure 9.6(d). The tile calorimeter is therefore not used during noise suppression.

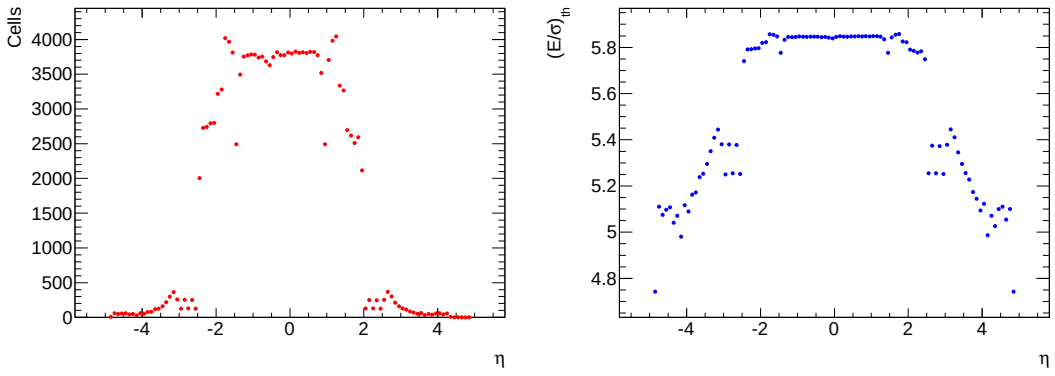

(a) (b)

Figure 9.7: Total number of cells per 0.1 units of η, integrated over all ϕ (a) and cell threshold significance cut per region (b). Taken from [1].

For each calorimeter topological cluster, the cell with the highest energy significance which does not come from the Tile calorimeter (see footnote 4 on page 113) is required to have a significance $S \geq S_{\text{th}}(\eta_{\text{Cell}})$ where η_{Cell} is the pseudorapidity of the cell. If this is not satisfied then the cluster is rejected.

In Figure 9.8 the E_{T} of all clusters in regions of $\Delta\eta = 0.2$, integrated over all ϕ, are plotted both with and without the noise suppression requirement. The subtle double peak structure at $E_{\text{T}} = 400$ MeV originates from the interactions of charged particles in the magnetic field (Section 9.4.1) while the complicated structure at $E_{\text{T}} < 300$ MeV derives from the application of noise suppression on the large noise peak. For clusters reconstructed with E_{T} above 200 MeV, the noise suppression is observed to reduce the cluster multiplicity at central pseudorapidity by a factor of six while in the forward regions, it has little effect. A mis-modelling of the forward energy flow is observed in the forward region, where the data are consistently higher than MC. This discrepancy does not cause any serious mis-modelling effects with our choice of gap reconstruction algorithm, as explained in Section 10.2.

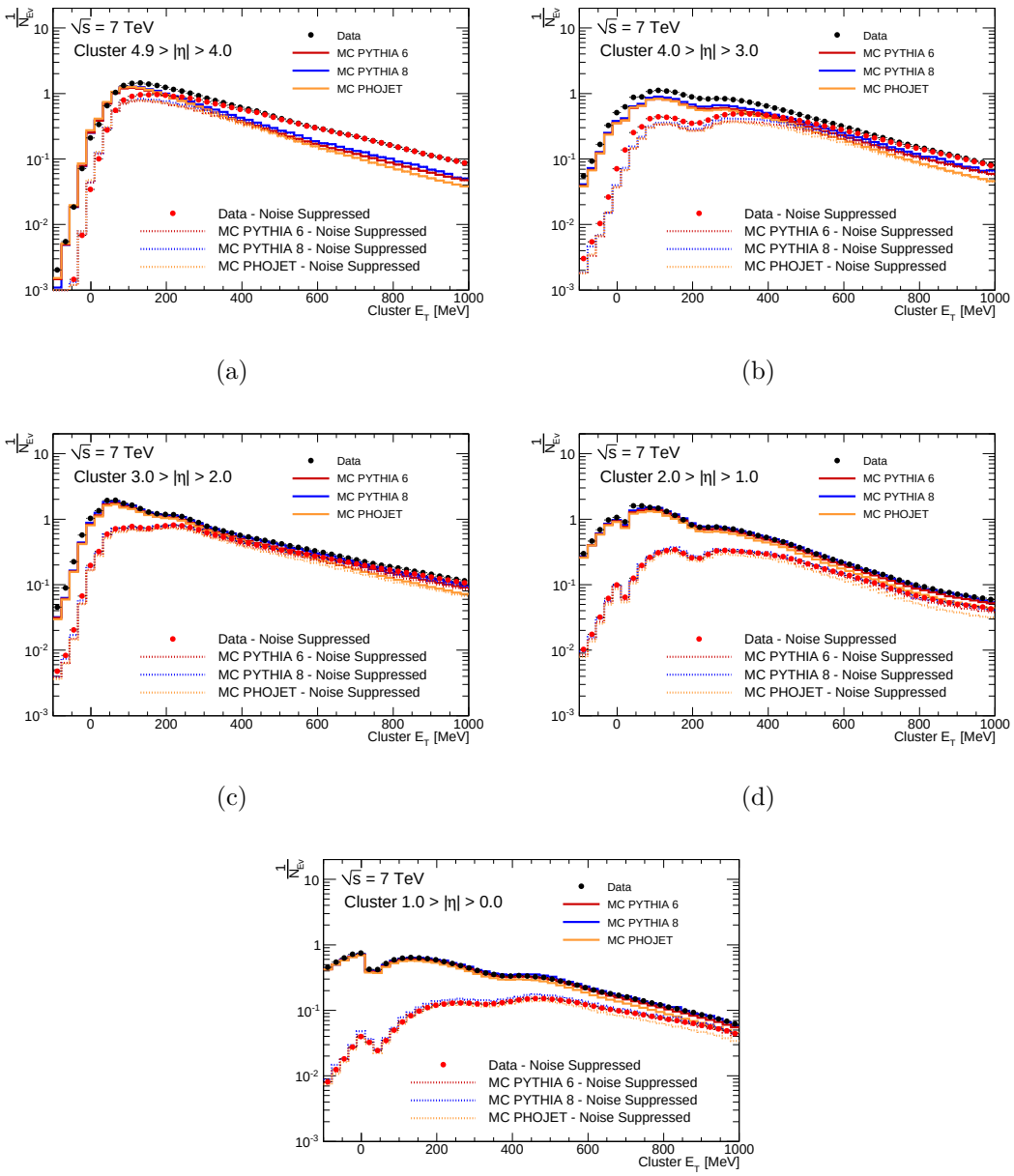

Figure 9.8: Cluster E_{T} spectrum in $|\eta|$ regions, showing MC (solid) and data (black points) for all topological clusters and also MC (dashed) and data (red points) for clusters passing the noise suppression requirements.

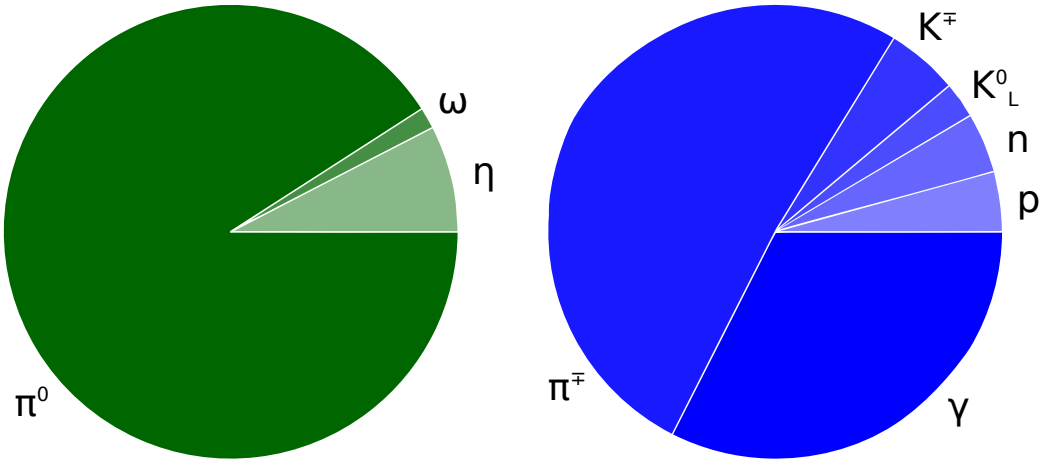

(a) (b)

Figure 9.9: The parent particle of photons at the hadron level (a). Breakdown of the major constituents of the hadron level in the PYTHIA MC for particles with p_{T} > 100 MeV (b).

9.3 DEFINITION OF GENERATOR LEVEL QUANTITIES

For the study of MC generator quantities, the *hadron level*[5] is defined to include all particles with proper lifetime greater than 10 ps. It should be noted that the π^0 does not satisfy this requirement. These are decayed by the generator; primarily to $\gamma\gamma$ (the parents of all hadron level photons in MC is plotted in Figure 9.9(a)).

The *hadron level* therefore predominately consists of charged pions and photons, along with a small fraction of protons, neutrons and kaons. A breakdown of final state particles in MC is presented in Figure 9.9(b).

9.4 OVERALL PARTICLE DETECTION PROBABILITY

The lowest p_{T} accessed by this analysis is 200 MeV. Utilising the cuts discussed in Section 9.2.1 and Section 9.2.2, the probability of reconstructing an object with

[5]Although not all particles in the final state are hadrons, this definition is named for historic reasons after the point in MC event generation at which hadronisation has been performed.

$p_{\mathrm{T}} > 200$ MeV is quantified in different $|\eta|$ regions according to the MC models as a function of the highest p_{T} hadron level particle generated in the same region. These turn-on curves are presented in Figure 9.10. The efficiency of detecting particles with $p_{\mathrm{T}} > 200$ MeV is shown to rise with pseudorapidity. In the most central region, the low efficiency is partly due to the number of soft photons produced in minimum bias events [96].

Though the per-particle reconstruction efficiency is slow to turn on, this is mitigated by the large multiplicity of particles produced in minimum bias events [5].

An additional cross-check is performed on the reconstruction efficiency of neutral particles in the most central region of the ID. Figure 9.11 shows the probability of reconstructing one or more calorimeter clusters at mid pseudorapidity ($|\eta| < 0.1$) which pass the noise suppression requirements and have $E_{\mathrm{T}} > 200$ MeV as a function of the highest momentum track reconstructed in the same region.

There is a visible kink in the distributions shown in Figure 9.11 at $p_{\mathrm{T}} = 400$ MeV. Above this both electrically charged and neutral particles deposit energy in the central calorimeter (see Section 9.4.1). Below $p_{\mathrm{T}} = 400$ MeV, the plot reduces to the neutral particle detection probability in the vicinity of charged particles. Though the efficiency is small, good agreement is observed between MC and data.

9.4.1 LOW MOMENTUM B FIELD TRAPPING

Charged particles with $p_{\mathrm{T}} < 400$ MeV do not reach the first level of the calorimeter. Rather they spiral in the B field, lose momentum via multiple scattering, and migrate to larger pseudorapidity. Figure 9.12 shows the result of extrapolating reconstructed tracks to the first layer of the calorimeter as a function of both the track p_{T} and the production $|\eta|$. In Figure 9.12(a), the homogeneous distribution of calorimeter impact points over the ID tracking volume for $p_{\mathrm{T}} > 400$ MeV shows that the charged particles are impacting the calorimeter at their track-reconstructed

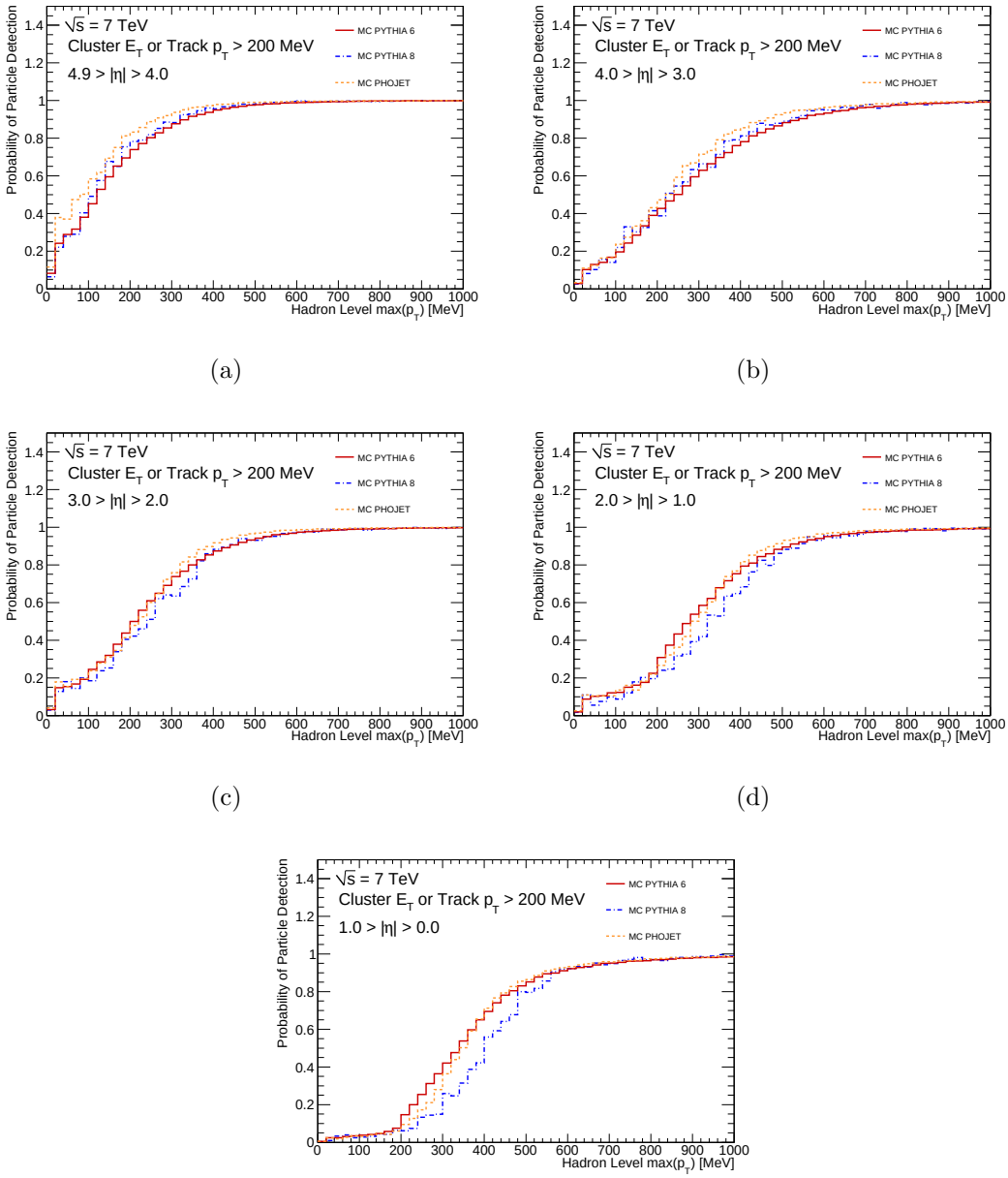

Figure 9.10: Probability per $|\eta|$ region of detecting at least one calorimeter energy deposit with $E_{\mathrm{T}} > 200$ MeV or at least one reconstructed track with $p_{\mathrm{T}} > 200$ MeV as a function of the highest p_{T} hadron level particle generated in the $|\eta|$ region.

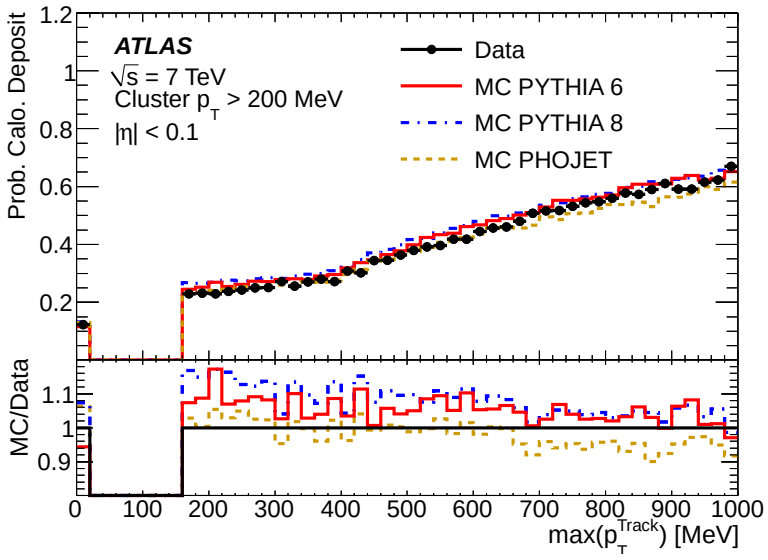

Figure 9.11: Probability of reconstruction of one or more calorimeter clusters, passing noise suppression requirements and with $E_{\mathrm{T}} > 200$ MeV, in the region $|\eta| < 0.1$, as a function of the highest p_{T} track reconstructed in the same region. The bin at zero contains events in which no charged particles are reconstructed with $p_{\mathrm{T}} > 160$ MeV.

η. Low momentum particles have a sufficiently small radius of curvature that they are unable to reach the central calorimeter, and it is observed that their impact points migrate out to large η due to helical spiralling and multiple interactions. Similar is shown in Figure 9.12(b), here particles which leave the ID at their track-reconstructed η lie along the track-η =calorimeter-η line. The extrapolation of track parameters takes into account the non-uniform ATLAS magnetic field map, multiple scattering and energy loss of the particles. The material maps in ATLAS are complex. Figure 9.13 shows the amount of material present in the calorimeter and ID systems as a function of $|\eta|$.

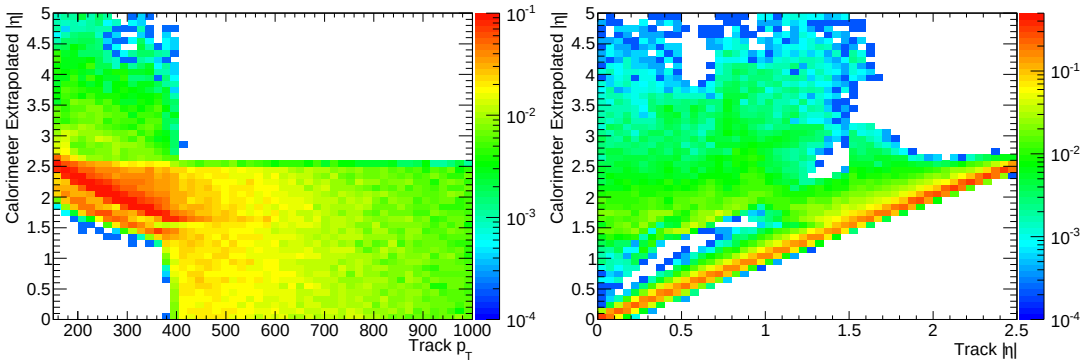

(a) (b)

Figure 9.12: Extrapolated impact point in $|\eta|$ in the first layer of the calorimeter, plotted against the p_{T} (a) and $|\eta|$ (b) of reconstructed tracks. Non-diffractive MC, normalised to a single event. See text for details.

In the context of the presented analysis, checks were performed to ascertain the effect of calorimeter energy deposition from loopers on the gap finding. It was found that after extrapolation, the low p_{T} loopers had energies which were in general too low to pass both the E_{T} and noise suppression requirements of the calorimeter systems at the extrapolated $|\eta|$. Furthermore, through detailed modelling in the detector simulation, the effect of loopers which *do* produce significant energy depositions in the calorimeter are corrected for in the unfolding process.

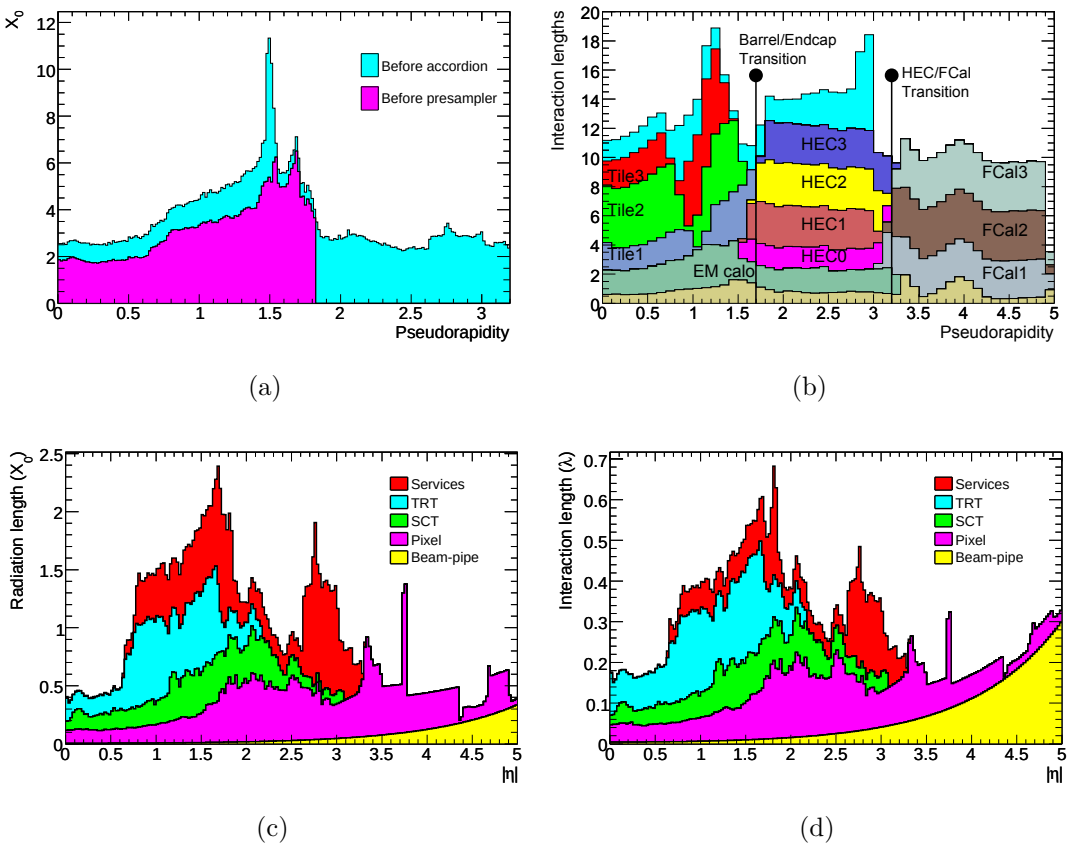

Figure 9.13: Amount of material in radiation lengths traversed by a particle before reaching the EM presampler and barrel EM calorimeter (labelled 'Before accordion') as a function of $|\eta|$ (a). Amount of material in interaction lengths before the barrel EM calorimeter and each layer of the hadronic calorimeter subsystems as a function of $|\eta|$ (b). The final unlabelled histogram in (b) is the total material before the first active layer of the muon spectrometer. Amount of material in radiation lengths within the ID thermal enclosure as a function of $|\eta|$ (c). Equivalent plot for interaction lengths in (d). Taken from [24].

CHAPTER 10

DIFFRACTIVE PHYSICS ANALYSIS

The minimum bias dataset triggered by the MBTS as described in Section 9.1 is subjected to a search for *forward rapidity gaps*, the data are corrected for detector effects using MC events which have been passed through the full ATLAS simulation. The results from data corrected to the hadron level are compared to hadron level MC.

10.1 RECONSTRUCTING RAPIDITY GAPS

An inclusive algorithm is used to calculate the largest forward rapidity gap in each event. The algorithm is symmetric about central rapidity as in SD interactions, either proton may dissociate. The larger of the forward gaps on the A and C sides of the detector is labelled $\Delta\eta^F$. This is defined in more detail to be the larger of the two pseudorapidity regions $max(|+4.9-\eta^+|, |-4.9-\eta^-|)$. η^+ and η^-, respectively,

denote the pseudorapidity of the most forward and most backward *objects*[1] in the event with $p_{\mathrm{T}} > p_{\mathrm{T}}^{\mathrm{cut}}$. We additionally define $p_{\mathrm{T}}^{\mathrm{cutMin}}$ to be the lowest experimentally accessed $p_{\mathrm{T}}^{\mathrm{cut}}$ value. For this measurement, $p_{\mathrm{T}}^{\mathrm{cutMin}} = 200$ MeV.

$\Delta\eta^F$ therefore corresponds to the largest continuous, empty, region of pseudorapidity which stretches from the outermost object to the edge of the detector, even if a larger gap is present elsewhere in the detector. An additional quantity, the forward rapidity gap polarity is defined to be `POSITIVE` (`NEGATIVE`) if $\Delta\eta^F$ is calculated to start from $\eta = +4.9$ ($\eta = -4.9$), respectively. For the SD topology, the polarity is therefore designed to correspond to Sign(p_z) of the intact proton.

This forward gap algorithm efficiently selects SD event topologies with large gaps generated between the system X and the scattered proton, along with the DD topology in the case where the lower mass Y system completely escapes the detector, i.e. if all dissociated particles of Y have $|\eta| > 4.9$. This occurs for $M_Y \lesssim 7$ GeV.

When reconstructing $\Delta\eta^F$ for values of $p_{\mathrm{T}}^{\mathrm{cut}} > p_{\mathrm{T}}^{\mathrm{cutMin}}$, a modified form of the algorithm is used. Higher values of $p_{\mathrm{T}}^{\mathrm{cut}}$ result, by definition, in fewer objects per event with which to identify the pseudorapidity gap. With low object multiplicity, one or more poorly reconstructed objects leads to a greater possibility of the reconstructed $\Delta\eta^F$ being identified as starting from the opposite edge of the detector from the hadron level $\Delta\eta^F$. When the data are unfolded, these mis-measured events contribute to an un-physical discontinuity in the cross section around they symmetry point $\eta = 0$ ($\Delta\eta^F = 4.9$). The algorithm is therefore modified to account for this circumstance.

All calculations of $\Delta\eta^F$ for $p_{\mathrm{T}}^{\mathrm{cut}} > p_{\mathrm{T}}^{\mathrm{cutMin}}$ do not search from both edges of the detector but instead use the forward rapidity gap polarity determined with $p_{\mathrm{T}}^{\mathrm{cut}} = p_{\mathrm{T}}^{\mathrm{cutMin}}$,

[1]Here *objects* are hadron level particles, good reconstructed tracks or good reconstructed calorimeter energy clusters. Depending on whether the reconstructed or hadron level is under consideration. See Section 9.2 for further details.

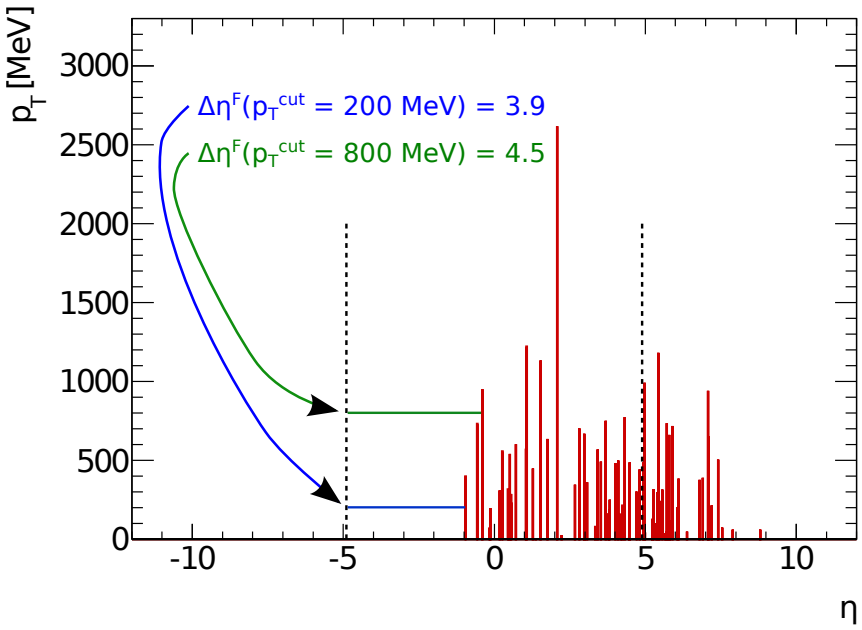

Figure 10.1: Example reconstruction of $\Delta\eta^F$ with a MC SD event at the hadron level for $p_{\mathrm{T}}^{\mathrm{cut}} = 200$ and 800 MeV. Red bars denote the η and p_{T} of hadron level particles, dotted black lines denote the acceptance of the ATLAS calorimeters. $\Delta\eta^F(p_{\mathrm{T}}^{\mathrm{cut}} = p_{\mathrm{T}}^{\mathrm{cutMin}} = 200\ \mathrm{MeV}) = |-4.9+1.0| = 3.9$ for this sample event as the forward gap starting from $\eta = +4.9$ is negligibly small. The polarity of the event is therefore determined to be `NEGATIVE`, and hence $\Delta\eta^F(p_{\mathrm{T}}^{\mathrm{cut}} = 800\ \mathrm{MeV}) = |-4.9+0.4| = 4.5$.

$$\Delta\eta^F\left(p_{\mathrm{T}}^{\mathrm{cut}} > p_{\mathrm{T}}^{\mathrm{cutMin}}\right) = \begin{cases} |+4.9-\eta^+| & : \mathrm{Polarity} = \texttt{POSITIVE} \\ |-4.9-\eta^-| & : \mathrm{Polarity} = \texttt{NEGATIVE} \end{cases} \tag{10.1}$$

The higher values of $p_{\mathrm{T}}^{\mathrm{cut}}$ used are 400, 600 and 800 MeV. These values cover the common range of particle transverse momenta in minimum bias interactions. An illustration of the algorithm is presented in Figure 10.1 and code to reproduce the analysis variables is presented in Appendix D, the data are catalogued online in the HepData database [97] and Appendix C.

10.1.1 BINNING

$\Delta\eta^F$ is binned with consideration given to the geometry of the detector at the start of the gap and the shape of the distribution. In the forward region $2.9 < |\eta| < 4.9$ ($\Delta\eta^F \leq 2$) a bin granularity of 0.4 in η is used. Elsewhere a bin granularity of 0.2 in η is used. Small gaps, characteristic of hadronisation fluctuations in ND events, are reconstructed at small $\Delta\eta^F$. The variation in the differential cross section is therefore steepest in this region and the coarser bin size improves the bin purity. Another consideration is the exponential reduction in the size of the solid angle covered by a fixed η interval at high pseudorapidity. Due to the size of the cells at the extremity of the FCal, it is unlikely for the centre of mass of a reconstructed cluster to lie beyond $|\eta| = 4.7$.

With the calorimeters spanning 9.8 units of η, $\Delta\eta^F$ takes the range 0 (for events with energy deposits at both extremes of the detector) to 10 (for totally empty events, containing zero *objects* with $p_{\mathrm{T}} > p_{\mathrm{T}}^{\mathrm{cut}}$).

10.2 DATA/MC COMPARISON AT RECONSTRUCTED LEVEL

Reconstructed quantities are compared between data and MC as a function of $\Delta\eta^F$. By using a range of MC models whose discriminating variables are close to, or preferably bracket, the data over the measured range of $\Delta\eta^F$, the model uncertainty derived from the subsequent use of the models in correcting the data will represent a reliable uncertainty on the measurement.

All quantities are investigated in four $\Delta\eta^F$ regions[2] which span the transition between non-diffractive and diffractive dominated regions and cover the range of event topologies under investigation. In Figure 10.2 the multiplicity of calorimeter clusters passing the selection requirements is plotted. This probes the particle multiplicity

[2]These are: $0 < \Delta\eta^F < 2$, $2 < \Delta\eta^F < 4$, $4 < \Delta\eta^F < 6$ and $6 < \Delta\eta^F < 8$.

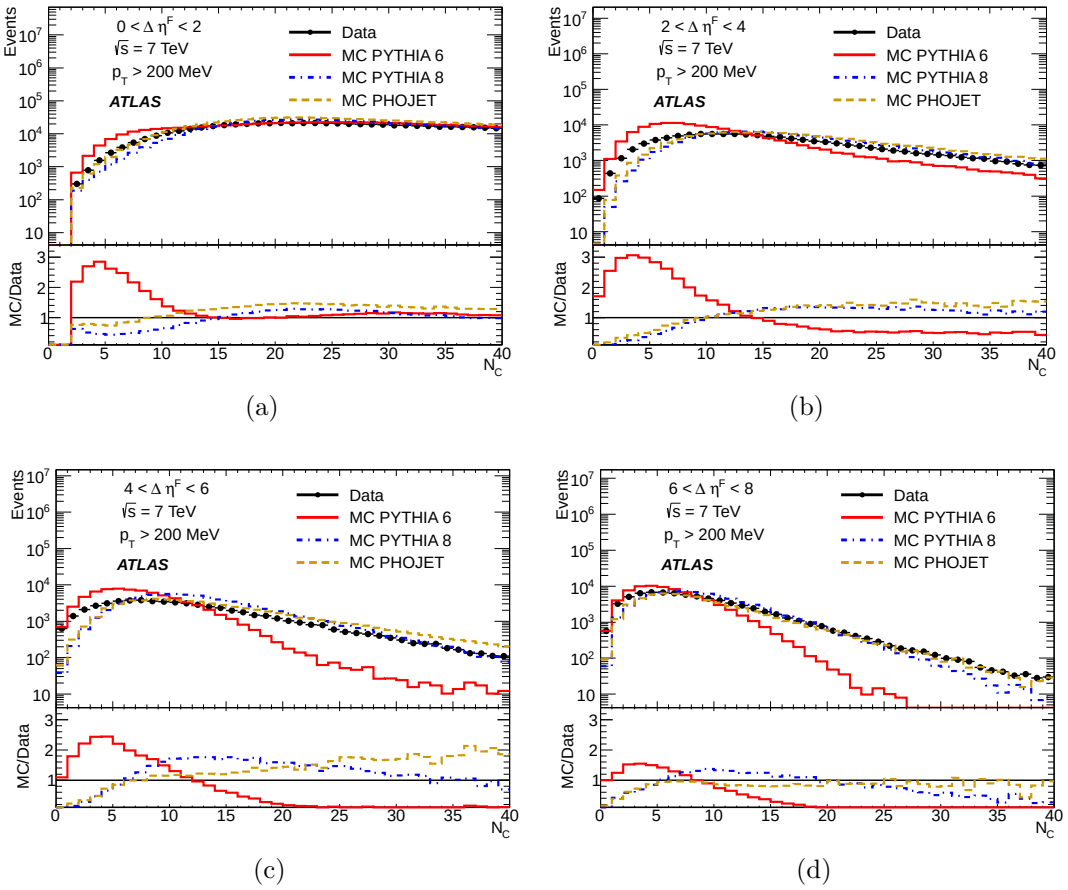

Figure 10.2: Per event multiplicity distribution of clusters passing the selection requirements for $p_{\mathrm{T}}^{\mathrm{cut}} = 200$ MeV. Uncorrected distributions are presented in data and MC for four different regions in $\Delta\eta^F$. Taken from [1].

per event as a function of $\Delta\eta^F$. For small gaps, $0 < \Delta\eta^F < 2$, the best description is provided by PHOJET, with PYTHIA8 providing the better description for larger gaps. For small cluster multiplicities $N_{\mathrm{C}} \simeq 5$, PYTHIA6 overestimates the data while both PYTHIA8 and PHOJET underestimate the distribution.

The corresponding p_{T} distribution for these clusters is presented in Figure 10.3. Here none of the MCs gives a complete description. For small gaps all models are shown to provide a reasonable description whilst for intermediate gaps, PYTHIA6 underestimates the p_{T} distribution and the other models overestimate. For large gaps, PYTHIA8 provides the best description, but all models tend to underestimate the slope.

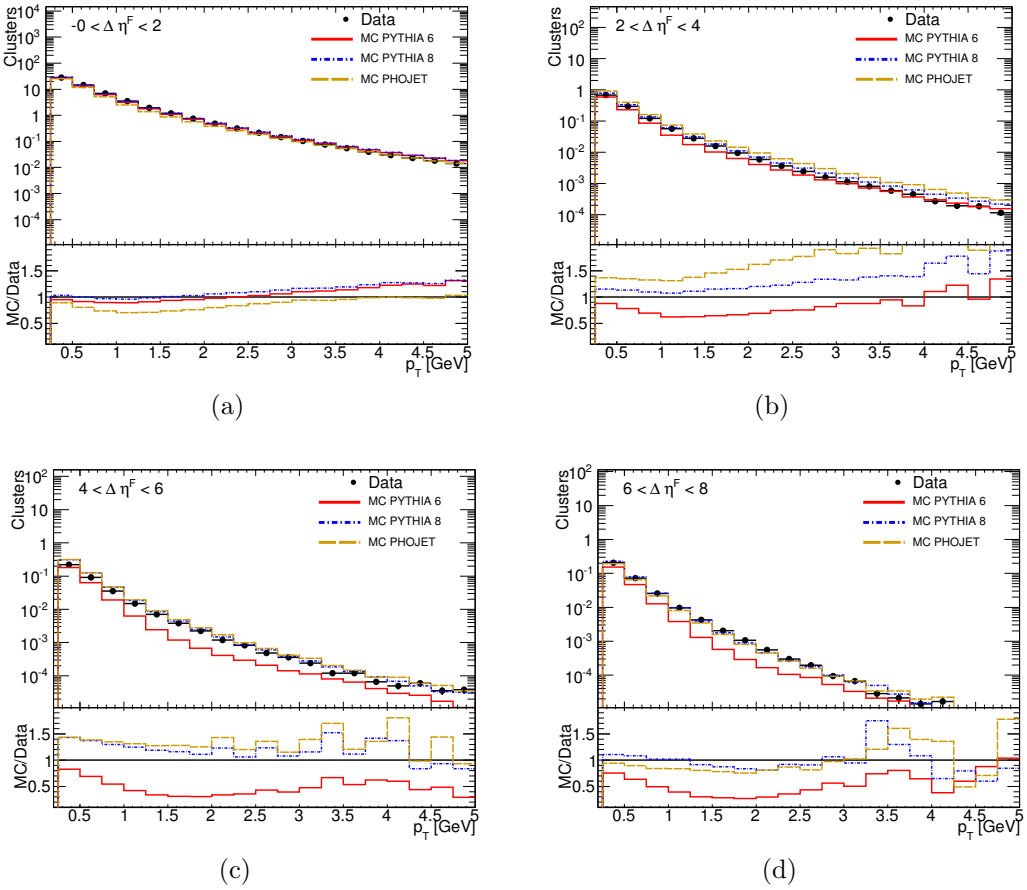

Figure 10.3: Per cluster p_{T} distribution of clusters passing the selection requirements for $p_{\mathrm{T}}^{\mathrm{cut}} = 200$ MeV. Uncorrected distributions are presented in data and MC for four different regions in $\Delta\eta^F$. Taken from [1].

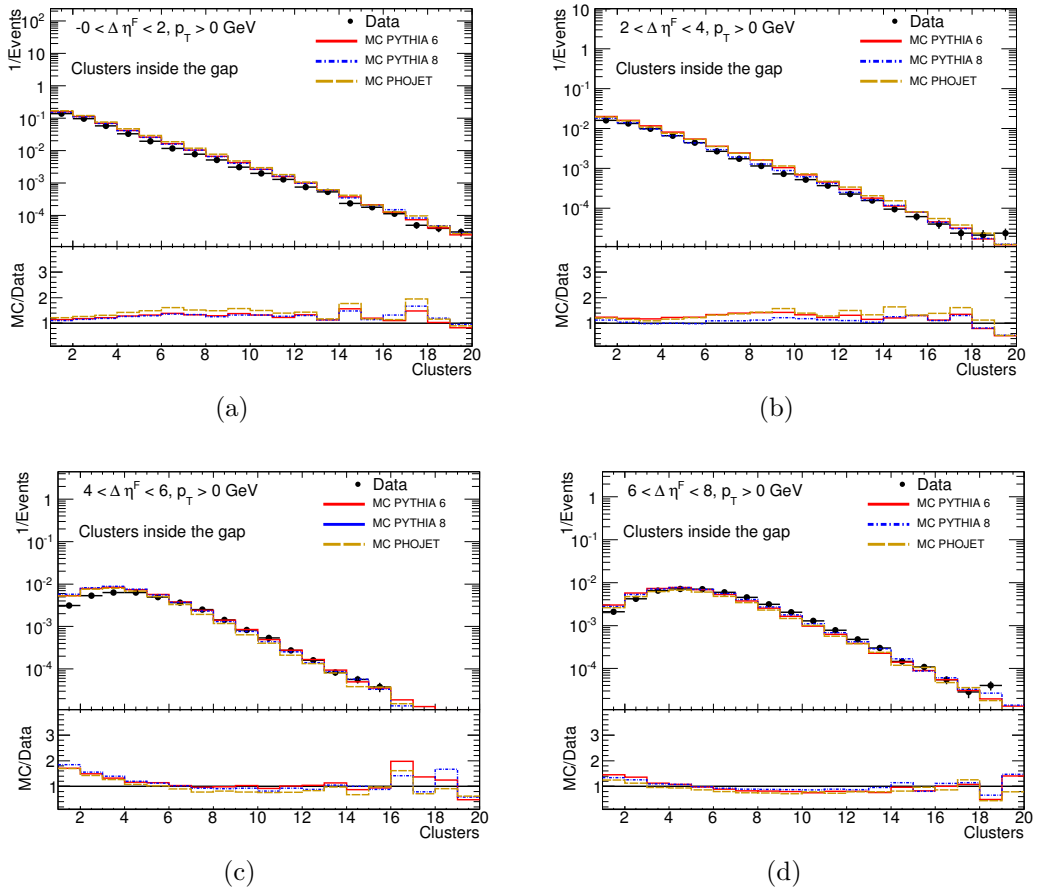

Figure 10.4: Per event multiplicity distribution of clusters *failing* the selection requirements. Uncorrected distributions are presented in data and MC for four different regions in $\Delta\eta^F$. Taken from [1].

Calorimeter clusters which *do not* pass the noise suppression requirements from Section 9.2.2 are plotted in Figure 10.4 (multiplicity distribution) and Figure 10.5 (p_{T} distribution). Here again, a degree of mis-modelling is observed in the MCs, with the regions at low p_{T} and events with low multiplicities being the worst affected. Over all of the distributions, the data are best modelled by PYTHIA8.

From the distributions presented in this section it is concluded that none of the MC models considered gives a full description of the data. Comparisons between all three MC models are required to fully quantify the model uncertainty in correcting the data, as only when an envelope spanning all three is considered are the data reasonably modelled over the full range of event topologies.

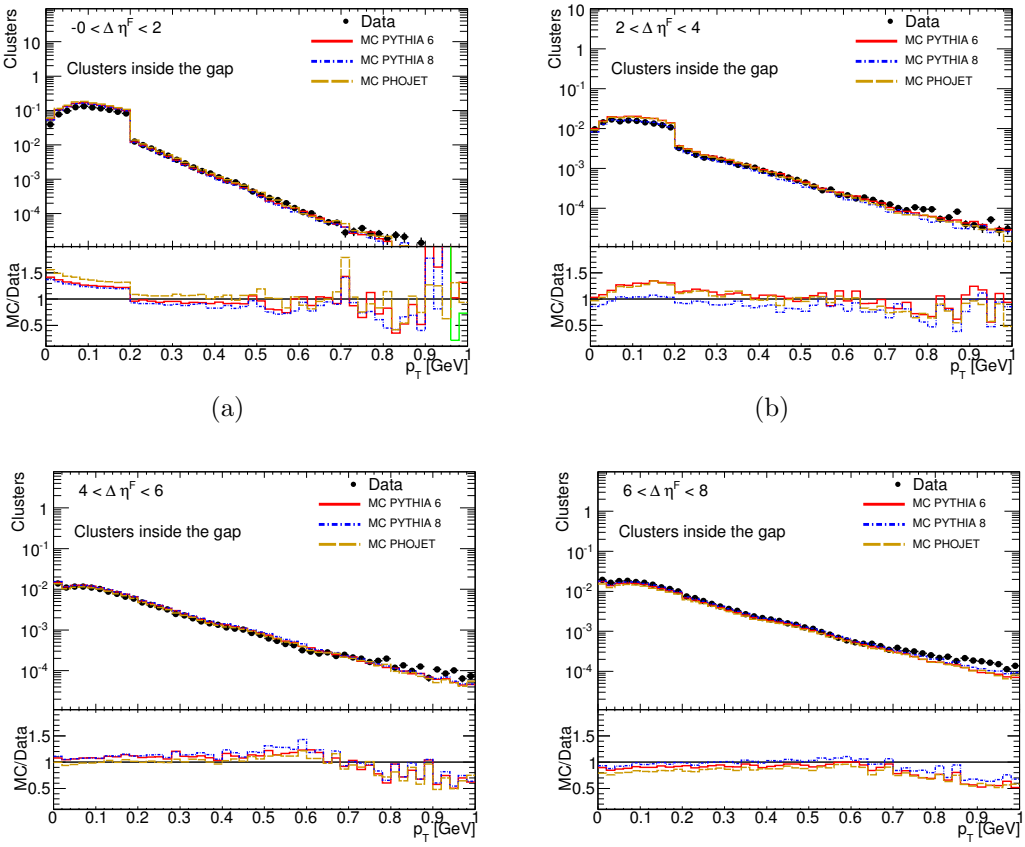

Figure 10.5: Per cluster p_{T} distribution of clusters *failing* the selection requirements. Uncorrected distributions are presented in data and MC for four different regions in $\Delta\eta^F$. Taken from [1].

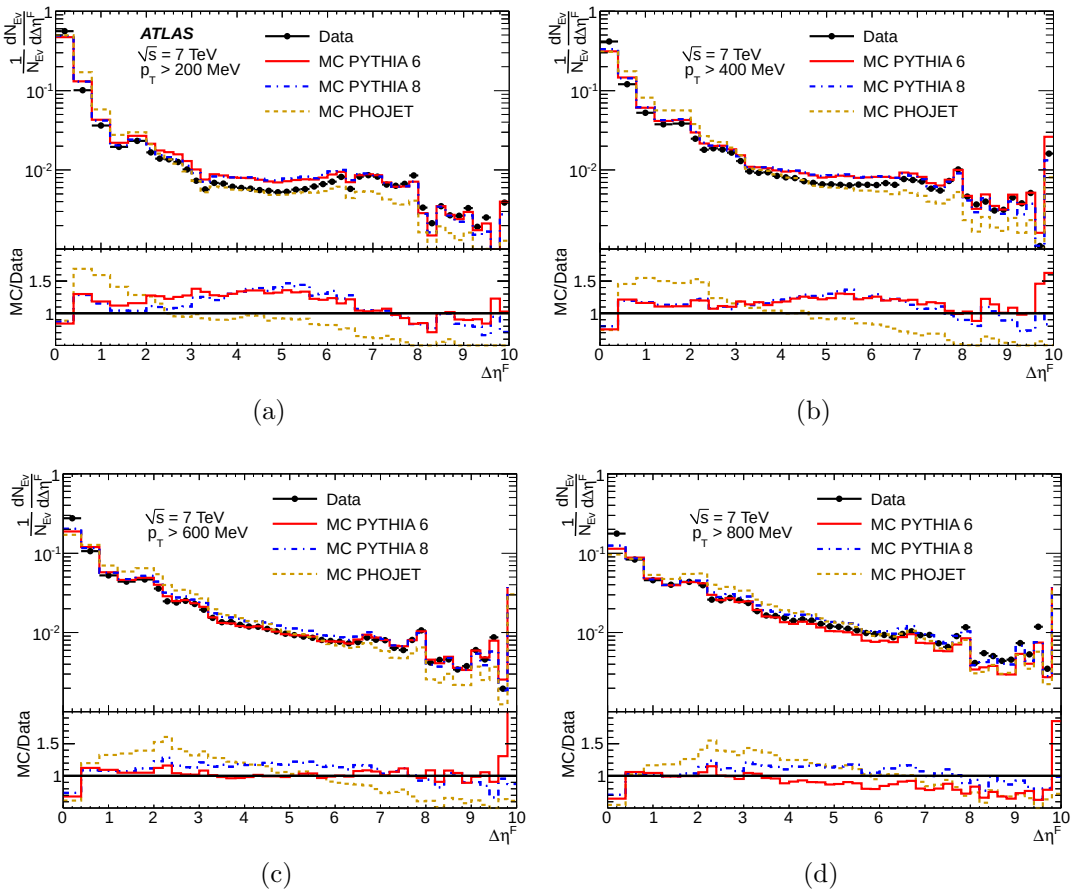

Figure 10.6: Fully inclusive $\Delta\eta^F$ spectrum at the reconstructed level for data and MC, both after applying the trigger requirement. Presented for all accessed values of $p_{\mathrm{T}}^{\mathrm{cut}}$ and normalised to unit area.

10.3 DATA CORRECTION PROCEDURE

The raw $\Delta\eta^F$ spectra for all values of $p_{\mathrm{T}}^{\mathrm{cut}}$ are presented in Figure 10.6 for data and hadron level MC after applying the triggering requirement.

The distribution for the lowest p_{T} at 200 MeV shows two key features. For $\Delta\eta^F < 2$ the spectrum exhibits an exponential slope, which is attributed to the probability of rapidity fluctuations from hadronisation effects in the bulk of ND collisions. These deposit energy in both the forward and backward regions of ATLAS. For $\Delta\eta^F > 3$ the spectrum is relatively flat as a function of $\Delta\eta^F$. Here the distribution probes in detail the diffractive contribution. Increasing the p_{T} cut decreases the slope of the

exponential fall off of ND events which populate regions of larger rapidity gap.

Structure is observed in the distribution whose origin lies not in the underlying physics of scattering or hadronisation, but rather in the details of the ATLAS detector. Notably a rise in the differential cross section is observed at $\Delta\eta^F = 1.7$. This corresponds to the FCal—HEC transition region. In addition, the localised reductions in cross section at $\Delta\eta^F = 3.2$ and $\Delta\eta^F = 6.4$ both correspond to a pseudorapidity gap which extends to $\eta = \pm 1.7$, corresponding to the barrel—endcap transition in the hadronic calorimeter systems, see Figure 9.13.

The data are corrected to remove the dependence on the experimental setup, observed in all MC models as well as data. First correction factors are derived from MC to correct the data for trigger efficiency at large gap sizes. Following this two methods are considered for removing the effects of the detector; the application of correction factors derived from bin-to-bin migrations as quantified in MC and a more sophisticated application of Bayes theorem, which is applied through the MC detector response matrix.

10.3.1 TRIGGER CORRECTION

Although the ATLAS detectors span 9.8 units of pseudorapidity, data events are selected using the MBTS, which limits the acceptance for events with very large pseudorapidity gaps. The trigger efficiency is quantified using MC. Different generators are used to span the range of possibilities in the underlying dynamical assumptions in diffractive models.

The trigger efficiency, as a function of $\Delta\eta^F$ at the hadron level, is defined as the fraction of events which contain at least two MBTS counters above the appropriate threshold levels from Table 9.1. In Figure 10.7 the trigger efficiency is presented for each of the three principal MC models used to correct the data as a function of $\Delta\eta^F$ and $p_{\mathrm{T}}^{\mathrm{cut}}$. At the lowest accessed $p_{\mathrm{T}}^{\mathrm{cut}} = 200$ MeV, the trigger efficiency for all models

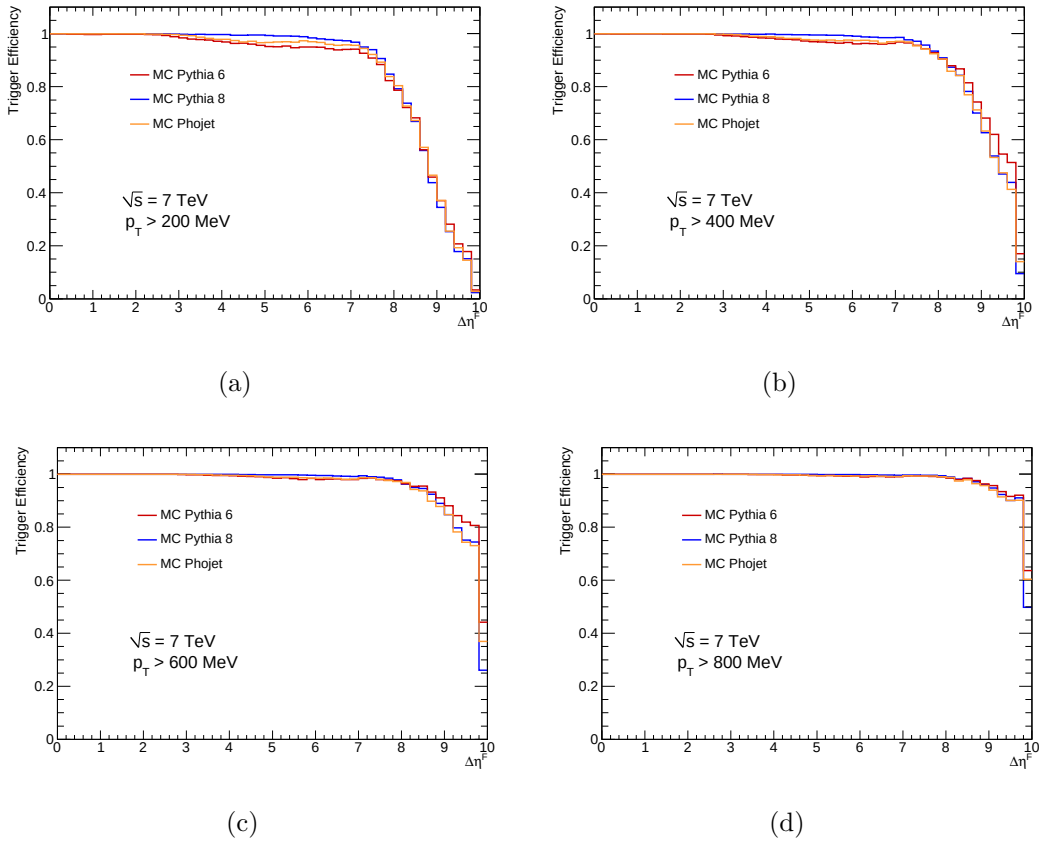

Figure 10.7: Efficiency of the MBTS trigger requirement as a function of $\Delta\eta^F$ for $p_{\mathrm{T}}^{\mathrm{cut}} = 200$, 400, 600, 800 MeV in (a), (b), (c)) and (d) respectively.

is $\approx 100\%$ for $\Delta\eta^F < 2$. For $2 < \Delta\eta^F < 7$, PYTHIA8 remains fully efficient while with PYTHIA6 and PHOJET the efficiency falls to $\approx 95\%$. In PYTHIA6 this is due to the effect of the softer diffractive particle p_{T} spectrum. In PHOJET, the additional CD topology creates systems in the centre of the detector whose particles can lie in between the acceptance of the two MBTS detector planes which also results in a small loss in efficiency.

For $\Delta\eta^F \gtrsim 8.3$, no particles with $p_{\mathrm{T}} > p_{\mathrm{T}}^{\mathrm{cut}}$ are generated within the acceptance of the MBTS. The trigger efficiency falls steeply beyond this point as the fiducial acceptance shrinks. At $\Delta\eta^F = 8$, the efficiency in all models falls to $\approx 80\%$ for $p_{\mathrm{T}}^{\mathrm{cut}} = 200$ MeV. The measurements are therefore truncated at $\Delta\eta^F = 8$ in the final result as the MC-derived correction grows quickly from this point on.

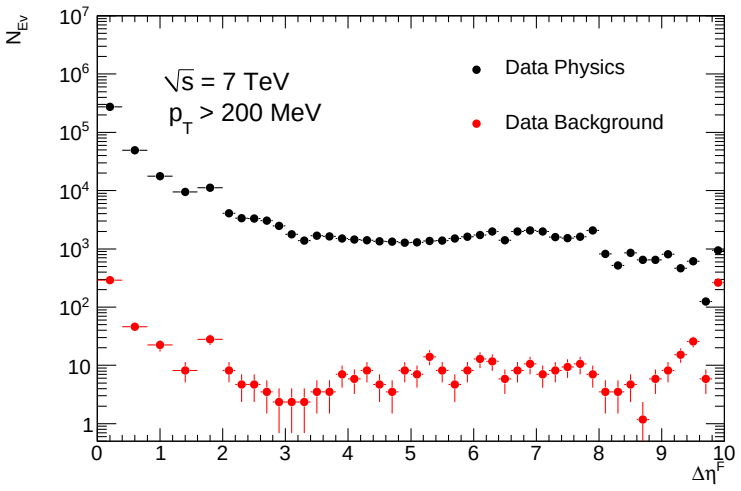

Figure 10.8: The normalised beam background distribution at the reconstructed level (red). This is subtracted from the distribution obtained with the physics trigger (black).

For larger values of $p_{\mathrm{T}}^{\mathrm{cut}}$, the trigger efficiency remains high for very large gaps. This is due to low momentum particles which are below $p_{\mathrm{T}}^{\mathrm{cut}}$ threshold and hence do not contribute to the calculation of $\Delta\eta^F$, but do leave a signal in the MBTS and may therefore trigger the event. Because the $\Delta\eta^F$ reconstruction for these higher values of $p_{\mathrm{T}}^{\mathrm{cut}}$ also relies on the event polarity as determined at $p_{\mathrm{T}}^{\mathrm{cut}} = 200$ MeV (see Section 10.1), these measurements are truncated at $\Delta\eta^F = 8$ nonetheless.

Correction factors equal to the reciprocal of the efficiencies in Figure 10.7 are applied in each bin to correct the data for trigger inefficiency. The differences between models are included in the overall systematic uncertainty as described in Section 10.4.1.

10.3.2 BEAM BACKGROUND SUBTRACTION

As discussed in Section 9.1.4, beam related backgrounds are subtracted from the physics sample after normalising the luminosity of the data. The background sample as triggered on unpaired bunches is shown in Figure 10.8 as a function of $\Delta\eta^F$ at the reconstructed level. This corresponds to a 0.22% correction.

10.3.3 UNFOLDING

Detector effects are manifest as systematic biases (primarily through reconstruction inefficiencies), and smearing due to finite experimental resolution. Two methods of correcting the data for detector effects using the MC simulations are considered. The bin-by-bin correction procedure derives the correction factor in each bin as $f = N_{\mathrm{R}}/N_{\mathrm{G}}$ where N_{G} is the number of events generated in a bin and N_{R} is the number of events reconstructed in a bin. Bin-by-bin corrections are applicable when migrations are small and hence the bin purity is high. This method neglects the correlations present between bins and has a relatively large dependence on the physics model. It is used primarily to provide a cross check of the Bayesian method.

The Bayesian technique employed was developed as a computational unfolding method by G. D'Agostini [98] and is implemented in the `RooUnfold` framework [99]. Initially a response matrix is constructed for each MC model which relates the *true* value of $\Delta\eta^F$ as determined at the hadron level to the reconstructed value of $\Delta\eta^F$ after the event has been passed through the detector simulation and reconstruction software. As the data have already been corrected for trigger efficiency, the response matrix is constructed from MC without any trigger requirement. One could consider simply inverting the response matrix and multiplying the inverse with the detector distribution in order to yield the corrected distribution. However this method is problematic in practice as there is no reason to assume the response matrix is non-singular and hence invertible. Even for invertible matrices, negative terms in the inverse are unavoidable and this can lead to unphysical results such as bins with negative content arising from fluctuations due to finite statistics.

Bayesian unfolding does not rely on direct matrix inversion[3]. Rather, Bayes statistics are used to make a statistical inference of the underlying causal distribution in data by utilising the hadron level distribution from the MC as a prior distribution. Bayes theorem states that for n_C independent *causes* (C_i) of an observed *effect* (E), the

[3]But does yield the inverse of the response matrix in the limit of infinite statistics.

probability of the effect being due to cause C_i is expressed as

$$P(C_i|E) = \frac{P(E|C_i) \cdot P(C_i)}{\sum_{k=1}^{n_C} P(E|C_k) \cdot P(C_k)}. \tag{10.2}$$

The probability that cause i results in the effect $P(E|C_i)$ and the probabilities of individual causes $P(C_i)$ are both quantifiable in MC.

By expanding the definition to include multiple effects (n_E) along with multiple causes (in this analysis n_C and n_E are the number of $\Delta\eta^F$ bins at the hadron and reconstructed level, respectively, and $n_C = n_E$), the Bayesian relation for conditional probabilities becomes

$$P(C_i|E_j) = \frac{P(E_j|C_i) \cdot P(C_i)}{\sum_{k=1}^{n_C} P(E_j|C_k) \cdot P(C_k)}. \tag{10.3}$$

For the presented analysis, a *cause* is the result of the forward gap finding algorithm at the hadron level and each *cause* maps probabilistically to many *effects* where the *effect* is the result of the forward gap finding algorithm at the reconstructed level. This is stored in the response matrix $R[n_E, n_C]$ which acts as the input to the $P(E_j|C_k)$ term in (10.3).

In Section 10.2 it was concluded that PYTHIA8 is the most reliable of the MC generators considered, and as such it is used to construct the nominal response matrix. The matrices for all considered values of $p_{\mathrm{T}}^{\mathrm{cut}}$ are presented in Figure 10.9. An anti-diagonal component is visible for large values of $p_{\mathrm{T}}^{\mathrm{cut}}$, such as in Figure 10.9(d), which is minimised through the use of the gap polarity as was discussed in Section 10.1. The remaining small entries in the off-diagonals are primarily from DD events where a small M_Y system is mis-reconstructed at one edge of the detector.

Running over the ATLAS data yields the measured multiplicities $N_{\mathrm{Obs}}(E_j)$ of effects $E_1, E_2, ..., E_{n_E}$. These multiplicities are then assigned probabilistically to the causes

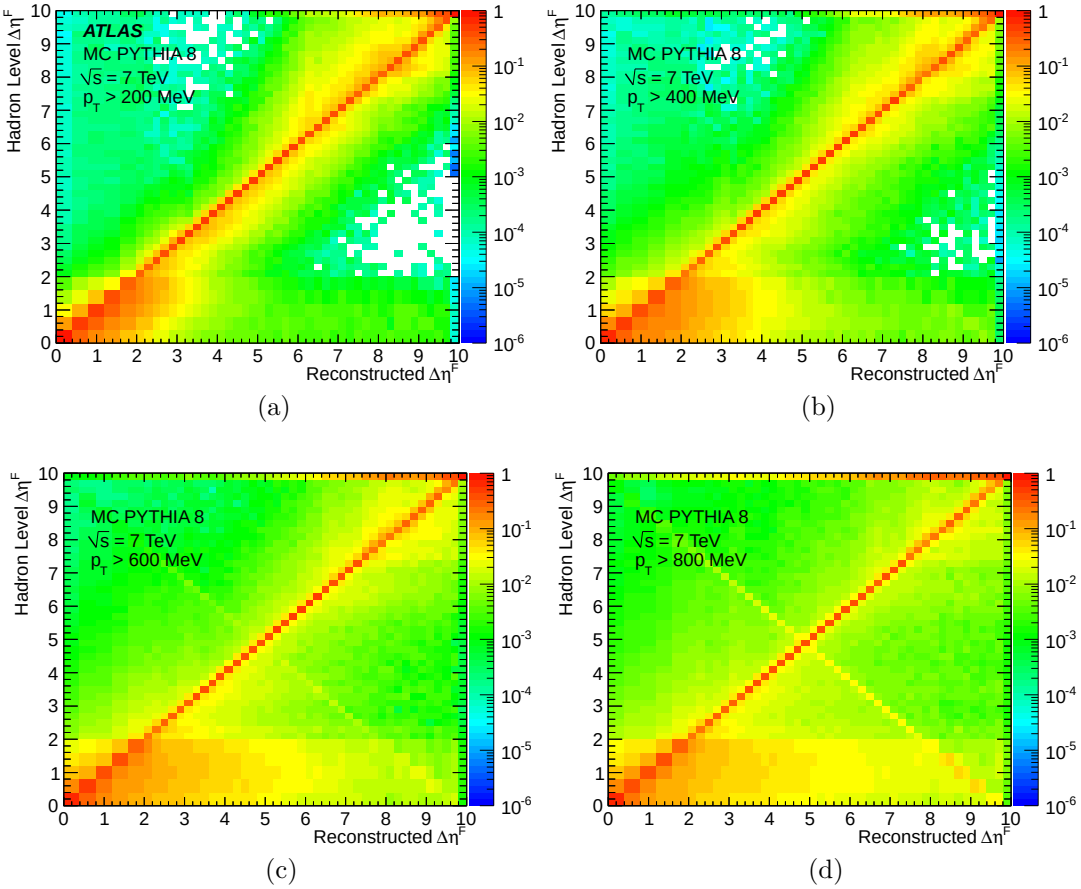

Figure 10.9: Response matrices between the reconstructed and hadron level values of $\Delta\eta^F$ for $p_{\mathrm{T}}^{\mathrm{cut}} = 200$, 400, 600, 800 MeV in (a), (b), (c) and (d), respectively. No trigger requirement was used and the distributions are normalised to unity in columns for display purposes.

$C_1, C_2, ..., C_{n_C}$ using (10.3) to obtain

$$N_{\mathrm{Unf}}(C_i) = \sum_{j=1}^{n_E} N_{\mathrm{Obs}}(E_j) \cdot P(C_i|E_j), \tag{10.4}$$

with $N_{\mathrm{Unf}}(C_i)$ being the estimator of the multiplicity of cause C_i (or in other words the number of *true* events) given the distribution observed in the detector, $N_{\mathrm{Obs}}(E_j)$ and the response matrix $R[n_E, n_C]$. This is the unfolded distribution.

Iteration of the procedure is achieved by replacing $P(C_i)$ with $\hat{P}(C_i)$ where $\hat{P}(C_i) = P(C_i|N_{\mathrm{Obs}}(E_j))$, though each iteration enhances fluctuations.

10.3.4 UNFOLDED DISTRIBUTIONS

The data are unfolded with one and three iterations of the Bayesian method with PYTHIA8 as the prior distribution and also via calculation of simple bin-to-bin correction factors. The unfolded distributions are compared with each other in Figure 10.10. It is observed that a single application of the Bayesian unfolding is optimal to correct the distribution, with subsequent applications driving unphysical statistical fluctuations. The distribution with three iterations shows similar deviations to the distribution unfolded with the bin-to-bin method, both reflecting the detector geometry. Therefore Bayesian unfolding with a PYTHIA8 prior and a single iteration is chosen as the nominal unfolding method.

A visualisation of the global event migration taking place in the unfolding procedure is presented in Figure 10.11. To avoid ambiguity in this paragraph, $\Delta\eta^F_{\mathrm{R}}$ and $\Delta\eta^F_{\mathrm{H}}$ correspond to the largest forward gap at the reconstructed level and the hadron level respectively. Here the reconstructed $\Delta\eta^F_{\mathrm{R}}$ distribution in the range $0 < \Delta\eta^F_{\mathrm{R}} < 10$ is subdivided into ten equal regions. The fractional makeup of each unfolded bin of $\Delta\eta^F_{\mathrm{H}}$ arising from the ten different reconstructed regions of $\Delta\eta^F_{\mathrm{R}}$ is plotted. It is observed that migration of events reconstructed in the peak of the distribution at $0 < \Delta\eta^F_{\mathrm{R}} < 1$ to the plateau region at $\Delta\eta^F_{\mathrm{H}} > 3$ (solid green line) makes up between

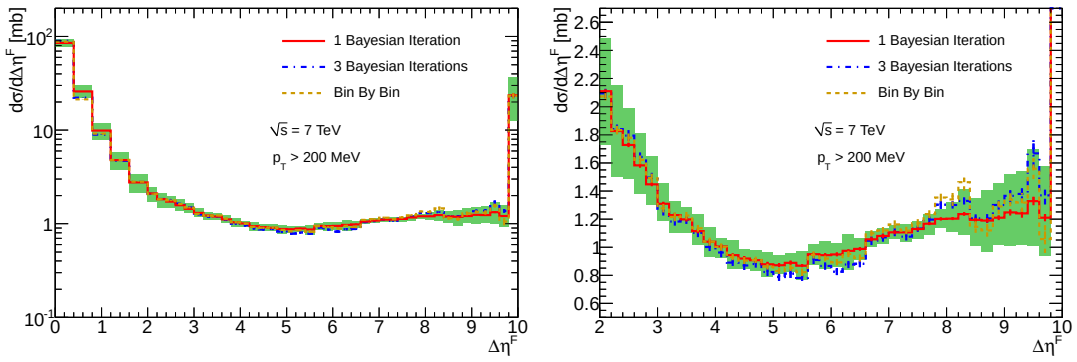

(a) (b)

Figure 10.10: Comparison of results obtained with one and three iterations of Bayesian unfolding and via bin-to-bin unfolding. The error bars are statistical. The shaded region represents the total uncertainty as discussed in Section 10.4. The whole distribution is shown in (a) while (b) shows a zoom of the region $2 < \Delta\eta^F < 10$ on a linear scale. The final bin at $\Delta\eta^F = 10$ contains the low-mass *invisible* (to ATLAS) diffractive cross section which does not result in any particles with $p_{\mathrm{T}} > 200$ MeV within the detector acceptance.

1.5 and 4% of the differential cross section at large forward gap sizes. The size of this migration is due to the large fraction of the total inelastic cross section contained in the region $0 < \Delta\eta^F_{\mathrm{R}} < 1$. It is also important to monitor the overall migration of events from the region $\Delta\eta^F_{\mathrm{R}} > 8$, where the trigger efficiency is known to be poor and the cross section is not well constrained, into the measured distribution at $\Delta\eta^F_{\mathrm{H}} < 8$. The measurement is truncated at $\Delta\eta^F_{\mathrm{H}} = 8$ so we consider the final bin included in the measurement at $7.8 < \Delta\eta^F_{\mathrm{H}} < 8.0$. Here the contribution from events which were reconstructed at $8 < \Delta\eta^F_{\mathrm{R}} < 9$ (blue dashed line) is 10% and for $9 < \Delta\eta^F_{\mathrm{R}} < 10$ (red dot-dash line) the contribution is 5% according to the PYTHIA8 model. The contribution to subsequent bins at smaller values of $\Delta\eta^F_{\mathrm{H}}$ reduces exponentially. We consider this fraction of events migrating from the region of poor trigger efficiency to be acceptable.

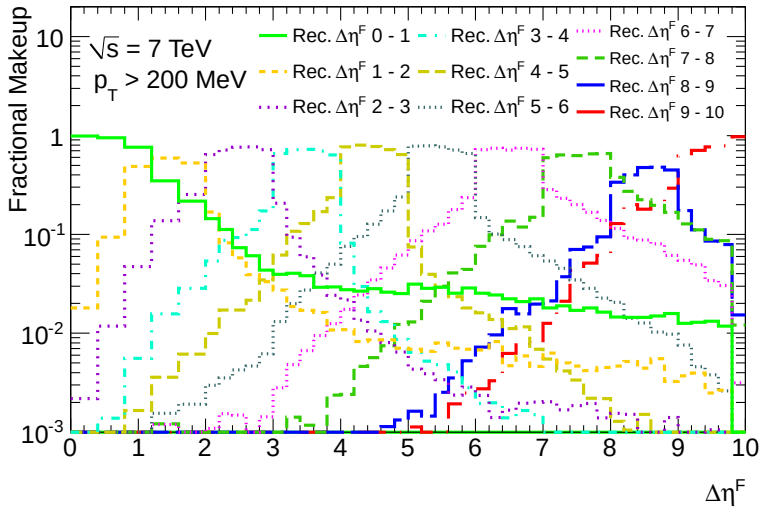

Figure 10.11: Visualisation of event migration between bins taking place in the Bayesian unfolding. The histograms denote the fraction of events placed at each $\Delta\eta^F$ at the hadron level arising from each of the ten indicated regions of $\Delta\eta^F$ at the reconstructed level.

10.3.5 STATISTICAL ERROR

Poisson statistics apply to the observed distribution. However, after unfolding, each observed event is redistributed probabilistically. The statistical uncertainty is therefore dependent on the covariance of the response matrix. The error was quantified by running 1000 toy models, in which the measured distribution is smeared by a Poisson distribution. The error was taken as the variation of the covariance matrix over the toy models. This was compared with errors quantified directly from the covariance of the response matrix. Both approaches were shown to yield compatible errors.

The percentage statistical error on the measurement is shown as a function of $\Delta\eta^F$ in Figure 10.12, along with the total systematic uncertainty which is discussed in the next section.

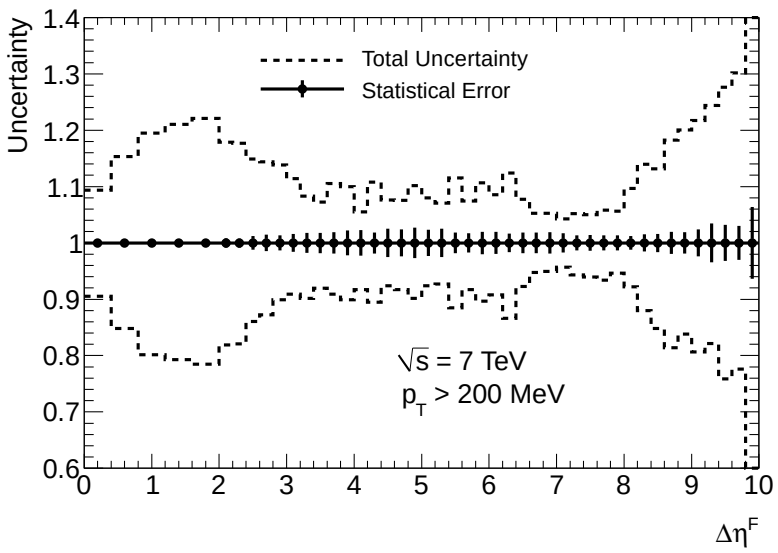

Figure 10.12: Statistical error quantified from 1000 toy MC iterations for $p_{\mathrm{T}}^{\mathrm{cut}} = 200$ MeV, compared with the total uncertainty band.

10.4 QUANTIFICATION OF SYSTEMATIC UNCERTAINTY

Many sources of uncertainty were considered while performing the analysis and their impact on the final result evaluated. Unless stated otherwise, the pull of each systematic uncertainty listed below is symmetrised about the nominal result. The separate sources of systematic uncertainty are uncorrelated and hence are added in quadrature, along with the statistical error for each data point, to form the total uncertainty on the measurement. The systematic uncertainty is strongly correlated between neighbouring bins.

10.4.1 MODEL UNCERTAINTY

In addition to the nominal correction MC, PYTHIA8 4C, the trigger correction and unfolding procedures are also performed with PYTHIA6 `AMBT1` and PHOJET, using the tuned sub-process fractions from Section 8.4. Details of MC tunes are found in Section 8.4.1.

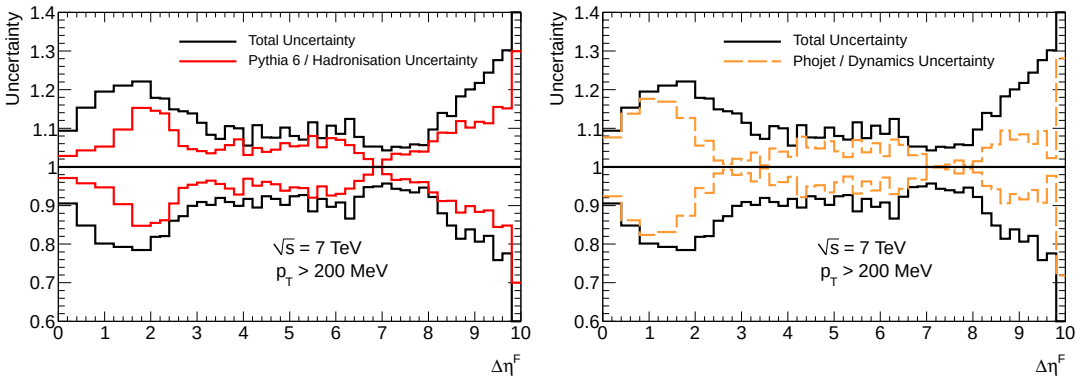

(a) (b)

Figure 10.13: Systematic uncertainty arising from modelling of the final state (PYTHIA6) and assumptions on diffractive and other minimum bias dynamics (PHOJET) for $p_{\mathrm{T}}^{\mathrm{cut}} = 200$ MeV. The contributions to the uncertainty are dominant for small $\Delta\eta^F$.

The lack of partonic diffraction is a known limitation in PYTHIA6, as was observed in Figure 8.3. From Section 10.2 however, it was seen that this omission resulted in PYTHIA6 providing a lower bound on the reconstructed cluster multiplicity and the slope of the p_{T} spectra over a range of forward gap sizes, whereas the other models exhibit spectra which are in general harder than that observed in data. A PYTHIA6 prior is therefore used as a conservative estimator of the effect of the modelling of the final state.

PHOJET is used since it offers alternative ξ_X, ξ_Y and t distributions and ND modelling. The deviation of the result when the data are corrected using a PHOJET prior is taken as the uncertainty due to dynamical assumptions in modelling the diffractive dynamics.

Both model uncertainties are evaluated separately in each measurement interval and contribute symmetrically to the total uncertainty. They form the dominant uncertainty in the measurement over a wide range of gap sizes. The uncertainty bands are plotted in Figure 10.13.

Table 10.1: Systematic variation of the fractions f_{SD} and f_{DD} as percentages of f_D for the PYTHIA8 MC. These bounds are derived from the constraint $0.29 < \sigma_{SD}/\sigma_{DD} < 0.68$, see Section 8.4.

	MC Default	**Lower Bound**	**Tuned Nominal**	**Upper Bound**
f_{SD}	59.4%	77.8%	69.1%	62.1%
f_{DD}	40.6%	22.2%	30.9%	37.9%

10.4.2 UNCERTAINTY ON THE DIFFRACTIVE CONTRIBUTIONS

The uncertainty on the relative contributions to the diffractive cross section can influence the unfolding procedure. The amount of DD present in particular affects the size of the migrations as was discussed in Section 10.3.3.

The relative f_{SD}/f_{DD} uncertainty is derived using PYTHIA8. The bounds are calculated by propagating the limits on the ratio of the cross sections from Section 8.4. The values used to determine the f_{SD}/f_{DD} uncertainty are listed in Table 10.1 and the effect on the measurement is presented in Figure 10.14(a). The systematic uncertainty is less than 1% over the full measured range.

An additional uncertainty is quantified on the sub-leading double Pomeron CD process modelled by PHOJET. When tuning PHOJET in Section 8.4, the CD component was left at the generator default. The f_{CD}/f_{SD} ratio in PHOJET is modified to satisfy the Tevatron measured value $f_{CD}/f_{SD} = 0.093$ (see Section 8.4). The systematic uncertainty in this change of the amount of CD modelling in PHOJET is quantified against PHOJET using the tuned nominal values and is symmetrised. This is presented in Figure 10.14(b) where it is observed to contribute an uncertainty of less than 1% in the diffractive dominated plateau.

10.4.3 ENERGY SCALE UNCERTAINTY

The uncertainty in the energy scale calibration of the calorimeter systems propagates into a corresponding uncertainty in the measurement. The energy scale in the

Table 10.2: Systematic variation of the fractions f_{SD} and f_{CD} as percentages of f_D in the PHOJET MC. The nominal tune is derived from the centre of the constraint bound at $\sigma_{SD}/\sigma_{DD} = 0.69$ whilst leaving CD unchanged, and then subsequently modified to satisfy $\sigma_{CD}/\sigma_{SD} = 0.093$ leaving DD unchanged to quantify the CD systematic.

	MC Default	**Tuned Nominal**	**CD Systematic**
f_{SD}	67.1%	54.2%	57.0%
f_{DD}	24.6%	37.5%	37.5%
f_{CD}	8.3%	8.3%	5.6%

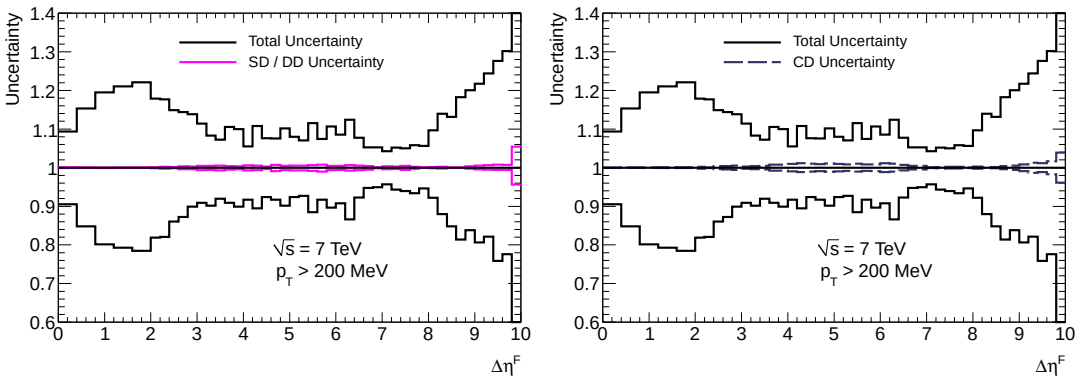

(a) (b)

Figure 10.14: Systematic uncertainty arising from changing the ratio of f_{SD}/f_{DD} and from modification of the ratio f_{CD}/f_{SD} for $p_{\mathrm{T}}^{\mathrm{cut}} = 200$ MeV.

Table 10.3: Kinematic cuts applied to individual and pairs of topological clusters within each η bin to enhance the $\pi^0 \to \gamma\gamma$ signal in data and MC.

	p_{T} **of Cluster**	p_{T} **of Pair**	$\Delta\eta$ **or** $\Delta\phi$ **of Pair**
$\lvert\eta\rvert < 2.37$	> 200 MeV	> 600 MeV	> 0.15
$2.37 < \lvert\eta\rvert < 3.50$	> 100 MeV	> 450 MeV	> 0.30
$3.50 < \lvert\eta\rvert < 4.80$	> 50 MeV	> 450 MeV	> 0.30

central region is constrained through a comparison of the energy reconstructed in isolated calorimeter clusters with the momentum determination of an associated ID track [100][101][102]. For $|\eta| < 2.3$, these E/p studies constrain the energy scale uncertainty to be below 5% for transverse momenta down to a few hundred MeV, with no strong dependence on p_{T}.

At higher η, beyond the tracker acceptance, the deviation between data and MC in the mass peaks of the $\pi^0 \to \gamma\gamma$ signal [96] is used. The π^0 mass peak is reconstructed by dividing the detector into bins in η whose sizes are matched to detector regions of similar performance. The average bin size is $\Delta\eta = 0.6$. A π^0 candidate requires exactly two topological clusters in the same η bin which pass the cuts in Table 10.3. The p_{T} cut values were chosen to give a good signal-to-background ratio while the $\Delta\eta$ and $\Delta\phi$ separation requirements reduce contamination from split topological clusters.

The shape of the combinatorial background is independently confirmed via the random combination of topological clusters from different events. This event-mixed sample has the disadvantage that it lacks contributions from additional resonances and reflections which may be present in the combinatorial background of topological clusters from the same event but yields consistent results nonetheless. An example of a forward π^0 mass peak is presented in Figure 10.15.

From Figure 9.9(b), this EM response is applicable to approximately one third of particles in the final state. Additional factors, as described below, are added in quadrature to account for the uncertainty in the response to hadronic showers from the mesons and baryons which dominate the other two thirds of the final state.

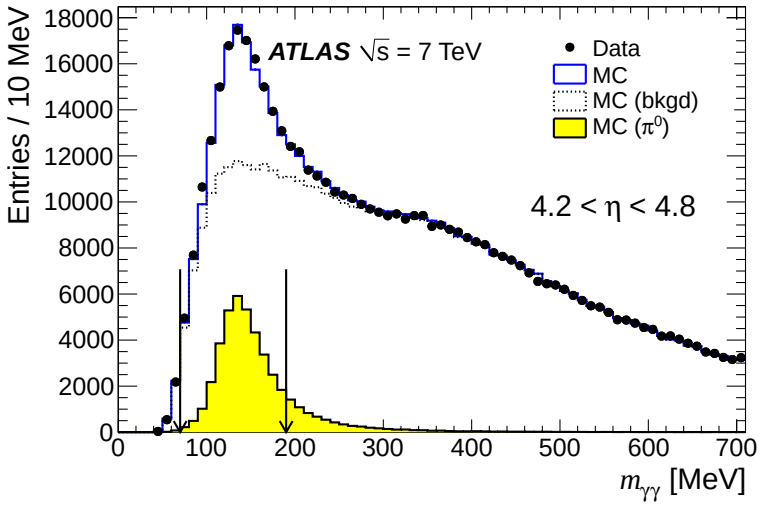

Figure 10.15: Reconstruction of the π^0 mass peak in the most forward region. MC $\pi^0 \to \gamma\gamma$ and background templates are shown separately. Taken from [103].

The hadronic energy scale relative to the EM scale is taken from the test beam results in [104]. Charged pions, muons and electrons from the CERN SPS in the energy range $E_{\text{Beam}} = 10$–200 GeV were fired into EM and hadronic endcap as well as forward calorimeter modules. The endcap modules were arranges to model the response of the systems in ATLAS at $|\eta| \approx 2.73$ with the FCal set-up modelling $|\eta| \approx 3.2$. The lowest probe energy was $E_{\text{Beam}} = 10$ GeV. An additional hadronic scale uncertainty of 8% in the FCal and 4% in the HEC are derived from the deviations between the data and MC responses to the 10 GeV test beam analysis [1].

The combined hadronic energy scale uncertainties are applied to all topological clusters. The final uncertainties applied in different pseudorapidity regions are listed in Table 10.4.

The effect of the energy scale uncertainty on the measurement is quantified using MC. Two special MC samples are produced in which the energy deposition from simulated particles is enhanced or suppressed by the amounts given in Table 10.4, the jump in uncertainty at $1.37 < |\eta| < 1.52$ is due to the hadronic barrel–endcap transition region. The contribution from simulated electronic noise is left unchanged. In constructing these samples, the shifts are applied to the response of 'real' particles

Table 10.4: Energy scale uncertainty values used in the analysis. The values are obtained by combining results from E/p studies, $\pi^0 \to \gamma\gamma$ studies and hadronic test beam data.

	Scale Uncertainty
$\lvert\eta\rvert < 1.37$	5%
$1.37 < \lvert\eta\rvert < 1.52$	21%
$1.52 < \lvert\eta\rvert < 2.30$	5%
$2.30 < \lvert\eta\rvert < 3.20$	13%
$3.20 < \lvert\eta\rvert < 4.90$	12%

at the cell level and the systematically shifted sets of cells are subsequently passed through the standard reconstruction algorithms. This procedure therefore addresses the sensitivity of the measurement to the topological clustering algorithm whilst correctly treating the additional noise suppression requirements.

The difference between of the nominal measurement and that where the data are corrected with the two systematically shifted MC samples is taken as a source of uncertainty. This is presented in Figure 10.16. The maximum uncertainty on the measurement from this source is 12% at $\Delta\eta^F = 2.6$, where calorimeter information alone is used to identify the gap and the hyperbolic enhancement of the equivalent E cut with respect to the fixed p_{T} cut is small.

10.4.4 MBTS RESPONSE UNCERTAINTY

Following from the quantification of the MBTS efficiency in Section 9.1.2, the MBTS response was modified in MC to the values listed in Table 9.1. The variation in the thresholds propagates to a less than 1% systematic uncertainty over the measured region, as plotted in Figure 10.17(a).

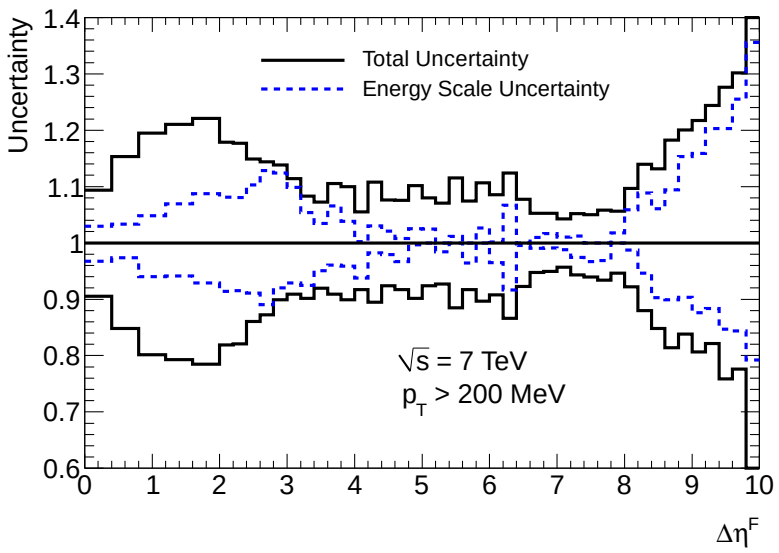

Figure 10.16: Systematic uncertainty arising from systematic modification of the energy scale for MC simulated particles in calorimeter cells (for $p_{\mathrm{T}}^{\mathrm{cut}} = 200$ MeV).

10.4.5 TRACKING UNCERTAINTY

From [5], the dominant source of uncertainty in the charged particle track reconstruction efficiency comes from inaccuracies in modelling the material of the ID within the simulation. The measurement uncertainty coming from material effects is derived by using a special MC sample in which the material budget of the ID support is enhanced by 10%. The effect on the amount of material traversed by charged particles as a function of $|\eta|$ is presented in Figure 9.13.

The PYTHIA6 MC is simulated with the enhanced material detector geometry and the systematic deviation of the forward gap measurement is taken with respect to the nominal PYTHIA6 forward gap distribution and symmetrised. The softer particle p_{T} spectrum in PYTHIA6 compared with PYTHIA8 enhances the magnitude of the uncertainty slightly. The final measurement is sensitive to the placement of detector services in ATLAS. The resulting uncertainty on the cross section therefore varies considerably as a function of $\Delta\eta^F$. The maximum material uncertainty is 2% as shown in Figure 10.17(b).

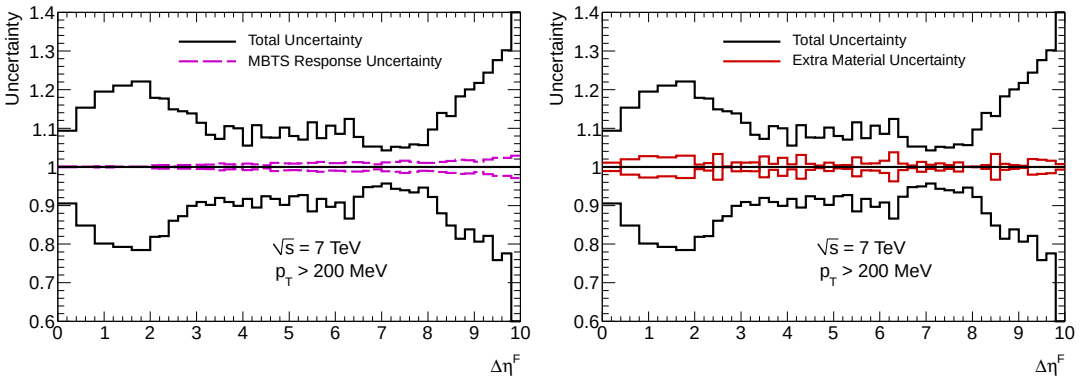

(a) (b)

Figure 10.17: Systematic uncertainty arising from modification of the MBTS response in MC (a) and the addition of 10% extra dead material to the ID support structures for $p_{\mathrm{T}}^{\mathrm{cut}} = 200$ MeV (b).

10.4.6 LUMINOSITY UNCERTAINTY

The ATLAS luminosity determination with LUCID is described in Section 4.5.

The uncertainty in the integrated luminosity for the analysis dataset as calibrated via the vdM scan is 3.4%.

10.5 EVOLUTION OF UNCERTAINTY WITH $p_{\mathrm{T}}^{\mathrm{cut}}$

In Figure 10.18 the three dominant sources of uncertainty, the model dependence quantified with PYTHIA6 and PHOJET priors and the energy scale uncertainty are shown along with the statistical error for each value of $p_{\mathrm{T}}^{\mathrm{cut}}$. For $p_{\mathrm{T}}^{\mathrm{cut}} \geq 400$ MeV the, model dependence from PHOJET remains the dominant source of uncertainty for small forward gaps, whilst the energy scale or PYTHIA6 dominate the uncertainty on the diffractive plateau. For $p_{\mathrm{T}}^{\mathrm{cut}} = 600$ and 800 MeV, the contribution to the uncertainty from PYTHIA6 in the diffractive plateau grows considerably due to the soft p_{T} spectrum generated by the PYTHIA6 diffractive model, as investigated in Section 8.1.2.

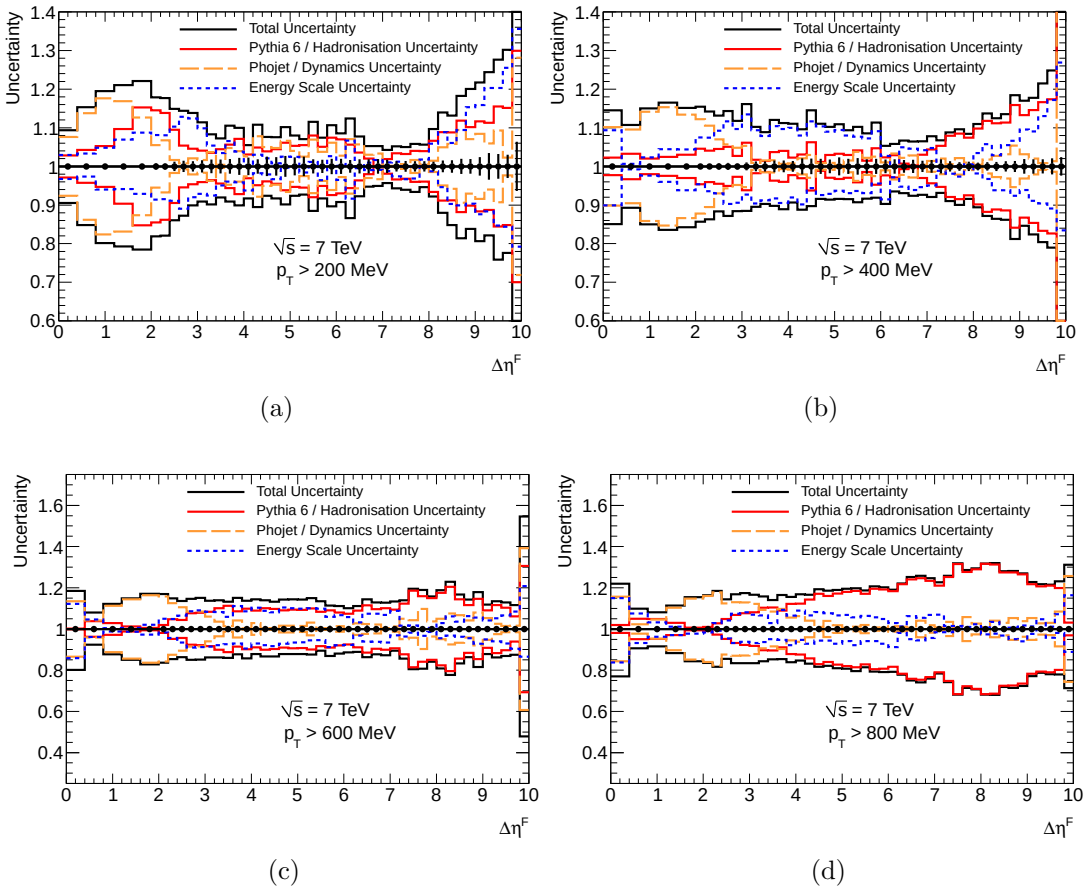

Figure 10.18: Statistical error on points and dominant systematic uncertainties for p_T^{cut} = 200, 400, 600 and 800 MeV. Note the enlarged scale on the y-axis in (c) and (d).

CHAPTER 11

RESULTS

A great deal more is known than has been proved.

Richard Feynman

11.1 FORWARD GAP CROSS SECTION AT $p_T^{cut} = 200$ MeV

The unfolded $\Delta\eta^F$ distribution for $p_T^{cut} = 200$ MeV is presented in Figure 11.1. The MC samples are normalised to the luminosity of the data, assuming the total inelastic cross section according to each model. The majority of the cross section is contained at small $\Delta\eta^F$. The agreement between the data and the MC generators considered is within the experimental uncertainty in the first bin where no forward gap is found, but deviates significantly in subsequent bins, with PHOJET overestimating the cross section by a factor of 1.8 at $\Delta\eta^F = 1.0$. All the considered models overestimate the cross section in this ND dominated region, with PYTHIA8 providing the best

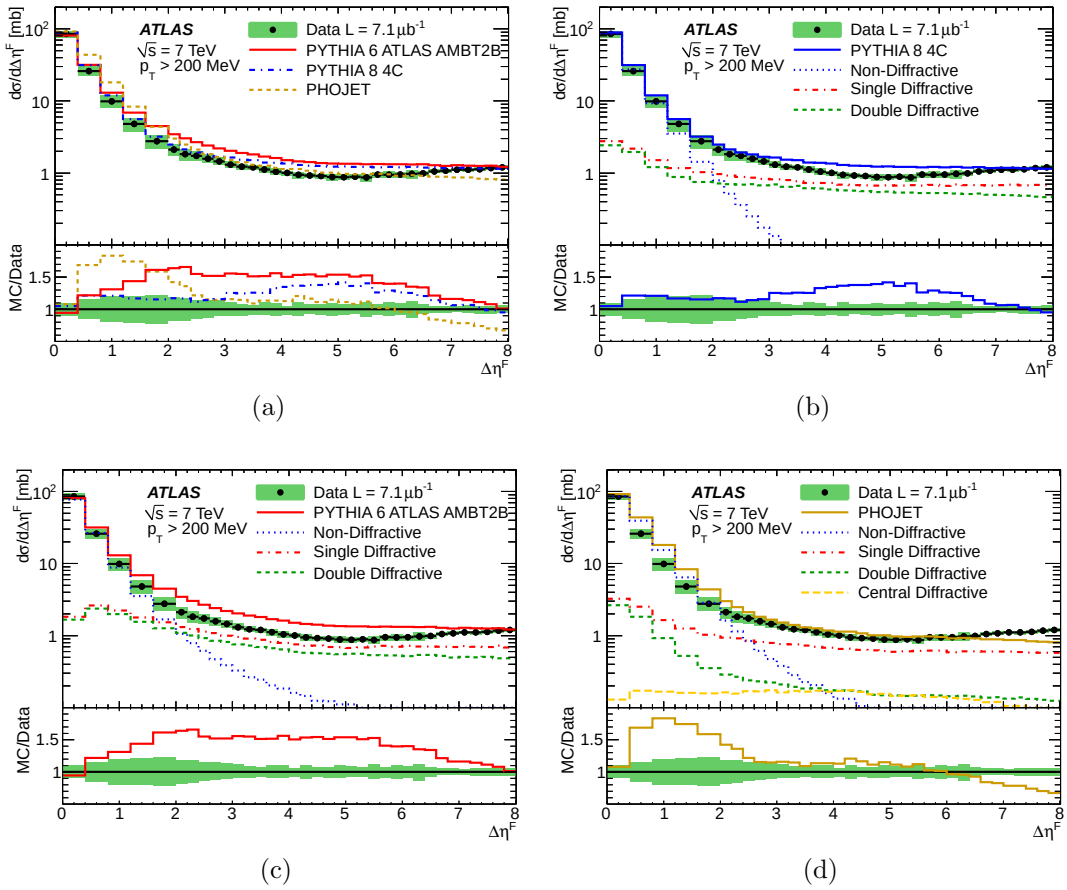

Figure 11.1: Differential inelastic forward gap cross section for particles with p_T> 200 MeV and $\Delta\eta^F < 8$. Shaded band represents the total uncertainty. The lines show the hadron level predictions of PHOJET, PYTHIA6 and PYTHIA8. In (b) – (d), the individual contributions of the ND, SD, DD and, for the case of PHOJET, CD components are shown separately.

description of both the normalisation and slope of the falling differential cross section with increasing forward gap size.

The plateau in the differential cross section at large gap sizes is studied in more detail in Figure 11.2, where the forward gap spectrum is plotted on a linear scale. The cross section in the region $3 < \Delta\eta^F < 8$ is approximately 1 mb per unit pseudorapidity. This near flat cross section is expected in Pomeron models as a consequence of the approximate $1/M_X^2$ dependence of the cross section on the diffractive mass (see Section 7.7). Using the correlation between $\Delta\eta^F$ and $-\ln\xi_X$ discussed in Section 7.8.1, events in this region at $\sqrt{s} = 7$ TeV are predicted to have diffractive

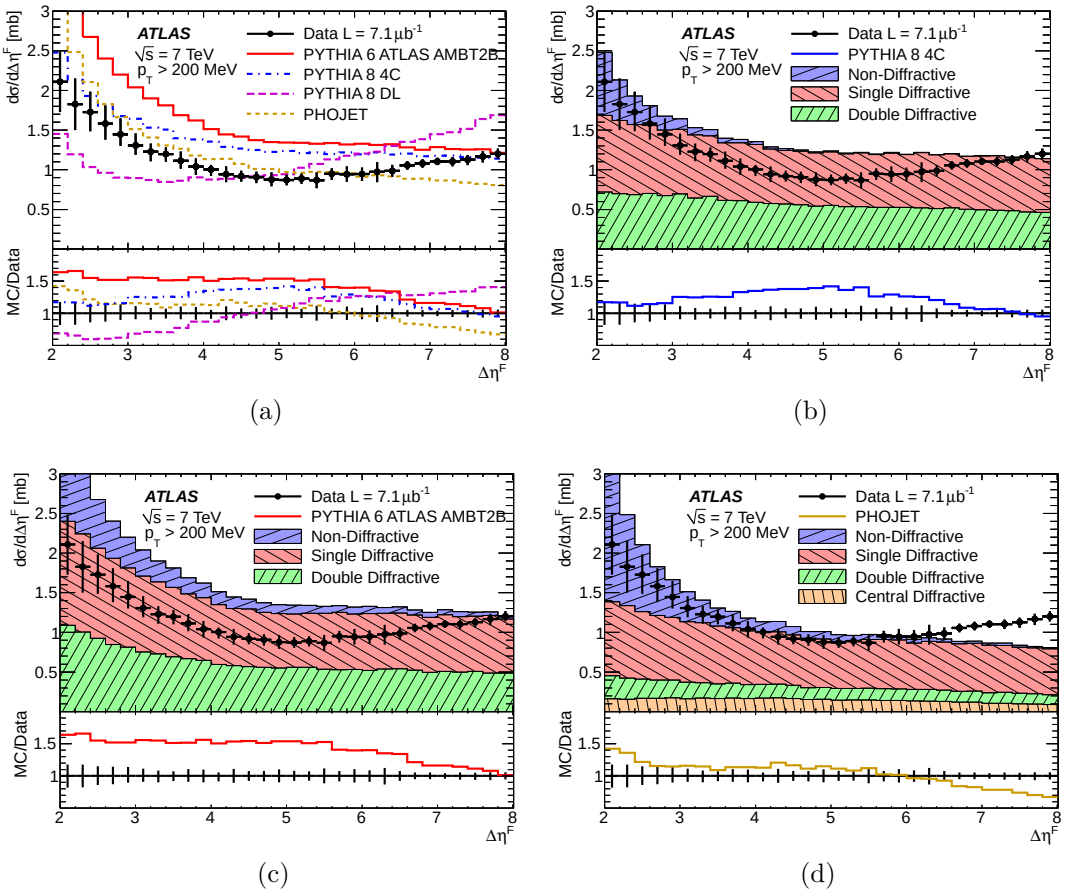

Figure 11.2: Differential forward gap inelastic cross section for particles with $p_{\mathrm{T}}>$ 200 MeV and $2 < \Delta\eta^F < 8$. Error bars represent the total uncertainty. The lines show the hadron level predictions of PHOJET, PYTHIA6, PYTHIA8 and PYTHIA8 with the Donnachie-Landshoff Pomeron flux. In (b) – (d), the individual contributions of the ND, SD, DD and, for the case of PHOJET, CD components are shown separately.

masses $20 < M_X < 250$ GeV, as this satisfies $s \gg M_X^2$ and $M_X^2 \gg t$, the triple Pomeron amplitude from Regge theory dominates throughout this plateau.

PHOJET provides the best model of the normalisation in this region. It is the only generator to model the CD contribution and contains a significantly smaller DD contribution than is present in PYTHIA. However, none of the generators considered are able to recreate the small rise in the differential cross section observed for large gaps. Figure 11.2(a) shows in addition PYTHIA8 with the super-critical Donnachie-Landshoff Pomeron. This model produces a rise in the cross section which is faster than that observed in the data.

11.2 FORWARD GAP CROSS SECTION AT $p_T^{cut} > 200$ MeV

In [105] the authors demonstrate that the simulated probability of a large rapidity gap arising from fluctuations in hadronisation in ND events is strongly dependent on the choice of either Lund string or cluster hadronisation (see Section 8.1, Section 8.3) models. It also depends strongly on the choice of p_T^{cut}.

The deviation between models is shown to be maximal for large rapidity gaps at a threshold $p_T^{cut} = 500$ MeV. Here the probability of a rapidity gap of $\Delta\eta = 5$ being produced[1] by such fluctuation is shown to be a factor of five times greater with cluster hadronisation than with the Lund string method.

This difference between model predictions is explored experimentally here for the first time by making measurements at additional values of $p_T^{cut} = 400, 600$ and 800 MeV. By viewing the $\Delta\eta^F$ distributions together in Figure 11.3(a), the primary feature observed as p_T^{cut} grows is the reduction in differential cross section at small gaps and a corresponding increase in the differential cross section at large gap sizes. This is a logical outcome as by increasing p_T^{cut}, fewer hadron level particles are included in the gap finding algorithm, hence increasing the size of the reconstructed gap.

In Figure 11.3(b)–(d), the differential cross section is compared with PYTHIA6, PYTHIA8 and PHOJET, all of which are Lund string based MC models. The full differential cross section is shown along with the ND contribution according to each model. In all models, the ND contribution is shown to retain an exponential form as p_T^{cut} increases. As $\Delta\eta^F$ is an inclusive distribution, the total cross section is the same for all plots[2]. The reduction in slope with increasing p_T^{cut} is compensated by a reduction in the cross section at smaller gap size. The contribution to the differential

[1] $\Delta\eta$ as used in [105] is defined as the largest pseudorapidity gap separation between any two neighbouring particles in η at the hadron level, with $p_T > p_T^{cut}$. This (without the p_T cut) is the same as the $\Delta\eta$ described in Section 7.8.2.

[2] True when integrated up to $\Delta\eta^F = 10$. However the distributions presented are truncated at $\Delta\eta^F = 8$ due to the aforementioned trigger efficiency constraint.

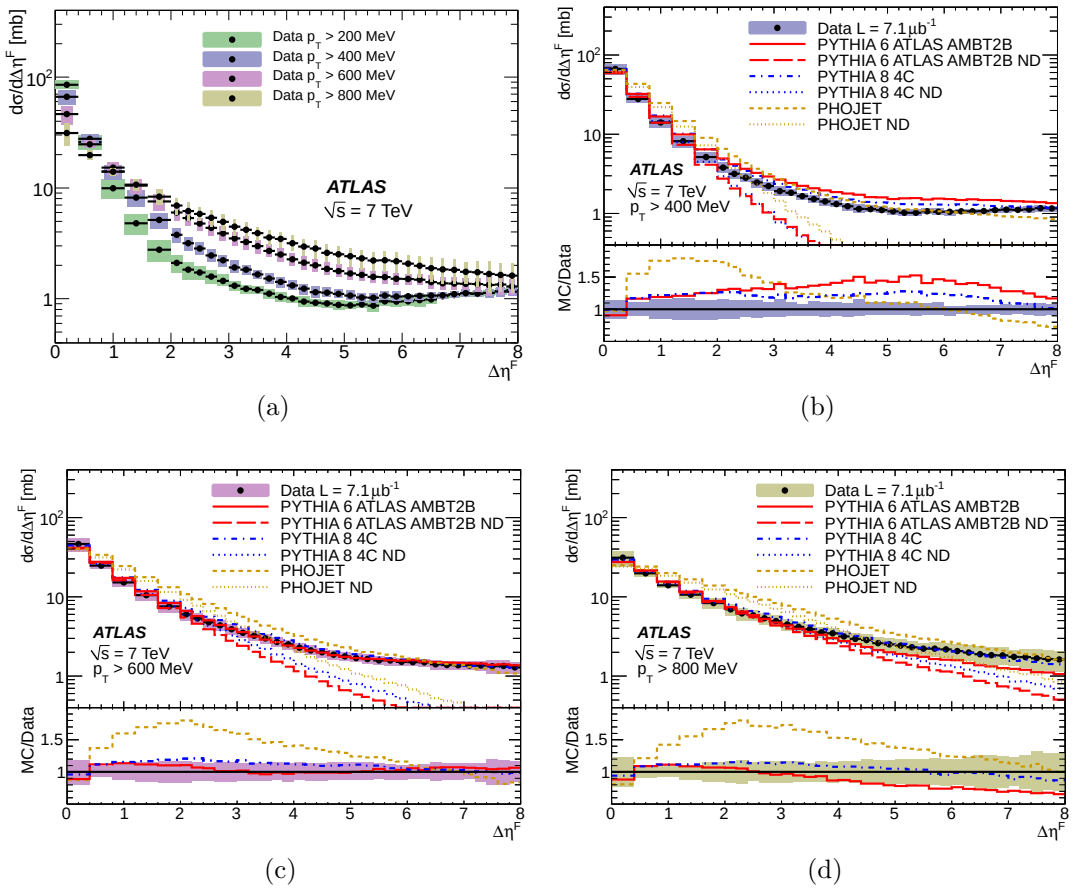

Figure 11.3: Differential inelastic cross section for particles for different values of $p_{\mathrm{T}}^{\mathrm{cut}}$ in (a) and for $p_{\mathrm{T}} > 400, 600, 800$ MeV in (b), (c) and (d) respectively. Total uncertainty is shown and uncertainties are correlated between choices of $p_{\mathrm{T}}^{\mathrm{cut}}$. Total MC predictions for PYTHIA6, PYTHIA8 and PHOJET are shown along with their corresponding ND components.

cross section from diffraction becomes more similar in shape to that from ND processes as $p_{\mathrm{T}}^{\mathrm{cut}}$ increases. Overall PHOJET provides the poorest match to data, with a consistent overestimation of the differential cross section for $\Delta\eta^F \approx 2$. PYTHIA8 provides the best description, which improves with increasing $p_{\mathrm{T}}^{\mathrm{cut}}$.

11.3 CLUSTER HADRONISATION MODELS

As motivated in the previous section, there is strong theoretical interest in comparing data with a cluster based hadronisation model. The HERWIG++ MC model is chosen,

as described in Section 8.3. Data at all considered values of $p_{\mathrm{T}}^{\mathrm{cut}}$ are compared to the HERWIG++UE7-2[3] tune in Figure 11.4.

The UE7-2 tune contains no explicit model of diffraction. However, the model produces a significant fraction of events at large values of $\Delta\eta^F$, overestimating the differential cross section by up to a factor of four in the region $2 < \Delta\eta^F < 7$ and containing an enchantment at $\Delta\eta^F = 6$ which persists at all values of $p_{\mathrm{T}}^{\mathrm{cut}}$. Two modifications to UE7-2 are made in an attempt to understand and remove these features of the $\Delta\eta^F$ spectrum. With the colour reconnection (see Section 8.3) machinery switched off, the differential cross section reduces at large gap sizes but the features are still present. Similarly HERWIG++ can generate *empty* events when both zero *semi-hard* and zero *soft* interactions are chosen by the two Poisson distributions in (8.14). These events have a pseudo-DD topology, consisting solely of the dissociated remnants of both protons. Vetoing these events again reduces the fraction of events with large gaps, but still fails to remove fully the events observed at large $\Delta\eta^F$ and the bump at $\Delta\eta^F = 6$.

Although it is the interpretation of the authors of this analysis that a triple Regge interpretation of events at large gap sizes is the most appropriate, HERWIG++ is able to partially match the spectrum observed without any explicit diffractive model.

11.4 BEST FIT FOR POMERON INTERCEPT

For events with large gaps, $\Delta\eta^F > 5$, there is negligible contribution to the cross section from non-diffractive interactions according to all Lund string based models. The slow rise in the cross section at large gap size is attributed to the $\mathbb{PPP}$ term in Regge models, for a supercritical Pomeron trajectory with intercept above unity. This was demonstrated in Figure 8.6 for both the Donnachie and Landshoff (DL) and Berger and Streng models. When the standard Schuler and Sjöstrand Pomeron flux

[3] `http://herwig.hepforge.org/MB_UE_tunes/input_cards/LHC-UE7-2.in`

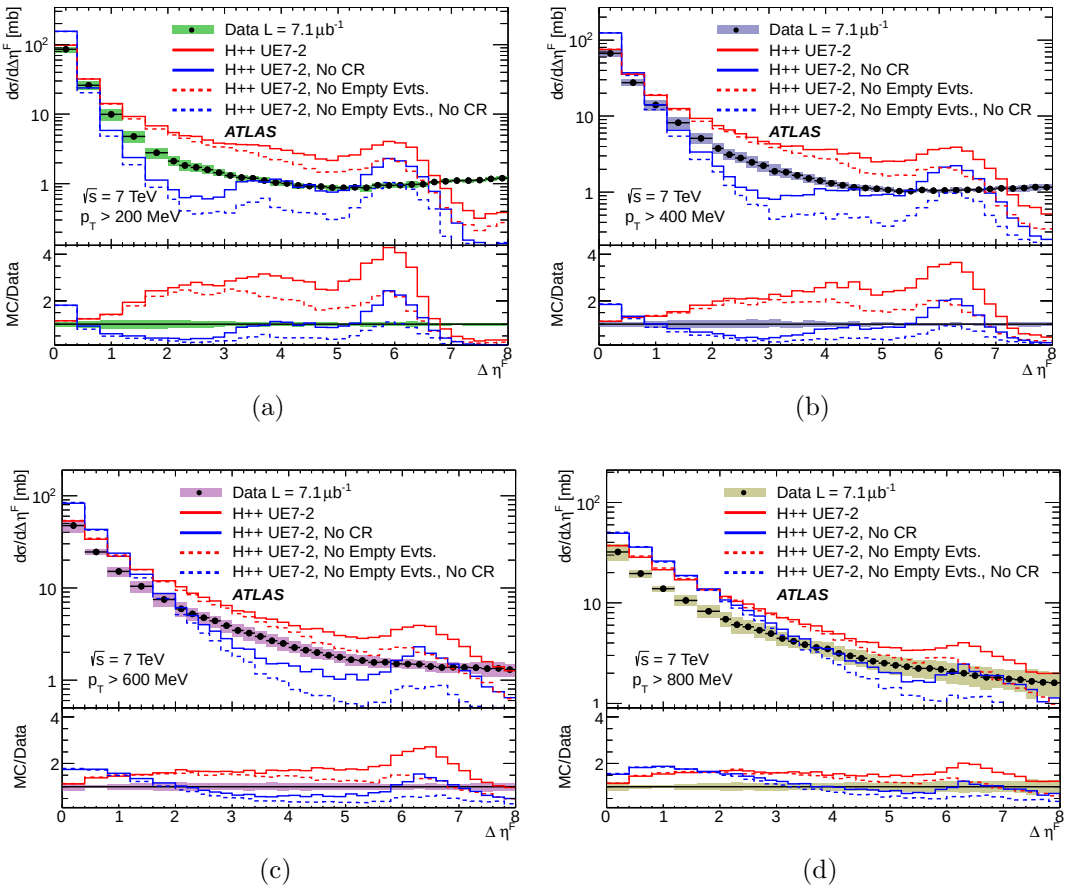

Figure 11.4: Differential inelastic forward gap cross section for different values of $p_{\mathrm{T}}^{\mathrm{cut}}$, compared with the UE7-2 tune of HERWIG++. The additional lines show the change in the distribution upon switching off colour reconnection, removing zero scatter events and the combination of both.

in PYTHIA8 is replaced by the DL flux with default trajectory $\alpha_{\mathbb{P}}(t) = 1.085 + 0.25t$, a rise in cross section at large gap sizes which is qualitatively similar to data is observed, as is seen in Figure 11.2(a). It therefore seems reasonable that the DL flux with smaller $\alpha_{\mathbb{P}}(0)$ may give an optimal description of the data.

High statistics[4] hadron level MC templates were constructed over the range of allowed supercriticalities ϵ (where $\epsilon = \alpha_{\mathbb{P}}(0) - 1$, see Section 7.4) in the PYTHIA8 DL implementation. MC was generated for values in the range $0.02 \leq \epsilon \leq 0.15$ in steps of 0.005 with additional higher granularity steps of 0.002 in the range 0.04–0.06. The ND, SD and DD samples were mixed with the fitted fractions from Section 8.4.

The fitting procedure is a χ^2 minimisation of the templates to the data using the MINUIT package [106]. The ten data points in the range $6 < \Delta\eta^F < 8$ are fitted to each ϵ template separately with the overall normalisation allowed to float as one free parameter in the fit. When the normalisation has been found which results in the smallest value of χ^2, this χ^2 is recorded. These χ^2 values, one per ϵ-template, lie on a parabola. The ϵ which best fits the data is found at the parabola minimum. This minimum is determined by fitting the parabola to a 2^{nd} order polynomial and the statistical uncertainty is determined by moving up the parabola from the minimum in both directions until the χ^2 has increased by 1 unit [106].

To quantify the systematic uncertainty, the procedure is repeated after shifting the measurement according to each correlated systematic in turn. The same symmetrisation is applied to the resulting systematic uncertainties as is discussed in Section 10.4. The total systematic uncertainty is the sum in quadrature of the deviations of the systematics with respect to the nominal result. The nominal and systematically shifted parabola are plotted in Figure 11.5.

The result obtained, $\alpha_{\mathbb{P}}(0) = 1.058 \pm 0.003(\text{stat.})^{+0.034}_{-0.039}(\text{syst.})$, is in agreement with [49] and [68]. The fitting procedure was repeated with the maximum allowed variation within the MC model of the Pomeron trajectory slope ($\alpha'_{\mathbb{P}} = 0.1$ and 0.4 GeV^{-2})

[4] 15 million events per template.

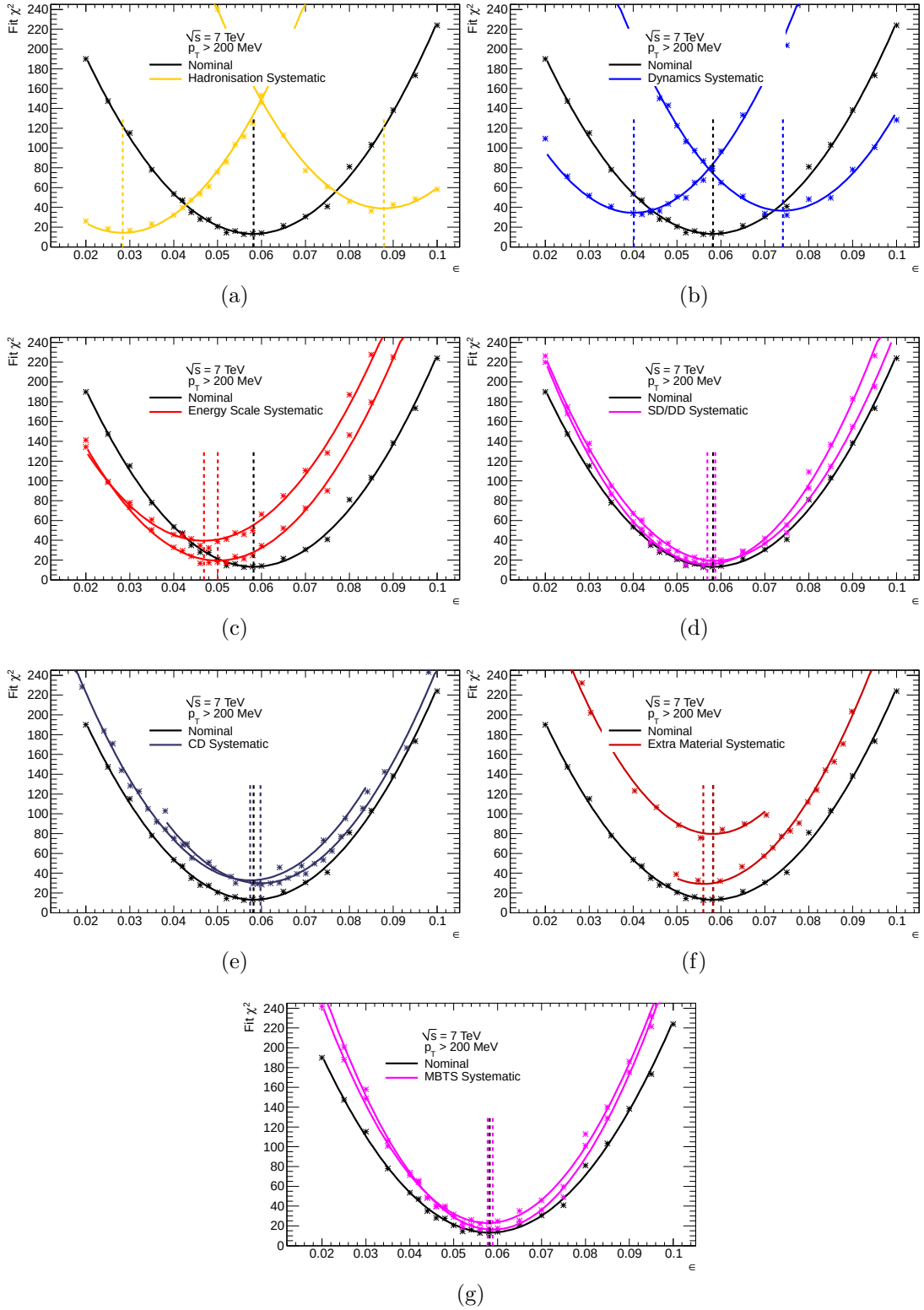

Figure 11.5: χ^2 parabola for the nominal result and each correlated systematic shift for PYTHIA8 templates with varying ϵ with the Donnachie and Landshoff flux. The extra material and CD curves are deviations from the PYTHIA6 and PHOJET minima, respectively. They are therefore presented with an appropriate offset in these figures.

and with the Berger and Streng Pomeron flux model. The fitted ϵ for these three parametrisations ($\alpha_{\mathbb{P}}(0) = 1.054, 1.060, 1.056$, respectively) are all comparable with the statistical error.

With nine Degrees of Freedom (DoF), the quality of fit $\chi^2/\text{DoF} = 1.5$. The normalisation of the fit, defined as

$$\int_6^8 \frac{\mathrm{d}\sigma}{\mathrm{d}\Delta\eta^F}\mathrm{d}\Delta\eta^F \tag{11.1}$$

is presented as a function of ϵ in Figure 11.6(a). For the best fit this gives a normalisation of 2.15 mb over the fitted region with statistical error and stability[5] both less than 1%.

It was observed in Figure 8.7 that there is a correlation between to f_D and ϵ. By taking the value of f_D which corresponds to the measured result, a model dependent tune of the diffractive fraction is achieved. This was performed with the PYTHIA8 model by interpolating between results with the DL flux for $\epsilon = 0.06, 0.085$ and 0.1 as shown previously in Figure 8.7 from [52]. The appropriate values of f_D for these models are presented in Figure 11.6(b), along with a linear interpolation through the best fits and their associated uncertainties. For the nominal result obtained here of $\epsilon = 0.058$, the best fit value of the diffractive fraction for events triggered by the MBTS ($\xi_X \gtrsim 5 \times 10^{-6}$) with the DL flux is $f_D(\epsilon = 0.058) = 25.6^{+2.8}_{-0.9}\%$.

Taking the PYTHIA8 MC with $\epsilon = 0.058$ and combining the diffractive and non-diffractive samples with $f_D = 0.256$ and the tuned fraction f_{SD}/f_{DD} from Section 8.4, the full forward gap distribution is plotted in Figure 11.7. The description of the data within the fitted region $6 < \Delta\eta^F < 8$ is excellent. However, the MC underestimates the differential cross section by up to 40% in the range $1 < \Delta\eta^F < 5$. This region encompasses the transition from the non-diffractive to the diffractive dominated domains. There are various possibilities which could be responsible for the deficiency in the simulation such as the contribution from sub-leading exchanges, the missing CD contribution or mis-modelling of the tail of the ND forward gap dis-

[5]The variation of the cross section normalisation over the range of ϵ allowed by the systematic uncertainty, $0.024 < \epsilon < 0.097$.

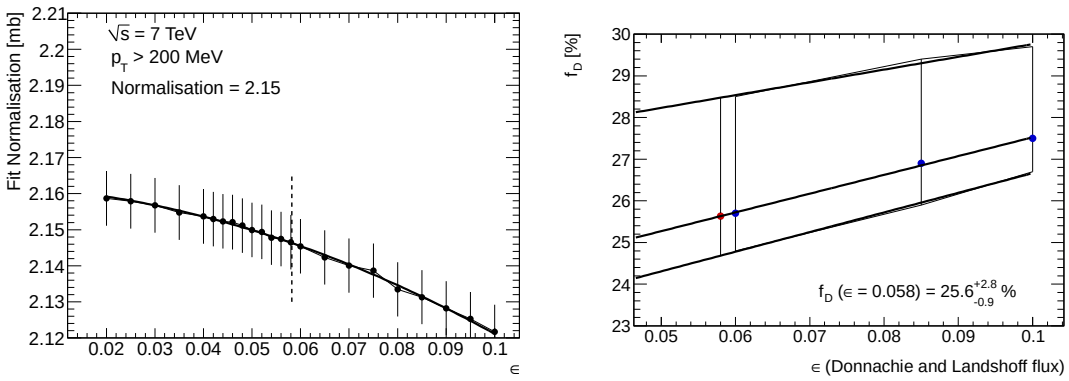

(a) (b)

Figure 11.6: Integrated cross section normalisation in the range $6 <= \Delta\eta^F < 8$ of the χ^2 fit to the MC templates as a function of supercriticality ϵ (a). The best fit values, in blue, for the fraction of diffraction, f_D, for three values of ϵ using the PYTHIA8 MC with the DL flux (from [52]). In red, the value of f_D for the fitted value of ϵ extracted via linear interpolation (b).

tribution. Overall the MC is observed to lie below the data. However this is partly a consequence of extrapolating the fitted cross section from the region $6 < \Delta\eta^F < 8$ to the whole distribution. For $\Delta\eta^F < 1.6$, the MC prediction lies within the experimental uncertainty (with a small exception in the first bin). The majority of the cross section is contained within this small $\Delta\eta^F$ region.

11.5 ξ_X DEPENDENCE ON INELASTIC CROSS SECTION

Being an inclusive distribution, an integral over all measured $\Delta\eta^F$ corresponds to the total inelastic cross section excluding the events with forward gaps $\Delta\eta^F > 8$. Integrating up to different maximum $\Delta\eta^F$ values allows comparison with independent measurements of the inelastic cross section in different ranges. In Figure 11.2 it was observed that for forward gaps $\Delta\eta^F \geq 3$, the contribution to the differential cross section from ND events is small according to MC models. The integral of the forward gaps distribution is calculated from a forward gap size of zero up to a variable maximum $\Delta\eta^F_{\text{Cut}}$ where $3 < \Delta\eta^F_{\text{Cut}} < 8$. As the end point $\Delta\eta^F_{\text{Cut}}$ is always in a diffractive dominated region, this integrated cross section in gap size is correlated

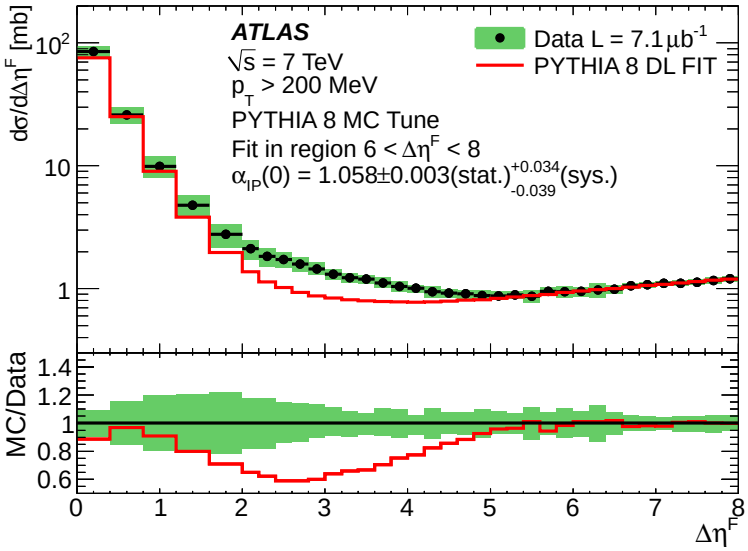

Figure 11.7: Differential inelastic cross section for $p_{\mathrm{T}} > 200$ MeV. Data are compared to a version of PYTHIA8 with the DL flux which has been tuned in the region $6 < \Delta\eta^F < 8$.

to an integrated cross section over ξ_X.

With a small correction, the $\Delta\eta^F$ integral can therefore be expressed as an integral of the inelastic cross section down to some minimum value of ξ_X. The correction procedure utilises the kinematic correlation between the ξ_X of a diffractive system and the absolute pseudorapidity range it spans. This relation is plotted in Figure 7.10 and yields a conversion function to translate from the $\Delta\eta^F$ domain to the ξ_X domain of $\log_{10}(\xi_{\mathrm{Cut}}) = -0.45\Delta\eta^F_{\mathrm{Cut}} - 1.52$ as was described in Section 7.8.1. The model uncertainty on this conversion is quantified by repeating the procedure with the PHOJET MC, which results in the same slope but a modified intercept of -1.56.

A small MC derived correction factor and its associated uncertainty are calculated at each value of $\Delta\eta^F_{\mathrm{Cut}}$ over the range $3 < \Delta\eta^F_{\mathrm{Cut}} < 8$ (corresponding to a ξ_{Cut} of $1.3 \times 10^{-3} > \xi_X > 7.6 \times 10^{-6}$). The nominal MC is PYTHIA8 using the DL flux with tuned $\epsilon = 0.058$ and the tuned f_{ND}, f_{SD} and f_{DD} values. The correction factor is

defined as

$$\frac{\int_{\xi_{\rm Cut}}^{1} \frac{{\rm d}\sigma}{{\rm d}\xi_X} {\rm d}\xi_X}{\int_{0}^{\Delta\eta^F_{\rm Cut}} \frac{{\rm d}\sigma}{{\rm d}\Delta\eta^F} {\rm d}\Delta\eta^F} \tag{11.2}$$

and corrects the data for the following:

- A correction is applied to SD events to remove the finite 200 MeV $p_{\rm T}$ cut of the measured distribution. The finite $p_{\rm T}$ cut causes slightly larger gaps to be reconstructed than would have been the case were it possible to measure to arbitrarily low $p_{\rm T}$ in ATLAS and therefore provides a positive contribution to the correction factor.

- A correction is applied for the fraction of ND events which contain a large forward gap such that $\Delta\eta^F > \Delta\eta^F_{\rm Cut}$. This provides a negative contribution to the correction for the smallest values of $\Delta\eta^F_{\rm Cut}$ and vanishes for large $\Delta\eta^F_{\rm Cut}$.

- For DD events, the correction removes the finite $p_{\rm T}$ cut as for SD events. In addition, as was noted in Section 7.8.3, approximately 30% of DD events with $\xi_Y \gtrsim 10^{-6}$ are reconstructed by the forward gap algorithm as having $\Delta\eta^F \approx 0$ regardless of their true ξ_X. This is due to the two large diffractive systems depositing energy in both the forward and backward regions of ATLAS. The correction factor corrects such events based on the ξ_X value of the larger system as taken directly from the MC. This correction is largest at small $\Delta\eta^F_{\rm Cut}$, this is because a small $\Delta\eta^F_{\rm Cut}$ equates to a large ξ_X. It is observed in Figure 7.13 that the majority of events which satisfy $\xi_Y \gtrsim 10^{-6}$ also have large ξ_X, this is to be expected as by definition $\xi_X > \xi_Y$.

Model induced systematic uncertainties in the correction are quantified by using PYTHIA 8 with the default Schuler and Sjöstrand flux and PHOJET. Additional systematics are determined by systematic variation of the tuned fractional cross sections.

Figure 11.8 shows the nominal correction factor over the range of the measurement and the total systematic uncertainty on the correction. The correction is at most

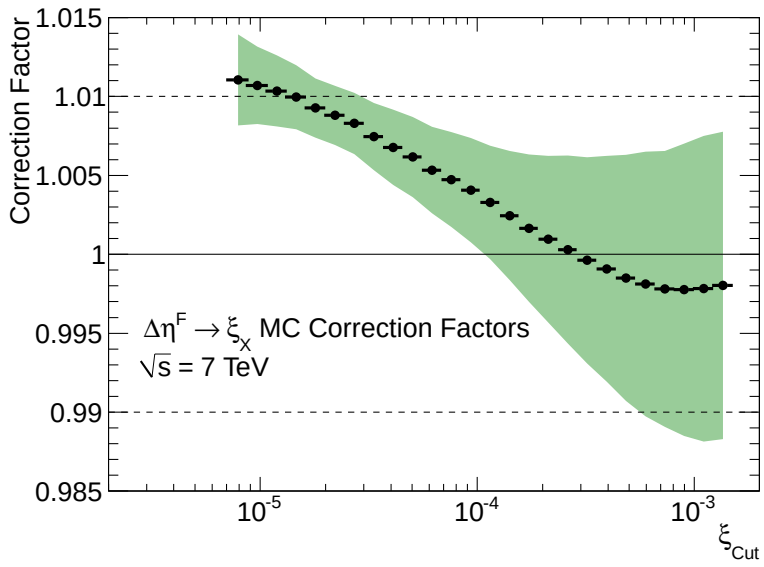

Figure 11.8: MC derived $\Delta\eta^F \rightarrow \xi_X$ correction factors applied to convert from $\Delta\eta^F$ domain to ξ_X domain. Green band represents the total systematic uncertainty in the correction factor.

+1.1% at $\Delta\eta^F_{\text{Cut}} = 8$ ($\xi_{\text{Cut}} = 7.6 \times 10^{-6}$) and has a maximal systematic uncertainty of ±1.1% at $\Delta\eta^F_{\text{Cut}} = 3$ ($\xi_{\text{Cut}} = 1.3 \times 10^{-3}$).

The inelastic cross section integrated over the range $0 < \Delta\eta^F < \Delta\eta^F_{\text{Cut}}$ and corrected to $\xi_{\text{Cut}} < \xi_X < 1$ is plotted in Figure 11.9 with all sources of systematic uncertainties in Section 10.4.1 included, along with the systematic uncertainty in the conversion from $\Delta\eta^F_{\text{Cut}}$ to ξ_{Cut}. For both shown ATLAS measurements, the vertical error bars represent all sources of uncertainty excluding that on the luminosity measurement, which is dominant, whilst the shaded area represents the total uncertainty. For the TOTEM measurement the error bars represent the statistical error whilst the shaded area represents the total uncertainty. MC curves are presented for the default versions of PYTHIA6, PYTHIA8 and PHOJET, along with two versions of the RMK model (see below). The uncertainties between neighbouring data points for the presented analysis are strongly correlated. The datapoints are available in Appendix C.

The recent Ryskin, Martin and Khoze (RMK) [107][108] model implements a $\mathbb{PPP}$ model for high ξ_X diffraction, along with a low mass 'Good & Walker' [54] approach based on an s-channel approach in which proton and excited proton eigenstates are

scattered elastically with different probabilities. This results in an enhancement of the low mass cross section compatible with UA4 data [109]. The two RMK curves shown in Figure 11.9 are calculated using different radii for the low ξ_X elastically scattered eigenstates, with the lower curve being the preferred model and the upper curve being representative of the flexibility in the model whilst remaining compatible with pre-LHC data [107][108].

The data allow for the tuning of the rate-of-change of the diffractive cross section over two orders of magnitude in ξ_X. While the MC models considered are shown to have reasonable shape agreements, the normalisation is not well described. This is partly due to the modelling of the inelastic non-diffractive cross section, upon which the diffractive cross section is presented.

Upon assuming a linear extrapolation through the ATLAS results to the total inelastic cross section, as roughly favoured by the considered models in this region. A disagreement is observed with the TOTEM result at around the 2σ level. This could be an indication of the presence of additional enhancement to the diffractive cross section for very low diffractive masses, $\xi_X < 5 \times 10^{-6}$.

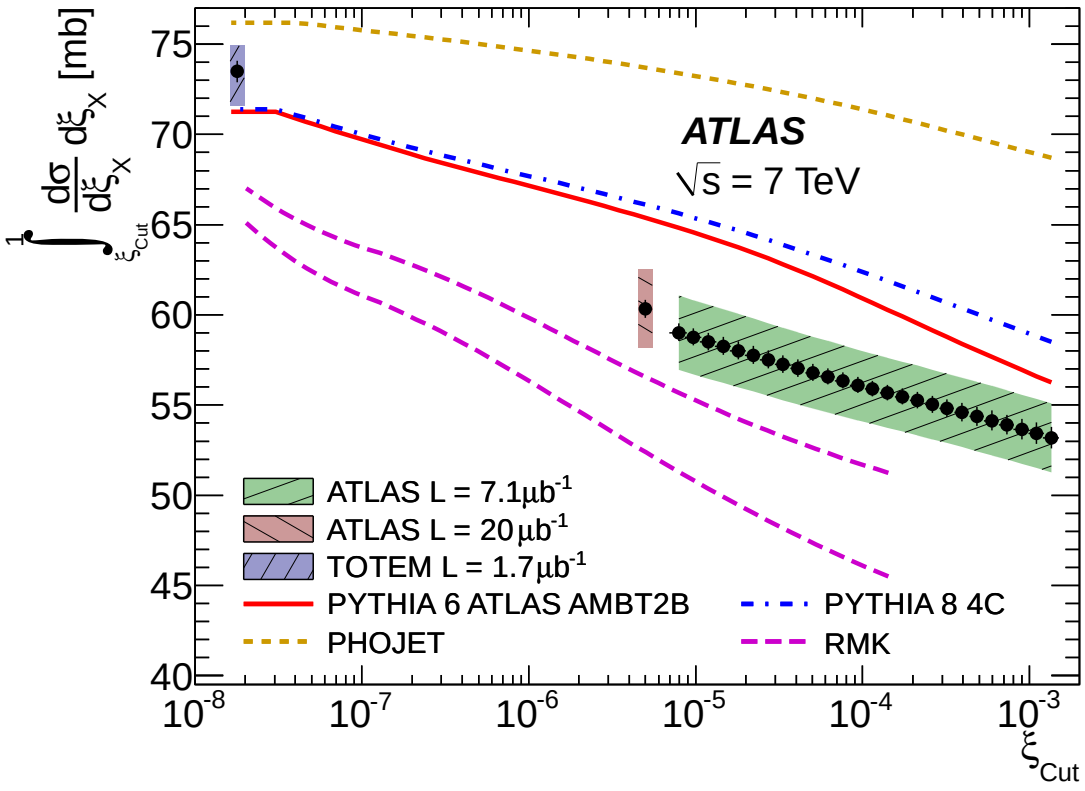

Figure 11.9: Total inelastic cross section excluding events with $\xi_X < \xi_{\text{Cut}}$ obtained via the integration of the differential cross section from $\Delta\eta^F = 0$ up to a variable maximum $3 < \Delta\eta^F_{\text{Cut}} < 8$. The result from this analysis ('ATLAS L = 7.1 μb^{-1}') is presented alongside a previous ATLAS result [52] and a measurement by TOTEM [51] integrated over all accessible ξ_X values. Further details in text.

CHAPTER 12

CONCLUSION

Clean, low background, low pile-up data from the LHC has allowed for many analyses studying the large dominantly non-pertubative cross section of hadron interactions. ATLAS has so far published 11 papers on soft physics, all corrected to the hadron level, and with yet more in preparation. The scope of the analyses has shifted over time from the measurements of simple event quantities to the complex inter-correlation of particles over many orders of magnitude [110][111].

Rapidity gaps have long been known to be a strong classifier of diffractive exchanges in the high energy interactions of composite hadrons. In this document, significant steps have been taken in understanding this poorly understood component of the inelastic cross section, pushing down the sensitivity of the ATLAS detector in the process to just above its electronic noise levels. The inelastic cross section is presented differentially in forward rapidity gap size for gaps up to eight units of pseudorapidity. This allows for comparison with various models in a diffraction dominated plateau

over two orders of magnitude in ξ_X. By additionally correcting the data to different values of $p_{\mathrm{T}}^{\mathrm{cut}}$, the evolution in slope of the exponential fall of the cross section with increasing gap size from the effects of hadronisation is studied in a novel manner.

First interpretations of these results are presented. The supercriticality, $\epsilon = \alpha_{I\!P}(0) - 1$, of the Pomeron trajectory has a large experimental backing from the slow rise of the total inelastic cross section with increasing $\sqrt{s}$. It is confirmed here from the enhancement to the low-ξ_X diffractive cross section that the ϵ term introduces into the triple Regge model. This enhancement is fitted in the context of the Donnachie and Landshoff Pomeron flux parametrisation with the MC machinery of PYTHIA8. A value of ϵ compatible with fits to the total cross section performed by Donnachie and Landshoff is obtained, $\alpha_{\mathbb{P}}(0) = 1.058 \pm 0.003(\mathrm{stat.})^{+0.034}_{-0.039}(\mathrm{syst.})$. Such a parametrisation, when combined with modifications to the cross sections of the different inelastic processes, allows for a good modelling of the data for small and large values of the forward gap size distribution. Further modifications are still required to fully match the data as this model underestimates $\frac{\mathrm{d}\sigma}{\mathrm{d}\Delta\eta^F}$ by a factor of three at $\Delta\eta^F = 3$.

By exploiting the kinematic correlation between rapidity gap size and the size of the underlying diffractive mass, the inelastic cross section is additionally presented as an integral over ξ_X for events which satisfy $\xi_X > \xi_{\mathrm{Cut}}$ in the range $(7.6 \times 10^{-6} < \xi_{\mathrm{Cut}} < 1.3 \times 10^{-3})$. The data are compared with MC models along with the TOTEM measurement of the total inelastic cross section. Upon assuming a linear extrapolation of the ATLAS data to all ξ_X, a discrepancy is observed between the two results at the 2σ level, which is not well described by current models. Future measurements at ultra-low ξ_X will help to resolve this tension.

REFERENCES

[1] T. A. Martin, P. Newman, O. Kepka, and P. Ruzicka, "Rapidity Gap Cross Sections in pp Interactions at $\sqrt{s} = 7$ TeV," *ATLAS Internal Note*, 2011. ATL-COM-PHYS-2011-1038.

[2] `http://commons.wikimedia.org/wiki/File:Laser_Interference.JPG`. Modified work under Creative Commons Attribution-Share Alike 3.0 licence.

[3] The ATLAS Collaboration, "Observation of a new particle in the search for the Standard Model Higgs boson with the ATLAS detector at the LHC," *Phys. Lett.*, vol. B716, pp. 1–29, 2012.

[4] The CMS Collaboration, "Observation of a new boson at a mass of 125 GeV with the CMS experiment at the LHC," *Phys. Lett.*, vol. B716, pp. 30–61, 2012.

[5] The ATLAS Collaboration, "Charged-particle multiplicities in pp interactions measured with the ATLAS detector at the LHC," *New J. Phys.*, vol. 13, p. 053033, 2011.

[6] P. Watkins, *Story of the W and Z*. Cambridge University Press, 1986.

[7] G. Baur *et al.*, "Production of antihydrogen," *Phys. Lett. B.*, vol. 368, no. 3, pp. 251 – 258, 1996.

[8] Wikimedia Commons, "Map of the CERN accelerator complex." [Online; `http://en.wikipedia.org/wiki/File:Cern-accelerator-complex.svg`; accessed 1-February-2012] Creative Commons Attribution-Share Alike 3.0 Unported.

[9] D. J. Simon, "The CERN PS complex: a versatile particle factory," 1996. CERN-PS-96-019-DI.

[10] P. Lefèvre and D. Möhl, "A low energy accumulation ring of ions for LHC (a feasibility study)," 1993. CERN-PS-93-62. CERN-PS-93-62-DI. LHC-NOTE-259. CERN-LHC-Note-259.

[11] L. Evans and P. Bryant, "LHC Machine," *Journal of Instrumentation*, vol. 3, no. 08, p. S08001, 2008.

[12] S. Baird, "Accelerators for pedestrians; rev. version," 2007. AB-Note-2007-014. CERN-AB-Note-2007-014. PS-OP-Note-95-17-Rev-2. CERN-PS-OP-Note-95-17-Rev-2.

[13] L. Ducimetiere, N. Garrel, M. Barnes, and G. Wait, "The LHC injection kicker magnet," vol. 2, pp. 1162 – 1164 Vol.2, 2003.

[14] O. S. Bruning, P. Collier, P. Lebrun, S. Myers, R. Ostojic, J. Poole, and P. Proudlock, *LHC Design Report*. CERN, 2004.

[15] The ALICE Collaboration, "The ALICE experiment at the CERN LHC," *Journal of Instrumentation*, vol. 3, no. 08, p. S08002, 2008.

[16] The ALICE Collaboration, "Charged-particle multiplicity measurement in proton-proton collisions at $\sqrt{s} = 7$ TeV with ALICE at LHC," *Eur. Phys. J.*, vol. C68, pp. 345–354, 2010.

[17] The CMS Collaboration, *CMS Physics Technical Design Report Volume I: Detector Performance and Software*. Technical Design Report CMS, CERN, 2006.

[18] The LHCb Collaboration, *LHCb reoptimized detector design and performance: Technical Design Report*. Technical Design Report LHCb, CERN, 2003.

[19] The LHCf Collaboration, "Technnical Proposal for the CERN LHCf Experiment: Measurement of Photons and Neutral Pions in the Very Forward Region of LHC," 2005. CERN-LHCC-2005-032. LHCC-P-007.

[20] The LHCf Collaboration, "Measurement of forward neutral pion transverse momentum spectra for $\sqrt{s} = 7$ TeV proton-proton collisions at LHC," 2012.

[21] G. Antchev *et al.*, "Proton-proton elastic scattering at the LHC energy of $\sqrt{s} = 7$ TeV," *Europhys. Lett.*, vol. 95, no. 4, p. 41001, 2011.

[22] The MoEDAL Collaboration, "Technical design report of the moedal experiment," 2009. CERN-LHCC-2009-006. MoEDAL-TDR-001.

[23] J. Schwinger, "A Magnetic Model of Matter," *Science*, vol. 165, pp. 757–761, 1969.

[24] The ATLAS Collaboration, *ATLAS detector and physics performance: Technical Design Report, 1.* Technical Design Report ATLAS, CERN, 1999.

[25] J. Beringer *et al.*, "Particle Data Group," *Phys. Rev. D*, vol. 86, 2012.

[26] W. R. Nelson, T. M. Jenkins, R. C. McCall, and J. K. Cobb, "Electron-induced cascade showers in copper and lead at 1 gev," *Phys. Rev.*, vol. 149, pp. 201–208, 1966.

[27] V. Epshteyn, P. Shatalov, and G. P, "ATLAS-FCAL beam tests Note 6," 2004.

[28] S. van der Meer, "Calibration of the effective beam height in the isr.," no. CERN-ISR-PO-68-31. ISR-PO-68-31, 1968.

[29] The ATLAS Collaboration, "Luminosity Determination in pp Collisions at $\sqrt{s} = 7$ TeV Using the ATLAS Detector at the LHC," *Eur. Phys. J.*, vol. C71, p. 1630, 2011.

[30] The ATLAS Collaboration, "Performance of the ATLAS Inner Detector Track and Vertex Reconstruction in the High Pile-Up LHC Environment," *ATLAS Note*, 2012. ATLAS-CONF-2012-042.

[31] The ATLAS Collaboration, "ATLAS first-level trigger," *ATLAS Note*, 1998. CERN-LHCC-98-14.

[32] T. A. Martin, "Development and online operation of minimum bias triggers in ATLAS," *Journal of Instrumentation*, vol. 5, no. 12, p. C12051, 2010.

[33] United States NIM Committee, *Standard NIM instrumentation system.* U.S. Dept. of Energy, 1990.

[34] C. Eck *et al.*, *LHC computing Grid: Technical Design Report. Version 1.06.* Technical Design Report LCG, CERN, 2005.

[35] The ATLAS Collaboration, *Atlas Computing: technical design report.* Technical Design Report ATLAS, CERN, 2005. ATLAS-TDR-017, CERN-LHCC-2005-022.

[36] R. Brun and F. Rademakers, "Root an object oriented data analysis framework," *Nucl. Instr. A*, vol. 389, no. 12, pp. 81 – 86, 1997.

[37] S. Glashow, "Partial Symmetries of Weak Interactions," *Nucl. Phys.*, vol. 22, pp. 579–588, 1961.

[38] D. J. Gross and F. Wilczek, "Asymptotically free gauge theories. i," *Phys. Rev. D*, vol. 8, pp. 3633–3652, 1973.

[39] M. Froissart, "Asymptotic behavior and subtractions in the Mandelstam representation," *Phys. Rev.*, vol. 123, pp. 1053–1057, 1961.

[40] A. Martin, *Proceedings of the 1962 International Conference on High-Energy Physics at CERN; Geneva, 4-11th July, 1962.* Geneva: CERN: European Org. Nuc. Research., 1962.

[41] P. D. B. Collins, *An Introduction to Regge Theory and High Energy Physics.* Cambridge University Press, 1977.

[42] P. Newman, "A Study of the Dynamics of Diffractive Photoproduction at HERA," *PhD Thesis*, 1996. RAL-TH-96-011.

[43] J. Bjorken, "Hard diffraction," 1994. SLAC-PUB-6463, C93-07-26.

[44] The WA91 Collaboration, "Observation of a narrow scalar meson at 1450 MeV in the reaction $pp \to p_f(\pi^+\pi^-\pi^+\pi^-)p_s$ at 450 GeV/c using the CERN Omega Spectrometer," *Phys. Lett.*, vol. B324, pp. 509–514, 1994.

[45] A. Austregesilo and T. Schlueter, "Partial-Wave Analysis of the Centrally Produced $\pi^+\pi^-$ System in pp Reactions at COMPASS," 2012.

[46] I. Pomerančuk, "Equality Of The Nucleon And Antinucleon Total Interaction Cross Section At High Energies," *Soviet Physics JETP-USSR*, vol. 7, no. 3, pp. 499–501, 1958.

[47] R. G. Newton, "Optical theorem and beyond," *American Journal of Physics*, vol. 44, pp. 639–642, 1976.

[48] G. F. Chew, S. C. Frautschi, and S. Mandelstam, "Regge poles in pi pi scattering," *Phys.Rev.*, vol. 126, pp. 1202–1208, 1961.

[49] P. Landshoff, "The Two Pomerons," 1994.

[50] The Auger Collaboration, "Measurement of the proton-air cross-section at $\sqrt{s} = 57$ TeV with the Pierre Auger Observatory," *Phys. Rev. Lett. 109,*, vol. 062002, 2012.

[51] The TOTEM Collaboration, "First measurement of the total proton-proton cross section at the LHC energy of $\sqrt{s} = 7$ TeV," *Europhys. Lett.*, vol. 96, p. 21002, 2011.

[52] The ATLAS Collaboration, "Measurement of the Inelastic Proton-Proton Cross-Section at $\sqrt{s}$=7 TeV with the ATLAS Detector.," *Nature Commun.*, vol. 2, no. arXiv:1104.0326. CERN-PH-EP-2011-047, p. 463. 19 p, 2011.

[53] The ALICE Collaboration, "Diffraction dissociation in proton-proton collisions at $\sqrt{s} = 0.9$ TeV, 2.76 TeV and 7 TeV with ALICE at the LHC," *J.Phys.*, vol. G38, p. 124044, 2011.

[54] M. Good and W. Walker, "Diffraction disssociation of beam particles," *Phys. Rev.*, vol. 120, pp. 1857–1860, 1960.

[55] The UA5 Collaboration, "Diffraction dissociation at the CERN pulsed collider at cm energies of 900 and 200 GeV.," *Z. Phys. C*, vol. 33, no. BONN-HE-86-19, pp. 175–185. 21 p, 1986.

[56] The ATLAS Collaboration, "ALFA Runs for $\sqrt{s} = 8$ TeV: Optics, Beam Profiles, Elastic and Diffractive Event Patterns and Rates," *ATLAS Note*, 2012. ATL-COM-LUM-2012-012.

[57] O. Kepka, C. Royon, and A. Kupco, "QCD and Diffraction in the ATLAS Experiment at the LHC," *PhD Thesis*, 2009. CERN-THESIS-2010-045.

[58] The CDF Collaboration, "Inclusive double pomeron exchange at the Fermilab Tevatron $p\bar{p}$ collider," *Phys. Rev. Lett.*, vol. 93, p. 141601, 2004.

[59] A. M. Mueller, "$O(2,\ 1)$ Analysis of Single-Particle Spectra at High Energy," *Phys. Rev. D*, vol. 2, pp. 2963–2968, 1970.

[60] A. Kaidalov, "Diffractive Production Mechanisms," *Phys. Rept.*, vol. 50, pp. 157–226, 1979.

[61] O. Kancheli, "Inelastic differential cross sections at high energies and duality," *JETP Lett.*, vol. 11, pp. 267–270, 1970.

[62] The CDF Collaboration, "Double diffraction dissociation at the Fermilab Tevatron collider," *Phys. Rev. Lett.*, vol. 87, p. 141802, 2001.

[63] The ATLAS Collaboration, "ATLAS tunes of PYTHIA 6 and Pythia 8 for MC11," 2011. ATL-PHYS-PUB-2011-009.

[64] T. Sjostrand, S. Mrenna, and P. Z. Skands, "A Brief Introduction to PYTHIA 8.1," *Comput. Phys. Commun.*, vol. 178, pp. 852–867, 2008.

[65] A. Donnachie and P. V. Landshoff, "Elastic Scattering and Diffraction Dissociation," *Nucl. Phys.*, vol. B244, p. 322, 1984.

[66] G. A. Schuler and T. Sjöstrand, "Hadronic diffractive cross sections and the rise of the total cross section," *Phys. Rev. D*, vol. 49, pp. 2257–2267, 1994.

[67] S. Navin, "Diffraction in Pythia," 2010.

[68] The H1 Collaboration, "Measurement and QCD analysis of the diffractive deep-inelastic scattering cross-section at HERA," *Eur. Phys. J.*, vol. C48, pp. 715–748, 2006.

[69] J. Ebke, P. Waller, and T. Brooks, "MCViz." Version used 2011.09.15.

[70] P. Bruni and G. Ingelman, "Diffractive W and Z production at pp colliders and the pomeron parton content," *Phy. Lett. B.*, vol. 311, no. 14, pp. 317 – 323, 1993.

[71] The UA4 Collaboration, "The cross section of diffraction dissociation at the CERN SPS collider," *Phys. Lett. B*, vol. 186, no. 2, pp. 227 – 232, 1987.

[72] E. L. Berger, J. C. Collins, D. E. Soper, and G. F. Sterman, "Diffractive Hard Scattering," *Nucl. Phys.*, vol. B286, p. 704, 1987.

[73] K. H. Streng, "Hard QCD scatterings in diffractive reactions at HERA," CERN-TH-4949.

[74] H. Jung, "Hard diffractive scattering in high-energy e p collisions and the Monte Carlo generator RAPGAP," *Comp. Phys. Commun.*, vol. 86, pp. 147–161, 1995.

[75] S. Navin, "Diffraction in ALICE and trigger efficiencies," *"PhD Thesis"*, 2011.

[76] A. Buckley, J. Butterworth, S. Gieseke, D. Grellscheid, S. Hoche, *et al.*, "General-purpose event generators for LHC physics," *Phys. Rept.*, vol. 504, pp. 145–233, 2011.

[77] Z. Koba, H. B. Nielsen, and P. Olesen, "Scaling of multiplicity distributions in high-energy hadron collisions," *Nucl. Phys.*, vol. B40, pp. 317–334, 1972.

[78] R. Engel, "Photoproduction within the two component dual parton model. 1. Amplitudes and cross-sections," *Z. Phys.*, vol. C66, p. 203, 1995.

[79] R. Engel, "PHOJET manual (program version 1.05c)," 1996.

[80] A. Capella *et al.*, "Jets in Small p_T Hadronic Collisions, Universality of Quark Fragmentation, and Rising Rapidity Plateaus," *Phys. Lett.*, vol. B81, p. 68, 1979.

[81] A. Capella, U. Sukhatme, C.-I. Tan, and J. Tran Thanh Van, "Dual parton model," *Phys. Rep.*, vol. 236, pp. 225–329, 1994.

[82] V. A. Abramovsky, V. N. Gribov, and O. V. Kancheli, "Character of inclusive spectra and fluctuations produced in inelastic processes by multi - pomeron exchange," *Yad. Fiz.*, vol. 18, pp. 595–616, 1973.

[83] A. Capella, A. Kaidalov, C. Merino, D. Pertermann, and J. Tran Thanh Van, "Hard diffraction at HERA and the gluonic content of the pomeron," *Phys. Rev.*, vol. D53, pp. 2309–2316, 1996.

[84] A. Capella, A. Kaidalov, C. Merino, and J. Tran Thanh Van, "Diffractive dissociation in deep inelastic scattering at HERA," *Phys. Lett.*, vol. B343, pp. 403–409, 1995.

[85] H.-U. Bengtsson and T. Sjostrand, "The Lund Monte Carlo for Hadronic Processes: Pythia Version 4.8," *Comput. Phys. Commun.*, vol. 46, p. 43, 1987.

[86] A. Donnachie and P. Landshoff, "Does the hard pomeron obey Regge factorization?," *Phys. Lett.*, vol. B595, pp. 393–399, 2004.

[87] S. Gieseke, D. Grellscheid, K. Hamilton, A. Papaefstathiou, S. Platzer, *et al.*, "Herwig++ 2.5 Release Note," 2011.

[88] The ATLAS Collaboration, "Studies of Diffractive Enhanced Minimum Bias Events in ATLAS," *ATLAS Note*, 2010. ATLAS-CONF-2010-048.

[89] The CDF Collaboration, "Measurement of $\bar{p}p$ single diffraction dissociation at $\sqrt{s} = 546$ GeV and 1800 GeV," *Phys. Rev.*, vol. D50, p. 5535, 1994.

[90] The ATLAS Collaboration, "Charged particle multiplicities in pp interactions at $\sqrt{s} = 0.9$ and 7 TeV in a diffractive limited phase space measured with the ATLAS detector at the LHC and a new Pythia6 tune," ATLAS-CONF-2010-031.

[91] The ATLAS Collaboration, "Performance of the Minimum Bias Trigger in pp Collisions at $\sqrt{s} = 7$ TeV," *ATLAS Note*, 2010. ATLAS-CONF-2010-068.

[92] W. Bell, E. Feng, B. Heinemann, E. Nurse, P. Steinberg, and L. Tompkins, "Offline Performance of the ATLAS Minimum Bias Trigger Scintillator Detector at $\sqrt{s} = 7$ TeV," *ATLAS Internal Note*, vol. ATL-COM-LUM-2010-033, 2010.

[93] R. E. Kalman, "A New Approach to Linear Filtering and Prediction Problems," *Transactions of the ASME–Journal of Basic Engineering*, vol. 82, no. Series D, pp. 35–45, 1960.

[94] T. Cornelissen, M. Elsing, I. Gavrilenko, W. Liebig, E. Moyse, and A. Salzburger, "The new ATLAS track reconstruction (NEWT)," *Journal of Physics: Conference Series*, vol. 119, no. 3, p. 032014, 2008.

[95] The ATLAS Collaboration, "Calorimeter Clustering Algorithms: Description and Performance," *ATLAS Note*, 2008. ATL-LARG-PUB-2008-002.

[96] F. Colecchia, J. Monk, E. Nurse, R. Prabhu, and P. Wijeratne, "Validation of the calorimeter energy response with $\pi^0 \to \gamma\gamma$ candidates," *ATLAS Note*, 2011. ATL-COM-CAL-2011-003.

[97] "The Durham HepData Reaction Database," `http://durpdg.dur.ac.uk/`.

[98] G. D'Agostini, "A Multidimensional unfolding method based on Bayes' theorem," *Nucl. Instr. Meth.*, vol. A362, p. 487, 1995.

[99] T. Adye, "Unfolding algorithms and tests using RooUnfold," *ArXiv e-prints*, 2011. 1105.1160.

[100] The ATLAS Collaboration, "Response of the ATLAS Calorimeters to Single Isolated Hadrons Produced in Proton-proton Collisions at $\sqrt{s} = 900$ GeV," *ATLAS Note*. ATLAS-CONF-2010-017.

[101] The ATLAS Collaboration, "ATLAS Calorimeter Response to Single Isolated Hadrons and Estimation of the Calorimeter Jet Energy Scale Uncertainty," *ATLAS Note*. ATLAS-CONF-2010-052.

[102] The ATLAS Collaboration, "ATLAS Calorimeter Response to Single Isolated Hadrons and Estimation of the Calorimeter Jet Scale Uncertainty," *ATLAS Note*. ATLAS-CONF-2011-028.

[103] The ATLAS Collaboration, "Measurements of the pseudorapidity dependence of the total transverse energy in proton-proton collisions at $\sqrt{s} = 7$ TeV with ATLAS," 2012.

[104] A. Kiryunic and P. Strizenec, "Validation of the Local Hadronic Calibration Scheme of ATLAS with Combined Beam Test Data in the Endcap and Forward Regions," *Proceedings of the 13th ICATPP Conference, Como, Italy*, 2011. ATL-LARG-PROC-2011-005.

[105] V. Khoze, F. Krauss, A. Martin, M. Ryskin, and K. Zapp, "Diffraction and correlations at the LHC: definitions and observables," *Eur. Phys. J.* , vol. C69, p. 85, 2010.

[106] F. James, "MINUIT – Function Minimization and Error Analysis – Reference Manual," *CERN Program Library Long Writeup*, vol. D506, 1994.

[107] M. Ryskin, A. Martin, and V. Khoze, "High-energy strong interactions: from 'hard' to 'soft'," *Eur. Phys. J.*, vol. C71, p. 1617, 2011.

[108] A. Martin, H. Hoeth, V. Khoze, F. Krauss, M. Ryskin, *et al.*, "Diffractive Physics," 2012.

[109] The UA4 Collaboration, "The cross-section of diffraction dissociation at the CERN SPS Collider," *Phys. Lett.*, vol. B186, p. 227, 1987.

[110] The ATLAS Collaboration, "Forward-backward correlations and charged-particle azimuthal distributions in *pp* interactions using the ATLAS detector," *JHEP*, vol. 1207, p. 019, 2012.

[111] The ATLAS Collaboration, "Measurement of the azimuthal ordering of charged hadrons with the ATLAS detector," 2012.

[112] A. B. Poy, H. Boterenbrood, H. J. Burckhart, J. Cook, V. Filimonov, S. Franz, O. Gutzwiller, B. Hallgren, V. Khomutnikov, S. Schlenker, and F. Varela, "The detector control system of the ATLAS experiment," *Journal of Instrumentation*, vol. 3, no. 05, p. P05006, 2008.

[113] O. Beltramello *et al.*, "The Detector Safety System of the ATLAS experiment," *Journal of Instrumentation*, vol. 4, no. 09, p. P09012, 2009.

[114] A. Buckley *et al.*, "Rivet user manual," 2010.

APPENDIX A

DETECTOR CONTROL SYSTEMS

The DCS is a distributed command and control network, used to monitor and interact with the infrastructure of ATLAS [112]. The remit of the system is to provide a standardised interface to the detector hardware along with monitoring capacity for operational quantities such as voltages and active cooling systems. The DCS is not responsible for machine or human safety; faults serious enough to jeopardise the safety of the detector or human life are the responsibility of the Detector Safety System (DSS) [113]. The DSS will attempt to transition the detector into a safe state upon fault and may instigate an evacuation. Information is shared between DCS and the DSS but the former is prohibited from interfering with the actions of the DSS.

A.1 LAYOUT OF THE DCS

The back-end of the ATLAS DCS has a top-down structure split into three logical layers. At the highest level are the Global Control Station (GCS) systems, these sit above the Subdetector Control Station (SCS) systems and in turn sit above many Local Control Stations (LCSs), forming an inverted tree hierarchy. As each node has exactly one parent, it is possible to partition the detector, assigning an individual user control of part of the tree. Only vertical communication is supported within the hierarchy; commands issued responsively by the system or manually by users propagate vertically down from their point of issue and state-information about the tree nodes propagates upwards.

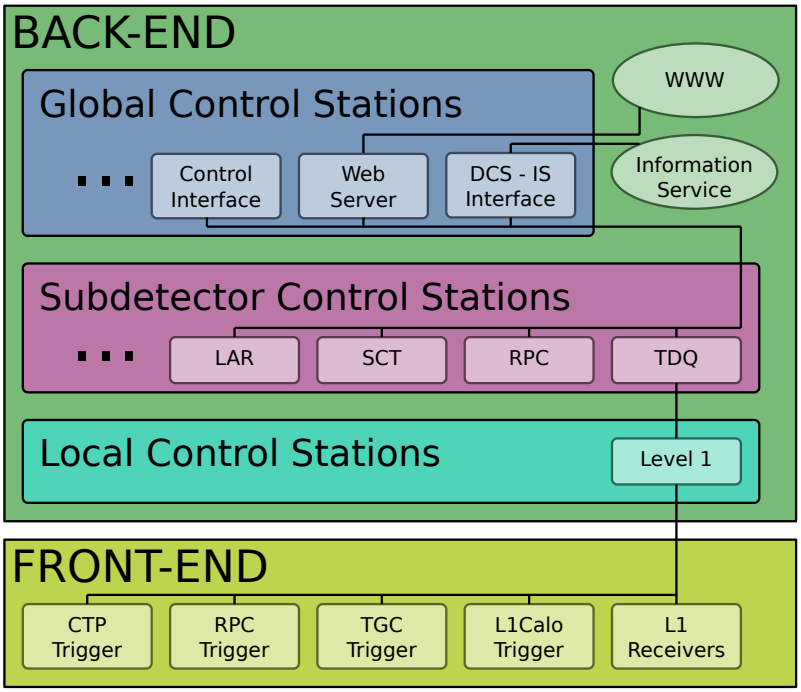

Figure A.1: Overview of the back-end and front-end of the ATLAS DCS, following the TDAQ SCS tree. TDAQ only possesses one LCS but other, larger sub detectors possess significantly more.

At the top of the tree is the ATLAS node. This node is typically owned by the GCS which operates on the DCS PC in the ATLAS control room. During normal operation, this desk will take control of the whole detector. Additional systems at the GCS level provide data sharing interfaces with other on-line systems and operate a read-only web interface.

Each SCS encompasses the operation of a whole sub detector. They form the lowest point from which the detector may be partitioned. Each SCS generally provides a summary overview of the state of its respective sub detector.

Finally at the lowest level, the LCS PCs provide the interface with the detector hardware. Each may host up to 12 Controller Area Network (CAN) bus interfaces, a CAN being a standardised serial bus allowing for communication between micro-controllers and the host PC. Each LCS holds in memory the state information for its responsible hardware and interprets any commands which propagate down to it, translating them appropriately and broadcasting them over the CAN.

An overview of the DCS is presented in Figure A.1

A.2 THE ATLAS FINITE STATE MACHINE

The back end control structure of the ATLAS DCS operates as a Finite State Machine (FSM). Each node in the inverted tree hierarchy is either a Device Unit (DU), a Logical Unit (LU) or a Control Unit (CU). At the leaf-node level, each monitored piece of hardware is encapsulated under a DU, which is responsible for monitoring the physical hardware and deriving an appropriate status. LUs are abstracted collections of DUs and other LUs/CUs, which represent a physical system. For example, an LU may represent a crate of hardware, containing one DU for each module installed in the crate. The status of an LU is derived from the status of its branches/leaves. A CU is operationally indistinct from an LU. However only CUs may be partitioned.

Each node in the FSM tree possesses two independent characteristics, the *state* and the *status* of the node. This approach, unique to ATLAS, separates the condition of the hardware from its operational status. The node *state* holds information about the current physical state of the hardware. Simple states such as `OFF` and `ON` are defined. Some hardware such as High Voltage (HV) power supplies use additional transitory states such as `RAMPING` and higher-level LU nodes use states such as `SHUTDOWN` to indicate that all of the LUs children nodes are off.

The *status* of a node represents the well-being of the hardware. A hardware module running fully within acceptable parameters will have the status `OK`. Should a parameter exceed typically a 10% margin from nominal then the state will transition to `WARNING` denoting that there may be an underlying problem and the hardware should receive attention. Typically a 15% deviation will result in an `ERROR` state which could affect the operation of the detector or a `FATAL` state which has serious operational impact and should be followed up immediately.

In keeping with the top-down arrangement of the system, *state* and *status* information propagates upwards through the tree. Upon change of state/status, the FSM is programmed with rule sets to perform automated action. This is generally the automated shutdown of any hardware which propagates an `ERROR` status.

A.3 PVSS

ATLAS DCS is implemented in ProzessVisualisierungs und Steuerungs-System (PVSS), provided by ETM. PVSS was chosen as the most suitable Supervisory Control And Data Acquisition (SCADA) package by the CERN Joint ContrOls Project (JCOP) and has subsequently been deployed for all LHC experiments. Binaries are available for Windows and Linux. Many machines on the DCS network run Scientific Linux. However some proprietary CAN servers only operate under Windows so the TDAQ LCS which interfaces with the hardware continues to run Windows XP. PVSS maintains an internal database of *data points*. A data point is akin to the concept of a *class*

template in object-oriented programming. Multiple instances of a datapoint are analogous to multiple objects of a given type. A datapoint may contain variables of many types such as booleans, floating point numbers etc. and these variables may be mapped to read their values from hardware over the CAN. They may also perform calculations and interface with offline archives and alarm systems.

Manipulation of data points is handled via a scripting language while PVSS manages additional functionality such as the historic archiving of data points to a database and the configuration of alarms which warn operators about data points with non ideal status. Many standardised tools and libraries have been developed in PVSS by JCOP for common use among the LHC experiments. These have been further developed by central ATLAS DCS.

A.4 TDAQ DETECTOR CONTROL SYSTEMS

TDAQ DCS monitors the hardware installed in the service cavern, which is responsible for forming the L1 trigger decision. The majority of the hardware is monitored at the level of the Wiener VME crates which house the electronics. For initial running in 2009, this comprised the trigger hardware for the TGC, CTP and the L1 receivers for L1Calo. No automated action is taken by the FSM on Wiener crates as they contain internal logic which defines their response to errors. They do still however propagate their state and status. The crates are connected to the FSM via a custom JCOP Wiener component. The L1Calo branch differs in that it uses a bespoke system of much greater granularity to monitor each hardware module within the Wiener crates, recording the voltage drops, current draws and temperatures of individual components.

Since 2008, TDAQ DCS has been maintained and progressively upgraded to include new hardware and monitoring. Some examples of how TDAQ DCS has evolved as part of the service work described in this thesis are briefly documented.

The 16 crates which comprise the RPC trigger hardware had their CAN connection migrated from their initial home under the RPC SCS to TDAQ, this brought them in line with the other L1 hardware and they were integrated into the TDAQ FSM.

Connectivity issues were identified in 2011, where communications were on occasions lost over one of the CAN buses while the bus appeared to remain connected. Active monitoring was introduced at the server level and individual bus level. The CAN server is monitored via the time-stamp of the last updated datapoint. Each of the five individual Wiener CAN buses are also monitored via a statistical datapoint which computes the difference in the up-time of one crate on each bus over a timespan of five minutes. Should this difference fall to zero, the up-time value no longer increases linearly with time, which is highly symptomatic of a communication failure. An alarm is raised to the DCS shifter if any communications fail. The information is

displayed graphically to the operator as in Figure A.2(a).

In addition to their crate level monitoring, CTP had access to other module level operational monitoring parameters interfaced with the ATLAS information service. This information is included in TDAQ DCS for display, archiving and alarm purposes. The data are interfaced using DCS-DAQ-Communication (DDC) and incorporated into the CTP FSM graphical interface as displayed in Figure A.2(b).

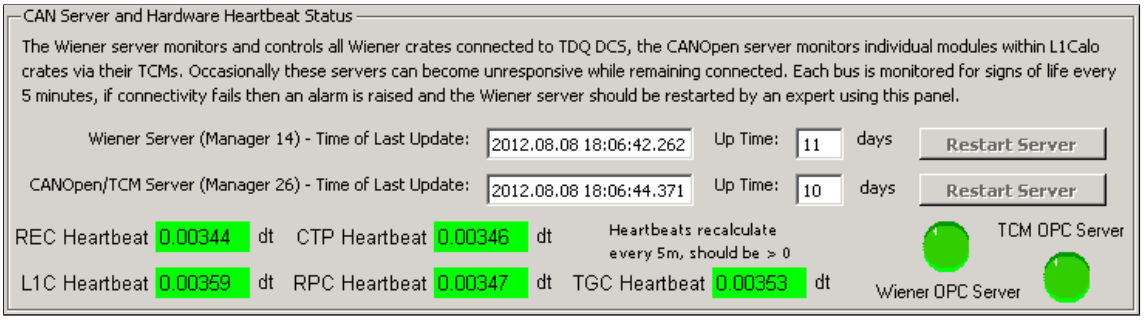

(a)

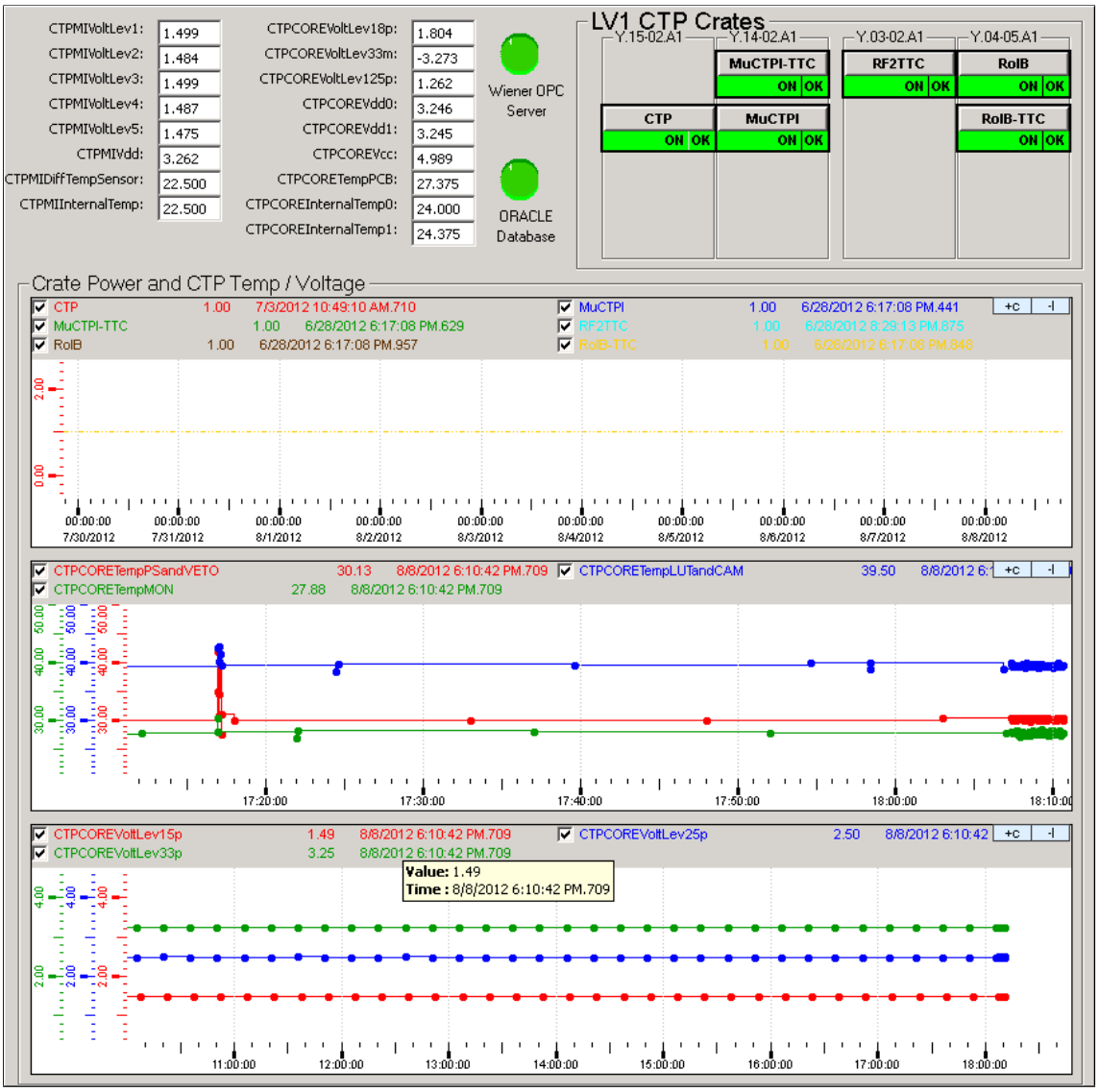

(b)

Figure A.2: Active monitoring of CAN server communications and hardware on individual CAN buses (a). Additional information imported into DCS via DDC for CTP (b).

APPENDIX B

ANALYSIS PAPER

Here follows the analysis presented in this thesis as published in
Eur. Phys. J. C 72 (2012) 1926

Eur.Phys.J.C
DOI10.1140/epjc/s10052-012-1926-0

CERN-PH-EP-2011-220 Eur.Phys.J.C(2012)72:1926

Rapidity Gap Cross Sections measured with the ATLAS Detector in *pp* Collisions at $\sqrt{s} = 7$ TeV

The ATLAS Collaboration

January 13, 2012

Abstract Pseudorapidity gap distributions in proton-proton collisions at $\sqrt{s} = 7$ TeV are studied using a minimum bias data sample with an integrated luminosity of 7.1 μb^{-1}. Cross sections are measured differentially in terms of $\Delta\eta^F$, the larger of the pseudorapidity regions extending to the limits of the ATLAS sensitivity, at $\eta = \pm 4.9$, in which no final state particles are produced above a transverse momentum threshold $p_{\mathrm{T}}^{\mathrm{cut}}$. The measurements span the region $0 < \Delta\eta^F < 8$ for $200 < p_{\mathrm{T}}^{\mathrm{cut}} < 800$ MeV. At small $\Delta\eta^F$, the data test the reliability of hadronisation models in describing rapidity and transverse momentum fluctuations in final state particle production. The measurements at larger gap sizes are dominated by contributions from the single diffractive dissociation process ($pp \to Xp$), enhanced by double dissociation ($pp \to XY$) where the invariant mass of the lighter of the two dissociation systems satisfies $M_Y \lesssim 7$ GeV. The resulting cross section is $\mathrm{d}\sigma/\mathrm{d}\Delta\eta^F \approx 1$ mb for $\Delta\eta^F \gtrsim 3$. The large rapidity gap data are used to constrain the value of the Pomeron intercept appropriate to triple Regge models of soft diffraction. The cross section integrated over all gap sizes is compared with other LHC inelastic cross section measurements.

PACS 12.40.Nn · 12.38.Lg

1 Introduction

When two protons collide inelastically at a centre-of-mass energy of 7 TeV in the Large Hadron Collider (LHC), typically around six charged particles are produced with transverse momentum[1] $p_{\mathrm{T}} > 100$ MeV per unit of pseudorapidity in the central region [1–3]. On average, the rapidity difference between neighbouring particles is therefore around 0.15 units of rapidity, with larger gaps occurring due to statistical fluctuations in the hadronisation process. Such random processes lead to an exponential suppression with gap size [4], but very large gaps are produced where a t-channel colour singlet exchange takes place. This may be due to an electroweak exchange, but occurs much more frequently through the exchange of strongly interacting states. At high energies such processes are termed 'diffractive' and are associated with 'Pomeron' exchange [5, 6].

The total cross section in hadronic scattering experiments is commonly decomposed into four main components: elastic ($pp \to pp$ in the LHC context), single-diffractive dissociation (SD, $pp \to Xp$ or $pp \to pX$, Figure 1a), double-diffractive dissociation (DD, $pp \to XY$, Figure 1b) and non-diffractive (ND) contributions. The more complex central diffractive configuration (CD, $pp \to pXp$, Figure 1c), in which final state particles are produced in the central region with intact protons on both sides, is suppressed relative to the SD process by a factor of around 10 at high energies [7]. Together, the diffractive channels contribute approximately 25–30% of the total inelastic cross section at LHC energies [8]. Following measurements at the LHC of the elastic [9], total [10] and total inelastic [8, 10] cross sections, this article contains the first detailed exploration of diffractive dissociation processes.

[1] In the ATLAS coordinate system, the z-axis points in the direction of the anti-clockwise beam viewed from above. Polar angles θ and transverse momenta p_{T} are measured with respect to this axis. The pseudorapidity $\eta = -\ln\tan(\theta/2)$ is a good approximation to the rapidity of a particle whose mass is negligible compared with its energy and is used here, relative to the nominal $z = 0$ point at the centre of the apparatus, to describe regions of the detector.

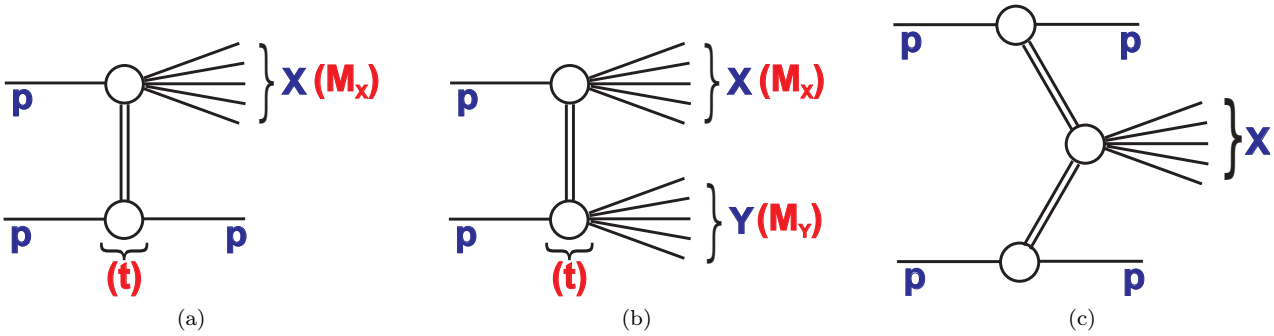

Fig. 1: Schematic illustrations of the single-diffractive dissociation (a), double-diffractive dissociation (b) and central diffractive (c) processes and the kinematic variables used to describe them. By convention, the mass M_Y is always smaller than M_X in the double dissociation case and $M_Y = M_p$ in the single dissociation case, M_p being the proton mass.

Understanding diffractive processes is important in its own right, as they are the dominant contribution to high energy quasi-elastic scattering between hadrons and, via ideas derived from the optical theorem [11], are also related to the total cross section. They are often interpreted at the parton level in terms of the exchange of pairs of gluons [12,13] and are thus sensitive to possible parton saturation effects in the low Bjorken-x regime of proton structure [14–16]. Diffractive cross sections also have relevance to cosmic ray physics [17] and may be related to the string theory of gravity [18]. At the LHC, diffractive dissociation must be well understood for a good description of the additional inelastic proton-proton interactions (pile-up) which accompany most events. It also produces a significant uncertainty in approaches to luminosity monitoring which rely on measurements of the total, or total inelastic, cross section [19].

Diffractive dissociation cross sections have been measured previously over a wide range of centre-of-mass energies. Early measurements are reviewed in [20–24]. SD measurements have been made in $p\bar{p}$ scattering at the SPS [25, 26] and the Tevatron [27, 28], and also in photoproduction [29, 30] and deep inelastic scattering [31–33] at HERA. Limited high energy DD [26, 29, 34] and CD [7,35,36] data are also available. In most cases, the momentum transfer is too small to permit an interpretation in terms of partonic degrees of freedom [37]. Instead, phenomenological models such as those based on Regge theory have been developed [22,38,39], which underlie the Monte Carlo generators typically used to predict the properties of soft inelastic collisions [40–42]. Mixed approaches have also been developed which employ perturbative QCD where possible [43, 44]. Large theoretical uncertainties remain in the detailed dynamics expected at the LHC.

Direct measurements of the masses M_X and M_Y of the dissociated systems are difficult at ATLAS, since many of the final state particles are produced beyond the acceptance of the detector. However, the dissociation masses are closely correlated with the size of the rapidity region in which particle production is completely suppressed due to the net colour-singlet Pomeron exchange. This correlation is exploited in this paper, with cross sections reported as a function of the size of a pseudorapidity region which is devoid of final state particle production. These unpopulated pseudorapidity regions are referred to in the following as 'rapidity gaps', or simply 'gaps'.

To maximise the pseudorapidity coverage and sensitivity to charged and neutral particle production, rapidity gaps are identified using both the ATLAS calorimeters and tracking detectors. The specific observable studied is $\Delta\eta^F$, the larger of the two 'forward' pseudorapidity regions extending to at least $\eta = \pm 4.9$ in which no particles are produced with $p_{\mathrm{T}} > p_{\mathrm{T}}^{\mathrm{cut}}$, where $p_{\mathrm{T}}^{\mathrm{cut}}$ is varied between 200 MeV and 800 MeV. ND contributions appear at small gap sizes, with $p_{\mathrm{T}}^{\mathrm{cut}}$ and $\Delta\eta^F$ dependences which are sensitive to fluctuations in the hadronisation process. For small $p_{\mathrm{T}}^{\mathrm{cut}}$ choices, the large gap size region is dominated by SD events and DD events in which one of the dissociation masses is small.

2 Experimental Method

2.1 The ATLAS detector

The ATLAS detector is described in detail elsewhere [45]. The beam-line is surrounded by the 'inner detector' tracking system, which covers the pseudorapidity range $|\eta| < 2.5$. This detector consists of silicon pixel,

silicon strip and straw tube detectors and is enclosed within a uniform 2 T solenoidal magnetic field.

The calorimeters lie outside the tracking system. A highly segmented electromagnetic (EM) liquid argon sampling calorimeter covers the range $|\eta| < 3.2$. The EM calorimeter also includes a pre-sampler covering $|\eta| < 1.8$. The hadronic end-cap (HEC, $1.5 < |\eta| < 3.2$) and forward (FCal, $3.1 < |\eta| < 4.9$) calorimeters also use liquid argon technology, with granularity decreasing with increasing $|\eta|$. Hadronic energy in the central region ($|\eta| < 1.7$) is reconstructed in a steel/scintillator-tile calorimeter.

Minimum bias trigger scintillator (MBTS) detectors are mounted in front of the end-cap calorimeters on both sides of the interaction point and cover the pseudorapidity range $2.1 < |\eta| < 3.8$. The MBTS is divided into inner and outer rings, both of which have eight-fold segmentation. The MBTS is used to trigger the events analysed here.

In 2010, the luminosity was measured using a Čerenkov light detector which is located 17 m from the interaction point. The luminosity calibration is determined through van der Meer beam scans [19, 46].

2.2 Event selection and backgrounds

The data used in this analysis were collected during the first LHC run at $\sqrt{s} = 7$ TeV in March 2010, when the LHC was filled with two bunches per beam, one pair colliding at the ATLAS interaction point. The peak instantaneous luminosity was 1.1×10^{27} cm^{-2} s^{-1}. Events were collected from colliding proton bunch crossings in which the MBTS trigger recorded one or more inner or outer segments above threshold on at least one side of ATLAS. After reconstruction, events are required to have hits in at least two of the MBTS segments above a threshold of 0.15 pC. This threshold cut suppresses contributions from noise, which are well modelled by a Gaussian with 0.02 pC width. No further event selection requirements are applied.

The data sample corresponds to an integrated luminosity of 7.1 ± 0.2 μb^{-1} and the number of recorded events is 422776. The mean number of interactions per bunch crossing is below 0.005, which is consistent with the approximately 400 events which have multiple reconstructed vertices. Pile-up contamination is thus negligible.

The data sample contains a contribution from beam-induced background, mainly due to scattering of beam protons from residual gas particles inside the detector region. This contamination is estimated using events collected in unpaired bunches and is subtracted statistically in each measurement interval. Averaged over the full measurement region, it amounts to 0.2% of the sample. More complex backgrounds in which beam-induced background is overlaid on a physics event are negligible.

2.3 Reconstruction of rapidity gaps

The analysis of final state activity in the central region ($|\eta| < 2.5$) is based on combined information from inner detector tracks and calorimeter modules. In the region $2.5 < |\eta| < 4.9$, beyond the acceptance of the inner detector, calorimeter information alone is used. The track selection is as detailed in [1]. Energy deposits from final state particles in the calorimeters are identified using a topological clustering algorithm [47, 48], with a further requirement to improve the control over noise contributions, as described below.

The identification of rapidity gap signatures relies crucially on the suppression of calorimeter noise contributions. The root-mean-squared cell energies due to noise vary from around 20 MeV in the most central region to around 200 MeV for the most forward region [49]. The shapes of the cell noise distributions in each calorimeter are well described by Gaussian distributions of standard deviation σ_{noise}, with the exception of the tile calorimeter, which has extended tails. The default clustering algorithm [48] is seeded by cells for which the significance of the measured energy, E, is $S = E/\sigma_{\text{noise}} > 4$. However, with this threshold there are on average six clusters reconstructed per empty event due to fluctuations in the noise distributions. To suppress noise contributions to acceptable levels for gap finding, clusters of calorimeter energy deposits are thus considered only if they contain at least one cell outside the tile calorimeter with an energy significance above an η-dependent threshold, S_{th}. This threshold is determined separately in pseudorapidity slices of size 0.1 such that the probability of finding at least one noisy cell in each η-slice has a common value, 1.4×10^{-4}. This choice optimises the resolution of the reconstructed gap sizes with respect to the gaps in the generated final state particle distributions according to MC studies. Since the number of cells in an η-slice varies from about 4000 in the central region to 10 in the outer part of the FCal, the cell thresholds vary between $S_{\text{th}} = 5.8$ in the central region and $S_{\text{th}} = 4.8$ at the highest $|\eta|$ values in the FCal.

The level of understanding of the calorimeter noise is illustrated in Figure 2, which shows the distributions of the cell significance S for each of the liquid argon modules. MBTS-triggered data from colliding bunch crossings are compared with a Monte Carlo simulation

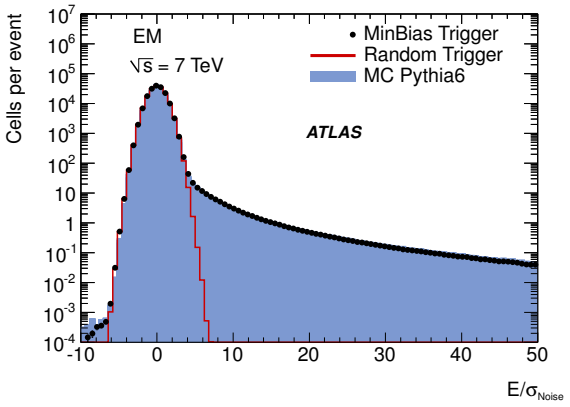

(a)

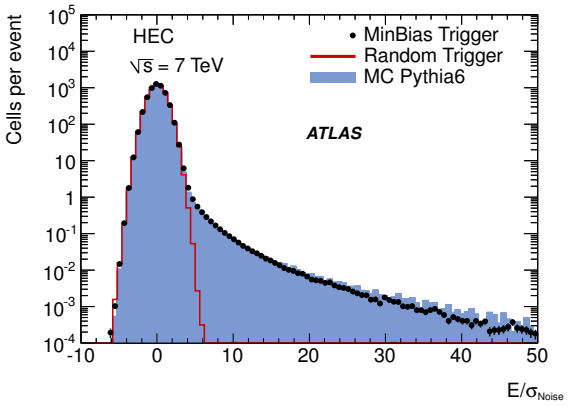

(b)

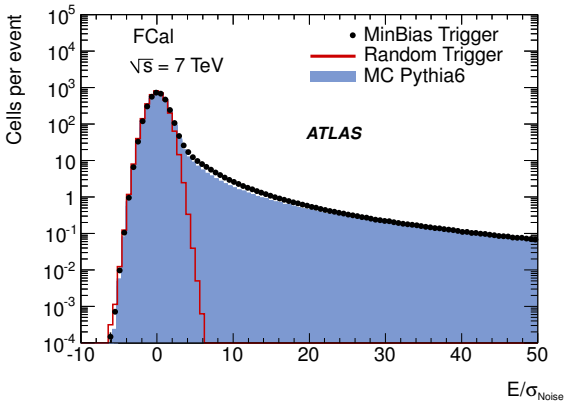

(c)

Fig. 2: Cell energy significance, $S = E/\sigma_{\text{noise}}$, distributions for the EM (a), HEC (b) and FCal (c) calorimeters. Each cell used in the analysis is included for every event, with the normalisation set to a single event. MBTS-triggered minimum bias data (points) are compared with events randomly triggered on empty bunch crossings (histograms) and with a Monte Carlo simulation (shaded areas).

and with events which are required to exhibit no activity in the non-calorimeter components of the detector, triggered randomly on empty bunch crossings. The signal from pp collisions is clearly visible in the long positive tails, which are well described by the simulation. The data from the empty bunch crossings show the shape of the noise distribution with no influence from physics signals. The empty bunch crossing noise distributions are symmetric around zero and their negative sides closely match the negative parts of the MBTS-triggered data distributions. The noise distribution is well described over seven orders of magnitude by the MC simulation, the small residual differences at positive significances being attributable to deficiencies in the modelling of pp collision processes.

The measured energies of calorimeter clusters which pass the noise requirements are discriminated using a given value of $p_{\text{T}}^{\text{cut}}$, neglecting particle masses. The calorimeter energy scale for electromagnetic showers is determined from electron test-beam studies and $Z \to e^+e^-$ data [50], confirmed at the relatively small energies relevant to the gap finding algorithm through a dedicated study of $\pi^0 \to \gamma\gamma$ decays. The calorimeter response to hadronic showers is substantially lower than that to electromagnetic showers. In the central region, the scale of the hadronic energy measurements is determined relative to the electromagnetic scale through comparisons between the calorimeter and inner detector measurements of single isolated hadrons [51–53]. Beyond the acceptance region of the tracking detectors, the difference between the electromagnetic and the hadronic response is determined from test-beam results [54–56]. For the purposes of discriminating against thresholds in the gap finding algorithm, all cluster energy measurements are taken at this hadronic scale. An interval in η is deemed to contain final state particles if at least one cluster in that interval passes the noise suppression requirements and has a transverse momentum above $p_{\text{T}}^{\text{cut}}$, or if there is at least one good inner detector track with transverse momentum above $p_{\text{T}}^{\text{cut}}$.

2.4 Definition of forward rapidity gap observable

The reconstructed forward gap size $\Delta\eta^F$ is defined by the larger of the two empty pseudorapidity regions extending between the edges of the detector acceptance at $\eta = 4.9$ or $\eta = -4.9$ and the nearest track or calorimeter cluster passing the selection requirements at smaller $|\eta|$. No requirements are placed on particle production at $|\eta| > 4.9$ and no attempt is made to identify gaps in the central region of the detector. The rapidity gap size relative to $\eta = \pm 4.9$ lies in the range $0 < \Delta\eta^F < 8$, such that for example $\Delta\eta^F = 8$ implies that there is

no reconstructed particle with $p_{\mathrm{T}} > p_{\mathrm{T}}^{\mathrm{cut}}$ in one of the regions $-4.9 < \eta < 3.1$ or $-3.1 < \eta < 4.9$. The upper limit on the gap size is constrained via the requirement of a high trigger efficiency by the acceptance of the MBTS detector.

The measurement is performed in $\Delta\eta^F$ intervals of 0.2, except at the smallest values $\Delta\eta^F < 2.0$, where the differential cross section varies fastest with $\Delta\eta^F$ and the gap end-point determination is most strongly dependent on the relatively coarse cell granularity of the FCal. The bin sizes in this region are increased to 0.4 pseudorapidity units, commensurate with the resolution.

The default value of the transverse momentum threshold is chosen to be $p_{\mathrm{T}}^{\mathrm{cut}} = 200$ MeV. This value lies within the acceptance of the track reconstruction for the inner detector and ensures that the efficiency of the calorimeter cluster selection is greater than 50% throughout the η region which lies beyond the tracking acceptance.

As described in Section 3.4, the data are fully corrected for experimental effects using the Monte Carlo simulations introduced in Section 3.2. The rapidity gap observable defining the measured differential cross sections are thus specified in terms of stable (proper lifetime > 10 ps) final state particles (hereafter referred to as the 'hadron level'), with transverse momentum larger than the threshold, $p_{\mathrm{T}}^{\mathrm{cut}}$, used in the gap reconstruction algorithm.

3 Theoretical Models and Simulations

3.1 Kinematic Variables and Theory

As illustrated in Figure 1a and b, diffractive dissociation kinematics can be described in terms of the invariant masses M_X and M_Y of the dissociation systems X and Y, respectively (with $M_Y = M_p$ in the SD case), and the squared four-momentum transfer t. In the following, the convention $M_Y < M_X$ is adopted. The cross section is vastly dominated by small values of $|t| \lesssim 1$ GeV^2, such that the intact proton in SD events is scattered through only a small angle, gaining transverse momentum $p_{\mathrm{T}} \simeq \sqrt{|t|}$. Further commonly used kinematic variables are defined as

$$\xi_X = \frac{M_X^2}{s} , \qquad \xi_Y = \frac{M_Y^2}{s} , \tag{1}$$

where s is the square of the centre-of-mass energy.

Diffractive dissociation cross sections can be modelled using Regge phenomenology [38,39,57], with Pomeron exchange being the dominant process at small ξ_X values. For the SD case, the amplitude is factorised into a Pomeron flux associated with the proton which remains intact, and a total probability for the interaction of the Pomeron with the dissociating proton. The latter can be described in terms of a further Pomeron exchange using Muller's generalisation of the optical theorem [11], which is applicable for $s \gg M_X^2 \gg m_p^2$. The SD cross section can then be expressed as a triple Pomeron ($\mathbb{P}\mathbb{P}\mathbb{P}$) amplitude,

$$\frac{\mathrm{d}\sigma}{\mathrm{d}t\,\mathrm{d}M_X^2} = G_{3\mathbb{P}}(0) s^{2\alpha_{\mathbb{P}}(t)-2} \left(M_X^2\right)^{\alpha_{\mathbb{P}}(0)-2\alpha_{\mathbb{P}}(t)} f(t) \tag{2}$$

where $G_{3\mathbb{P}}(0)$ is a product of couplings and $\alpha_{\mathbb{P}}(t) = \alpha_{\mathbb{P}}(0) + \alpha'_{\mathbb{P}} t$ is the Pomeron trajectory. The term $f(t)$ is usually taken to be exponential such that $\mathrm{d}\sigma/\mathrm{d}t \propto e^{B(s,M_X^2)\,t}$ at fixed s and M_X, B being the slope parameter. With $\alpha_{\mathbb{P}}(0)$ close to unity and $|t|$ small, equation (2) leads to an approximately constant $\mathrm{d}\sigma/\mathrm{d}\ln\xi_X$ at fixed s. The DD cross section follows a similar dependence at fixed ξ_Y. The deviations from this behaviour are sensitive to the intercept $\alpha_{\mathbb{P}}(0)$ of the Pomeron trajectory [58,59] and to absorptive corrections associated with unitarity constraints [43,44].

The rapidity gap size and its location are closely correlated with the variables ξ_X and ξ_Y. For the SD process, the size $\Delta\eta$ of the rapidity gap between the final state proton and the X system satisfies

$$\Delta\eta \simeq -\ln\xi_X \ . \tag{3}$$

The $\Delta\eta^F$ observable studied here differs from $\Delta\eta$ in that $\Delta\eta^F$ takes no account of particle production at $|\eta| > 4.9$. For the SD process, where the intact proton has $\eta \simeq \pm\frac{1}{2}\ln(s/m_p^2) \simeq \pm 8.9$, the gap variables are related by $\Delta\eta^F \simeq \Delta\eta - 4$. Equations (2) and (3) thus lead to approximately constant predicted cross sections $\mathrm{d}\sigma/\mathrm{d}\Delta\eta^F$ for SD and low M_Y DD events. With the high centre-of-mass energy of the LHC and the extensive acceptance of the ATLAS detector, events with ξ_X between around 10^{-6} and 10^{-2} can be selected on the basis of their rapidity gap signatures, corresponding approximately to $7 < M_X < 700$ GeV.

Previous proton-proton scattering [25] and photoproduction [29,30] experiments have observed enhancements relative to triple-Pomeron behaviour at the smallest M_X values in the triple Regge region. This effect has been interpreted in terms of a further triple Regge term ($\mathbb{P}\mathbb{P}\mathbb{P}\mathbb{R}$) in which the reaction still proceeds via Pomeron exchange, but where the total Pomeron-proton cross section is described by a sub-leading Reggeon ($\mathbb{R}$) with intercept $\alpha_{\mathbb{R}}(0) \simeq 0.5$ [58]. This leads by analogy with equation (2) to a contribution to the cross section which falls as $\mathrm{d}\sigma/\mathrm{d}M_X^2 \propto 1/M_X^3$. In the recent model of Ryskin, Martin and Khoze (RMK) [43], a modified triple-Pomeron approach to the large ξ_X region is combined with a dedicated treatment of low mass diffrac-

tive dissociation, motivated by the original s-channel picture of Good and Walker [60], in which proton and excited proton eigenstates scatter elastically from the target with different absorption coefficients. This leads to a considerable enhancement in the low ξ_X cross section which is compatible with that observed in the pre-LHC data [25].

3.2 Monte Carlo Simulations

Triple Pomeron-based parameterisations are implemented in the commonly used Monte Carlo (MC) event generators, PYTHIA [40, 41] and PHOJET [42, 61]. These generators are used to correct the data for experimental effects and as a means of comparing the corrected data with theoretical models.

By default, the PYTHIA model of diffractive dissociation processes uses the Schuler and Sjöstrand parameterisation [62] of the Pomeron flux, which assumes a Pomeron intercept of unity and an exponential t dependence $e^{B(\xi_X,\xi_Y)t}$. Three alternative flux models are also implemented. The Bruni and Ingelman version [63] is similar to Schuler and Sjöstrand, except that its t dependence is given by the sum of two exponentials. In the Berger and Streng [64,65] and Donnachie and Landshoff [66] models, the Pomeron trajectory is linear, with variable parameters, the default being $\alpha_{I\!P}(t) = 1.085{+}0.25t$ [67], consistent with results from fits to total [58, 59] and elastic [68] hadronic cross section data. Whilst the model attributed to Berger and Streng has an exponential t dependence, the Donnachie and Landshoff version is based on a dipole model of the proton elastic form factor. For all flux parameterisations in PYTHIA, additional factors are applied to modify the distributions in kinematic regions in which a triple-Pomeron approach is known to be inappropriate. Their main effects are to enhance the low mass components of the dissociation spectra, to suppress the production of very large masses and, in the DD case, to reduce the probability of the systems X and Y overlapping in rapidity space [41, 62].

Above the very low mass resonance region, dissociation systems are treated in the PYTHIA6 generator using the Lund string model [69], with final state hadrons distributed in a longitudinal phase space with limited transverse momentum. In PYTHIA8, diffractive parton distribution functions from HERA [31] are used to include diffractive final states which are characteristic of hard partonic collisions, whilst preserving the ξ_X, ξ_Y, s and t dependences of the diffractive cross sections from the PYTHIA6 model [70]. This approach yields a significantly harder final state particle transverse momentum spectrum in SD and DD processes in PYTHIA8 compared with PYTHIA6, in better agreement with the present data. The default PYTHIA multiple parton interaction model is applied to ND events and, in the case of PYTHIA8, also within the dissociated systems in SD and DD events.

The specific versions used to correct the data are PYTHIA6.4.21 (with the AMBT1 tune performed by ATLAS [71]) and PYTHIA8.145 (with the 4C tune [72]). Updated versions, PYTHIA8.150 and PYTHIA6.4.25 (using the 4C and AMBT2B tunes, respectively), are used for comparisons with the corrected data (see Table 1). The 4C tune of PYTHIA8 takes account of the measurement of the diffractive fraction f_D of the inelastic cross section in [8], whilst keeping the total cross section fixed, resulting in a somewhat smaller diffractive cross section than in PYTHIA6.

The PHOJET model uses the two component dual parton model [73] to combine features of Regge phenomenology with AGK cutting rules [74] and leading order QCD. Diffractive dissociation is described in a two-channel eikonal model, combining a triple Regge approach to soft processes with lowest order QCD for processes with parton scattering transverse momenta above 3 GeV. The Pomeron intercept is taken to be $\alpha_{I\!P}(0) = 1.08$ and for hard diffraction, the diffractive parton densities are taken from [75, 76]. Hadronisation follows the Lund string model, as for PYTHIA. The CD process is included at the level of 1.7% of the total inelastic cross section. The specific version used is PHOJET1.12.1.35, with fragmentation and hadronisation as in PYTHIA6.1.15.

After integration over t, ξ_X and ξ_Y, the cross sections for the diffractive processes vary considerably between the default MC models, as shown in Table 1. The DD variation is particularly large, due to the lack of experimental constraints. For use in the data correction procedure, the overall fractional non-diffractive (f_{ND}) and diffractive ($f_D = f_{SD} + f_{DD} + f_{CD} = 1 - f_{ND}$) contributions to the total inelastic cross section are modified to match the results obtained in the context of each model in a previous ATLAS analysis [8]. Despite the close agreement between the diffractive fractions $f_D \sim 30\%$ determined for the three default models (see the 'Tuned' fractions in Table 1), the f_D parameter is rather sensitive to the choice of Pomeron flux model and to the value of $\alpha_{I\!P}(0)$, for example reaching $f_D \sim 25\%$ for the Bruni and Ingelman flux in PYTHIA8 [8].

The default PHOJET and PYTHIA models do not take into account Tevatron data which are relevant to the decomposition of the diffractive cross section into SD, DD and CD components, so these fractions are also adjusted for the present analysis. Based on CDF SD [28] and DD [34] cross section data, extrapolated to the full diffractive kinematic ranges in each of the mod-

Table 1: Predicted ND, SD, DD and CD cross sections, together with the fractions of the total inelastic cross section f_{ND}, f_{SD}, f_{DD} and f_{CD} attributed to each process according to the default versions of the MC models (PYTHIA8.150, PYTHIA6.4.25 and PHOJET1.12.1.35), used for comparisons with the measured cross sections. The modified fractions used in the trigger efficiency and migration unfolding procedure, tuned as explained in the text, are also given.

Cross section at $\sqrt{s} = 7$ TeV			
Process	PYTHIA6	PYTHIA8	PHOJET
σ_{ND} (mb)	48.5	50.9	61.6
σ_{SD} (mb)	13.7	12.4	10.7
σ_{DD} (mb)	9.2	8.1	3.9
σ_{CD} (mb)	0.0	0.0	1.3
Default f_{ND} (%)	67.9	71.3	79.4
Default f_{SD} (%)	19.2	17.3	13.8
Default f_{DD} (%)	12.9	11.4	5.1
Default f_{CD} (%)	0.0	0.0	1.7
Tuned f_{ND} (%)	70.0	70.2	70.2
Tuned f_{SD} (%)	20.7	20.6	16.1
Tuned f_{DD} (%)	9.3	9.2	11.2
Tuned f_{CD} (%)	0.0	0.0	2.5

els, constraints of $0.29 < \sigma_{DD}/\sigma_{SD} < 0.68$ and $0.44 < \sigma_{DD}/\sigma_{SD} < 0.94$ are derived for the PYTHIA and PHOJET models of diffraction, respectively. The tuned ratios used in the correction procedure are taken at the centres of these bounds. The CD contribution in PHOJET is compatible with the measured Tevatron value of 9.3% of the SD cross Section [7] and σ_{CD}/σ_{SD} is therefore kept fixed, with f_{CD} increasing in proportion to f_{SD}. Table 1 summarises the tuned decomposition of the inelastic cross section for each MC model.

Despite the substantial differences between the approaches to diffraction taken in PHOJET and PYTHIA, the two models both employ the Lund string model [69] of hadronisation. In order to investigate the sensitivity of the data at small gap sizes to the hadronisation model for ND processes, comparisons of the measured cross sections are also made with the HERWIG++ generator [77] (version 2.5.1 with the UE7-2 tune [78, 79]), which uses an alternative cluster-based model. The HERWIG++ minimum bias generator takes the total inelastic cross section to be 81 mb, based on a Donnachie-Landshoff model [80]. Perturbatively treated semi-hard processes are distinguished from soft processes according to whether they produce objects with transverse momentum above a fixed threshold which is taken to be 3.36 GeV. Partons produced from the parton shower are combined into colour singlet pairs called clusters, which can be interpreted as excited hadronic resonances. The clusters are then successively split into new clusters until they reach the required mass to form hadrons. The most recent HERWIG++ versions contain a mechanism to reconnect partons between cluster pairs via a colour reconnection (CR) algorithm, which improves the modelling of charged particle multiplicities in pp collisions [81]. Similarly to PYTHIA, HERWIG++ contains an eikonalised underlying event model, which assumes that separate scatterings in the same event are independent. At fixed impact parameter, this leads to Poisson distributions for both the number of soft scatters and the number of semi-hard processes per event. There is thus a small probability for 'empty' events to occur with no scatterings of either type. Under these circumstances, particle production occurs only in association with the dissociation of the beam protons, in a manner which is reminiscent of diffractive dissociation processes.

3.3 Comparisons between Monte Carlo simulations and uncorrected data

For use in the correction procedure, MC events are processed through the ATLAS detector simulation program [82], which is based on GEANT4 [83]. They are then subjected to the same reconstruction and analysis chain as is used for the data.

The quality of the MC description of the most important distributions for the correction procedure is tested through a set of control plots which compare the uncorrected data and MC distributions. These include energy flows, track and calorimeter cluster multiplicities and transverse momentum distributions, as well as leading cell energy significances in different pseudorapidity regions. All such distributions are reasonably well described. Examples are shown in Figures 3a-d, where the total multiplicities of calorimeter clusters which pass the selection described in Section 2.3 are shown for events in four different regions of reconstructed forward rapidity gap size. Whilst none of the MC models gives a perfect description, particularly at small multiplicities, the three models tend to bracket the data, with PYTHIA6 showing an excess at low multiplicities and PYTHIA8 and PHOJET showing a deficiency in the same region.

A further example control distribution is shown in Figure 3e. The probability of detecting at least one calorimeter cluster passing the noise requirements with $p_{\mathrm{T}} > p_{\mathrm{T}}^{\mathrm{cut}} = 200$ MeV in the most central region ($|\eta| < 0.1$) is shown as a function of the p_{T} of the leading track reconstructed in the same η region. In cases where this track has p_{T} below around 400 MeV, it spirals in the solenoidal field outside the acceptance of the EM

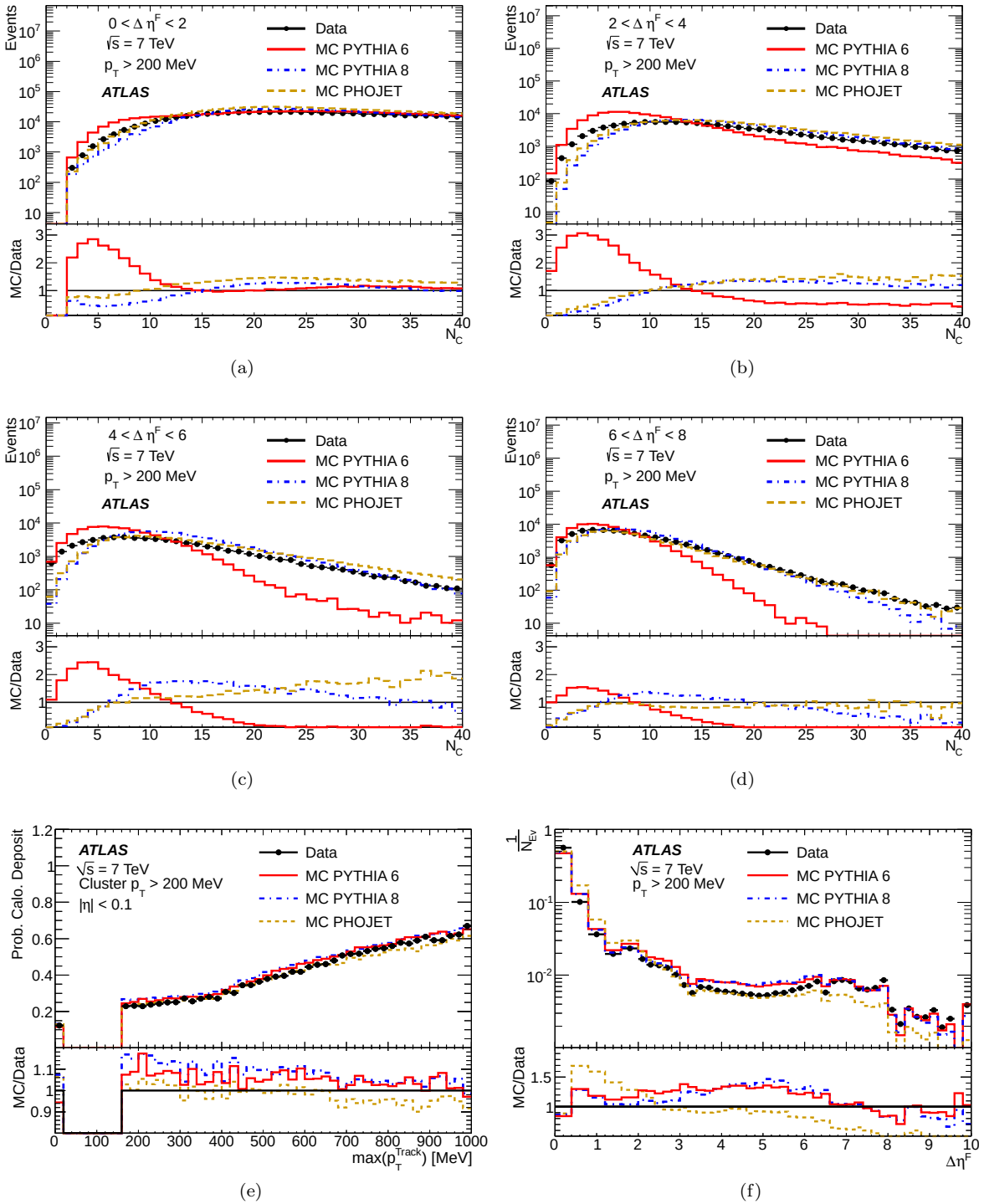

Fig. 3: Comparisons of uncorrected distributions between data and MC models. (a)-(d) Total calorimeter cluster multiplicities N_C for events reconstructed with (a) $0 < \Delta\eta^F < 2$, (b) $2 < \Delta\eta^F < 4$, (c) $4 < \Delta\eta^F < 6$ and (d) $6 < \Delta\eta^F < 8$. (e) Probability of detecting significant calorimeter energy in the most central region $|\eta| < 0.1$ as a function of the highest transverse momentum $\max(p_{\mathrm{T}}^{\mathrm{Track}})$ of the tracks reconstructed in the inner detector in the same $|\eta|$ range. The bin at zero corresponds to events where no charged track with $p_{\mathrm{T}} > 160$ MeV is reconstructed. (f) Forward rapidity gap distribution for $p_{\mathrm{T}}^{\mathrm{cut}} = 200$ MeV. The final bin at $\Delta\eta^F = 10$ corresponds to cases where no reconstructed particles have $p_{\mathrm{T}} > p_{\mathrm{T}}^{\mathrm{cut}}$.

calorimeter. The plotted quantity then corresponds to the detection probability for neutral particles in the vicinity of a track. Good agreement is observed between MC and data.

The shape of the uncorrected $\Delta\eta^F$ distribution for $p_{\mathrm{T}}^{\mathrm{cut}} = 200$ MeV is compared between the data and the MC models in Figure 3f. The binning reflects that used in the final result (Section 2.4) except that contributions with $\Delta\eta^F > 8$, where the trigger efficiency becomes small, are also shown. None of the models considered are able to describe the data over the full $\Delta\eta^F$ range, with the largest deviations observed for small non-zero gaps in PHOJET. All of the models give an acceptable description of the shape of the distribution for large gaps up to the limit of the measurement at $\Delta\eta^F = 8$ and beyond.

Considering all control plots together, PYTHIA8 provides the best description of the shapes of the distributions. Hence this generator is chosen to correct the data. The deviations from PYTHIA8 of PYTHIA6 and PHOJET, which often lie in opposite directions and tend to enclose the data, are used to evaluate the systematic uncertainties on the unfolding procedure.

3.4 Corrections for Experimental Effects

After the statistical subtraction of the beam-induced background in each interval of $\Delta\eta^F$ (Section 2.2), the data are corrected for the influence of the limited acceptance and small particle detection inefficiencies of the MBTS using the MC simulation. For the ND, SD and DD processes, the trigger efficiency is close to 100% for $\Delta\eta^F < 7$, dropping to around 80% at $\Delta\eta^F = 8$. Since the topology of CD events sometimes involves hadronic activity in the central region of the detector, with gaps on either side, a larger fraction fail the trigger requirement, with efficiencies of close to 100% for $\Delta\eta^F < 3$ and between 85% and 95% for $3 < \Delta\eta^F < 8$.

The data are corrected for migrations between the reconstructed and hadron level $\Delta\eta^F$ values, due to missed or spurious activity and cases where a final state particle is observed in a different η interval from that in which it is produced. The migration corrections are obtained using a Bayesian unfolding method [84] with a single iteration. The priors for the unfolding procedure with each MC model are taken after tuning the diffractive cross sections as described in Section 3.2. The migration matrix between the reconstructed and hadron level forward gap distributions according to the PYTHIA8 MC is shown for $p_{\mathrm{T}}^{\mathrm{cut}} = 200$ MeV in Figure 4. An approximately diagonal matrix is obtained.

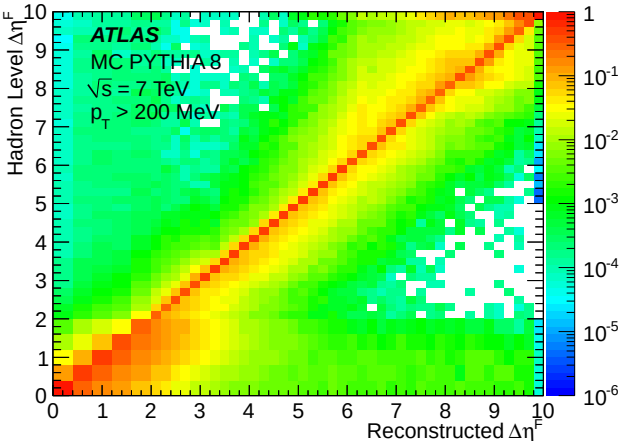

Fig. 4: Migration matrix between the reconstructed and hadron level values of $\Delta\eta^F$ for $p_{\mathrm{T}}^{\mathrm{cut}} = 200$ MeV, according to PYTHIA8. The distribution is normalised to unity in columns and is shown to beyond the limit of the measurement at $\Delta\eta^F = 8$.

4 Systematic Uncertainties

The sources of systematic uncertainty on the measurement are outlined below.

MC Model and Unfolding Method Dependence: The trigger efficiency and migration correction procedure is carried out using each of the PYTHIA6, PYTHIA8 and PHOJET models. The deviation of the data unfolded with PHOJET from those obtained with PYTHIA8 is used to obtain a systematic uncertainty due to the assumed ξ_X, ξ_Y and t dependences in the unfolding procedure. The model dependence due to the details of the final state particle production is obtained from the difference between the results obtained with PYTHIA6 and PYTHIA8. Both of these model dependences are evaluated separately in each measurement interval and are applied symmetrically as upward and downward uncertainties. They produce the largest uncertainty on the measurement over most of the measured range. For $p_{\mathrm{T}}^{\mathrm{cut}} = 200$ MeV, the contributions from the PYTHIA6 and PHOJET variations are of similar size. Their combined effect is typically at the 6% level for large $\Delta\eta^F$, growing to 20% for gaps of around 1.5 pseudorapidity units. At larger $p_{\mathrm{T}}^{\mathrm{cut}}$ values, the PYTHIA6 source becomes dominant. The dependence on the unfolding technique has also been studied by switching between the default Bayesian method [84], a method using a Singular Value Decomposition of the unfolding matrix [85] and a simple bin-to-bin method. The resulting variations in the measured cross section are always within

the systematic uncertainty defined by varying the MC model.

Modelling of Diffractive Contributions: In addition to the differences between the Monte Carlo generators, additional systematic uncertainties are applied on the modelling of the fractional diffractive cross sections. The SD and DD cross sections in the PYTHIA8 model are each varied to the limits of the constraints from Tevatron data described in Section 3.2. The fraction f_{DD} is enhanced to 11.3% of the total inelastic cross section, with f_{SD} reduced to 18.5% to compensate. At the opposite extreme, f_{SD} is enhanced to 23.2% of the cross section, with f_{DD} reduced to 6.6%. These changes result in an uncertainty at the 1% level for $\Delta\eta^F > 3$. A systematic uncertainty on the CD cross section is obtained by varying the CD and SD cross sections in PHOJET between the tuned values and $\sigma_{CD}/\sigma_{SD} = 0.093$, corresponding to the CDF measurement in [7]. This variation also results in a 1% uncertainty in the large gap region.

Calorimeter Energy Scale: The uncertainty on the calorimeter energy scale is constrained to be below the 5% level down to energies of a few hundred MeV in the central region, $|\eta| < 2.3$, through comparisons between isolated calorimeter cluster energy measurements and momentum determinations of matched tracks in the inner detector [51–53]. This method is not available for larger $|\eta|$ values beyond the tracking acceptance. However, as $|\eta|$ grows, the default $p_{\mathrm{T}}^{\mathrm{cut}} = 200$ MeV threshold corresponds to increasingly large energies, reaching beyond 10 GeV at the outer limits of the FCal. The uncertainty on the response to electromagnetic showers in this energy range is determined as a function of $|\eta|$ from the maximum observed deviations between the data and the MC simulation in the peaks of $\pi^0 \to \gamma\gamma$ signals, under a variety of assumptions on background shapes and cluster energy resolutions. The relative response to charged pions compared with the electromagnetic scale has been studied in the relevant energy range for the FCal [55, 86] and HEC [54, 86] test-beam data, with systematic uncertainties of 8% and 4%, respectively, determined from the difference between data and MC. Adding the uncertainties in the electromagnetic scale and in the relative response to hadrons in quadrature, energy scale uncertainties of 5% for $|\eta| < 1.37$, 21% for $1.37 < |\eta| < 1.52$ (transition region between barrel and end-cap), 5% for $1.52 < |\eta| < 2.3$, 13% for $2.3 < |\eta| < 3.2$ and 12% for $3.2 < |\eta| < 4.9$ are ascribed. In addition to the absolute calorimeter response, these values account for systematic effects arising from dead material uncertainties and from the final state decomposition into different particle species. In the unfolding procedure, the corresponding systematic variation is applied to energy depositions from simulated final state particles in MC, with noise contributions left unchanged. The clustering algorithm is then re-run over the modified calorimeter cells. The scale uncertainty variation is thus considered both in the application of the $p_{\mathrm{T}}^{\mathrm{cut}}$ threshold to the clusters and in the discrimination of cells within selected clusters against the significance cut used to veto noise. The resulting fractional uncertainties on the differential cross sections at the default $p_{\mathrm{T}}^{\mathrm{cut}} = 200$ MeV are largest (reaching $\sim 12\%$) in the region $\Delta\eta^F \lesssim 3$, where the gap identification relies most strongly on the calorimeter information. For larger gaps, the well measured tracks play an increasingly important role in defining the gap size and the cross section is dominated by low ξ_X diffractive events for which particle production in the gap region is completely suppressed. The sensitivity to the calorimeter scale is correspondingly reduced to a few percent.

MBTS Efficiency: The description of the MBTS efficiency in the MC models leads to a potential systematic effect on the trigger efficiency and on the off-line MBTS requirement. Following [8], the associated uncertainty is evaluated by increasing the thresholds of all MBTS counters in the simulation to match the maximum variation in the measured response in data according to studies with particles extrapolated from the tracker or FCal. This systematic error amounts to typically $0.5 - 1\%$ for $\Delta\eta^F > 2$ and is negligible at the smallest $\Delta\eta^F$.

Tracking Efficiency: The dominant uncertainty in the charged particle track reconstruction efficiency arises due to possible inadequacies in the modelling of the material through which the charged particles pass [1]. This uncertainty is quantified by studying the influence on the data correction procedure of using an MC sample produced with a 10% enhancement in the support material in the inner detector. The resulting uncertainty is smaller than 3.5% throughout the measured distribution.

Luminosity: Following the van der Meer scan results in [46], the normalisation uncertainty due to the uncertainty on the integrated luminosity is 3.4%.

Each of the systematic uncertainties is determined with correlations between bins taken into account in the unfolding by repeating the full analysis using data or MC distributions after application of the relevant systematic shift. The final systematic error on the differential cross section is taken to be the sum in quadrature

of all sources. Compared with the systematic uncertainties, the statistical errors are negligible at the smallest gap sizes, where the differential cross section is largest. For gap sizes $\Delta\eta^F \gtrsim 3$, the statistical errors are at the 1% level and are typically smaller than the systematic errors by factors between five and ten.

5 Results

5.1 Differential cross section for forward rapidity gaps

In this section, measurements are presented of the inelastic cross section differential in forward rapidity gap size, $\Delta\eta^F$, as defined in Section 2.4. The data cover the range $0 < \Delta\eta^F < 8$. In the large gap region which is populated by diffractive processes, the cross section corresponds to a t-integrated sum of SD events in which either of the colliding protons dissociates and DD events with $\xi_Y \lesssim 10^{-6}$ ($M_Y \lesssim 7$ GeV). The data span the range $\xi_X \gtrsim 10^{-5}$. Diffractive events with smaller ξ_X values are subject to large MBTS trigger inefficiencies and thus lie beyond the kinematic range of the measurement.

As discussed in Section 2.4, the lowest transverse momentum requirement for the gap definition which is directly accessible experimentally is $p_{\mathrm{T}}^{\mathrm{cut}} = 200$ MeV. Figure 5a shows the differential gap cross section for this choice of $p_{\mathrm{T}}^{\mathrm{cut}}$, which is also given numerically in Table 2. The uncertainty on the measurement is typically less than 8% for $\Delta\eta^F > 3$, growing to around 20% at $\Delta\eta^F = 1.5$ before improving to around 10% for events with little or no forward gap. The data are compared with the predictions of the default settings of the PYTHIA6 (labelled 'PYTHIA6 ATLAS AMBT2B') PYTHIA8 ('PYTHIA8 4C') and PHOJET models. In Figures 5b-d, the results are compared with each of the MC models separately, with the default decomposition of the cross section into ND, SD, DD and CD contributions according to the models (Table 1) also indicated.

5.2 Small gap sizes and constraints on hadronisation models

At $\Delta\eta^F \lesssim 2$, all models agree that the ND process is dominant and the expected [4] exponential decrease of the cross section with increasing gap size, characteristic of hadronisation fluctuations, is the dominant feature of the data. According to the models, this region also contains DD events which have $\xi_Y \gtrsim 10^{-6}$, such that the Y system extends into the ATLAS detector acceptance, as well as both SD and DD events with very large ξ_X, such that no large rapidity gap is present within the region $|\eta| < 4.9$. The default MC models tend to lie above the data in this region, a result which is consistent with the overestimates of the total inelastic cross section observed for the same models in [8]. The PYTHIA8 model is closest in shape to the data, which is partly due to the modification of f_D in the most recent versions made in light of the previous ATLAS data [8]. Both PYTHIA models are closer to the small $\Delta\eta^F$ data than PHOJET, which exhibits an excess of almost a factor of two for $\Delta\eta^F \sim 1$.

As can be inferred from comparisons between the predicted shapes of the ND contributions in the different MC models (Figures 5b-d), there are considerable uncertainties in the probability of obtaining large hadronisation fluctuations among low transverse momentum final state particles [87]. Studying the dependence of the measured differential cross section on $p_{\mathrm{T}}^{\mathrm{cut}}$ provides a detailed probe of fluctuations in the hadronisation process in soft scattering and of hadronisation models in general. The measurement is thus repeated with different choices of $p_{\mathrm{T}}^{\mathrm{cut}}$, applied both in the rapidity gap reconstruction and in the definition of the measured hadron level cross section. To avoid cases where the largest gap switches from one side of the detector to the other when low p_{T} particles are excluded by the increased $p_{\mathrm{T}}^{\mathrm{cut}}$ choice, the side of the detector on which the gap is located is fixed to that determined at $p_{\mathrm{T}}^{\mathrm{cut}} = 200$ MeV for all measured cross sections.

A comparison between the results with $p_{\mathrm{T}}^{\mathrm{cut}} = 200$, 400, 600 and 800 MeV is shown in Figure 6a. Figures 6b-d show the results for $p_{\mathrm{T}}^{\mathrm{cut}} = 400, 600$ and 800 MeV, respectively, compared with the PYTHIA8, PYTHIA6 and PHOJET MC models. The ND contributions according to each of the models are also shown. As $p_{\mathrm{T}}^{\mathrm{cut}}$ increases, the exponential fall becomes less steep, so larger $\Delta\eta^F$ values become more heavily populated and the non-diffractive and diffractive contributions in the models become similar. Also, the uncertainties due to the MC model dependence of the unfolding procedure grow.

The influence of changing from $p_{\mathrm{T}}^{\mathrm{cut}} = 200$ MeV to $p_{\mathrm{T}}^{\mathrm{cut}} = 400$ MeV is small at large $\Delta\eta^F$, where the cross section is dominated by small ξ_X diffractive events and particle production is kinematically forbidden over a wide range of pseudorapidity. For $\Delta\eta^F \lesssim 4$, where ND contributions become important, a significant fraction of events are assessed as having larger gaps for $p_{\mathrm{T}}^{\mathrm{cut}} = 400$ MeV than for $p_{\mathrm{T}}^{\mathrm{cut}} = 200$ MeV. As the value of $p_{\mathrm{T}}^{\mathrm{cut}}$ increases to 600 and 800 MeV, soft ND events migrate to larger $\Delta\eta^F$ values, giving significant contributions throughout most of the distribution and confirming [1] that the production of final state particles with more than a few hundred MeV is rare in minimum

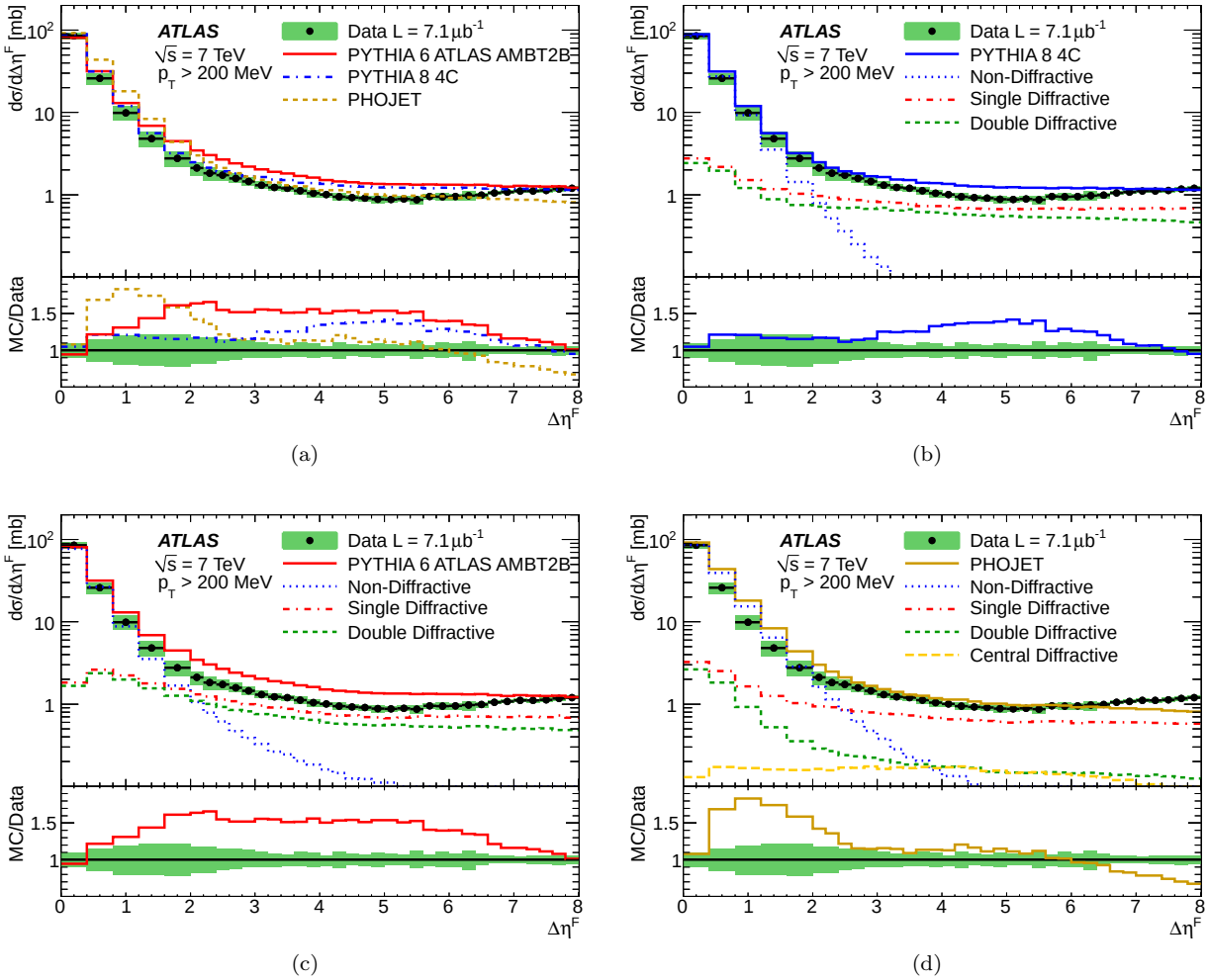

Fig. 5: Inelastic cross section differential in forward gap size $\Delta\eta^F$ for particles with $p_{\mathrm{T}} > 200$ MeV. The shaded bands represent the total uncertainties. The full lines show the predictions of PHOJET and the default versions of PYTHIA6 and PYTHIA8 The dashed lines in (b-d) represent the contributions of the ND, SD and DD components according to the models. The CD contribution according to PHOJET is also shown in (d).

bias events, even at LHC energies. All MC models are able to reproduce the general trends of the data, though none provides a full description.

It is interesting to investigate the extent to which the alternative cluster-based approach to hadronisation in the non-diffractive HERWIG++ model is able to describe the data at small gap sizes, where the contribution from ND processes is dominant. A comparison of the data at each of the $p_{\mathrm{T}}^{\mathrm{cut}}$ values with HERWIG++ is shown in Figure 7. Four versions of the UE7-2 tune are shown, with variations in the details of the model which are expected to have the largest influence on rapidity gap distributions. These are the default version (UE7-2), a version in which the colour reconnection model is switched off (UE7-2, No CR) and similar versions which exclude events with no scatterings of either the soft or semi-hard types (UE7-2, No Empty Evts and UE7-2, No Empty Evts, No CR). At small gap sizes, all versions of the model produce an exponential fall with increasing gap size, though the dependence on $\Delta\eta^F$ is not steep enough in the default model and is too steep when colour recombination effects are switched off.

Despite not containing an explicit diffractive component, the default HERWIG++ minimum bias model produces a sizeable fraction of events with large gaps, overshooting the measured cross section by up to factor of four in the interval $2 < \Delta\eta^F < 7$ and producing an enhancement centred around $\Delta\eta^F = 6$. When colour

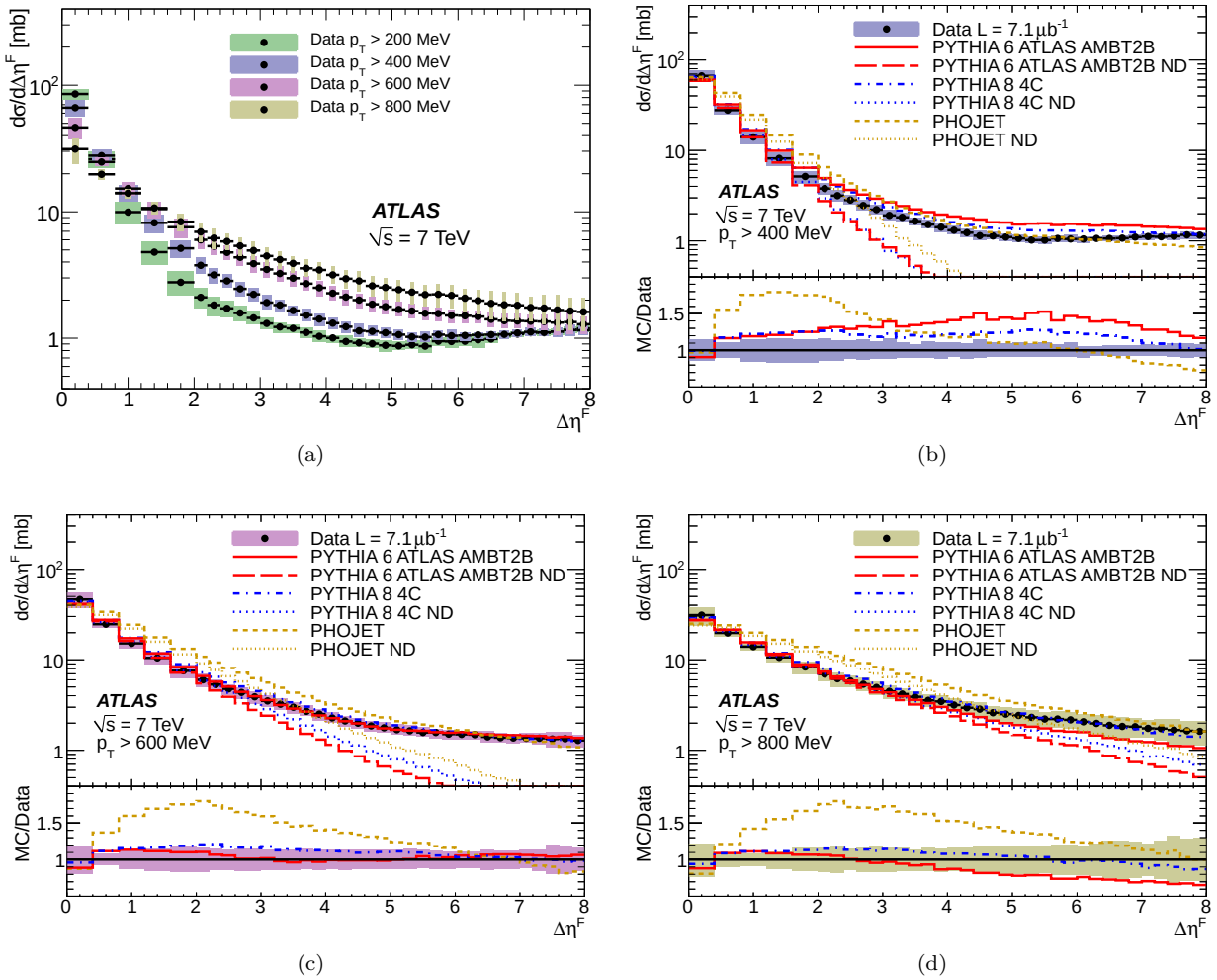

Fig. 6: Inelastic cross section differential in forward gap size $\Delta\eta^F$ for different $p_{\mathrm{T}}^{\mathrm{cut}}$ values. (a) Comparison between the measured cross sections. The full uncertainties are shown. They are correlated between the different $p_{\mathrm{T}}^{\mathrm{cut}}$ choices. (b-d) Comparison between the data and the MC models for $p_{\mathrm{T}}^{\mathrm{cut}} = 400, 600$ and 800 MeV. The non-diffractive component in each MC model is also shown.

reconnection is switched off, this large gap contribution is reduced considerably, but remains at a similar level to that measured in the range $3 < \Delta\eta^F < 5$. The enhancement near $\Delta\eta^F \approx 6$ is still present. The events with zero scatters in the HERWIG++ underlying event model provide a partial explanation for the large gap contribution. Removing this contribution reduces the predicted large gap cross section, but the non-exponential tail and large $\Delta\eta^F$ enhancement persist. For all scenarios considered, the alternative cluster based hadronisation model in HERWIG++ shows structure which is incompatible with the data.

5.3 Large gap sizes and sensitivity to diffractive dynamics

At large $\Delta\eta^F$, the differential cross section exhibits a plateau, which is attributed mainly to diffractive processes (SD events, together with DD events at $\xi_Y \lesssim 10^{-6}$) and is shown in detail in Figure 8. According to the PHOJET MC model, the CD contribution is also distributed fairly uniformly across this region. Over a wide range of gap sizes with $\Delta\eta^F \gtrsim 3$, the differential cross section is roughly constant at around 1 mb per unit of rapidity gap size. Given the close correlation between $\Delta\eta^F$ and $-\ln\xi$ (Section 3.1), this behaviour is expected as a consequence of the dominance of soft

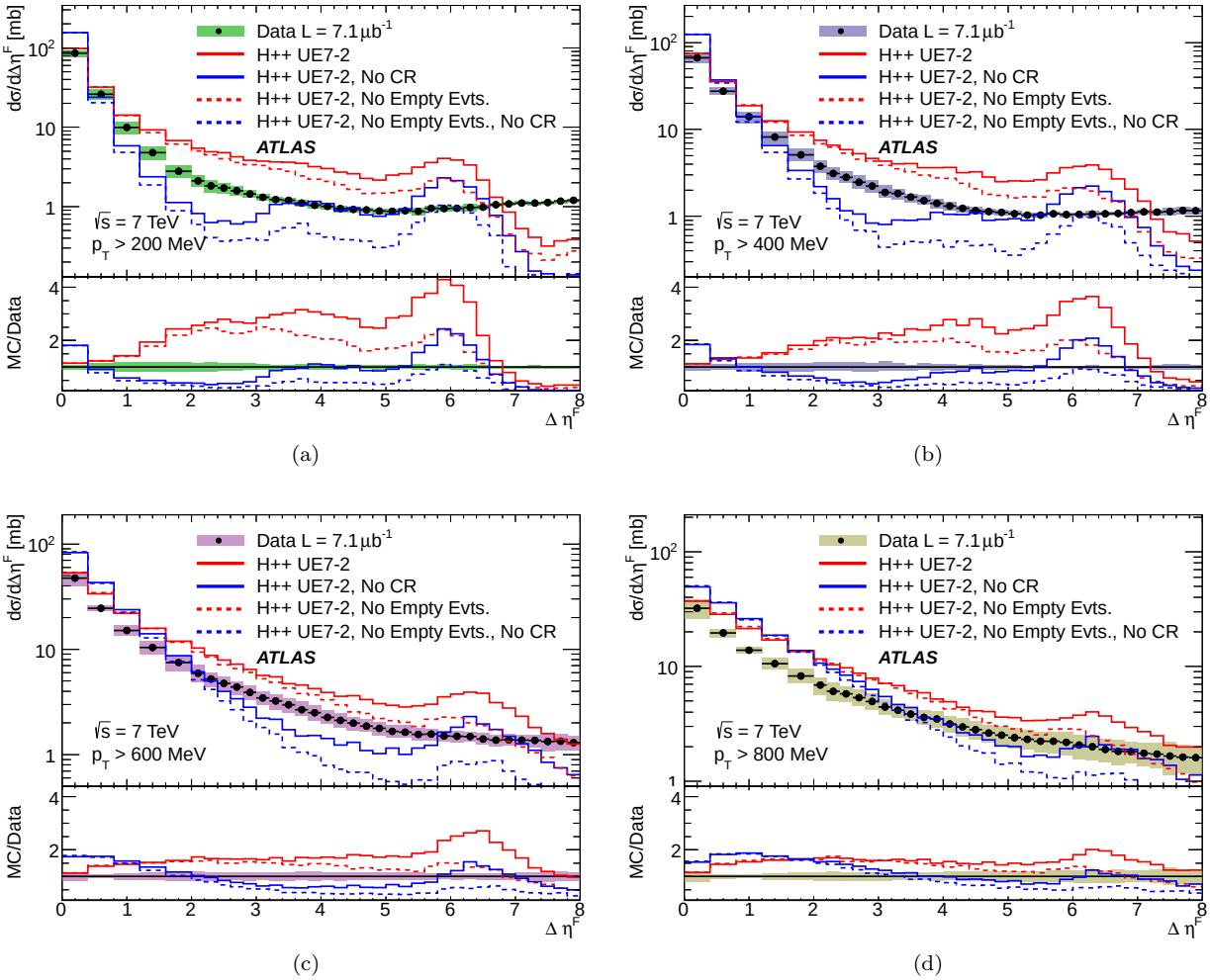

Fig. 7: Inelastic cross section differential in forward gap size $\Delta\eta^F$ for $p_{\mathrm{T}}^{\mathrm{cut}}$ = (a) 200 MeV, (b) 400 MeV, (c) 600 MeV and (d) 800 MeV. The data are compared with the UE7-2 tune of the HERWIG++ model. In addition to the default tune, versions are shown in which the colour reconnection model is switched off and in which events with zero scatters are excluded (see text for further details).

diffractive processes. All MC models roughly reproduce the diffractive plateau, though none gives a detailed description of the shape as a function of $\Delta\eta^F$.

When absolutely normalised, the PYTHIA predictions overshoot the data throughout most of the diffractive region, despite the tuning of f_D to previous ATLAS data [8] in these models. The excess here is partially a reflection of the 10% overestimate of the PYTHIA prediction in the total inelastic cross section and may also be associated with the large DD cross section in the measured region, which exceeds that expected based on Tevatron data [34] and gives rise to almost equal SD and DD contributions at large $\Delta\eta^F$. For PHOJET, the underestimate of the diffractive fraction f_D is largely compensated by the excess in the total inelastic cross section, such that the large gap cross section is in fair agreement with the measurement up to $\Delta\eta^F \approx 6$. The DD contribution to the cross section in PHOJET is heavily suppressed compared with that in the PYTHIA models.

Integrated over the diffractive-dominated region $5 < \Delta\eta^F < 8$, corresponding approximately to $-5.1 \lesssim \log_{10}(\xi_X) \lesssim -3.8$ according to the MC models, the measured cross section is 3.05 ± 0.23 mb, approximately 4% of the total inelastic cross section. This can be compared with 3.58 mb, 3.89 mb and 2.71 mb for the default versions of PYTHIA8, PYTHIA6 and PHOJET, respectively.

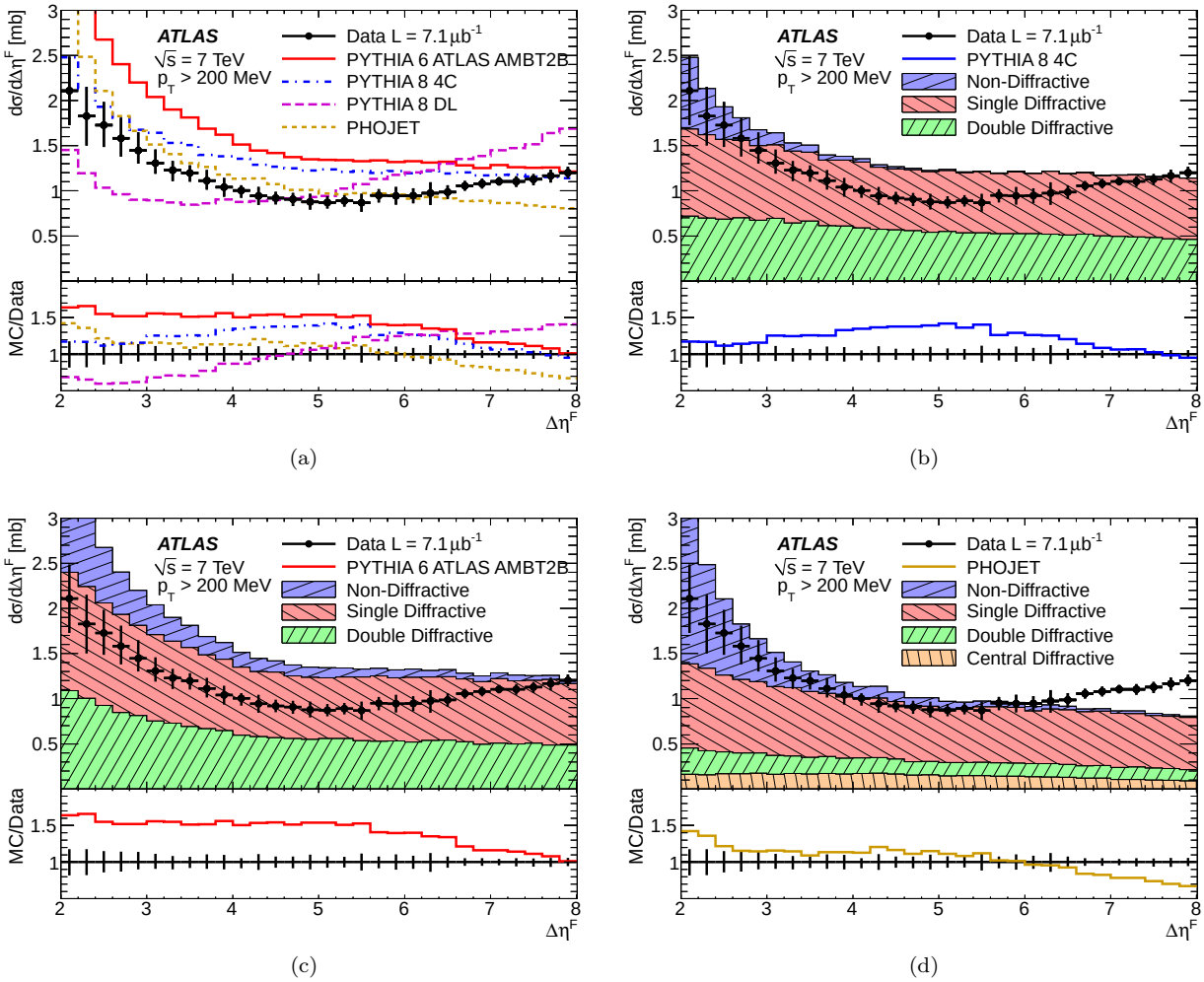

Fig. 8: Inelastic cross section differential in forward gap size $\Delta\eta^F$ for particles with $p_{\mathrm{T}} > 200$ MeV and $\Delta\eta^F > 2$. The error bars indicate the total uncertainties. In (a), the full lines show the predictions of PHOJET, the default versions of PYTHIA6 and PYTHIA8, and PYTHIA8 with the Donnachie-Landshoff Pomeron flux. The remaining plots show the contributions of the SD, DD and ND components according to each generator. The CD contribution according to PHOJET is also shown in (d).

As can be seen in Figure 8, the differential cross section rises slowly with increasing $\Delta\eta^F$ for $\Delta\eta^F \gtrsim 5$. Non-diffractive contributions in this region are small and fall with increasing $\Delta\eta^F$ according to all models, so this rise is attributable to the dynamics of the SD and DD processes. Specifically the rising cross section is as expected from the $\mathbb{P}\mathbb{P}\mathbb{P}$ term in triple Regge models with a Pomeron intercept in excess of unity (see equation (2)). In Figure 8a, a comparison is made with the PYTHIA8 model, after replacing the default Schuler and Sjöstrand Pomeron flux with the Donnachie and Landshoff (DL) version using the default Pomeron trajectory, $\alpha_{\mathbb{P}}(t) = 1.085 + 0.25t$ ('PYTHIA8 DL'). It is clear that the data at large $\Delta\eta^F$ are not perfectly described with this choice.

Whilst the data are insensitive to the choice of $\alpha_{\mathbb{P}}\prime$, there is considerable sensitivity to the value of $\alpha_{\mathbb{P}}(0)$. The data in the cleanest diffractive region $\Delta\eta^F > 6$ are used to obtain a best estimate of the appropriate choice of the Pomeron intercept to describe the data. SD and DD PYTHIA8 samples are generated with the DL Pomeron flux for a range of $\alpha_{\mathbb{P}}(0)$ values. In each case, the default $\alpha_{\mathbb{P}}\prime$ value of 0.25 GeV^{-2} is taken and the tuned ratios of the SD and DD contributions appropriate to PYTHIA8 from Table 1 are used. The χ^2 value for the best fit to the data in the region $6 < \Delta\eta^F < 8$

is obtained for each of the samples with different $\alpha_{I\!P}(0)$ values, with the cross section integrated over the fitted region allowed to float as a free parameter. The optimum $\alpha_{I\!P}(0)$ is determined from the minimum of the resulting χ^2 parabola.

The full procedure is repeated for data points shifted according to each of the systematic effects described in Section 4, such that correlations between the uncertainties on the data points are taken into account in evaluating the uncertainties. The systematic uncertainty is dominated by the MC model dependence of the data correction procedure, in particular the effect of unfolding using PYTHIA6 in place of PYTHIA8, which leads to a significantly flatter dependence of the data on $\Delta\eta^F$ at large gap sizes.

The result obtained in the context of the PYTHIA8 model with the DL flux parameterisation is

$$\alpha_{I\!P}(0) = 1.058 \pm 0.003(\text{stat.})^{+0.034}_{-0.039}(\text{syst.}) \ . \qquad (4)$$

The data are thus compatible with a value of $\alpha_{I\!P}(0)$ which matches that appropriate to the description of total hadronic cross sections [58,59]. When the Berger-Streng Pomeron flux, which differs from the DL version in the modelling of the t dependence, is used in the fit procedure, the result is modified to $\alpha_{I\!P}(0) = 1.056$. The effects of varying $\alpha_{I\!P}\prime$ between 0.1 GeV^{-2} and 0.4 GeV^{-2} and of varying the f_{SD} and f_{DD} fractions assumed in the fit in the ranges given in Section 4 are also smaller than the statistical uncertainty. Compatible results are obtained by fitting the higher $p_{\mathrm{T}}^{\mathrm{cut}}$ data.

A comparison between the data and a modified version of PYTHIA8, with $\alpha_{I\!P}(0)$ as obtained from the fit, is shown in Figure 9. Here, the diffractive contribution to the inelastic cross section $f_D = 25.6\%$ is matched[2] to the fitted value of $\alpha_{I\!P}(0)$ using the results in [8]. Together with the cross section integrated over the region $6 < \Delta\eta^F < 8$ as obtained from the fit and the tuned ratio f_{DD}/f_{SD} from Table 1, this fixes the normalisation of the full distribution. The description of the data at large $\Delta\eta^F$ is excellent and the exponential fall at small $\Delta\eta^F$ is also adequately described. There is a discrepancy in the region $2 < \Delta\eta^F < 4$, which may be a consequence of the uncertainty in modelling large hadronisation fluctuations in ND events (compare the ND tails to large $\Delta\eta^F$ in Figure 8b, c and d). It may also be attributable to sub-leading trajectory exchanges [29, 31] or to the lack of a CD component in the PYTHIA model.

[2] Since only data at large $\Delta\eta^F$ are included in the fit, the result for $\alpha_{I\!P}(0)$ is insensitive to systematic variations in f_D.

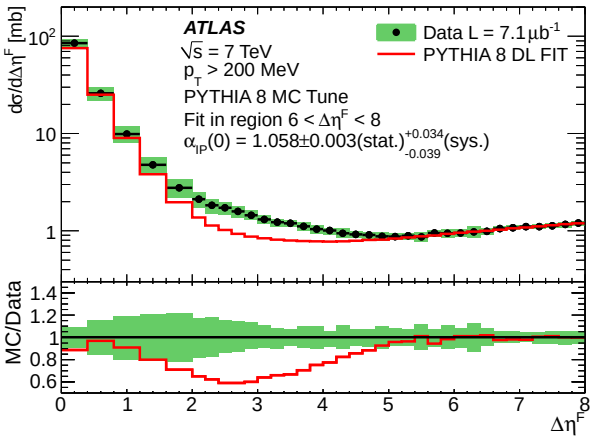

Fig. 9: Inelastic cross section differential in forward gap size $\Delta\eta^F$ for particles with $p_{\mathrm{T}} > 200$ MeV. The data are compared with a modified version of the PYTHIA8 model with the DL flux, in which the Pomeron intercept $\alpha_{I\!P}(0)$ is determined from fits to the data in the region $6 < \Delta\eta^F < 8$. See text for further details.

5.4 The integrated inelastic cross section

By summing over the $\Delta\eta^F$ distribution from zero to a maximum gap size $\Delta\eta^F_{\mathrm{Cut}}$, the integrated inelastic cross section can be obtained, excluding the contribution from events with very large gaps $\Delta\eta^F > \Delta\eta^F_{\mathrm{Cut}}$. As discussed in Section 3.1, there is a strong correlation between the size of the gap and the kinematics of diffraction (see e.g. equation (3) for the SD process). The cross section integrated over a given range of gap size can thus be converted into an integral over the inelastic pp cross section down to some minimum value ξ_{Cut} of ξ_X. The variation in the integrated inelastic cross section with $\Delta\eta^F_{\mathrm{Cut}}$ can then be used to compare inelastic cross section results with different lower limits, ξ_{Cut}.

The integral of the forward gap cross section

$$\int_0^{\Delta\eta^F_{\mathrm{Cut}}} \frac{\mathrm{d}\sigma}{\mathrm{d}\Delta\eta^F}\,\mathrm{d}\Delta\eta^F$$

is obtained for $\Delta\eta^F_{\mathrm{Cut}}$ values varying between 3 and 8 by cumulatively adding the cross section contributions from successive bins of the measured gap distribution. The correspondence between maximum gap size and minimum ξ_X used here is determined from the PYTHIA8 model to be $\log_{10}\xi_{\mathrm{Cut}} = -0.45\,\Delta\eta^F_{\mathrm{Cut}} - 1.52$. The uncertainty on this correlation is small; for example the PHOJET model results in the same slope of -0.45 with an intercept of -1.56. This correlation is applied to convert to an integral

$$\int_{\xi_{\mathrm{Cut}}}^1 \frac{\mathrm{d}\sigma}{\mathrm{d}\xi_X}\,\mathrm{d}\xi_X \ .$$

A small correction is applied to account for the fact that the gap cross section neglects particles with[3] $p_{\mathrm{T}} < p_{\mathrm{T}}^{\mathrm{cut}} = 200$ MeV and includes a contribution from ND processes. This correction factor is calculated using PYTHIA8 with the DL flux, and the optimised $\alpha_{I\!P}(0)$ and f_D values, as determined in Section 5.3. The integration range is chosen such that the correction is always smaller than ±1.3%. The systematic uncertainty on the correction factor, evaluated by comparison with results obtained using PHOJET or PYTHIA8 with the default Schuler and Sjöstrand flux, together with the systematic variations of the tuned fractions f_{SD} and f_{DD} as in Section 4, is also small.

The integrated inelastic cross section is shown as a function of ξ_{Cut} in Figure 10, where it is also compared with a previous ATLAS result [8] and with the TOTEM extraction of the full inelastic cross section [10], derived from a measurement of the elastic cross section via the optical theorem. The errors on all of the experimental data points are dominated by the luminosity uncertainties. The previous ATLAS result was also based on MBTS-triggered data, but is quoted at the ξ_X value corresponding to 50% trigger efficiency, which is slightly beyond the range accessed here. Extrapolating according to the measured dependence on ξ_{Cut}, the new data are in good agreement with the previous result, the small apparent difference being well within the uncertainty due to run-to-run luminosity measurement variations.

It is instructive to compare the TOTEM result with the ATLAS measurements, since the latter omit the poorly understood lowest ξ_X region. By comparing the lowest ξ_{Cut} data point from the present analysis with the TOTEM measurement and neglecting any correlations between the ATLAS and TOTEM uncertainties, the inelastic cross section integrated over $\xi_X < 8 \times 10^{-6}$ is inferred to be $14.5^{+2.0}_{-1.5}$ mb. Significantly smaller contributions are predicted by the default versions of PYTHIA ($\sim$ 6 mb) and PHOJET ($\sim$ 3 mb). Figure 10 also shows two versions of the RMK model (see Section 3.1), corresponding to versions (i) (upper curve) and (ii) (lower curve) in [43]. These versions differ in the radii attributed to the elastically scattered eigenstates comprising the low ξ_X contribution which is added to the more standard triple Pomeron

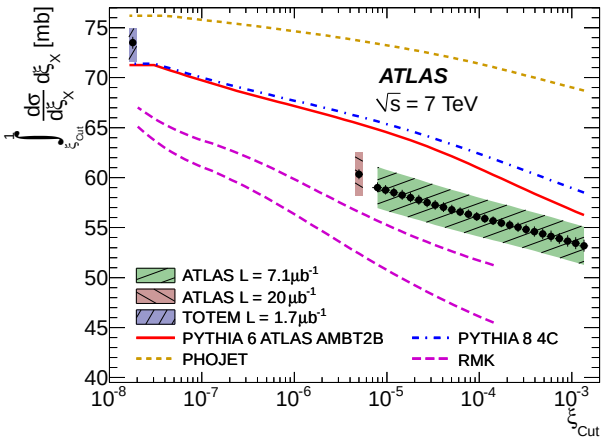

Fig. 10: Inelastic cross section excluding diffractive processes with $\xi_X < \xi_{\mathrm{Cut}}$, obtained by integration of the differential cross section from gap sizes of zero to a variable maximum. The results from the present analysis ('ATLAS L = 7.1 μb^{-1}') are compared with a previous ATLAS result [8] and a TOTEM measurement integrated over all kinematically accessible ξ_X values [10]. The predictions of the default versions of the PYTHIA6, PYTHIA8 and PHOJET models are also shown, along with two versions of the RMK model [43] (see text). The vertical error bars on the ATLAS measurements denote the systematic uncertainties excluding that on the luminosity measurement, whilst the shaded area represents the full systematic uncertainty. For the TOTEM point, the error bar represents the statistical uncertainty whilst the shaded area represents the full uncertainty. The uncertainties on the data points obtained in the present analysis are strongly correlated between neighbouring points.

calculation in the model, (ii) being the favoured version and (i) being indicative of the flexibility in the model whilst preserving an acceptable description of pre-LHC data. The additional low ξ_X processes enhance the inelastic cross section by 5.5 mb and 6.7 mb in versions (i) and (ii), respectively. Although the RMK model lies below the data in general, the low ξ_X enhancement is compatible with that observed [88]. The shape of the distribution at low ξ_X is not predicted in the model, but is compatible with the data if, as shown here [89], it is assumed to have the steep ξ_X dependence associated with the $I\!P I\!P I\!R$, rather than the $I\!P I\!P I\!P$ triple Regge term. Similar conclusions have been reached previously from proton-proton [25] and photoproduction [29, 30] data.

[3] The finite $p_{\mathrm{T}}^{\mathrm{cut}}$ value in the measured gap cross sections tends to increase gap sizes slightly relative to $p_{\mathrm{T}}^{\mathrm{cut}} = 0$. However, MC studies indicate that this effect has the biggest influence on the exponentially falling distribution at small gap sizes, whereas the difference for the $\Delta\eta^F$ values which are relevant to the integrated cross section are relatively small. According to the MC models, the cross section integrated over $5 < \Delta\eta^F < 8$ decreases by 2% when changing from $p_{\mathrm{T}}^{\mathrm{cut}} = 200$ MeV to $p_{\mathrm{T}}^{\mathrm{cut}} = 0$.

6 Summary

A novel algorithm has been devised for identifying rapidity gaps in the final state of minimum bias ATLAS data, leading to measurements in which particle production is considered down to transverse momentum thresholds $p_{\mathrm{T}}^{\mathrm{cut}}$ between 200 MeV and 800 MeV. The differential cross section $\mathrm{d}\sigma/\mathrm{d}\Delta\eta^F$ is measured for forward rapidity gaps of size $0 < \Delta\eta^F < 8$, corresponding to the larger of the two gaps extending to $\eta = \pm 4.9$, with no requirements on activity at $|\eta| > 4.9$. An exponentially falling non-diffractive contribution is observed at small gap sizes, which is also a feature of the PYTHIA, PHOJET and HERWIG++ Monte Carlo models. However, none of the models describes the $\Delta\eta^F$ or $p_{\mathrm{T}}^{\mathrm{cut}}$ dependence of this region in detail. At large gap sizes, the differential cross section exhibits a plateau, which corresponds to a mixture of the single-diffractive dissociation process and double dissociation with $\xi_Y \lesssim 10^{-6}$. This plateau amounts to a cross section close to 1 mb per unit of gap size and its magnitude is roughly described by the PYTHIA and PHOJET Monte Carlo models. None of the default models reproduce the rise of the differential cross section as a function of gap size at the largest $\Delta\eta^F$ values. This rise is interpreted within the triple Pomeron-based approach of the PYTHIA8 model with a Donnachie-Landshoff Pomeron flux in terms of a Pomeron intercept of $\alpha_{\mathbb{P}}(0) = 1.058 \pm 0.003(\mathrm{stat.})\,^{+0.034}_{-0.039}(\mathrm{syst.})$. Since the bulk of the inelastic pp cross section is contained within the measured range, integrated cross sections are also obtained and compared with previous measurements. The contribution to the total inelastic cross section from the region $\xi_X < 10^{-5}$ is determined to be around 20%, which is considerably larger than is predicted by most models.

Acknowledgements

We are grateful to the HERWIG++ collaboration for their assistance in investigating the low p_{T} rapidity gap spectrum produced by their generator and to M. Ryskin, A. Martin and V. Khoze for supplying their prediction for the behaviour of the inelastic cross section as a function of ξ_{Cut}.

We thank CERN for the very successful operation of the LHC, as well as the support staff from our institutions, without whom ATLAS could not be operated efficiently.

We acknowledge the support of ANPCyT, Argentina; YerPhI, Armenia; ARC, Australia; BMWF, Austria; ANAS, Azerbaijan; SSTC, Belarus; CNPq and FAPESP, Brazil; NSERC, NRC and CFI, Canada; CERN; CONICYT, Chile; CAS, MOST and NSFC, China; COLCIENCIAS, Colombia; MSMT CR, MPO CR and VSC CR, Czech Republic; DNRF, DNSRC and Lundbeck Foundation, Denmark; ARTEMIS and ERC, European Union; IN2P3-CNRS, CEA-DSM/IRFU, France; GNAS, Georgia; BMBF, DFG, HGF, MPG and AvH Foundation, Germany; GSRT, Greece; ISF, MINERVA, GIF, DIP and Benoziyo Center, Israel; INFN, Italy; MEXT and JSPS, Japan; CNRST, Morocco; FOM and NWO, Netherlands; RCN, Norway; MNiSW, Poland; GRICES and FCT, Portugal; MERYS (MECTS), Romania; MES of Russia and ROSATOM, Russian Federation; JINR;

MSTD, Serbia; MSSR, Slovakia; ARRS and MVZT, Slovenia; DST/NRF, South Africa; MICINN, Spain; SRC and Wallenberg Foundation, Sweden; SER, SNSF and Cantons of Bern and Geneva, Switzerland; NSC, Taiwan; TAEK, Turkey; STFC, the Royal Society and Leverhulme Trust, United Kingdom; DOE and NSF, United States of America.

The crucial computing support from all WLCG partners is acknowledged gratefully, in particular from CERN and the ATLAS Tier-1 facilities at TRIUMF (Canada), NDGF (Denmark, Norway, Sweden), CC-IN2P3 (France), KIT/GridKA (Germany), INFN-CNAF (Italy), NL-T1 (Netherlands), PIC (Spain), ASGC (Taiwan), RAL (UK) and BNL (USA) and in the Tier-2 facilities worldwide.

References

1. ATLAS Collaboration, New J. Phys. **13** (2011) 053033 [arXiv:1012.5104 [hep-ex]].
2. CMS Collaboration, JHEP **1101** (2011) 079 [arXiv:1011.5531 [hep-ex]].
3. ALICE Collaboration, Eur. Phys. J. **C68** (2010) 345 [arXiv:1004.3514 [hep-ex]].
4. J. Bjorken, S. Brodsky and H. J. Lu, Phys. Lett. **B286** (1992) 153.
5. E. Feinberg and I. Pomerančuk, Suppl. Nuovo Cimento **3** (1956) 652.
6. G. Chew and S. Frautschi, Phys. Rev. Lett. **7** (1961) 394.
7. CDF Collaboration, Phys. Rev. Lett. **93** (2004) 141601 [hep-ex/0311023].
8. ATLAS Collaboration, Nature Comm. **2** (2011) 463.
9. TOTEM Collaboration, Europhys. Lett. **95** (2011) 41001 [arXiv:1110.1385 [hep-ex]].
10. TOTEM Collaboration, Europhys. Lett. **96** (2011) 21002 [arXiv:1110.1395 [hep-ex]].
11. A. Mueller, Phys. Rev. **D2** (1970) 2963.
12. F. Low, Phys. Rev. **D12** (1975) 163.
13. S. Nussinov, Phys. Rev. Lett. **34** (1975) 1286.
14. L. Gribov, E. Levin and M. Ryskin, Phys. Rep. **100** (1983) 1.
15. K. Golec-Biernat and M. Wüsthoff, Phys. Rev. **D59** (1998) 014017 [hep-ph/9807513].
16. E. Iancu, A. Leonidov and L. McLerran, Nucl. Phys. **A692** (2001) 583 [hep-ph/0011241].
17. Z. Ajaltouni *et al.*, *Proceedings of the 'HERA and the LHC' workshop series, chapter 5*, arXiv:0903.3861 [hep-ex].

Table 2: The measured differential cross section data points for $p_{\mathrm{T}}^{\mathrm{cut}} = 200$ MeV, with each value corresponding to an average over the given $\Delta\eta^F$ range. Also quoted are the percentage statistical (δ_{stat}) uncertainty and the upward ($+\delta_{\mathrm{tot}}$) and downward ($-\delta_{\mathrm{tot}}$) total uncertainties, obtained by adding all uncertainties in quadrature. The remaining columns contain the percentage shifts due to each of the contributing systematic sources, which are correlated between data points. Those due to the modelling of final state particle production (δ_{py6}), the modelling of the ξ_X, ξ_Y and t dependences (δ_{pho}) and variation of the CD (δ_{cd}) cross section in the unfolding procedure are applied symmetrically as upward and downward uncertainties, as are those due to the dead material budget in the tracking region (δ_{mat}) and the MBTS response (δ_{mbts}). The uncertainties due to variations in the relative energy scale in data and MC are evaluated separately for upward (δ_{e+}) and downward (δ_{e-}) shifts, as are the modelling uncertainties due to enhancing (δ_{sd}) or reducing (δ_{dd}) the σ_{SD}/σ_{DD} cross section ratio. Minus signs appear where the shift in a variable is anti-correlated rather than correlated with the shift in the differential cross section. The 3.4% normalisation uncertainty due to the luminosity measurement is also included in the $\pm\delta_{\mathrm{tot}}$ values. These data points can be obtained from the HEPDATA database [90], along with their counterparts for $p_{\mathrm{T}}^{\mathrm{cut}} = 400$, 600 and 800 MeV. A Rivet [91] routine is also available.

$\Delta\eta^F$	$\mathrm{d}\sigma/\mathrm{d}\Delta\eta^F$ [mb]	δ_{stat} [%]	$+\delta_{\mathrm{tot}}$ [%]	$-\delta_{\mathrm{tot}}$ [%]	δ_{py6} [%]	δ_{pho} [%]	$\delta_{\mathrm{e+}}$ [%]	$\delta_{\mathrm{e-}}$ [%]	δ_{sd} [%]	δ_{dd} [%]	δ_{cd} [%]	δ_{mat} [%]	δ_{mbts} [%]
0.0–0.4	85	0.2	9.4	-9.5	-2.9	-7.6	3.0	-3.2	0.1	-0.1	0.0	-1.1	-0.1
0.4–0.8	26	0	15	-15	4	14	-3	3	-0	0	0	2	0
0.8–1.2	10	0	20	-20	5	18	-6	5	-0	0	0	3	0
1.2–1.6	5	0	21	-21	10	17	-6	7	0	-0	0	2	-0
1.6–2.0	2.8	0	22	-22	15	13	-7	9	0	-0	-0	3	0
2.0–2.2	2.1	1	18	-18	15	5	-9	8	-0	0	-0	1	0
2.2–2.4	1.8	1	18	-18	14	7	-8	8	-0	0	-0	1	0
2.4–2.6	1.7	1	15	-14	9	2	-9	10	-0	0	-0	-3	0
2.6–2.8	1.6	1	14	-13	5	1	-11	13	-0	0	-0	-0	0
2.8–3.0	1.4	1	14	-10	5	2	-8	12	-0	0	-1	-1	0
3.0–3.2	1.3	1	11	-9	4	2	-7	10	-1	0	-0	1	1
3.2–3.4	1.2	1.3	8.4	-9.9	3.5	3.7	-7.5	5.4	-0.6	0.4	-0.4	1.1	0.6
3.4–3.6	1.20	1.3	7.3	-8.2	4.4	0.4	-4.9	3.4	-0.7	0.6	-0.5	-2.6	0.9
3.6–3.8	1.1	1	11	-9	6	5	-4	7	-1	0	-1	-1	1
3.8–4.0	1.0	2	10	-10	7	4	-4	4	-0	0	-1	-2	1
4.0–4.2	1.01	1.6	5.7	-8.5	3.1	2.6	-6.2	0.2	-0.7	0.6	-1.0	-0.6	0.8
4.2–4.4	0.9	1	11	-11	5	8	-2	3	-1	1	-1	-3	1
4.4–4.6	0.92	1.8	7.8	-7.8	3.9	5.0	-2.1	2.1	-0.3	0.3	-1.0	-0.7	0.4
4.6–4.8	0.91	1.7	7.8	-8.4	4.5	4.8	-3.3	0.8	-0.9	0.7	-0.9	-0.3	1.1
4.8–5.0	0.88	2	10	-10	6	7	-0	3	-1	1	-1	-1	1
5.0–5.2	0.87	1.6	8.2	-7.8	5.3	4.0	0.5	2.5	-0.7	0.5	-0.9	-0.4	0.9
5.2–5.4	0.89	1.8	7.3	-7.5	5.5	2.5	-1.5	-1.6	-0.7	0.5	-0.8	-0.5	0.9
5.4–5.6	0.9	1	12	-12	8	7	1	1	-1	1	-1	2	1
5.6–5.8	0.95	1.2	7.5	-8.4	5.1	3.8	-2.2	-3.5	-1.0	0.8	-0.8	0.8	1.3
5.8–6.0	0.9	1	11	-10	7	6	3	0	-1	0	-1	1	1
6.0–6.2	0.95	1.4	8.6	-9.3	7.0	2.7	0.2	-3.5	-0.6	0.5	-1.1	1.5	1.0
6.2–6.4	1.0	1	12	-13	6	7	7	-8	-1	1	-1	4	1
6.4–6.6	0.99	1.3	7.8	-7.9	3.6	5.7	-0.2	-0.5	-0.6	0.5	-0.7	0.8	1.2
6.6–6.8	1.06	1.3	5.4	-5.4	2.0	3.0	-0.9	1.0	-0.5	0.4	-0.5	-0.4	1.0
6.8–7.0	1.08	1.3	5.4	-5.2	-0.0	3.3	-0.9	1.7	-0.1	0.1	-0.5	-1.3	0.6
7.0–7.2	1.11	1.2	4.4	-4.5	-1.9	-0.2	-1.2	1.0	-0.4	0.3	-0.1	-0.6	1.1
7.2–7.4	1.11	0.9	5.3	-5.7	-3.4	0.1	1.2	-2.5	-0.4	0.3	-0.2	-1.0	1.3
7.4–7.6	1.13	1.0	5.1	-6.1	-3.2	-0.6	-0.0	-3.3	-0.6	0.4	-0.2	0.5	1.6
7.6–7.8	1.17	1.0	5.9	-6.7	-4.0	-1.7	-0.0	-3.1	-0.3	0.2	-0.2	1.2	1.3
7.8–8.0	1.20	1.0	5.7	-5.4	-4.0	-0.5	1.0	1.8	-0.0	0.0	-0.1	-0.0	1.0

18. R. Brower, J. Polchinski, M. Strassler and C. Tan, JHEP **0712** (2007) 005 [hep-th/0603115].
19. ATLAS Collaboration, Eur. Phys. J. **C71** (2011) 1630 [arXiv:1101.2185 [hep-ex]].
20. K. Goulianos, Phys. Rep. **101** (1983) 169.
21. G. Alberi and G. Goggi, Phys. Rep. **74** (1981) 1.
22. N. Zotov and V. Tsarev, Sov. Phys. Usp. **31** (1988) 119.
23. A. Kaidalov, Phys. Rep. **50** (1979) 157.
24. M. Albrow, T. Coughlin and J. Forshaw, Prog. Part. Nucl. Phys. **65** (2010) 149 [arXiv:1006.1289 [hep-ph]].
25. UA4 Collaboration, Phys. Lett. **B186** (1987) 227.
26. UA5 Collaboration, Z. Phys. **C33** (1986) 175.
27. E710 Collaboration, Phys. Lett. **B301** (1993) 313.
28. CDF Collaboration, Phys. Rev. **D50** (1994) 5535.
29. H1 Collaboration, Z. Phys. **C74** (1997) 221 [hep-ex/9702003].
30. ZEUS Collaboration, Z. Phys. **C75** (1997) 421 [hep-ex/9704008].
31. H1 Collaboration, Eur. Phys. J. **C48** (2006) 715 [hep-ex/0606004].
32. ZEUS Collaboration, Nucl. Phys. **B816** (2009) 1 [arXiv:0812.2003 [hep-ex]].
33. H1 Collaboration, Eur. Phys. J. **C71** (2011) 1578 [arXiv:1010.1476 [hep-ex]].
34. CDF Collaboration, Phys. Rev. Lett. **87** (2001) 141802 [hep-ex/0107070].
35. D. Joyce *et al.*, Phys. Rev. **D48** (1993) 1943.
36. UA8 Collaboration, Eur. Phys. J. **C25** (2002) 361 [hep-ex/0205037].
37. G. Ingelman and P. Schlein, Phys. Lett. **B152** (1985) 256.
38. A. Kaidalov, V. Khoze, Y. Pirogov and N. Ter-Isaakyan, Phys. Lett. **B45** (1973) 493.
39. R. Field and G. Fox, Nucl. Phys. **B80** (1974) 367.
40. T. Sjöstrand, S. Mrenna and P. Skands, JHEP **0605** (2006) 026 [hep-ph/0603175].
41. T. Sjöstrand, S. Mrenna and P. Skands, Comput. Phys. Commun. **178** (2008) 852 [arXiv:0710.3820 [hep-ph]].
42. R. Engel, Z. Phys. **C66** (1995) 203.
43. M. Ryskin, A. Martin and V. Khoze, Eur. Phys. J. **C71** (2011) 1617 [arXiv:1102.2844 [hep-ph]].
44. E. Gotsman, E. Levin and U. Maor, Eur. Phys. J. **C71** (2011) 1553 [arXiv:1010.5323 [hep-ph]].
45. ATLAS Collaboration, JINST **3** (2008) S08003.
46. ATLAS Collaboration, *Updated Luminosity Determination in pp Collisions at* $\sqrt{s} = 7$ TeV *using the ATLAS Detector*, ATLAS-CONF-2011-011 (2011).
47. ATLAS Collaboration, Eur. Phys. J. **C71** (2011) 1512 [arXiv:1009.5908 [hep-ex]].
48. W. Lampl *et al.*, *Calorimeter Clustering Algorithms: Description and Performance*, ATL-LARG-PUB-2008-002; ATL-COM-LARG-2008-003 (2008).
49. ATLAS Collaboration, Eur. Phys. J. C **70** (2010) 723 [arXiv:0912.2642 [physics.ins-det]].
50. ATLAS Collaboration, JHEP **1012** (2010) 060 [arXiv:1010.2130 [hep-ex]].
51. ATLAS Collaboration, *Response of the ATLAS Calorimeters to Single Isolated Hadrons Produced in Proton-proton Collisions at* $\sqrt{s} = 900$ GeV, ATLAS-CONF-2010-017 (2010).
52. ATLAS Collaboration, *ATLAS Calorimeter Response to Single Isolated Hadrons and Estimation of the Calorimeter Jet Energy Scale Uncertainty*, ATLAS-CONF-2010-052 (2010).
53. ATLAS Collaboration, *ATLAS Calorimeter Response to Single Isolated Hadrons and Estimation of the Calorimeter Jet Scale Uncertainty*, ATLAS-CONF-2011-028 (2011).
54. J. Pinfold *et al.*, Nucl. Instrum. Meth. **A593** (2008) 324.
55. J. Archambault *et al.*, JINST **3** (2008) P02002.
56. B. Dowler *et al.*, Nucl. Instrum. Meth. **A482** (2002) 94.
57. D. Roy and R. Roberts, Nucl. Phys. **B77** (1974) 240.
58. A. Donnachie and P. Landshoff, Phys. Lett. **B296** (1992) 227 [hep-ph/9209205].
59. J. Cudell, K. Kang and S. Kim, Phys. Lett. **B395** (1997) 311 [hep-ph/9601336].
60. M. Good and W. Walker, Phys. Rev. **120** (1960) 1857.
61. F. Bopp, R. Engel and J. Ranft, *Rapidity gaps and the PHOJET Monte Carlo*, hep-ph/9803437.
62. G. Schuler and T. Sjöstrand, Phys. Rev. **D49** (1994) 2257.
63. P. Bruni and G. Ingelman, Phys. Lett. **B311** (1993) 317.
64. E. Berger, J. Collins, D. Soper and G. Sterman, Nucl. Phys. **B286** (1987) 704.
65. K. Streng, *Hard QCD scatterings in diffractive reactions at HERA*, CERN-TH-4949 (1988).
66. A. Donnachie and P. Landshoff, Nucl. Phys. **B244** (1984) 322.
67. H. Jung, Comput. Phys. Commun. **86** (1995) 147.
68. CDF Collaboration, Phys. Rev. **D50** (1994) 5518.
69. B. Andersson, G. Gustafson, G. Ingelman and T. Sjöstrand, Phys. Rep. **97** (1983) 31.
70. S. Navin, *Diffraction in Pythia*, arXiv:1005.3894 [hep-ph].
71. ATLAS Collaboration, *Charged particle multiplicities in pp interactions at* $\sqrt{s} = 0.9$ *and* 7 TeV *in a diffractive limited phase space measured with the ATLAS detector at the LHC and a new* PYTHIA*6 tune*, ATLAS-CONF-2010-031 (2010).
72. ATLAS Cololaboration, *ATLAS tunes of PYTHIA 6 and Pythia 8 for MC11*, ATL-PHYS-PUB-2011-009 (2009).
73. A. Capella, U. Sukhatme, C. Tan and J. Tran Thanh Van, Phys. Rep. **236** (1994) 225.
74. V. Abramovsky, V. Gribov and O. Kancheli, Yad. Fiz. **18** (1973) 595 [Sov. J. Nucl. Phys. **18** (1974) 308].
75. A. Capella, A. Kaidalov, C. Merino and J. Tran Thanh Van, Phys. Lett. **B343** (1995) 403 [hep-ph/9407372].
76. A. Capella *et al.*, Phys. Rev. **D53** (1996) 2309 [hep-ph/9506454].
77. M. Bähr *et al.*, Eur. Phys. J. **C58** (2008) 639 [arXiv:0803.0883 [hep-ph]].
78. S. Gieseke, C. A. Röhr and A. Siódmok, *Multiple Partonic Interaction Developments in Herwig++*, arXiv:1110.2675 [hep-ph].
79. HERWIG++ Collaboration, *Minimum Bias and Underlying Event tunes*, URL: http://projects.hepforge.org/herwig/trac/wiki/MB_UE_tunes.
80. A. Donnachie and P. Landshoff, Phys. Lett. **B595** (2004) 393 [hep-ph/0402081].
81. S. Gieseke *et al.*, *Herwig++ 2.5 Release Note*, arXiv:1102.1672 [hep-ph].
82. ATLAS Collaboration, Eur. Phys. J. **C70** (2010) 823 [arXiv:1005.4568 [physics.ins-det]].
83. GEANT4 Collaboration, Nucl. Instrum. Meth. **A506** (2003) 250.
84. G. D'Agostini, Nucl. Instrum. Meth. **A362** (1995) 487.
85. A. Höcker and V. Kartvelishvili, Nucl. Instrum. Meth. **A372** (1996) 469 [hep-ph/9509307].
86. A. Kiryunic and P. Strizenec, *Validation of the Local Hadronic Calibration Scheme of ATLAS with Combined Beam Test Data in the Endcap and Forward Regions*, Proceedings of the 13th ICATPP Conference, Como, Italy, 2011.
87. V. A. Khoze *et al.*, Eur. Phys. J. **C69** (2010) 85 [arXiv:1005.4839 [hep-ph]].

88. A. Martin, M. Ryskin and V. Khoze, *From hard to soft high-energy pp interactions*, arXiv:1110.1973 [hep-ph].
89. M. Ryskin, private communication.
90. *The Durham HepData Reaction Database*, URL: http://durpdg.dur.ac.uk/.
91. B. Waugh *et al.*, *HZTool and Rivet: Toolkit and Framework for the Comparison of Simulated Final States and Data at Colliders*, hep-ph/0605034.

The ATLAS Collaboration

G. Aad[48], B. Abbott[110], J. Abdallah[11], A.A. Abdelalim[49], A. Abdesselam[117], O. Abdinov[10], B. Abi[111], M. Abolins[87], O.S. AbouZeid[157], H. Abramowicz[152], H. Abreu[114], E. Acerbi[88a,88b], B.S. Acharya[163a,163b], L. Adamczyk[37], D.L. Adams[24], T.N. Addy[56], J. Adelman[174], M. Aderholz[98], S. Adomeit[97], P. Adragna[74], T. Adye[128], S. Aefsky[22], J.A. Aguilar-Saavedra[123b,a], M. Aharrouche[80], S.P. Ahlen[21], F. Ahles[48], A. Ahmad[147], M. Ahsan[40], G. Aielli[132a,132b], T. Akdogan[18a], T.P.A. Åkesson[78], G. Akimoto[154], A.V. Akimov [93], A. Akiyama[66], M.S. Alam[1], M.A. Alam[75], J. Albert[168], S. Albrand[55], M. Aleksa[29], I.N. Aleksandrov[64], F. Alessandria[88a], C. Alexa[25a], G. Alexander[152], G. Alexandre[49], T. Alexopoulos[9], M. Alhroob[20], M. Aliev[15], G. Alimonti[88a], J. Alison[119], M. Aliyev[10], P.P. Allport[72], S.E. Allwood-Spiers[53], J. Almond[81], A. Aloisio[101a,101b], R. Alon[170], A. Alonso[78], B. Alvarez Gonzalez[87], M.G. Alviggi[101a,101b], K. Amako[65], P. Amaral[29], C. Amelung[22], V.V. Ammosov[127], A. Amorim[123a,b], G. Amorós[166], N. Amram[152], C. Anastopoulos[29], L.S. Ancu[16], N. Andari[114], T. Andeen[34], C.F. Anders[20], G. Anders[58a], K.J. Anderson[30], A. Andreazza[88a,88b], V. Andrei[58a], M-L. Andrieux[55], X.S. Anduaga[69], A. Angerami[34], F. Anghinolfi[29], A. Anisenkov[106], N. Anjos[123a], A. Annovi[47], A. Antonaki[8], M. Antonelli[47], A. Antonov[95], J. Antos[143b], F. Anulli[131a], S. Aoun[82], L. Aperio Bella[4], R. Apolle[117,c], G. Arabidze[87], I. Aracena[142], Y. Arai[65], A.T.H. Arce[44], J.P. Archambault[28], S. Arfaoui[147], J-F. Arguin[14], E. Arik[18a,*], M. Arik[18a], A.J. Armbruster[86], O. Arnaez[80], C. Arnault[114], A. Artamonov[94], G. Artoni[131a,131b], D. Arutinov[20], S. Asai[154], R. Asfandiyarov[171], S. Ask[27], B. Åsman[145a,145b], L. Asquith[5], K. Assamagan[24], A. Astbury[168], A. Astvatsatourov[52], B. Aubert[4], E. Auge[114], K. Augsten[126], M. Aurousseau[144a], G. Avolio[162], R. Avramidou[9], D. Axen[167], C. Ay[54], G. Azuelos[92,d], Y. Azuma[154], M.A. Baak[29], G. Baccaglioni[88a], C. Bacci[133a,133b], A.M. Bach[14], H. Bachacou[135], K. Bachas[29], G. Bachy[29], M. Backes[49], M. Backhaus[20], E. Badescu[25a], P. Bagnaia[131a,131b], S. Bahinipati[2], Y. Bai[32a], D.C. Bailey[157], T. Bain[157], J.T. Baines[128], O.K. Baker[174], M.D. Baker[24], S. Baker[76], E. Banas[38], P. Banerjee[92], Sw. Banerjee[171], D. Banfi[29], A. Bangert[149], V. Bansal[168], H.S. Bansil[17], L. Barak[170], S.P. Baranov[93], A. Barashkou[64], A. Barbaro Galtieri[14], T. Barber[48], E.L. Barberio[85], D. Barberis[50a,50b], M. Barbero[20], D.Y. Bardin[64], T. Barillari[98], M. Barisonzi[173], T. Barklow[142], N. Barlow[27], B.M. Barnett[128], R.M. Barnett[14], A. Baroncelli[133a], G. Barone[49], A.J. Barr[117], F. Barreiro[79], J. Barreiro Guimarães da Costa[57], P. Barrillon[114], R. Bartoldus[142], A.E. Barton[70], V. Bartsch[148], R.L. Bates[53], L. Batkova[143a], J.R. Batley[27], A. Battaglia[16], M. Battistin[29], F. Bauer[135], H.S. Bawa[142,e], S. Beale[97], B. Beare[157], T. Beau[77], P.H. Beauchemin[160], R. Beccherle[50a], P. Bechtle[20], H.P. Beck[16], S. Becker[97], M. Beckingham[137], K.H. Becks[173], A.J. Beddall[18c], A. Beddall[18c], S. Bedikian[174], V.A. Bednyakov[64], C.P. Bee[82], M. Begel[24], S. Behar Harpaz[151], P.K. Behera[62], M. Beimforde[98], C. Belanger-Champagne[84], P.J. Bell[49], W.H. Bell[49], G. Bella[152], L. Bellagamba[19a], F. Bellina[29], M. Bellomo[29], A. Belloni[57], O. Beloborodova[106,f], K. Belotskiy[95], O. Beltramello[29], S. Ben Ami[151], O. Benary[152], D. Benchekroun[134a], C. Benchouk[82], M. Bendel[80], N. Benekos[164], Y. Benhammou[152], E. Benhar Noccioli[49], J.A. Benitez Garcia[158b], D.P. Benjamin[44], M. Benoit[114], J.R. Bensinger[22], K. Benslama[129], S. Bentvelsen[104], D. Berge[29], E. Bergeaas Kuutmann[41], N. Berger[4], F. Berghaus[168], E. Berglund[104], J. Beringer[14], P. Bernat[76], R. Bernhard[48], C. Bernius[24], T. Berry[75], C. Bertella[82], A. Bertin[19a,19b], F. Bertinelli[29], F. Bertolucci[121a,121b], M.I. Besana[88a,88b], N. Besson[135], S. Bethke[98], W. Bhimji[45], R.M. Bianchi[29], M. Bianco[71a,71b], O. Biebel[97], S.P. Bieniek[76], K. Bierwagen[54], J. Biesiada[14], M. Biglietti[133a], H. Bilokon[47], M. Bindi[19a,19b], S. Binet[114], A. Bingul[18c], C. Bini[131a,131b], C. Biscarat[176], U. Bitenc[48], K.M. Black[21], R.E. Blair[5], J.-B. Blanchard[135], G. Blanchot[29], T. Blazek[143a], C. Blocker[22], J. Blocki[38], A. Blondel[49], W. Blum[80], U. Blumenschein[54], G.J. Bobbink[104], V.B. Bobrovnikov[106], S.S. Bocchetta[78], A. Bocci[44], C.R. Boddy[117], M. Boehler[41], J. Boek[173], N. Boelaert[35], S. Böser[76], J.A. Bogaerts[29], A. Bogdanchikov[106], A. Bogouch[89,*], C. Bohm[145a], V. Boisvert[75], T. Bold[37], V. Boldea[25a], N.M. Bolnet[135], M. Bona[74], V.G. Bondarenko[95], M. Bondioli[162], M. Boonekamp[135], G. Boorman[75], C.N. Booth[138], S. Bordoni[77], C. Borer[16], A. Borisov[127], G. Borissov[70], I. Borjanovic[12a], M. Borri[81], S. Borroni[86], K. Bos[104], D. Boscherini[19a], M. Bosman[11], H. Boterenbrood[104], D. Botterill[128], J. Bouchami[92], J. Boudreau[122], E.V. Bouhova-Thacker[70], D. Boumediene[33], C. Bourdarios[114], N. Bousson[82], A. Boveia[30], J. Boyd[29], I.R. Boyko[64], N.I. Bozhko[127], I. Bozovic-Jelisavcic[12b], J. Bracinik[17], A. Braem[29], P. Branchini[133a], G.W. Brandenburg[57], A. Brandt[7], G. Brandt[117], O. Brandt[54], U. Bratzler[155], B. Brau[83], J.E. Brau[113], H.M. Braun[173], B. Brelier[157], J. Bremer[29], R. Brenner[165], S. Bressler[170], D. Breton[114], D. Britton[53], F.M. Brochu[27], I. Brock[20], R. Brock[87], T.J. Brodbeck[70], E. Brodet[152], F. Broggi[88a], C. Bromberg[87], J. Bronner[98], G. Brooijmans[34], W.K. Brooks[31b], G. Brown[81], H. Brown[7], P.A. Bruckman de Renstrom[38], D. Bruncko[143b], R. Bruneliere[48], S. Brunet[60], A. Bruni[19a], G. Bruni[19a], M. Bruschi[19a], T. Buanes[13], Q. Buat[55], F. Bucci[49], J. Buchanan[117], N.J. Buchanan[2], P. Buchholz[140], R.M. Buckingham[117], A.G. Buckley[45], S.I. Buda[25a], I.A. Budagov[64], B. Budick[107], V. Büscher[80], L. Bugge[116], O. Bulekov[95], M. Bunse[42], T. Buran[116], H. Burckhart[29], S. Burdin[72], T. Burgess[13], S. Burke[128], E. Busato[33], P. Bussey[53], C.P. Buszello[165], F. Butin[29], B. Butler[142], J.M. Butler[21], C.M. Buttar[53], J.M. Butterworth[76], W. Buttinger[27], S. Cabrera Urbán[166], D. Caforio[19a,19b], O. Cakir[3a], P. Calafiura[14], G. Calderini[77], P. Calfayan[97], R. Calkins[105], L.P. Caloba[23a], R. Caloi[131a,131b], D. Calvet[33], S. Calvet[33], R. Camacho Toro[33], P. Camarri[132a,132b], M. Cambiaghi[118a,118b], D. Cameron[116], L.M. Caminada[14], S. Campana[29], M. Campanelli[76], V. Canale[101a,101b], F. Canelli[30,g], A. Canepa[158a], J. Cantero[79], L. Capasso[101a,101b], M.D.M. Capeans Garrido[29], I. Caprini[25a], M. Caprini[25a], D. Capriotti[98], M. Capua[36a,36b], R. Caputo[80], C. Caramarcu[24], R. Cardarelli[132a], T. Carli[29], G. Carlino[101a], L. Carminati[88a,88b], B. Caron[84], S. Caron[103], G.D. Carrillo Montoya[171], A.A. Carter[74], J.R. Carter[27], J. Carvalho[123a,h], D. Casadei[107], M.P. Casado[11], M. Cascella[121a,121b], C. Caso[50a,50b,*], A.M. Castaneda Hernandez[171], E. Castaneda-Miranda[171], V. Castillo Gimenez[166], N.F. Castro[123a], G. Cataldi[71a], F. Cataneo[29], A. Catinaccio[29], J.R. Catmore[29], A. Cattai[29], G. Cattani[132a,132b], S. Caughron[87], D. Cauz[163a,163c], P. Cavalleri[77], D. Cavalli[88a], M. Cavalli-Sforza[11], V. Cavasinni[121a,121b], F. Ceradini[133a,133b], A.S. Cerqueira[23b], A. Cerri[29], L. Cerrito[74], F. Cerutti[47], S.A. Cetin[18b], F. Cevenini[101a,101b], A. Chafaq[134a], D. Chakraborty[105], K. Chan[2], B. Chapleau[84], J.D. Chapman[27], J.W. Chapman[86], E. Chareyre[77], D.G. Charlton[17], V. Chavda[81], C.A. Chavez Barajas[29], S. Cheatham[84], S. Chekanov[5], S.V. Chekulaev[158a], G.A. Chelkov[64], M.A. Chelstowska[103], C. Chen[63], H. Chen[24], S. Chen[32c], T. Chen[32c], X. Chen[171], S. Cheng[32a],

A. Cheplakov[64], V.F. Chepurnov[64], R. Cherkaoui El Moursli[134e], V. Chernyatin[24], E. Cheu[6], S.L. Cheung[157], L. Chevalier[135], G. Chiefari[101a,101b], L. Chikovani[51a], J.T. Childers[29], A. Chilingarov[70], G. Chiodini[71a], M.V. Chizhov[64], G. Choudalakis[30], S. Chouridou[136], I.A. Christidi[76], A. Christov[48], D. Chromek-Burckhart[29], M.L. Chu[150], J. Chudoba[124], G. Ciapetti[131a,131b], K. Ciba[37], A.K. Ciftci[3a], R. Ciftci[3a], D. Cinca[33], V. Cindro[73], M.D. Ciobotaru[162], C. Ciocca[19a], A. Ciocio[14], M. Cirilli[86], M. Citterio[88a], M. Ciubancan[25a], A. Clark[49], P.J. Clark[45], W. Cleland[122], J.C. Clemens[82], B. Clement[55], C. Clement[145a,145b], R.W. Clifft[128], Y. Coadou[82], M. Cobal[163a,163c], A. Coccaro[171], J. Cochran[63], P. Coe[117], J.G. Cogan[142], J. Coggeshall[164], E. Cogneras[176], J. Colas[4], A.P. Colijn[104], N.J. Collins[17], C. Collins-Tooth[53], J. Collot[55], G. Colon[83], P. Conde Muiño[123a], E. Coniavitis[117], M.C. Conidi[11], M. Consonni[103], V. Consorti[48], S. Constantinescu[25a], C. Conta[118a,118b], F. Conventi[101a,i], J. Cook[29], M. Cooke[14], B.D. Cooper[76], A.M. Cooper-Sarkar[117], K. Copic[14], T. Cornelissen[173], M. Corradi[19a], F. Corriveau[84,j], A. Cortes-Gonzalez[164], G. Cortiana[98], G. Costa[88a], M.J. Costa[166], D. Costanzo[138], T. Costin[30], D. Côté[29], R. Coura Torres[23a], L. Courneyea[168], G. Cowan[75], C. Cowden[27], B.E. Cox[81], K. Cranmer[107], F. Crescioli[121a,121b], M. Cristinziani[20], G. Crosetti[36a,36b], R. Crupi[71a,71b], S. Crépé-Renaudin[55], C.-M. Cuciuc[25a], C. Cuenca Almenar[174], T. Cuhadar Donszelmann[138], M. Curatolo[47], C.J. Curtis[17], C. Cuthbert[149], P. Cwetanski[60], H. Czirr[140], P. Czodrowski[43], Z. Czyczula[174], S. D'Auria[53], M. D'Onofrio[72], A. D'Orazio[131a,131b], P.V.M. Da Silva[23a], C. Da Via[81], W. Dabrowski[37], T. Dai[86], C. Dallapiccola[83], M. Dam[35], M. Dameri[50a,50b], D.S. Damiani[136], H.O. Danielsson[29], D. Dannheim[98], V. Dao[49], G. Darbo[50a], G.L. Darlea[25b], C. Daum[104], W. Davey[20], T. Davidek[125], N. Davidson[85], R. Davidson[70], E. Davies[117,c], M. Davies[92], A.R. Davison[76], Y. Davygora[58a], E. Dawe[141], I. Dawson[138], J.W. Dawson[5,*], R.K. Daya-Ishmukhametova[22], K. De[7], R. de Asmundis[101a], S. De Castro[19a,19b], P.E. De Castro Faria Salgado[24], S. De Cecco[77], J. de Graat[97], N. De Groot[103], P. de Jong[104], C. De La Taille[114], H. De la Torre[79], B. De Lotto[163a,163c], L. de Mora[70], L. De Nooij[104], D. De Pedis[131a], A. De Salvo[131a], U. De Sanctis[163a,163c], A. De Santo[148], J.B. De Vivie De Regie[114], S. Dean[76], W.J. Dearnaley[70], R. Debbe[24], C. Debenedetti[45], D.V. Dedovich[64], J. Degenhardt[119], M. Dehchar[117], C. Del Papa[163a,163c], J. Del Peso[79], T. Del Prete[121a,121b], T. Delemontex[55], M. Deliyergiyev[73], A. Dell'Acqua[29], L. Dell'Asta[21], M. Della Pietra[101a,i], D. della Volpe[101a,101b], M. Delmastro[4], N. Delruelle[29], P.A. Delsart[55], C. Deluca[147], S. Demers[174], M. Demichev[64], B. Demirkoz[11,k], J. Deng[162], S.P. Denisov[127], D. Derendarz[38], J.E. Derkaoui[134d], F. Derue[77], P. Dervan[72], K. Desch[20], E. Devetak[147], P.O. Deviveiros[104], A. Dewhurst[128], B. DeWilde[147], S. Dhaliwal[157], R. Dhullipudi[24,l], A. Di Ciaccio[132a,132b], L. Di Ciaccio[4], A. Di Girolamo[29], B. Di Girolamo[29], S. Di Luise[133a,133b], A. Di Mattia[171], B. Di Micco[29], R. Di Nardo[47], A. Di Simone[132a,132b], R. Di Sipio[19a,19b], M.A. Diaz[31a], F. Diblen[18c], E.B. Diehl[86], J. Dietrich[41], T.A. Dietzsch[58a], S. Diglio[85], K. Dindar Yagci[39], J. Dingfelder[20], C. Dionisi[131a,131b], P. Dita[25a], S. Dita[25a], F. Dittus[29], F. Djama[82], T. Djobava[51b], M.A.B. do Vale[23c], A. Do Valle Wemans[123a], T.K.O. Doan[4], M. Dobbs[84], R. Dobinson [29,*], D. Dobos[29], E. Dobson[29,m], J. Dodd[34], C. Doglioni[49], T. Doherty[53], Y. Doi[65,*], J. Dolejsi[125], I. Dolenc[73], Z. Dolezal[125], B.A. Dolgoshein[95,*], T. Dohmae[154], M. Donadelli[23d], M. Donega[119], J. Donini[33], J. Dopke[29], A. Doria[101a], A. Dos Anjos[171], M. Dosil[11], A. Dotti[121a,121b], M.T. Dova[69], J.D. Dowell[17], A.D. Doxiadis[104], A.T. Doyle[53], Z. Drasal[125], J. Drees[173], N. Dressnandt[119], H. Drevermann[29], C. Driouichi[35], M. Dris[9], J. Dubbert[98], S. Dube[14], E. Duchovni[170], G. Duckeck[97], A. Dudarev[29], F. Dudziak[63], M. Dührssen [29], I.P. Duerdoth[81], L. Duflot[114], M-A. Dufour[84], M. Dunford[29], H. Duran Yildiz[3a], R. Duxfield[138], M. Dwuznik[37], F. Dydak [29], M. Düren[52], W.L. Ebenstein[44], J. Ebke[97], S. Eckweiler[80], K. Edmonds[80], C.A. Edwards[75], N.C. Edwards[53], W. Ehrenfeld[41], T. Ehrich[98], T. Eifert[142], G. Eigen[13], K. Einsweiler[14], E. Eisenhandler[74], T. Ekelof[165], M. El Kacimi[134c], M. Ellert[165], S. Elles[4], F. Ellinghaus[80], K. Ellis[74], N. Ellis[29], J. Elmsheuser[97], M. Elsing[29], D. Emeliyanov[128], R. Engelmann[147], A. Engl[97], B. Epp[61], A. Eppig[86], J. Erdmann[54], A. Ereditato[16], D. Eriksson[145a], J. Ernst[1], M. Ernst[24], J. Ernwein[135], D. Errede[164], S. Errede[164], E. Ertel[80], M. Escalier[114], C. Escobar[122], X. Espinal Curull[11], B. Esposito[47], F. Etienne[82], A.I. Etienvre[135], E. Etzion[152], D. Evangelakou[54], H. Evans[60], L. Fabbri[19a,19b], C. Fabre[29], R.M. Fakhrutdinov[127], S. Falciano[131a], Y. Fang[171], M. Fanti[88a,88b], A. Farbin[7], A. Farilla[133a], J. Farley[147], T. Farooque[157], S.M. Farrington[117], P. Farthouat[29], P. Fassnacht[29], D. Fassouliotis[8], B. Fatholahzadeh[157], A. Favareto[88a,88b], L. Fayard[114], S. Fazio[36a,36b], R. Febbraro[33], P. Federic[143a], O.L. Fedin[120], W. Fedorko[87], M. Fehling-Kaschek[48], L. Feligioni[82], D. Fellmann[5], C. Feng[32d], E.J. Feng[30], A.B. Fenyuk[127], J. Ferencei[143b], J. Ferland[92], W. Fernando[108], S. Ferrag[53], J. Ferrando[53], V. Ferrara[41], A. Ferrari[165], P. Ferrari[104], R. Ferrari[118a], A. Ferrer[166], M.L. Ferrer[47], D. Ferrere[49], C. Ferretti[86], A. Ferretto Parodi[50a,50b], M. Fiascaris[30], F. Fiedler[80], A. Filipčič[73], A. Filippas[9], F. Filthaut[103], M. Fincke-Keeler[168], M.C.N. Fiolhais[123a,h], L. Fiorini[166], A. Firan[39], G. Fischer[41], P. Fischer [20], M.J. Fisher[108], M. Flechl[48], I. Fleck[140], J. Fleckner[80], P. Fleischmann[172], S. Fleischmann[173], T. Flick[173], L.R. Flores Castillo[171], M.J. Flowerdew[98], M. Fokitis[9], T. Fonseca Martin[16], D.A. Forbush[137], A. Formica[135], A. Forti[81], D. Fortin[158a], J.M. Foster[81], D. Fournier[114], A. Foussat[29], A.J. Fowler[44], K. Fowler[136], H. Fox[70], P. Francavilla[11], S. Franchino[118a,118b], D. Francis[29], T. Frank[170], M. Franklin[57], S. Franz[29], M. Fraternali[118a,118b], S. Fratina[119], S.T. French[27], F. Friedrich [43], R. Froeschl[29], D. Froidevaux[29], J.A. Frost[27], C. Fukunaga[155], E. Fullana Torregrosa[29], J. Fuster[166], C. Gabaldon[29], O. Gabizon[170], T. Gadfort[24], S. Gadomski[49], G. Gagliardi[50a,50b], P. Gagnon[60], C. Galea[97], E.J. Gallas[117], V. Gallo[16], B.J. Gallop[128], P. Gallus[124], K.K. Gan[108], Y.S. Gao[142,e], V.A. Gapienko[127], A. Gaponenko[14], F. Garberson[174], M. Garcia-Sciveres[14], C. García[166], J.E. García Navarro[166], R.W. Gardner[30], N. Garelli[29], H. Garitaonandia[104], V. Garonne[29], J. Garvey[17], C. Gatti[47], G. Gaudio[118a], O. Gaumer[49], B. Gaur[140], L. Gauthier[135], I.L. Gavrilenko[93], C. Gay[167], G. Gaycken[20], J-C. Gayde[29], E.N. Gazis[9], P. Ge[32d], C.N.P. Gee[128], D.A.A. Geerts[104], Ch. Geich-Gimbel[20], K. Gellerstedt[145a,145b], C. Gemme[50a], A. Gemmell[53], M.H. Genest[55], S. Gentile[131a,131b], M. George[54], S. George[75], P. Gerlach[173], A. Gershon[152], C. Geweniger[58a], H. Ghazlane[134b], N. Ghodbane[33], B. Giacobbe[19a], S. Giagu[131a,131b], V. Giakoumopoulou[8], V. Giangiobbe[11], F. Gianotti[29], B. Gibbard[24], A. Gibson[157], S.M. Gibson[29], L.M. Gilbert[117], V. Gilewsky[90], D. Gillberg[28], A.R. Gillman[128], D.M. Gingrich[2,d], J. Ginzburg[152], N. Giokaris[8], M.P. Giordani[163c], R. Giordano[101a,101b], F.M. Giorgi[15], P. Giovannini[98], P.F. Giraud[135], D. Giugni[88a], M. Giunta[92], P. Giusti[19a], B.K. Gjelsten[116], L.K. Gladilin[96], C. Glasman[79], J. Glatzer[48], A. Glazov[41], K.W. Glitza[173], G.L. Glonti[64], J.R. Goddard[74], J. Godfrey[141], J. Godlewski[29], M. Goebel[41], T. Göpfert[43], C. Goeringer[80], C. Gössling[42], T. Göttfert[98], S. Goldfarb[86], T. Golling[174], S.N. Golovnia[127], A. Gomes[123a,b],

L.S. Gomez Fajardo[41], R. Gonçalo[75], J. Goncalves Pinto Firmino Da Costa[41], L. Gonella[20], A. Gonidec[29], S. Gonzalez[171], S. González de la Hoz[166], G. Gonzalez Parra[11], M.L. Gonzalez Silva[26], S. Gonzalez-Sevilla[49], J.J. Goodson[147], L. Goossens[29], P.A. Gorbounov[94], H.A. Gordon[24], I. Gorelov[102], G. Gorfine[173], B. Gorini[29], E. Gorini[71a,71b], A. Gorišek[73], E. Gornicki[38], S.A. Gorokhov[127], V.N. Goryachev[127], B. Gosdzik[41], M. Gosselink[104], M.I. Gostkin[64], I. Gough Eschrich[162], M. Gouighri[134a], D. Goujdami[134c], M.P. Goulette[49], A.G. Goussiou[137], C. Goy[4], S. Gozpinar[22], I. Grabowska-Bold[37], P. Grafström[29], K-J. Grahn[41], F. Grancagnolo[71a], S. Grancagnolo[15], V. Grassi[147], V. Gratchev[120], N. Grau[34], H.M. Gray[29], J.A. Gray[147], E. Graziani[133a], O.G. Grebenyuk[120], T. Greenshaw[72], Z.D. Greenwood[24,l], K. Gregersen[35], I.M. Gregor[41], P. Grenier[142], J. Griffiths[137], N. Grigalashvili[64], A.A. Grillo[136], S. Grinstein[11], Y.V. Grishkevich[96], J.-F. Grivaz[114], M. Groh[98], E. Gross[170], J. Grosse-Knetter[54], J. Groth-Jensen[170], K. Grybel[140], V.J. Guarino[5], D. Guest[174], C. Guicheney[33], A. Guida[71a,71b], S. Guindon[54], H. Guler[84,n], J. Gunther[124], B. Guo[157], J. Guo[34], A. Gupta[30], Y. Gusakov[64], V.N. Gushchin[127], A. Gutierrez[92], P. Gutierrez[110], N. Guttman[152], O. Gutzwiller[171], C. Guyot[135], C. Gwenlan[117], C.B. Gwilliam[72], A. Haas[142], S. Haas[29], C. Haber[14], H.K. Hadavand[39], D.R. Hadley[17], P. Haefner[98], F. Hahn[29], S. Haider[29], Z. Hajduk[38], H. Hakobyan[175], D. Hall[117], J. Haller[54], K. Hamacher[173], P. Hamal[112], M. Hamer[54], A. Hamilton[144b,o], S. Hamilton[160], H. Han[32a], L. Han[32b], K. Hanagaki[115], K. Hanawa[159], M. Hance[14], C. Handel[80], P. Hanke[58a], J.R. Hansen[35], J.B. Hansen[35], J.D. Hansen[35], P.H. Hansen[35], P. Hansson[142], K. Hara[159], G.A. Hare[136], T. Harenberg[173], S. Harkusha[89], D. Harper[86], R.D. Harrington[45], O.M. Harris[137], K. Harrison[17], J. Hartert[48], F. Hartjes[104], T. Haruyama[65], A. Harvey[56], S. Hasegawa[100], Y. Hasegawa[139], S. Hassani[135], M. Hatch[29], D. Hauff[98], S. Haug[16], M. Hauschild[29], R. Hauser[87], M. Havranek[20], B.M. Hawes[117], C.M. Hawkes[17], R.J. Hawkings[29], A.D. Hawkins[78], D. Hawkins[162], T. Hayakawa[66], T. Hayashi[159], D. Hayden[75], H.S. Hayward[72], S.J. Haywood[128], E. Hazen[21], M. He[32d], S.J. Head[17], V. Hedberg[78], L. Heelan[7], S. Heim[87], B. Heinemann[14], S. Heisterkamp[35], L. Helary[4], C. Heller[97], M. Heller[29], S. Hellman[145a,145b], D. Hellmich[20], C. Helsens[11], R.C.W. Henderson[70], M. Henke[58a], A. Henrichs[54], A.M. Henriques Correia[29], S. Henrot-Versille[114], F. Henry-Couannier[82], C. Hensel[54], T. Henß[173], C.M. Hernandez[7], Y. Hernández Jiménez[166], R. Herrberg[15], A.D. Hershenhorn[151], G. Herten[48], R. Hertenberger[97], L. Hervas[29], N.P. Hessey[104], E. Higón-Rodriguez[166], D. Hill[5,*], J.C. Hill[27], N. Hill[5], K.H. Hiller[41], S. Hillert[20], S.J. Hillier[17], I. Hinchliffe[14], E. Hines[119], M. Hirose[115], F. Hirsch[42], D. Hirschbuehl[173], J. Hobbs[147], N. Hod[152], M.C. Hodgkinson[138], P. Hodgson[138], A. Hoecker[29], M.R. Hoeferkamp[102], J. Hoffman[39], D. Hoffmann[82], M. Hohlfeld[80], M. Holder[140], S.O. Holmgren[145a], T. Holy[126], J.L. Holzbauer[87], Y. Homma[66], T.M. Hong[119], L. Hooft van Huysduynen[107], T. Horazdovsky[126], C. Horn[142], S. Horner[48], J-Y. Hostachy[55], S. Hou[150], M.A. Houlden[72], A. Hoummada[134a], J. Howarth[81], D.F. Howell[117], I. Hristova [15], J. Hrivnac[114], I. Hruska[124], T. Hryn'ova[4], P.J. Hsu[80], S.-C. Hsu[14], G.S. Huang[110], Z. Hubacek[126], F. Hubaut[82], F. Huegging[20], A. Huettmann[41], T.B. Huffman[117], E.W. Hughes[34], G. Hughes[70], R.E. Hughes-Jones[81], M. Huhtinen[29], P. Hurst[57], M. Hurwitz[14], U. Husemann[41], N. Huseynov[64,p], J. Huston[87], J. Huth[57], G. Iacobucci[49], G. Iakovidis[9], M. Ibbotson[81], I. Ibragimov[140], R. Ichimiya[66], L. Iconomidou-Fayard[114], J. Idarraga[114], P. Iengo[101a], O. Igonkina[104], Y. Ikegami[65], M. Ikeno[65], Y. Ilchenko[39], D. Iliadis[153], N. Ilic[157], D. Imbault[77], M. Imori[154], T. Ince[20], J. Inigo-Golfin[29], P. Ioannou[8], M. Iodice[133a], V. Ippolito[131a,131b], A. Irles Quiles[166], C. Isaksson[165], A. Ishikawa[66], M. Ishino[67], R. Ishmukhametov[39], C. Issever[117], S. Istin[18a], A.V. Ivashin[127], W. Iwanski[38], H. Iwasaki[65], J.M. Izen[40], V. Izzo[101a], B. Jackson[119], J.N. Jackson[72], P. Jackson[142], M.R. Jaekel[29], V. Jain[60], K. Jakobs[48], S. Jakobsen[35], J. Jakubek[126], D.K. Jana[110], E. Jankowski[157], E. Jansen[76], H. Jansen[29], A. Jantsch[98], M. Janus[20], G. Jarlskog[78], L. Jeanty[57], K. Jelen[37], I. Jen-La Plante[30], P. Jenni[29], A. Jeremie[4], P. Ježˇ[35], S. Jézéquel[4], M.K. Jha[19a], H. Ji[171], W. Ji[80], J. Jia[147], Y. Jiang[32b], M. Jimenez Belenguer[41], G. Jin[32b], S. Jin[32a], O. Jinnouchi[156], M.D. Joergensen[35], D. Joffe[39], L.G. Johansen[13], M. Johansen[145a,145b], K.E. Johansson[145a], P. Johansson[138], S. Johnert[41], K.A. Johns[6], K. Jon-And[145a,145b], G. Jones[81], R.W.L. Jones[70], T.W. Jones[76], T.J. Jones[72], O. Jonsson[29], C. Joram[29], P.M. Jorge[123a], J. Joseph[14], T. Jovin[12b], X. Ju[171], C.A. Jung[42], R.M. Jungst[29], V. Juranek[124], P. Jussel[61], A. Juste Rozas[11], V.V. Kabachenko[127], S. Kabana[16], M. Kaci[166], A. Kaczmarska[38], P. Kadlecik[35], M. Kado[114], H. Kagan[108], M. Kagan[57], S. Kaiser[98], E. Kajomovitz[151], S. Kalinin[173], L.V. Kalinovskaya[64], S. Kama[39], N. Kanaya[154], M. Kaneda[29], S. Kaneti[27], T. Kanno[156], V.A. Kantserov[95], J. Kanzaki[65], B. Kaplan[174], A. Kapliy[30], J. Kaplon[29], D. Kar[43], M. Karagounis[20], M. Karagoz[117], M. Karnevskiy[41], K. Karr[5], V. Kartvelishvili[70], A.N. Karyukhin[127], L. Kashif[171], G. Kasieczka[58b], R.D. Kass[108], A. Kastanas[13], M. Kataoka[4], Y. Kataoka[154], E. Katsoufis[9], J. Katzy[41], V. Kaushik[6], K. Kawagoe[66], T. Kawamoto[154], G. Kawamura[80], M.S. Kayl[104], V.A. Kazanin[106], M.Y. Kazarinov[64], R. Keeler[168], R. Kehoe[39], M. Keil[54], G.D. Kekelidze[64], J. Kennedy[97], C.J. Kenney[142], M. Kenyon[53], O. Kepka[124], N. Kerschen[29], B.P. Kerševan[73], S. Kersten[173], K. Kessoku[154], J. Keung[157], F. Khalil-zada[10], H. Khandanyan[164], A. Khanov[111], D. Kharchenko[64], A. Khodinov[95], A.G. Kholodenko[127], A. Khomich[58a], T.J. Khoo[27], G. Khoriauli[20], A. Khoroshilov[173], N. Khovanskiy[64], V. Khovanskiy[94], E. Khramov[64], J. Khubua[51b], H. Kim[145a,145b], M.S. Kim[2], P.C. Kim[142], S.H. Kim[159], N. Kimura[169], O. Kind[15], B.T. King[72], M. King[66], R.S.B. King[117], J. Kirk[128], L.E. Kirsch[22], A.E. Kiryunin[98], T. Kishimoto[66], D. Kisielewska[37], T. Kittelmann[122], A.M. Kiver[127], E. Kladiva[143b], J. Klaiber-Lodewigs[42], M. Klein[72], U. Klein[72], K. Kleinknecht[80], M. Klemetti[84], A. Klier[170], P. Klimek[145a,145b], A. Klimentov[24], R. Klingenberg[42], J.A. Klinger[81], E.B. Klinkby[35], T. Klioutchnikova[29], P.F. Klok[103], S. Klous[104], E.-E. Kluge[58a], T. Kluge[72], P. Kluit[104], S. Kluth[98], N.S. Knecht[157], E. Kneringer[61], J. Knobloch[29], E.B.F.G. Knoops[82], A. Knue[54], B.R. Ko[44], T. Kobayashi[154], M. Kobel[43], M. Kocian[142], P. Kodys[125], K. Köneke[29], A.C. König[103], S. Koenig[80], L. Köpke[80], F. Koetsveld[103], P. Koevesarki[20], T. Koffas[28], E. Koffeman[104], L.A. Kogan[117], F. Kohn[54], Z. Kohout[126], T. Kohriki[65], T. Koi[142], T. Kokott[20], G.M. Kolachev[106], H. Kolanoski[15], V. Kolesnikov[64], I. Koletsou[88a], J. Koll[87], D. Kollar[29], M. Kollefrath[48], S.D. Kolya[81], A.A. Komar[93], Y. Komori[154], T. Kondo[65], T. Kono[41,q], A.I. Kononov[48], R. Konoplich[107,r], N. Konstantinidis[76], A. Kootz[173], S. Koperny[37], K. Korcyl[38], K. Kordas[153], V. Koreshev[127], A. Korn[117], A. Korol[106], I. Korolkov[11], E.V. Korolkova[138], V.A. Korotkov[127], O. Kortner[98], S. Kortner[98], V.V. Kostyukhin[20], M.J. Kotamäki[29], S. Kotov[98], V.M. Kotov[64], A. Kotwal[44], C. Kourkoumelis[8], V. Kouskoura[153], A. Koutsman[158a], R. Kowalewski[168], T.Z. Kowalski[37], W. Kozanecki[135], A.S. Kozhin[127], V. Kral[126], V.A. Kramarenko[96], G. Kramberger[73], M.W. Krasny[77], A. Krasznahorkay[107], J. Kraus[87], J.K. Kraus[20], A. Kreisel[152], F. Krejci[126],

J. Kretzschmar[72], N. Krieger[54], P. Krieger[157], K. Kroeninger[54], H. Kroha[98], J. Kroll[119], J. Kroseberg[20], J. Krstic[12a], U. Kruchonak[64], H. Krüger[20], T. Kruker[16], N. Krumnack[63], Z.V. Krumshteyn[64], A. Kruth[20], T. Kubota[85], S. Kuehn[48], A. Kugel[58c], T. Kuhl[41], D. Kuhn[61], V. Kukhtin[64], Y. Kulchitsky[89], S. Kuleshov[31b], C. Kummer[97], M. Kuna[77], N. Kundu[117], J. Kunkle[119], A. Kupco[124], H. Kurashige[66], M. Kurata[159], Y.A. Kurochkin[89], V. Kus[124], E.S. Kuwertz[146], M. Kuze[156], J. Kvita[141], R. Kwee[15], A. La Rosa[49], L. La Rotonda[36a,36b], L. Labarga[79], J. Labbe[4], S. Lablak[134a], C. Lacasta[166], F. Lacava[131a,131b], H. Lacker[15], D. Lacour[77], V.R. Lacuesta[166], E. Ladygin[64], R. Lafaye[4], B. Laforge[77], T. Lagouri[79], S. Lai[48], E. Laisne[55], M. Lamanna[29], C.L. Lampen[6], W. Lampl[6], E. Lancon[135], U. Landgraf[48], M.P.J. Landon[74], H. Landsman[151], J.L. Lane[81], C. Lange[41], A.J. Lankford[162], F. Lanni[24], K. Lantzsch[173], S. Laplace[77], C. Lapoire[20], J.F. Laporte[135], T. Lari[88a], A.V. Larionov [127], A. Larner[117], C. Lasseur[29], M. Lassnig[29], P. Laurelli[47], W. Lavrijsen[14], P. Laycock[72], A.B. Lazarev[64], O. Le Dortz[77], E. Le Guirriec[82], C. Le Maner[157], E. Le Menedeu[9], C. Lebel[92], T. LeCompte[5], F. Ledroit-Guillon[55], H. Lee[104], J.S.H. Lee[115], S.C. Lee[150], L. Lee[174], M. Lefebvre[168], M. Legendre[135], A. Leger[49], B.C. LeGeyt[119], F. Legger[97], C. Leggett[14], M. Lehmacher[20], G. Lehmann Miotto[29], X. Lei[6], M.A.L. Leite[23d], R. Leitner[125], D. Lellouch[170], M. Leltchouk[34], B. Lemmer[54], V. Lendermann[58a], K.J.C. Leney[144b], T. Lenz[104], G. Lenzen[173], B. Lenzi[29], K. Leonhardt[43], S. Leontsinis[9], C. Leroy[92], J-R. Lessard[168], J. Lesser[145a], C.G. Lester[27], A. Leung Fook Cheong[171], J. Levêque[4], D. Levin[86], L.J. Levinson[170], M.S. Levitski[127], A. Lewis[117], G.H. Lewis[107], A.M. Leyko[20], M. Leyton[15], B. Li[82], H. Li[171,s], S. Li[32b,t], X. Li[86], Z. Liang[117,u], H. Liao[33], B. Liberti[132a], P. Lichard[29], M. Lichtnecker[97], K. Lie[164], W. Liebig[13], R. Lifshitz[151], C. Limbach[20], A. Limosani[85], M. Limper[62], S.C. Lin[150,v], F. Linde[104], J.T. Linnemann[87], E. Lipeles[119], L. Lipinsky[124], A. Lipniacka[13], T.M. Liss[164], D. Lissauer[24], A. Lister[49], A.M. Litke[136], C. Liu[28], D. Liu[150], H. Liu[86], J.B. Liu[86], M. Liu[32b], S. Liu[2], Y. Liu[32b], M. Livan[118a,118b], S.S.A. Livermore[117], A. Lleres[55], J. Llorente Merino[79], S.L. Lloyd[74], E. Lobodzinska[41], P. Loch[6], W.S. Lockman[136], T. Loddenkoetter[20], F.K. Loebinger[81], A. Loginov[174], C.W. Loh[167], T. Lohse[15], K. Lohwasser[48], M. Lokajicek[124], J. Loken [117], V.P. Lombardo[4], R.E. Long[70], L. Lopes[123a,b], D. Lopez Mateos[57], J. Lorenz[97], M. Losada[161], P. Loscutoff[14], F. Lo Sterzo[131a,131b], M.J. Losty[158a], X. Lou[40], A. Lounis[114], K.F. Loureiro[161], J. Love[21], P.A. Love[70], A.J. Lowe[142,e], F. Lu[32a], H.J. Lubatti[137], C. Luci[131a,131b], A. Lucotte[55], A. Ludwig[43], D. Ludwig[41], I. Ludwig[48], J. Ludwig[48], F. Luehring[60], G. Luijckx[104], D. Lumb[48], L. Luminari[131a], E. Lund[116], B. Lund-Jensen[146], B. Lundberg[78], J. Lundberg[145a,145b], J. Lundquist[35], M. Lungwitz[80], G. Lutz[98], D. Lynn[24], J. Lys[14], E. Lytken[78], H. Ma[24], L.L. Ma[171], J.A. Macana Goia[92], G. Maccarrone[47], A. Macchiolo[98], B. Maček[73], J. Machado Miguens[123a], R. Mackeprang[35], R.J. Madaras[14], W.F. Mader[43], R. Maenner[58c], T. Maeno[24], P. Mättig[173], S. Mättig[41], L. Magnoni[29], E. Magradze[54], Y. Mahalalel[152], K. Mahboubi[48], G. Mahout[17], C. Maiani[131a,131b], C. Maidantchik[23a], A. Maio[123a,b], S. Majewski[24], Y. Makida[65], N. Makovec[114], P. Mal[135], B. Malaescu[29], Pa. Malecki[38], P. Malecki[38], V.P. Maleev[120], F. Malek[55], U. Mallik[62], D. Malon[5], C. Malone[142], S. Maltezos[9], V. Malyshev[106], S. Malyukov[29], R. Mameghani[97], J. Mamuzic[12b], A. Manabe[65], L. Mandelli[88a], I. Mandić[73], R. Mandrysch[15], J. Maneira[123a], P.S. Mangeard[87], L. Manhaes de Andrade Filho[23a], I.D. Manjavidze[64], A. Mann[54], P.M. Manning[136], A. Manousakis-Katsikakis[8], B. Mansoulie[135], A. Manz[98], A. Mapelli[29], L. Mapelli[29], L. March [79], J.F. Marchand[28], F. Marchese[132a,132b], G. Marchiori[77], M. Marcisovsky[124], A. Marin[21,*], C.P. Marino[168], F. Marroquim[23a], R. Marshall[81], Z. Marshall[29], F.K. Martens[157], S. Marti-Garcia[166], A.J. Martin[174], B. Martin[29], B. Martin[87], F.F. Martin[119], J.P. Martin[92], Ph. Martin[55], T.A. Martin[17], V.J. Martin[45], B. Martin dit Latour[49], S. Martin-Haugh[148], M. Martinez[11], V. Martinez Outschoorn[57], A.C. Martyniuk[168], M. Marx[81], F. Marzano[131a], A. Marzin[110], L. Masetti[80], T. Mashimo[154], R. Mashinistov[93], J. Masik[81], A.L. Maslennikov[106], I. Massa[19a,19b], G. Massaro[104], N. Massol[4], P. Mastrandrea[131a,131b], A. Mastroberardino[36a,36b], T. Masubuchi[154], M. Mathes[20], P. Matricon[114], H. Matsumoto[154], H. Matsunaga[154], T. Matsushita[66], C. Mattravers[117,c], J.M. Maugain[29], J. Maurer[82], S.J. Maxfield[72], D.A. Maximov[106,f], E.N. May[5], A. Mayne[138], R. Mazini[150], M. Mazur[20], M. Mazzanti[88a], E. Mazzoni[121a,121b], S.P. Mc Kee[86], A. McCarn[164], R.L. McCarthy[147], T.G. McCarthy[28], N.A. McCubbin[128], K.W. McFarlane[56], J.A. Mcfayden[138], H. McGlone[53], G. Mchedlidze[51b], R.A. McLaren[29], T. Mclaughlan[17], S.J. McMahon[128], R.A. McPherson[168,j], A. Meade[83], J. Mechnich[104], M. Mechtel[173], M. Medinnis[41], R. Meera-Lebbai[110], T. Meguro[115], R. Mehdiyev[92], S. Mehlhase[35], A. Mehta[72], K. Meier[58a], B. Meirose[78], C. Melachrinos[30], B.R. Mellado Garcia[171], L. Mendoza Navas[161], Z. Meng[150,s], A. Mengarelli[19a,19b], S. Menke[98], C. Menot[29], E. Meoni[11], K.M. Mercurio[57], P. Mermod[49], L. Merola[101a,101b], C. Meroni[88a], F.S. Merritt[30], A. Messina[29], J. Metcalfe[102], A.S. Mete[63], C. Meyer[80], C. Meyer[30], J-P. Meyer[135], J. Meyer[172], J. Meyer[54], T.C. Meyer[29], W.T. Meyer[63], J. Miao[32d], S. Michal[29], L. Micu[25a], R.P. Middleton[128], S. Migas[72], L. Mijović[41], G. Mikenberg[170], M. Mikestikova[124], M. Mikuž[73], D.W. Miller[30], R.J. Miller[87], W.J. Mills[167], C. Mills[57], A. Milov[170], D.A. Milstead[145a,145b], D. Milstein[170], A.A. Minaenko[127], M. Miñano Moya[166], I.A. Minashvili[64], A.I. Mincer[107], B. Mindur[37], M. Mineev[64], Y. Ming[171], L.M. Mir[11], G. Mirabelli[131a], L. Miralles Verge[11], A. Misiejuk[75], J. Mitrevski[136], G.Y. Mitrofanov[127], V.A. Mitsou[166], S. Mitsui[65], P.S. Miyagawa[138], K. Miyazaki[66], J.U. Mjörnmark[78], T. Moa[145a,145b], P. Mockett[137], S. Moed[57], V. Moeller[27], K. Mönig[41], N. Möser[20], S. Mohapatra[147], W. Mohr[48], S. Mohrdieck-Möck[98], A.M. Moisseev[127,*], R. Moles-Valls[166], J. Molina-Perez[29], J. Monk[76], E. Monnier[82], S. Montesano[88a,88b], F. Monticelli[69], S. Monzani[19a,19b], R.W. Moore[2], G.F. Moorhead[85], C. Mora Herrera[49], A. Moraes[53], N. Morange[135], J. Morel[54], G. Morello[36a,36b], D. Moreno[80], M. Moreno Llácer[166], P. Morettini[50a], M. Morii[57], J. Morin[74], A.K. Morley[29], G. Mornacchi[29], S.V. Morozov[95], J.D. Morris[74], L. Morvaj[100], H.G. Moser[98], M. Mosidze[51b], J. Moss[108], R. Mount[142], E. Mountricha[9,w], S.V. Mouraviev[93], E.J.W. Moyse[83], M. Mudrinic[12b], F. Mueller[58a], J. Mueller[122], K. Mueller[20], T.A. Müller[97], T. Mueller[80], D. Muenstermann[29], A. Muir[167], Y. Munwes[152], W.J. Murray[128], I. Mussche[104], E. Musto[101a,101b], A.G. Myagkov[127], M. Myska[124], J. Nadal[11], K. Nagai[159], K. Nagano[65], Y. Nagasaka[59], M. Nagel[98], A.M. Nairz[29], Y. Nakahama[29], K. Nakamura[154], T. Nakamura[154], I. Nakano[109], G. Nanava[20], A. Napier[160], R. Narayan[58b], M. Nash[76,c], N.R. Nation[21], T. Nattermann[20], T. Naumann[41], G. Navarro[161], H.A. Neal[86], E. Nebot[79], P.Yu. Nechaeva[93], T.J. Neep[81], A. Negri[118a,118b], G. Negri[29], S. Nektarijevic[49], A. Nelson[162], S. Nelson[142], T.K. Nelson[142], S. Nemecek[124], P. Nemethy[107], A.A. Nepomuceno[23a], M. Nessi[29,x], M.S. Neubauer[164], A. Neusiedl[80], R.M. Neves[107], P. Nevski[24], P.R. Newman[17], V. Nguyen Thi Hong[135], R.B. Nickerson[117], R. Nicolaidou[135], L. Nicolas[138],

B. Nicquevert[29], F. Niedercorn[114], J. Nielsen[136], T. Niinikoski[29], N. Nikiforou[34], A. Nikiforov[15], V. Nikolaenko[127], K. Nikolaev[64], I. Nikolic-Audit[77], K. Nikolics[49], K. Nikolopoulos[24], H. Nilsen[48], P. Nilsson[7], Y. Ninomiya [154], A. Nisati[131a], T. Nishiyama[66], R. Nisius[98], L. Nodulman[5], M. Nomachi[115], I. Nomidis[153], M. Nordberg[29], B. Nordkvist[145a,145b], P.R. Norton[128], J. Novakova[125], M. Nozaki[65], L. Nozka[112], I.M. Nugent[158a], A.-E. Nuncio-Quiroz[20], G. Nunes Hanninger[85], T. Nunnemann[97], E. Nurse[76], T. Nyman[29], B.J. O'Brien[45], S.W. O'Neale[17,*], D.C. O'Neil[141], V. O'Shea[53], L.B. Oakes[97], F.G. Oakham[28,d], H. Oberlack[98], J. Ocariz[77], A. Ochi[66], S. Oda[154], S. Odaka[65], J. Odier[82], H. Ogren[60], A. Oh[81], S.H. Oh[44], C.C. Ohm[145a,145b], T. Ohshima[100], H. Ohshita[139], S. Okada[66], H. Okawa[162], Y. Okumura[100], T. Okuyama[154], A. Olariu[25a], M. Olcese[50a], A.G. Olchevski[64], M. Oliveira[123a,h], D. Oliveira Damazio[24], E. Oliver Garcia[166], D. Olivito[119], A. Olszewski[38], J. Olszowska[38], C. Omachi[66], A. Onofre[123a,y], P.U.E. Onyisi[30], C.J. Oram[158a], M.J. Oreglia[30], Y. Oren[152], D. Orestano[133a,133b], I. Orlov[106], C. Oropeza Barrera[53], R.S. Orr[157], B. Osculati[50a,50b], R. Ospanov[119], C. Osuna[11], G. Otero y Garzon[26], J.P. Ottersbach[104], M. Ouchrif[134d], E.A. Ouellette[168], F. Ould-Saada[116], A. Ouraou[135], Q. Ouyang[32a], A. Ovcharova[14], M. Owen[81], S. Owen[138], V.E. Ozcan[18a], N. Ozturk[7], A. Pacheco Pages[11], C. Padilla Aranda[11], S. Pagan Griso[14], E. Paganis[138], F. Paige[24], P. Pais[83], K. Pajchel[116], G. Palacino[158b], C.P. Paleari[6], S. Palestini[29], D. Pallin[33], A. Palma[123a], J.D. Palmer[17], Y.B. Pan[171], E. Panagiotopoulou[9], B. Panes[31a], N. Panikashvili[86], S. Panitkin[24], D. Pantea[25a], M. Panuskova[124], V. Paolone[122], A. Papadelis[145a], Th.D. Papadopoulou[9], A. Paramonov[5], W. Park[24,z], M.A. Parker[27], F. Parodi[50a,50b], J.A. Parsons[34], U. Parzefall[48], E. Pasqualucci[131a], S. Passaggio[50a], A. Passeri[133a], F. Pastore[133a,133b], Fr. Pastore[75], G. Pásztor [49,aa], S. Pataraia[173], N. Patel[149], J.R. Pater[81], S. Patricelli[101a,101b], T. Pauly[29], M. Pecsy[143a], M.I. Pedraza Morales[171], S.V. Peleganchuk[106], H. Peng[32b], R. Pengo[29], A. Penson[34], J. Penwell[60], M. Perantoni[23a], K. Perez[34,ab], T. Perez Cavalcanti[41], E. Perez Codina[11], M.T. Pérez García-Estañ[166], V. Perez Reale[34], L. Perini[88a,88b], H. Pernegger[29], R. Perrino[71a], P. Perrodo[4], S. Persembe[3a], A. Perus[114], V.D. Peshekhonov[64], K. Peters[29], B.A. Petersen[29], J. Petersen[29], T.C. Petersen[35], E. Petit[4], A. Petridis[153], C. Petridou[153], E. Petrolo[131a], F. Petrucci[133a,133b], D. Petschull[41], M. Petteni[141], R. Pezoa[31b], A. Phan[85], P.W. Phillips[128], G. Piacquadio[29], E. Piccaro[74], M. Piccinini[19a,19b], S.M. Piec[41], R. Piegaia[26], D.T. Pignotti[108], J.E. Pilcher[30], A.D. Pilkington[81], J. Pina[123a,b], M. Pinamonti[163a,163c], A. Pinder[117], J.L. Pinfold[2], J. Ping[32c], B. Pinto[123a,b], O. Pirotte[29], C. Pizio[88a,88b], M. Plamondon[168], M.-A. Pleier[24], A.V. Pleskach[127], A. Poblaguev[24], S. Poddar[58a], F. Podlyski[33], L. Poggioli[114], T. Poghosyan[20], M. Pohl[49], F. Polci[55], G. Polesello[118a], A. Policicchio[36a,36b], A. Polini[19a], J. Poll[74], V. Polychronakos[24], D.M. Pomarede[135], D. Pomeroy[22], K. Pommès[29], L. Pontecorvo[131a], B.G. Pope[87], G.A. Popeneciu[25a], D.S. Popovic[12a], A. Poppleton[29], X. Portell Bueso[29], C. Posch[21], G.E. Pospelov[98], S. Pospisil[126], I.N. Potrap[98], C.J. Potter[148], C.T. Potter[113], G. Poulard[29], J. Poveda[171], R. Prabhu[76], P. Pralavorio[82], A. Pranko[14], S. Prasad[57], R. Pravahan[7], S. Prell[63], K. Pretzl[16], L. Pribyl[29], D. Price[60], J. Price[72], L.E. Price[5], M.J. Price[29], D. Prieur[122], M. Primavera[71a], K. Prokofiev[107], F. Prokoshin[31b], S. Protopopescu[24], J. Proudfoot[5], X. Prudent[43], M. Przybycien[37], H. Przysiezniak[4], S. Psoroulas[20], E. Ptacek[113], E. Pueschel[83], J. Purdham[86], M. Purohit[24,z], P. Puzo[114], Y. Pylypchenko[62], J. Qian[86], Z. Qian[82], Z. Qin[41], A. Quadt[54], D.R. Quarrie[14], W.B. Quayle[171], F. Quinonez[31a], M. Raas[103], V. Radescu[58b], B. Radics[20], P. Radloff[113], T. Rador[18a], F. Ragusa[88a,88b], G. Rahal[176], A.M. Rahimi[108], D. Rahm[24], S. Rajagopalan[24], M. Rammensee[48], M. Rammes[140], A.S. Randle-Conde[39], K. Randrianarivony[28], P.N. Ratoff[70], F. Rauscher[97], M. Raymond[29], A.L. Read[116], D.M. Rebuzzi[118a,118b], A. Redelbach[172], G. Redlinger[24], R. Reece[119], K. Reeves[40], A. Reichold[104], E. Reinherz-Aronis[152], A. Reinsch[113], I. Reisinger[42], D. Reljic[12a], C. Rembser[29], Z.L. Ren[150], A. Renaud[114], P. Renkel[39], M. Rescigno[131a], S. Resconi[88a], B. Resende[135], P. Reznicek[97], R. Rezvani[157], A. Richards[76], R. Richter[98], E. Richter-Was[4,ac], M. Ridel[77], M. Rijpstra[104], M. Rijssenbeek[147], A. Rimoldi[118a,118b], L. Rinaldi[19a], R.R. Rios[39], I. Riu[11], G. Rivoltella[88a,88b], F. Rizatdinova[111], E. Rizvi[74], S.H. Robertson[84,j], A. Robichaud-Veronneau[117], D. Robinson[27], J.E.M. Robinson[76], M. Robinson[113], A. Robson[53], J.G. Rocha de Lima[105], C. Roda[121a,121b], D. Roda Dos Santos[29], D. Rodriguez[161], A. Roe[54], S. Roe[29], O. Røhne[116], V. Rojo[1], S. Rolli[160], A. Romaniouk[95], M. Romano[19a,19b], V.M. Romanov[64], G. Romeo[26], E. Romero Adam[166], L. Roos[77], E. Ros[166], S. Rosati[131a], K. Rosbach[49], A. Rose[148], M. Rose[75], G.A. Rosenbaum[157], E.I. Rosenberg[63], P.L. Rosendahl[13], O. Rosenthal[140], L. Rosselet[49], V. Rossetti[11], E. Rossi[131a,131b], L.P. Rossi[50a], M. Rotaru[25a], I. Roth[170], J. Rothberg[137], D. Rousseau[114], C.R. Royon[135], A. Rozanov[82], Y. Rozen[151], X. Ruan[114,ad], I. Rubinskiy[41], B. Ruckert[97], N. Ruckstuhl[104], V.I. Rud[96], C. Rudolph[43], G. Rudolph[61], F. Rühr[6], F. Ruggieri[133a,133b], A. Ruiz-Martinez[63], V. Rumiantsev[90,*], L. Rumyantsev[64], K. Runge[48], Z. Rurikova[48], N.A. Rusakovich[64], D.R. Rust[60], J.P. Rutherfoord[6], C. Ruwiedel[14], P. Ruzicka[124], Y.F. Ryabov[120], V. Ryadovikov[127], P. Ryan[87], M. Rybar[125], G. Rybkin[114], N.C. Ryder[117], S. Rzaeva[10], A.F. Saavedra[149], I. Sadeh[152], H.F-W. Sadrozinski[136], R. Sadykov[64], F. Safai Tehrani[131a], H. Sakamoto[154], G. Salamanna[74], A. Salamon[132a], M. Saleem[110], D. Salihagic[98], A. Salnikov[142], J. Salt[166], B.M. Salvachua Ferrando[5], D. Salvatore[36a,36b], F. Salvatore[148], A. Salvucci[103], A. Salzburger[29], D. Sampsonidis[153], B.H. Samset[116], A. Sanchez[101a,101b], H. Sandaker[13], H.G. Sander[80], M.P. Sanders[97], M. Sandhoff[173], T. Sandoval[27], C. Sandoval [161], R. Sandstroem[98], S. Sandvoss[173], D.P.C. Sankey[128], A. Sansoni[47], C. Santamarina Rios[84], C. Santoni[33], R. Santonico[132a,132b], H. Santos[123a], J.G. Saraiva[123a], T. Sarangi[171], E. Sarkisyan-Grinbaum[7], F. Sarri[121a,121b], G. Sartisohn[173], O. Sasaki[65], N. Sasao[67], I. Satsounkevitch[89], G. Sauvage[4], E. Sauvan[4], J.B. Sauvan[114], P. Savard[157,d], V. Savinov[122], D.O. Savu[29], L. Sawyer[24,l], D.H. Saxon[53], L.P. Says[33], C. Sbarra[19a], A. Sbrizzi[19a,19b], O. Scallon[92], D.A. Scannicchio[162], M. Scarcella[149], J. Schaarschmidt[114], P. Schacht[98], U. Schäfer[80], S. Schaepe[20], S. Schaetzel[58b], A.C. Schaffer[114], D. Schaile[97], R.D. Schamberger[147], A.G. Schamov[106], V. Scharf[58a], V.A. Schegelsky[120], D. Scheirich[86], M. Schernau[162], M.I. Scherzer[34], C. Schiavi[50a,50b], J. Schieck[97], M. Schioppa[36a,36b], S. Schlenker[29], J.L. Schlereth[5], E. Schmidt[48], K. Schmieden[20], C. Schmitt[80], S. Schmitt[58b], M. Schmitz[20], A. Schöning[58b], M. Schott[29], D. Schouten[158a], J. Schovancova[124], M. Schram[84], C. Schroeder[80], N. Schroer[58c], S. Schuh[29], G. Schuler[29], J. Schultes[173], H.-C. Schultz-Coulon[58a], H. Schulz[15], J.W. Schumacher[20], M. Schumacher[48], B.A. Schumm[136], Ph. Schune[135], C. Schwanenberger[81], A. Schwartzman[142], Ph. Schwemling[77], R. Schwienhorst[87], R. Schwierz[43], J. Schwindling[135], T. Schwindt[20], M. Schwoerer[4], W.G. Scott[128], J. Searcy[113], G. Sedov[41], E. Sedykh[120], E. Segura[11], S.C. Seidel[102], A. Seiden[136], F. Seifert[43], J.M. Seixas[23a], G. Sekhniaidze[101a], K.E. Selbach[45], D.M. Seliverstov[120], B. Sellden[145a],

G. Sellers[72], M. Seman[143b], N. Semprini-Cesari[19a,19b], C. Serfon[97], L. Serin[114], R. Seuster[98], H. Severini[110], M.E. Sevior[85], A. Sfyrla[29], E. Shabalina[54], M. Shamim[113], L.Y. Shan[32a], J.T. Shank[21], Q.T. Shao[85], M. Shapiro[14], P.B. Shatalov[94], L. Shaver[6], K. Shaw[163a,163c], D. Sherman[174], P. Sherwood[76], A. Shibata[107], H. Shichi[100], S. Shimizu[29], M. Shimojima[99], T. Shin[56], M. Shiyakova[64], A. Shmeleva[93], M.J. Shochet[30], D. Short[117], S. Shrestha[63], M.A. Shupe[6], P. Sicho[124], A. Sidoti[131a], F. Siegert[48], Dj. Sijacki[12a], O. Silbert[170], J. Silva[123a,b], Y. Silver[152], D. Silverstein[142], S.B. Silverstein[145a], V. Simak[126], O. Simard[135], Lj. Simic[12a], S. Simion[114], B. Simmons[76], M. Simonyan[35], P. Sinervo[157], N.B. Sinev[113], V. Sipica[140], G. Siragusa[172], A. Sircar[24], A.N. Sisakyan[64], S.Yu. Sivoklokov[96], J. Sjölin[145a,145b], T.B. Sjursen[13], L.A. Skinnari[14], H.P. Skottowe[57], K. Skovpen[106], P. Skubic[110], N. Skvorodnev[22], M. Slater[17], T. Slavicek[126], K. Sliwa[160], J. Sloper[29], V. Smakhtin[170], S.Yu. Smirnov[95], L.N. Smirnova[96], O. Smirnova[78], B.C. Smith[57], D. Smith[142], K.M. Smith[53], M. Smizanska[70], K. Smolek[126], A.A. Snesarev[93], S.W. Snow[81], J. Snow[110], J. Snuverink[104], S. Snyder[24], M. Soares[123a], R. Sobie[168,j], J. Sodomka[126], A. Soffer[152], C.A. Solans[166], M. Solar[126], J. Solc[126], E. Soldatov[95], U. Soldevila[166], E. Solfaroli Camillocci[131a,131b], A.A. Solodkov[127], O.V. Solovyanov[127], N. Soni[2], V. Sopko[126], B. Sopko[126], M. Sosebee[7], R. Soualah[163a,163c], A. Soukharev[106], S. Spagnolo[71a,71b], F. Spanò[75], R. Spighi[19a], G. Spigo[29], F. Spila[131a,131b], R. Spiwoks[29], M. Spousta[125], T. Spreitzer[157], B. Spurlock[7], R.D. St. Denis[53], T. Stahl[140], J. Stahlman[119], R. Stamen[58a], E. Stanecka[38], R.W. Stanek[5], C. Stanescu[133a], S. Stapnes[116], E.A. Starchenko[127], J. Stark[55], P. Staroba[124], P. Starovoitov[90], A. Staude[97], P. Stavina[143a], G. Stavropoulos[14], G. Steele[53], P. Steinbach[43], P. Steinberg[24], I. Stekl[126], B. Stelzer[141], H.J. Stelzer[87], O. Stelzer-Chilton[158a], H. Stenzel[52], S. Stern[98], K. Stevenson[74], G.A. Stewart[29], J.A. Stillings[20], M.C. Stockton[84], K. Stoerig[48], G. Stoicea[25a], S. Stonjek[98], P. Strachota[125], A.R. Stradling[7], A. Straessner[43], J. Strandberg[146], S. Strandberg[145a,145b], A. Strandlie[116], M. Strang[108], E. Strauss[142], M. Strauss[110], P. Strizenec[143b], R. Ströhmer[172], D.M. Strom[113], J.A. Strong[75,*], R. Stroynowski[39], J. Strube[128], B. Stugu[13], I. Stumer[24,*], J. Stupak[147], P. Sturm[173], N.A. Styles[41], D.A. Soh[150,u], D. Su[142], HS. Subramania[2], A. Succurro[11], Y. Sugaya[115], T. Sugimoto[100], C. Suhr[105], K. Suita[66], M. Suk[125], V.V. Sulin[93], S. Sultansoy[3d], T. Sumida[67], X. Sun[55], J.E. Sundermann[48], K. Suruliz[138], S. Sushkov[11], G. Susinno[36a,36b], M.R. Sutton[148], Y. Suzuki[65], Y. Suzuki[66], M. Svatos[124], Yu.M. Sviridov[127], S. Swedish[167], I. Sykora[143a], T. Sykora[125], B. Szeless[29], J. Sánchez[166], D. Ta[104], K. Tackmann[41], A. Taffard[162], R. Tafirout[158a], N. Taiblum[152], Y. Takahashi[100], H. Takai[24], R. Takashima[68], H. Takeda[66], T. Takeshita[139], Y. Takubo[65], M. Talby[82], A. Talyshev[106,f], M.C. Tamsett[24], J. Tanaka[154], R. Tanaka[114], S. Tanaka[130], S. Tanaka[65], Y. Tanaka[99], A.J. Tanasijczuk[141], K. Tani[66], N. Tannoury[82], G.P. Tappern[29], S. Tapprogge[80], D. Tardif[157], S. Tarem[151], F. Tarrade[28], G.F. Tartarelli[88a], P. Tas[125], M. Tasevsky[124], E. Tassi[36a,36b], M. Tatarkhanov[14], Y. Tayalati[134d], C. Taylor[76], F.E. Taylor[91], G.N. Taylor[85], W. Taylor[158b], M. Teinturier[114], M. Teixeira Dias Castanheira[74], P. Teixeira-Dias[75], K.K. Temming[48], H. Ten Kate[29], P.K. Teng[150], S. Terada[65], K. Terashi[154], J. Terron[79], M. Testa[47], R.J. Teuscher[157,j], J. Thadome[173], J. Therhaag[20], T. Theveneaux-Pelzer[77], M. Thioye[174], S. Thoma[48], J.P. Thomas[17], E.N. Thompson[34], P.D. Thompson[17], P.D. Thompson[157], A.S. Thompson[53], E. Thomson[119], M. Thomson[27], R.P. Thun[86], F. Tian[34], M.J. Tibbetts[14], T. Tic[124], V.O. Tikhomirov[93], Y.A. Tikhonov[106,f], S Timoshenko[95], P. Tipton[174], F.J. Tique Aires Viegas[29], S. Tisserant[82], B. Toczek[37], T. Todorov[4], S. Todorova-Nova[160], B. Toggerson[162], J. Tojo[65], S. Tokár[143a], K. Tokunaga[66], K. Tokushuku[65], K. Tollefson[87], M. Tomoto[100], L. Tompkins[30], K. Toms[102], G. Tong[32a], A. Tonoyan[13], C. Topfel[16], N.D. Topilin[64], I. Torchiani[29], E. Torrence[113], H. Torres[77], E. Torró Pastor[166], J. Toth[82,aa], F. Touchard[82], D.R. Tovey[138], T. Trefzger[172], L. Tremblet[29], A. Tricoli[29], I.M. Trigger[158a], S. Trincaz-Duvoid[77], T.N. Trinh[77], M.F. Tripiana[69], W. Trischuk[157], A. Trivedi[24,z], B. Trocmé[55], C. Troncon[88a], M. Trottier-McDonald[141], M. Trzebinski[38], A. Trzupek[38], C. Tsarouchas[29], J.C-L. Tseng[117], M. Tsiakiris[104], P.V. Tsiareshka[89], D. Tsionou[4,ae], G. Tsipolitis[9], V. Tsiskaridze[48], E.G. Tskhadadze[51a], I.I. Tsukerman[94], V. Tsulaia[14], J.-W. Tsung[20], S. Tsuno[65], D. Tsybychev[147], A. Tua[138], A. Tudorache[25a], V. Tudorache[25a], J.M. Tuggle[30], M. Turala[38], D. Turecek[126], I. Turk Cakir[3e], E. Turlay[104], R. Turra[88a,88b], P.M. Tuts[34], A. Tykhonov[73], M. Tylmad[145a,145b], M. Tyndel[128], G. Tzanakos[8], K. Uchida[20], I. Ueda[154], R. Ueno[28], M. Ugland[13], M. Uhlenbrock[20], M. Uhrmacher[54], F. Ukegawa[159], G. Unal[29], D.G. Underwood[5], A. Undrus[24], G. Unel[162], Y. Unno[65], D. Urbaniec[34], G. Usai[7], M. Uslenghi[118a,118b], L. Vacavant[82], V. Vacek[126], B. Vachon[84], S. Vahsen[14], J. Valenta[124], P. Valente[131a], S. Valentinetti[19a,19b], S. Valkar[125], E. Valladolid Gallego[166], S. Vallecorsa[151], J.A. Valls Ferrer[166], H. van der Graaf[104], E. van der Kraaij[104], R. Van Der Leeuw[104], E. van der Poel[104], D. van der Ster[29], N. van Eldik[83], P. van Gemmeren[5], Z. van Kesteren[104], I. van Vulpen[104], M. Vanadia[98], W. Vandelli[29], G. Vandoni[29], A. Vaniachine[5], P. Vankov[41], F. Vannucci[77], F. Varela Rodriguez[29], R. Vari[131a], E.W. Varnes[6], D. Varouchas[14], A. Vartapetian[7], K.E. Varvell[149], V.I. Vassilakopoulos[56], F. Vazeille[33], G. Vegni[88a,88b], J.J. Veillet[114], C. Vellidis[8], F. Veloso[123a], R. Veness[29], S. Veneziano[131a], A. Ventura[71a,71b], D. Ventura[137], M. Venturi[48], N. Venturi[157], V. Vercesi[118a], M. Verducci[137], W. Verkerke[104], J.C. Vermeulen[104], A. Vest[43], M.C. Vetterli[141,d], I. Vichou[164], T. Vickey[144b,af], O.E. Vickey Boeriu[144b], G.H.A. Viehhauser[117], S. Viel[167], M. Villa[19a,19b], M. Villaplana Perez[166], E. Vilucchi[47], M.G. Vincter[28], E. Vinek[29], V.B. Vinogradov[64], M. Virchaux[135,*], J. Virzi[14], O. Vitells[170], M. Viti[41], I. Vivarelli[48], F. Vives Vaque[2], S. Vlachos[9], D. Vladoiu[97], M. Vlasak[126], N. Vlasov[20], A. Vogel[20], P. Vokac[126], G. Volpi[47], M. Volpi[85], G. Volpini[88a], H. von der Schmitt[98], J. von Loeben[98], H. von Radziewski[48], E. von Toerne[20], V. Vorobel[125], A.P. Vorobiev[127], V. Vorwerk[11], M. Vos[166], R. Voss[29], T.T. Voss[173], J.H. Vossebeld[72], N. Vranjes[12a], M. Vranjes Milosavljevic[104], V. Vrba[124], M. Vreeswijk[104], T. Vu Anh[80], R. Vuillermet[29], I. Vukotic[114], W. Wagner[173], P. Wagner[119], H. Wahlen[173], J. Wakabayashi[100], J. Walbersloh[42], S. Walch[86], J. Walder[70], R. Walker[97], W. Walkowiak[140], R. Wall[174], P. Waller[72], C. Wang[44], H. Wang[171], H. Wang[32b,ag], J. Wang[150], J. Wang[55], J.C. Wang[137], R. Wang[102], S.M. Wang[150], A. Warburton[84], C.P. Ward[27], M. Warsinsky[48], P.M. Watkins[17], A.T. Watson[17], I.J. Watson[149], M.F. Watson[17], G. Watts[137], S. Watts[81], A.T. Waugh[149], B.M. Waugh[76], M. Weber[128], M.S. Weber[16], P. Weber[54], A.R. Weidberg[117], P. Weigell[98], J. Weingarten[54], C. Weiser[48], H. Wellenstein[22], P.S. Wells[29], M. Wen[47], T. Wenaus[24], S. Wendler[122], Z. Weng[150,u], T. Wengler[29], S. Wenig[29], N. Wermes[20], M. Werner[48], P. Werner[29], M. Werth[162], M. Wessels[58a], C. Weydert[55], K. Whalen[28], S.J. Wheeler-Ellis[162], S.P. Whitaker[21], A. White[7], M.J. White[85], S.R. Whitehead[117], D. Whiteson[162], D. Whittington[60], F. Wicek[114], D. Wicke[173], F.J. Wickens[128], W. Wiedenmann[171],

M. Wielers[128], P. Wienemann[20], C. Wiglesworth[74], L.A.M. Wiik-Fuchs[48], P.A. Wijeratne[76], A. Wildauer[166], M.A. Wildt[41,q], I. Wilhelm[125], H.G. Wilkens[29], J.Z. Will[97], E. Williams[34], H.H. Williams[119], W. Willis[34], S. Willocq[83], J.A. Wilson[17], M.G. Wilson[142], A. Wilson[86], I. Wingerter-Seez[4], S. Winkelmann[48], F. Winklmeier[29], M. Wittgen[142], M.W. Wolter[38], H. Wolters[123a,h], W.C. Wong[40], G. Wooden[86], B.K. Wosiek[38], J. Wotschack[29], M.J. Woudstra[83], K.W. Wozniak[38], K. Wraight[53], C. Wright[53], M. Wright[53], B. Wrona[72], S.L. Wu[171], X. Wu[49], Y. Wu[32b,ah], E. Wulf[34], R. Wunstorf[42], B.M. Wynne[45], S. Xella[35], M. Xiao[135], S. Xie[48], Y. Xie[32a], C. Xu[32b,w], D. Xu[138], G. Xu[32a], B. Yabsley[149], S. Yacoob[144b], M. Yamada[65], H. Yamaguchi[154], A. Yamamoto[65], K. Yamamoto[63], S. Yamamoto[154], T. Yamamura[154], T. Yamanaka[154], J. Yamaoka[44], T. Yamazaki[154], Y. Yamazaki[66], Z. Yan[21], H. Yang[86], U.K. Yang[81], Y. Yang[60], Y. Yang[32a], Z. Yang[145a,145b], S. Yanush[90], Y. Yao[14], Y. Yasu[65], G.V. Ybeles Smit[129], J. Ye[39], S. Ye[24], M. Yilmaz[3c], R. Yoosoofmiya[122], K. Yorita[169], R. Yoshida[5], C. Young[142], S. Youssef[21], D. Yu[24], J. Yu[7], J. Yu[111], L. Yuan[32a,ai], A. Yurkewicz[105], B. Zabinski[38], V.G. Zaets [127], R. Zaidan[62], A.M. Zaitsev[127], Z. Zajacova[29], L. Zanello[131a,131b], P. Zarzhitsky[39], A. Zaytsev[106], C. Zeitnitz[173], M. Zeller[174], M. Zeman[124], A. Zemla[38], C. Zendler[20], O. Zenin[127], T. Ženiš[143a], Z. Zinonos[121a,121b], S. Zenz[14], D. Zerwas[114], G. Zevi della Porta[57], Z. Zhan[32d], D. Zhang[32b,ag], H. Zhang[87], J. Zhang[5], X. Zhang[32d], Z. Zhang[114], L. Zhao[107], T. Zhao[137], Z. Zhao[32b], A. Zhemchugov[64], S. Zheng[32a], J. Zhong[117], B. Zhou[86], N. Zhou[162], Y. Zhou[150], C.G. Zhu[32d], H. Zhu[41], J. Zhu[86], Y. Zhu[32b], X. Zhuang[97], V. Zhuravlov[98], D. Zieminska[60], R. Zimmermann[20], S. Zimmermann[20], S. Zimmermann[48], M. Ziolkowski[140], R. Zitoun[4], L. Živković[34], V.V. Zmouchko[127,*], G. Zobernig[171], A. Zoccoli[19a,19b], Y. Zolnierowski[4], A. Zsenei[29], M. zur Nedden[15], V. Zutshi[105], L. Zwalinski[29].

[1] University at Albany, Albany NY, United States of America
[2] Department of Physics, University of Alberta, Edmonton AB, Canada
[3] [(a)]Department of Physics, Ankara University, Ankara; [(b)]Department of Physics, Dumlupinar University, Kutahya; [(c)]Department of Physics, Gazi University, Ankara; [(d)]Division of Physics, TOBB University of Economics and Technology, Ankara; [(e)]Turkish Atomic Energy Authority, Ankara, Turkey
[4] LAPP, CNRS/IN2P3 and Université de Savoie, Annecy-le-Vieux, France
[5] High Energy Physics Division, Argonne National Laboratory, Argonne IL, United States of America
[6] Department of Physics, University of Arizona, Tucson AZ, United States of America
[7] Department of Physics, The University of Texas at Arlington, Arlington TX, United States of America
[8] Physics Department, University of Athens, Athens, Greece
[9] Physics Department, National Technical University of Athens, Zografou, Greece
[10] Institute of Physics, Azerbaijan Academy of Sciences, Baku, Azerbaijan
[11] Institut de Física d'Altes Energies and Departament de Física de la Universitat Autònoma de Barcelona and ICREA, Barcelona, Spain
[12] [(a)]Institute of Physics, University of Belgrade, Belgrade; [(b)]Vinca Institute of Nuclear Sciences, University of Belgrade, Belgrade, Serbia
[13] Department for Physics and Technology, University of Bergen, Bergen, Norway
[14] Physics Division, Lawrence Berkeley National Laboratory and University of California, Berkeley CA, United States of America
[15] Department of Physics, Humboldt University, Berlin, Germany
[16] Albert Einstein Center for Fundamental Physics and Laboratory for High Energy Physics, University of Bern, Bern, Switzerland
[17] School of Physics and Astronomy, University of Birmingham, Birmingham, United Kingdom
[18] [(a)]Department of Physics, Bogazici University, Istanbul; [(b)]Division of Physics, Dogus University, Istanbul; [(c)]Department of Physics Engineering, Gaziantep University, Gaziantep; [(d)]Department of Physics, Istanbul Technical University, Istanbul, Turkey
[19] [(a)]INFN Sezione di Bologna; [(b)]Dipartimento di Fisica, Università di Bologna, Bologna, Italy
[20] Physikalisches Institut, University of Bonn, Bonn, Germany
[21] Department of Physics, Boston University, Boston MA, United States of America
[22] Department of Physics, Brandeis University, Waltham MA, United States of America
[23] [(a)]Universidade Federal do Rio De Janeiro COPPE/EE/IF, Rio de Janeiro; [(b)]Federal University of Juiz de Fora (UFJF), Juiz de Fora; [(c)]Federal University of Sao Joao del Rei (UFSJ), Sao Joao del Rei; [(d)]Instituto de Fisica, Universidade de Sao Paulo, Sao Paulo, Brazil
[24] Physics Department, Brookhaven National Laboratory, Upton NY, United States of America
[25] [(a)]National Institute of Physics and Nuclear Engineering, Bucharest; [(b)]University Politehnica Bucharest, Bucharest; [(c)]West University in Timisoara, Timisoara, Romania
[26] Departamento de Física, Universidad de Buenos Aires, Buenos Aires, Argentina
[27] Cavendish Laboratory, University of Cambridge, Cambridge, United Kingdom
[28] Department of Physics, Carleton University, Ottawa ON, Canada
[29] CERN, Geneva, Switzerland
[30] Enrico Fermi Institute, University of Chicago, Chicago IL, United States of America
[31] [(a)]Departamento de Fisica, Pontificia Universidad Católica de Chile, Santiago; [(b)]Departamento de Física, Universidad Técnica Federico Santa María, Valparaíso, Chile
[32] [(a)]Institute of High Energy Physics, Chinese Academy of Sciences, Beijing; [(b)]Department of Modern Physics, University of Science and Technology of China, Anhui; [(c)]Department of Physics, Nanjing University, Jiangsu; [(d)]School of Physics, Shandong University, Shandong, China

[33] Laboratoire de Physique Corpusculaire, Clermont Université and Université Blaise Pascal and CNRS/IN2P3, Aubiere Cedex, France
[34] Nevis Laboratory, Columbia University, Irvington NY, United States of America
[35] Niels Bohr Institute, University of Copenhagen, Kobenhavn, Denmark
[36] [(a)]INFN Gruppo Collegato di Cosenza; [(b)]Dipartimento di Fisica, Università della Calabria, Arcavata di Rende, Italy
[37] AGH University of Science and Technology, Faculty of Physics and Applied Computer Science, Krakow, Poland
[38] The Henryk Niewodniczanski Institute of Nuclear Physics, Polish Academy of Sciences, Krakow, Poland
[39] Physics Department, Southern Methodist University, Dallas TX, United States of America
[40] Physics Department, University of Texas at Dallas, Richardson TX, United States of America
[41] DESY, Hamburg and Zeuthen, Germany
[42] Institut für Experimentelle Physik IV, Technische Universität Dortmund, Dortmund, Germany
[43] Institut für Kern- und Teilchenphysik, Technical University Dresden, Dresden, Germany
[44] Department of Physics, Duke University, Durham NC, United States of America
[45] SUPA - School of Physics and Astronomy, University of Edinburgh, Edinburgh, United Kingdom
[46] Fachhochschule Wiener Neustadt, Johannes Gutenbergstrasse 3 2700 Wiener Neustadt, Austria
[47] INFN Laboratori Nazionali di Frascati, Frascati, Italy
[48] Fakultät für Mathematik und Physik, Albert-Ludwigs-Universität, Freiburg i.Br., Germany
[49] Section de Physique, Université de Genève, Geneva, Switzerland
[50] [(a)]INFN Sezione di Genova; [(b)]Dipartimento di Fisica, Università di Genova, Genova, Italy
[51] [(a)]E.Andronikashvili Institute of Physics, Tbilisi State University, Tbilisi; [(b)]High Energy Physics Institute, Tbilisi State University, Tbilisi, Georgia
[52] II Physikalisches Institut, Justus-Liebig-Universität Giessen, Giessen, Germany
[53] SUPA - School of Physics and Astronomy, University of Glasgow, Glasgow, United Kingdom
[54] II Physikalisches Institut, Georg-August-Universität, Göttingen, Germany
[55] Laboratoire de Physique Subatomique et de Cosmologie, Université Joseph Fourier and CNRS/IN2P3 and Institut National Polytechnique de Grenoble, Grenoble, France
[56] Department of Physics, Hampton University, Hampton VA, United States of America
[57] Laboratory for Particle Physics and Cosmology, Harvard University, Cambridge MA, United States of America
[58] [(a)]Kirchhoff-Institut für Physik, Ruprecht-Karls-Universität Heidelberg, Heidelberg; [(b)]Physikalisches Institut, Ruprecht-Karls-Universität Heidelberg, Heidelberg; [(c)]ZITI Institut für technische Informatik, Ruprecht-Karls-Universität Heidelberg, Mannheim, Germany
[59] Faculty of Applied Information Science, Hiroshima Institute of Technology, Hiroshima, Japan
[60] Department of Physics, Indiana University, Bloomington IN, United States of America
[61] Institut für Astro- und Teilchenphysik, Leopold-Franzens-Universität, Innsbruck, Austria
[62] University of Iowa, Iowa City IA, United States of America
[63] Department of Physics and Astronomy, Iowa State University, Ames IA, United States of America
[64] Joint Institute for Nuclear Research, JINR Dubna, Dubna, Russia
[65] KEK, High Energy Accelerator Research Organization, Tsukuba, Japan
[66] Graduate School of Science, Kobe University, Kobe, Japan
[67] Faculty of Science, Kyoto University, Kyoto, Japan
[68] Kyoto University of Education, Kyoto, Japan
[69] Instituto de Física La Plata, Universidad Nacional de La Plata and CONICET, La Plata, Argentina
[70] Physics Department, Lancaster University, Lancaster, United Kingdom
[71] [(a)]INFN Sezione di Lecce; [(b)]Dipartimento di Fisica, Università del Salento, Lecce, Italy
[72] Oliver Lodge Laboratory, University of Liverpool, Liverpool, United Kingdom
[73] Department of Physics, Jožef Stefan Institute and University of Ljubljana, Ljubljana, Slovenia
[74] School of Physics and Astronomy, Queen Mary University of London, London, United Kingdom
[75] Department of Physics, Royal Holloway University of London, Surrey, United Kingdom
[76] Department of Physics and Astronomy, University College London, London, United Kingdom
[77] Laboratoire de Physique Nucléaire et de Hautes Energies, UPMC and Université Paris-Diderot and CNRS/IN2P3, Paris, France
[78] Fysiska institutionen, Lunds universitet, Lund, Sweden
[79] Departamento de Fisica Teorica C-15, Universidad Autonoma de Madrid, Madrid, Spain
[80] Institut für Physik, Universität Mainz, Mainz, Germany
[81] School of Physics and Astronomy, University of Manchester, Manchester, United Kingdom
[82] CPPM, Aix-Marseille Université and CNRS/IN2P3, Marseille, France
[83] Department of Physics, University of Massachusetts, Amherst MA, United States of America
[84] Department of Physics, McGill University, Montreal QC, Canada
[85] School of Physics, University of Melbourne, Victoria, Australia
[86] Department of Physics, The University of Michigan, Ann Arbor MI, United States of America
[87] Department of Physics and Astronomy, Michigan State University, East Lansing MI, United States of America
[88] [(a)]INFN Sezione di Milano; [(b)]Dipartimento di Fisica, Università di Milano, Milano, Italy
[89] B.I. Stepanov Institute of Physics, National Academy of Sciences of Belarus, Minsk, Republic of Belarus
[90] National Scientific and Educational Centre for Particle and High Energy Physics, Minsk, Republic of Belarus
[91] Department of Physics, Massachusetts Institute of Technology, Cambridge MA, United States of America
[92] Group of Particle Physics, University of Montreal, Montreal QC, Canada

[93] P.N. Lebedev Institute of Physics, Academy of Sciences, Moscow, Russia
[94] Institute for Theoretical and Experimental Physics (ITEP), Moscow, Russia
[95] Moscow Engineering and Physics Institute (MEPhI), Moscow, Russia
[96] Skobeltsyn Institute of Nuclear Physics, Lomonosov Moscow State University, Moscow, Russia
[97] Fakultät für Physik, Ludwig-Maximilians-Universität München, München, Germany
[98] Max-Planck-Institut für Physik (Werner-Heisenberg-Institut), München, Germany
[99] Nagasaki Institute of Applied Science, Nagasaki, Japan
[100] Graduate School of Science, Nagoya University, Nagoya, Japan
[101] [(a)]INFN Sezione di Napoli; [(b)]Dipartimento di Scienze Fisiche, Università di Napoli, Napoli, Italy
[102] Department of Physics and Astronomy, University of New Mexico, Albuquerque NM, United States of America
[103] Institute for Mathematics, Astrophysics and Particle Physics, Radboud University Nijmegen/Nikhef, Nijmegen, Netherlands
[104] Nikhef National Institute for Subatomic Physics and University of Amsterdam, Amsterdam, Netherlands
[105] Department of Physics, Northern Illinois University, DeKalb IL, United States of America
[106] Budker Institute of Nuclear Physics, SB RAS, Novosibirsk, Russia
[107] Department of Physics, New York University, New York NY, United States of America
[108] Ohio State University, Columbus OH, United States of America
[109] Faculty of Science, Okayama University, Okayama, Japan
[110] Homer L. Dodge Department of Physics and Astronomy, University of Oklahoma, Norman OK, United States of America
[111] Department of Physics, Oklahoma State University, Stillwater OK, United States of America
[112] Palacký University, RCPTM, Olomouc, Czech Republic
[113] Center for High Energy Physics, University of Oregon, Eugene OR, United States of America
[114] LAL, Univ. Paris-Sud and CNRS/IN2P3, Orsay, France
[115] Graduate School of Science, Osaka University, Osaka, Japan
[116] Department of Physics, University of Oslo, Oslo, Norway
[117] Department of Physics, Oxford University, Oxford, United Kingdom
[118] [(a)]INFN Sezione di Pavia; [(b)]Dipartimento di Fisica, Università di Pavia, Pavia, Italy
[119] Department of Physics, University of Pennsylvania, Philadelphia PA, United States of America
[120] Petersburg Nuclear Physics Institute, Gatchina, Russia
[121] [(a)]INFN Sezione di Pisa; [(b)]Dipartimento di Fisica E. Fermi, Università di Pisa, Pisa, Italy
[122] Department of Physics and Astronomy, University of Pittsburgh, Pittsburgh PA, United States of America
[123] [(a)]Laboratorio de Instrumentacao e Fisica Experimental de Particulas - LIP, Lisboa, Portugal; [(b)]Departamento de Fisica Teorica y del Cosmos and CAFPE, Universidad de Granada, Granada, Spain
[124] Institute of Physics, Academy of Sciences of the Czech Republic, Praha, Czech Republic
[125] Faculty of Mathematics and Physics, Charles University in Prague, Praha, Czech Republic
[126] Czech Technical University in Prague, Praha, Czech Republic
[127] State Research Center Institute for High Energy Physics, Protvino, Russia
[128] Particle Physics Department, Rutherford Appleton Laboratory, Didcot, United Kingdom
[129] Physics Department, University of Regina, Regina SK, Canada
[130] Ritsumeikan University, Kusatsu, Shiga, Japan
[131] [(a)]INFN Sezione di Roma I; [(b)]Dipartimento di Fisica, Università La Sapienza, Roma, Italy
[132] [(a)]INFN Sezione di Roma Tor Vergata; [(b)]Dipartimento di Fisica, Università di Roma Tor Vergata, Roma, Italy
[133] [(a)]INFN Sezione di Roma Tre; [(b)]Dipartimento di Fisica, Università Roma Tre, Roma, Italy
[134] [(a)]Faculté des Sciences Ain Chock, Réseau Universitaire de Physique des Hautes Energies - Université Hassan II, Casablanca; [(b)]Centre National de l'Energie des Sciences Techniques Nucleaires, Rabat; [(c)]Faculté des Sciences Semlalia, Université Cadi Ayyad, LPHEA-Marrakech; [(d)]Faculté des Sciences, Université Mohamed Premier and LPTPM, Oujda; [(e)]Faculté des Sciences, Université Mohammed V- Agdal, Rabat, Morocco
[135] DSM/IRFU (Institut de Recherches sur les Lois Fondamentales de l'Univers), CEA Saclay (Commissariat a l'Energie Atomique), Gif-sur-Yvette, France
[136] Santa Cruz Institute for Particle Physics, University of California Santa Cruz, Santa Cruz CA, United States of America
[137] Department of Physics, University of Washington, Seattle WA, United States of America
[138] Department of Physics and Astronomy, University of Sheffield, Sheffield, United Kingdom
[139] Department of Physics, Shinshu University, Nagano, Japan
[140] Fachbereich Physik, Universität Siegen, Siegen, Germany
[141] Department of Physics, Simon Fraser University, Burnaby BC, Canada
[142] SLAC National Accelerator Laboratory, Stanford CA, United States of America
[143] [(a)]Faculty of Mathematics, Physics & Informatics, Comenius University, Bratislava; [(b)]Department of Subnuclear Physics, Institute of Experimental Physics of the Slovak Academy of Sciences, Kosice, Slovak Republic
[144] [(a)]Department of Physics, University of Johannesburg, Johannesburg; [(b)]School of Physics, University of the Witwatersrand, Johannesburg, South Africa
[145] [(a)]Department of Physics, Stockholm University; [(b)]The Oskar Klein Centre, Stockholm, Sweden
[146] Physics Department, Royal Institute of Technology, Stockholm, Sweden
[147] Departments of Physics & Astronomy and Chemistry, Stony Brook University, Stony Brook NY, United States of America
[148] Department of Physics and Astronomy, University of Sussex, Brighton, United Kingdom
[149] School of Physics, University of Sydney, Sydney, Australia

[150] Institute of Physics, Academia Sinica, Taipei, Taiwan
[151] Department of Physics, Technion: Israel Inst. of Technology, Haifa, Israel
[152] Raymond and Beverly Sackler School of Physics and Astronomy, Tel Aviv University, Tel Aviv, Israel
[153] Department of Physics, Aristotle University of Thessaloniki, Thessaloniki, Greece
[154] International Center for Elementary Particle Physics and Department of Physics, The University of Tokyo, Tokyo, Japan
[155] Graduate School of Science and Technology, Tokyo Metropolitan University, Tokyo, Japan
[156] Department of Physics, Tokyo Institute of Technology, Tokyo, Japan
[157] Department of Physics, University of Toronto, Toronto ON, Canada
[158] [(a)]TRIUMF, Vancouver BC; [(b)]Department of Physics and Astronomy, York University, Toronto ON, Canada
[159] Institute of Pure and Applied Sciences, University of Tsukuba,1-1-1 Tennodai,Tsukuba, Ibaraki 305-8571, Japan
[160] Science and Technology Center, Tufts University, Medford MA, United States of America
[161] Centro de Investigaciones, Universidad Antonio Narino, Bogota, Colombia
[162] Department of Physics and Astronomy, University of California Irvine, Irvine CA, United States of America
[163] [(a)]INFN Gruppo Collegato di Udine; [(b)]ICTP, Trieste; [(c)]Dipartimento di Chimica, Fisica e Ambiente, Università di Udine, Udine, Italy
[164] Department of Physics, University of Illinois, Urbana IL, United States of America
[165] Department of Physics and Astronomy, University of Uppsala, Uppsala, Sweden
[166] Instituto de Física Corpuscular (IFIC) and Departamento de Física Atómica, Molecular y Nuclear and Departamento de Ingeniería Electrónica and Instituto de Microelectrónica de Barcelona (IMB-CNM), University of Valencia and CSIC, Valencia, Spain
[167] Department of Physics, University of British Columbia, Vancouver BC, Canada
[168] Department of Physics and Astronomy, University of Victoria, Victoria BC, Canada
[169] Waseda University, Tokyo, Japan
[170] Department of Particle Physics, The Weizmann Institute of Science, Rehovot, Israel
[171] Department of Physics, University of Wisconsin, Madison WI, United States of America
[172] Fakultät für Physik und Astronomie, Julius-Maximilians-Universität, Würzburg, Germany
[173] Fachbereich C Physik, Bergische Universität Wuppertal, Wuppertal, Germany
[174] Department of Physics, Yale University, New Haven CT, United States of America
[175] Yerevan Physics Institute, Yerevan, Armenia
[176] Domaine scientifique de la Doua, Centre de Calcul CNRS/IN2P3, Villeurbanne Cedex, France
[a] Also at Laboratorio de Instrumentacao e Fisica Experimental de Particulas - LIP, Lisboa, Portugal
[b] Also at Faculdade de Ciencias and CFNUL, Universidade de Lisboa, Lisboa, Portugal
[c] Also at Particle Physics Department, Rutherford Appleton Laboratory, Didcot, United Kingdom
[d] Also at TRIUMF, Vancouver BC, Canada
[e] Also at Department of Physics, California State University, Fresno CA, United States of America
[f] Also at Novosibirsk State University, Novosibirsk, Russia
[g] Also at Fermilab, Batavia IL, United States of America
[h] Also at Department of Physics, University of Coimbra, Coimbra, Portugal
[i] Also at Università di Napoli Parthenope, Napoli, Italy
[j] Also at Institute of Particle Physics (IPP), Canada
[k] Also at Department of Physics, Middle East Technical University, Ankara, Turkey
[l] Also at Louisiana Tech University, Ruston LA, United States of America
[m] Also at Department of Physics and Astronomy, University College London, London, United Kingdom
[n] Also at Group of Particle Physics, University of Montreal, Montreal QC, Canada
[o] Also at Department of Physics, University of Cape Town, Cape Town, South Africa
[p] Also at Institute of Physics, Azerbaijan Academy of Sciences, Baku, Azerbaijan
[q] Also at Institut für Experimentalphysik, Universität Hamburg, Hamburg, Germany
[r] Also at Manhattan College, New York NY, United States of America
[s] Also at School of Physics, Shandong University, Shandong, China
[t] Also at CPPM, Aix-Marseille Université and CNRS/IN2P3, Marseille, France
[u] Also at School of Physics and Engineering, Sun Yat-sen University, Guanzhou, China
[v] Also at Academia Sinica Grid Computing, Institute of Physics, Academia Sinica, Taipei, Taiwan
[w] Also at DSM/IRFU (Institut de Recherches sur les Lois Fondamentales de l'Univers), CEA Saclay (Commissariat a l'Energie Atomique), Gif-sur-Yvette, France
[x] Also at Section de Physique, Université de Genève, Geneva, Switzerland
[y] Also at Departamento de Fisica, Universidade de Minho, Braga, Portugal
[z] Also at Department of Physics and Astronomy, University of South Carolina, Columbia SC, United States of America
[aa] Also at Institute for Particle and Nuclear Physics, Wigner Research Centre for Physics, Budapest, Hungary
[ab] Also at California Institute of Technology, Pasadena CA, United States of America
[ac] Also at Institute of Physics, Jagiellonian University, Krakow, Poland
[ad] Also at Institute of High Energy Physics, Chinese Academy of Sciences, Beijing, China
[ae] Also at Department of Physics and Astronomy, University of Sheffield, Sheffield, United Kingdom
[af] Also at Department of Physics, Oxford University, Oxford, United Kingdom
[ag] Also at Institute of Physics, Academia Sinica, Taipei, Taiwan
[ah] Also at Department of Physics, The University of Michigan, Ann Arbor MI, United States of America

[ai] Also at Laboratoire de Physique Nucléaire et de Hautes Energies, UPMC and Université Paris-Diderot and CNRS/IN2P3, Paris, France
* Deceased

APPENDIX C

TABLES OF DATAPOINTS

The differential inelastic cross section $\mathrm{d}\sigma/\mathrm{d}\Delta\eta^F$ as measured by ATLAS over $0 \leq \Delta\eta^F < 8$ is presented for $p_{\mathrm{T}}^{\mathrm{cut}} = 200, 400, 600$ and 800 MeV. The statistical error is quoted along with correlated systematic uncertainties which are combined to form the total uncertainty. δ_{py6} corresponds to the uncertainty in the modelling of the final state, δ_{pho} to the uncertainty in modelling the ξ_X, ξ_Y and t distributions, $\delta_{\mathrm{e+}}$ and $\delta_{\mathrm{e-}}$ to the energy scale uncertainty, δ_{sd} and δ_{dd} to the uncertainty from the relative fractions of diffraction, δ_{cd} to uncertainty from the CD contribution in PHOJET, δ_{mat} to the uncertainty from the dead material budget in the tracking region and δ_{mbts} to the response of the MBTS trigger. The luminosity uncertainty is 3.4% and is included in the total.

The datapoints from Figure 11.9 are also presented. For each point, two uncertainties are shown. The first corresponds to the total uncertainty while the second corresponds to all sources, except for the dominant luminosity uncertainty. These sources are all of the above mentioned in addition to the uncertainty from the $\Delta\eta^F \to \xi_X$ correction described in Section 11.5.

Table C.1: Table of $\Delta\eta^F$ datapoints for $p_{\mathrm{T}} > 200$ MeV (see text).

$\Delta\eta^F$	$\mathrm{d}\sigma/\mathrm{d}\Delta\eta^F$ [mb]	δ_{stat} [%]	$+\delta_{\mathrm{tot}}$ [%]	$-\delta_{\mathrm{tot}}$ [%]	δ_{py6} [%]	δ_{pho} [%]	$\delta_{\mathrm{e+}}$ [%]	$\delta_{\mathrm{e-}}$ [%]	δ_{sd} [%]	δ_{dd} [%]	δ_{cd} [%]	δ_{mat} [%]	δ_{mbts} [%]
0.0–0.4	85	0.2	9.4	-9.5	-2.9	-7.6	3.0	-3.2	0.1	-0.1	0.0	-1.1	-0.1
0.4–0.8	26	0	15	-15	4	14	-3	3	-0	0	0	2	0
0.8–1.2	10	0	20	-20	5	18	-6	5	-0	0	0	3	0
1.2–1.6	5	0	21	-21	10	17	-6	7	0	-0	0	2	-0
1.6–2.0	2.8	0	22	-22	15	13	-7	9	0	-0	-0	3	0
2.0–2.2	2.1	1	18	-18	15	5	-9	8	-0	0	-0	1	0
2.2–2.4	1.8	1	18	-18	14	7	-8	8	-0	0	-0	1	0
2.4–2.6	1.7	1	15	-14	9	2	-9	10	-0	0	-0	-3	0
2.6–2.8	1.6	1	14	-13	5	1	-11	13	-0	0	-0	-0	0
2.8–3.0	1.4	1	14	-10	5	2	-8	12	-0	0	-1	-1	0
3.0–3.2	1.3	1	11	-9	4	2	-7	10	-1	0	-0	1	1
3.2–3.4	1.2	1.3	8.4	-9.9	3.5	3.7	-7.5	5.4	-0.6	0.4	-0.4	1.1	0.6
3.4–3.6	1.20	1.3	7.3	-8.2	4.4	0.4	-5.0	3.5	-0.7	0.6	-0.5	-2.7	0.9
3.6–3.8	1.1	1	11	-9	6	5	-4	7	-1	0	-1	-1	1
3.8–4.0	1.0	2	10	-10	7	4	-4	4	-0	0	-1	-2	1
4.0–4.2	1.01	1.6	5.7	-8.5	3.1	2.6	-6.2	0.2	-0.7	0.6	-1.0	-0.7	0.8
4.2–4.4	0.9	1	11	-11	5	8	-2	3	-1	1	-1	-3	1
4.4–4.6	0.92	1.8	7.8	-7.8	3.9	5.0	-2.1	2.1	-0.3	0.3	-1.0	-0.8	0.4
4.6–4.8	0.91	1.7	7.8	-8.4	4.5	4.8	-3.3	0.8	-0.9	0.7	-0.9	-0.4	1.1
4.8–5.0	0.88	2	10	-10	6	7	-0	3	-1	1	-1	-1	1
5.0–5.2	0.87	1.6	8.2	-7.8	5.3	4.0	0.5	2.5	-0.7	0.5	-0.9	-0.4	0.9
5.2–5.4	0.89	1.8	7.3	-7.5	5.5	2.5	-1.5	-1.6	-0.7	0.5	-0.9	-0.5	0.9
5.4–5.6	0.9	1	12	-12	8	7	1	1	-1	1	-1	2	1
5.6–5.8	0.95	1.2	7.5	-8.4	5.1	3.8	-2.3	-3.6	-1.0	0.8	-0.9	0.9	1.3
5.8–6.0	0.9	1	11	-10	7	6	3	0	-1	0	-1	1	1
6.0–6.2	0.95	1.4	8.6	-9.3	7.0	2.7	0.2	-3.5	-0.6	0.5	-1.2	1.6	1.0
6.2–6.4	1.0	1	12	-13	6	7	7	-8	-1	1	-1	4	1
6.4–6.6	0.99	1.3	7.8	-7.9	3.6	5.7	-0.2	-0.5	-0.6	0.5	-0.7	0.8	1.2
6.6–6.8	1.06	1.3	5.4	-5.4	2.0	3.0	-0.9	1.0	-0.5	0.4	-0.5	-0.4	1.0
6.8–7.0	1.08	1.3	5.4	-5.2	-0.0	3.3	-0.9	1.7	-0.1	0.1	-0.5	-1.3	0.6
7.0–7.2	1.11	1.2	4.4	-4.5	-1.9	-0.2	-1.2	1.0	-0.4	0.3	-0.1	-0.6	1.1
7.2–7.4	1.11	0.9	5.3	-5.7	-3.4	0.1	1.2	-2.6	-0.4	0.3	-0.2	-0.9	1.3
7.4–7.6	1.13	1.0	5.1	-6.1	-3.2	-0.6	-0.0	-3.3	-0.6	0.4	-0.2	0.5	1.6
7.6–7.8	1.17	1.0	5.9	-6.7	-4.0	-1.7	-0.0	-3.2	-0.3	0.2	-0.2	1.2	1.3
7.8–8.0	1.20	1.0	5.7	-5.4	-4.0	-0.5	1.0	1.8	-0.0	0.0	-0.1	-0.0	1.0

Table C.2: Table of $\Delta\eta^F$ datapoints for $p_{\mathrm{T}} > 400$ MeV (see text).

$\Delta\eta^F$	$\mathrm{d}\sigma/\mathrm{d}\Delta\eta^F$ [mb]	δ_{stat} [%]	$+\delta_{\mathrm{tot}}$ [%]	$-\delta_{\mathrm{tot}}$ [%]	δ_{py6} [%]	δ_{pho} [%]	$\delta_{\mathrm{e+}}$ [%]	$\delta_{\mathrm{e-}}$ [%]	δ_{sd} [%]	δ_{dd} [%]	δ_{cd} [%]	δ_{mat} [%]	δ_{mbts} [%]
0.0–0.4	66	0	14	-15	-2	-10	9	-10	0	-0	0	-1	-0
0.4–0.8	28	0	11	-11	3	10	1	-1	0	-0	0	1	0
0.8–1.2	14	0	15	-15	2	14	-2	2	0	-0	0	2	-0
1.2–1.6	8	0	17	-16	2	15	-4	4	0	-0	0	1	0
1.6–2.0	5.2	0	15	-16	3	13	-6	4	0	-0	0	3	-0
2.0–2.2	3.8	0	15	-14	5	12	-5	7	0	-0	-0	1	0
2.2–2.4	3.2	0	14	-14	4	11	-6	7	0	-0	-0	3	-0
2.4–2.6	2.8	1	13	-12	5	7	-7	9	-0	0	-0	-3	0
2.6–2.8	2.5	1	14	-13	5	6	-10	12	-0	0	-0	-0	0
2.8–3.0	2.2	1	12	-12	3	5	-9	10	-0	0	-0	2	0
3.0–3.2	1.9	1	16	-12	6	5	-7	13	-0	0	-0	-1	0
3.2–3.4	1.8	1	10	-10	2	-1	-10	9	-0	0	-0	1	0
3.4–3.6	1.7	0.9	8.9	-9.8	1.4	-1.5	-8.8	7.9	-0.3	0.2	-0.4	0.8	0.3
3.6–3.8	1.5	1	12	-10	4	2	-8	10	-0	0	-1	3	1
3.8–4.0	1.4	1	11	-11	4	-1	-9	10	-1	1	-1	-2	1
4.0–4.2	1.3	1	11	-9	2	1	-8	10	-1	1	-1	2	0
4.2–4.4	1.2	1	10	-11	3	2	-10	8	-1	1	-1	-1	1
4.4–4.6	1.1	1	15	-10	6	3	-6	12	-1	0	-1	-4	1
4.6–4.8	1.1	1	11	-9	1	-1	-7	10	-1	0	-1	1	1
4.8–5.0	1.1	1	10	-9	3	1	-7	9	-1	0	-1	-1	1
5.0–5.2	1.1	2	11	-9	3	0	-6	9	-0	0	-1	-3	0
5.2–5.4	1.03	1.4	9.5	-8.6	2.9	1.5	-6.9	8.0	-0.6	0.5	-0.8	0.4	0.6
5.4–5.6	1.0	2	10	-9	4	4	-6	8	-1	0	-1	-1	1
5.6–5.8	1.07	1.3	8.7	-8.4	1.5	2.2	-6.9	7.2	-0.9	0.7	-1.0	-0.0	1.1
5.8–6.0	1.0	1	11	-8	5	3	-4	9	-1	1	-1	-2	1
6.0–6.2	1.1	1.3	5.5	-9.8	2.3	1.0	-8.6	2.7	-0.7	0.5	-1.2	0.5	1.1
6.2–6.4	1.06	1.3	6.0	-6.6	2.9	3.4	-2.8	-0.5	-0.7	0.6	-1.0	-0.2	1.1
6.4–6.6	1.07	1.2	6.8	-7.0	-0.7	2.2	-5.2	5.0	-0.6	0.5	-0.9	1.1	0.9
6.6–6.8	1.07	1.2	6.6	-7.7	-0.2	2.9	-6.1	4.6	-0.3	0.3	-0.6	0.3	0.6
6.8–7.0	1.10	1.0	6.6	-7.4	-3.0	0.4	-5.4	4.2	-0.1	0.1	-0.7	-1.7	0.6
7.0–7.2	1.12	1.2	7.9	-8.0	-4.4	-1.4	-5.0	4.8	-0.4	0.3	-0.2	-2.1	0.8
7.2–7.4	1.11	1.3	6.9	-7.0	-5.3	-2.0	-1.1	-0.2	-0.5	0.4	-0.3	0.4	1.2
7.4–7.6	1.1	0.9	8.8	-9.0	-7.9	-0.6	-1.4	-1.9	-0.2	0.2	-0.4	1.1	0.9
7.6–7.8	1.2	1	10	-10	-8	-2	-1	-3	-0	0	-0	2	1
7.8–8.0	1.16	0.8	8.5	-8.4	-7.5	1.0	0.1	0.5	0.1	-0.0	-0.2	1.4	0.6

Table C.3: Table of $\Delta\eta^F$ datapoints for $p_{\mathrm{T}} > 600$ MeV (see text).

$\Delta\eta^F$	$\mathrm{d}\sigma/\mathrm{d}\Delta\eta^F$ [mb]	δ_{stat} [%]	$+\delta_{\mathrm{tot}}$ [%]	$-\delta_{\mathrm{tot}}$ [%]	δ_{py6} [%]	δ_{pho} [%]	$\delta_{\mathrm{e+}}$ [%]	$\delta_{\mathrm{e-}}$ [%]	δ_{sd} [%]	δ_{dd} [%]	δ_{cd} [%]	δ_{mat} [%]	δ_{mbts} [%]
0.0–0.4	46	0	19	-20	0	-13	12	-14	0	-0	0	-1	-0
0.4–0.8	25	0.2	8.0	-7.6	3.8	4.1	4.6	-3.9	0.1	-0.1	0.0	0.1	-0.1
0.8–1.2	15	0	12	-12	3	11	0	-1	0	-0	0	2	-0
1.2–1.6	10	0	15	-15	1	14	-1	1	0	-0	0	1	-0
1.6–2.0	8	0	17	-17	-1	16	-3	2	0	-0	0	3	-0
2.0–2.2	6	0	17	-16	-2	16	-2	5	0	-0	0	1	0
2.2–2.4	5.3	0	15	-15	-5	13	-4	5	0	-0	0	2	-0
2.4–2.6	4.8	0	14	-14	-4	11	-7	6	0	-0	0	-1	0
2.6–2.8	4.4	0	15	-15	-8	9	-9	9	-0	0	-0	0	0
2.8–3.0	3.9	0	15	-15	-8	8	-9	9	0	-0	-0	1	-0
3.0–3.2	3.5	0	14	-14	-8	6	-9	8	-0	0	-0	-1	-0
3.2–3.4	3.2	0	14	-14	-10	4	-8	8	-0	0	-0	1	0
3.4–3.6	3.0	0	13	-14	-11	1	-7	6	-0	0	-0	1	-0
3.6–3.8	2.7	1	15	-12	-9	4	-7	11	-0	0	-0	-1	0
3.8–4.0	2.5	1	14	-14	-10	0	-9	9	-0	0	-0	-2	1
4.0–4.2	2.3	1	14	-12	-9	3	-7	10	-0	0	-0	0	-0
4.2–4.4	2.1	1	14	-13	-10	0	-8	9	-0	0	-0	1	0
4.4–4.6	2.0	1	13	-13	-10	-0	-8	8	-0	0	-0	-1	0
4.6–4.8	1.9	1	14	-12	-9	2	-7	10	-0	0	-0	-1	1
4.8–5.0	1.8	1	14	-12	-9	2	-7	10	-0	0	-0	1	1
5.0–5.2	1.7	1	14	-12	-9	-1	-6	10	-1	1	-0	-2	0
5.2–5.4	1.6	1	15	-12	-10	-3	-6	10	-0	0	-0	-1	1
5.4–5.6	1.6	1	13	-11	-8	-0	-5	10	-1	0	-0	-0	1
5.6–5.8	1.6	1	11	-13	-9	-0	-9	6	-1	0	-1	-0	1
5.8–6.0	1.5	1	11	-12	-8	1	-8	7	-1	0	-1	1	1
6.0–6.2	1.5	1	10	-11	-7	0	-8	6	-1	0	-1	-1	1
6.2–6.4	1.5	1	11	-11	-9	-3	-3	3	-0	0	-1	-4	1
6.4–6.6	1.4	1	14	-14	-11	-2	-6	7	-1	1	-1	1	1
6.6–6.8	1.4	1	13	-12	-10	-2	-6	7	-1	1	-0	-1	1
6.8–7.0	1.4	1	13	-13	-10	-0	-7	7	-0	0	-1	-2	1
7.0–7.2	1.4	1	13	-11	-9	-1	-3	9	-0	0	-0	-1	0
7.2–7.4	1.4	1	14	-14	-12	-5	-4	2	-0	0	-0	-2	1
7.4–7.6	1.3	1	20	-20	-19	-4	-2	2	-0	0	-0	2	1
7.6–7.8	1.3	1	19	-19	-16	-10	-3	-1	-0	0	-0	-0	1
7.8–8.0	1.3	1	16	-16	-15	-4	-1	1	-0	0	-0	1	1

Table C.4: Table of $\Delta\eta^F$ datapoints for $p_{\mathrm{T}} > 800$ MeV (see text).

$\Delta\eta^F$	$\mathrm{d}\sigma/\mathrm{d}\Delta\eta^F$ [mb]	δ_{stat} [%]	$+\delta_{\mathrm{tot}}$ [%]	$-\delta_{\mathrm{tot}}$ [%]	δ_{py6} [%]	δ_{pho} [%]	$\delta_{\mathrm{e+}}$ [%]	$\delta_{\mathrm{e-}}$ [%]	δ_{sd} [%]	δ_{dd} [%]	δ_{cd} [%]	δ_{mat} [%]	δ_{mbts} [%]
0.0–0.4	31	0	22	-23	2	-16	15	-16	0	-0	0	-0	0
0.4–0.8	20	0.2	9.9	-9.4	5.0	-2.3	7.5	-6.8	0.1	-0.1	0.0	-0.1	-0.0
0.8–1.2	14	0.2	8.2	-8.4	4.8	4.7	3.2	-3.8	0.2	-0.1	0.0	0.3	-0.1
1.2–1.6	11	0	11	-12	3	10	1	-3	0	-0	0	1	-0
1.6–2.0	8	0	15	-16	1	15	-1	-2	0	-0	0	3	-0
2.0–2.2	7	0	16	-17	-1	16	-2	-0	0	-0	0	0	-0
2.2–2.4	6	0	19	-18	-3	18	-1	3	0	-0	0	1	-0
2.4–2.6	5.8	0	14	-15	-5	12	-5	4	0	-0	0	0	-0
2.6–2.8	5.4	0	17	-17	-7	13	-7	7	0	-0	0	-0	-0
2.8–3.0	4.9	0	17	-17	-8	13	-6	8	0	-0	0	0	-0
3.0–3.2	4.5	0	17	-17	-8	12	-7	7	0	-0	-0	-1	-0
3.2–3.4	4.2	0	16	-16	-10	9	-6	7	0	-0	0	1	-0
3.4–3.6	3.9	0	14	-15	-10	8	-5	3	0	-0	0	0	-0
3.6–3.8	3.6	0	16	-15	-9	10	-5	9	0	-0	0	0	0
3.8–4.0	3.5	0	16	-16	-12	6	-8	6	-0	0	-0	-3	-0
4.0–4.2	3.2	1	17	-15	-12	6	-5	9	-0	0	-0	-1	0
4.2–4.4	3.0	1	17	-17	-14	4	-7	7	-0	0	-0	1	-0
4.4–4.6	2.8	1	19	-18	-17	1	-6	8	-0	0	-0	0	-0
4.6–4.8	2.6	1	19	-18	-16	4	-6	8	-0	0	-0	2	0
4.8–5.0	2.5	1	19	-19	-17	2	-7	7	-0	0	-0	1	-0
5.0–5.2	2.4	1	20	-19	-18	1	-6	7	-0	0	-0	1	0
5.2–5.4	2.3	1	20	-20	-19	-1	-8	6	-0	0	-0	-1	0
5.4–5.6	2.2	1	19	-19	-17	2	-6	6	-0	0	-0	-2	0
5.6–5.8	2.2	1	21	-21	-20	1	-6	6	-0	0	-0	-0	0
5.8–6.0	2.2	1	20	-21	-19	1	-7	5	-0	0	-0	1	1
6.0–6.2	2.1	1	19	-21	-18	-1	-9	3	-0	0	-0	-3	0
6.2–6.4	2.0	1	22	-22	-22	-1	-2	1	-0	0	-0	-1	1
6.4–6.6	1.9	1	25	-25	-24	1	-5	6	-0	0	-0	-2	1
6.6–6.8	1.8	1	26	-26	-25	-4	-6	5	-0	0	-0	1	1
6.8–7.0	1.8	1	25	-24	-23	-2	-4	7	-0	0	-0	1	1
7.0–7.2	1.7	1	23	-22	-21	-1	-2	7	-1	0	-0	-3	1
7.2–7.4	1.7	1	26	-26	-25	-3	-2	1	-0	0	-0	-2	0
7.4–7.6	1.7	1	32	-32	-32	1	1	1	-0	0	0	2	1
7.6–7.8	1.6	0	29	-29	-28	-6	1	1	-0	0	0	-1	0
7.8–8.0	1.6	0	29	-29	-29	-3	2	-0	-0	0	-0	-0	0

Table C.5: Table of datapoints for $\sigma(\xi > \xi_{\mathrm{Cut}})$ (see text).

ξ_{Cut}	ξ_{Cut} $-_{\mathrm{ve}}$ Error	ξ_{Cut} $+_{\mathrm{ve}}$ Error	$\sigma(\xi > \xi_{\mathrm{Cut}})$ [mb]	Total $+_{\mathrm{ve}}$ Error [mb]	Total $-_{\mathrm{ve}}$ Error [mb]	$+_{\mathrm{ve}}$ Error [mb]	$-_{\mathrm{ve}}$ Error [mb]
1.36×10^{-3}	1.21×10^{-3}	1.52×10^{-3}	53.17	1.89	1.91	0.56	0.62
1.10×10^{-3}	9.84×10^{-4}	1.24×10^{-3}	53.43	1.90	1.92	0.57	0.61
8.98×10^{-4}	8.03×10^{-4}	1.01×10^{-3}	53.66	1.91	1.92	0.55	0.59
7.31×10^{-4}	6.55×10^{-4}	8.17×10^{-4}	53.89	1.91	1.92	0.53	0.57
5.95×10^{-4}	5.34×10^{-4}	6.64×10^{-4}	54.13	1.91	1.92	0.52	0.56
4.84×10^{-4}	4.35×10^{-4}	5.39×10^{-4}	54.36	1.92	1.93	0.51	0.54
3.94×10^{-4}	3.55×10^{-4}	4.39×10^{-4}	54.59	1.92	1.93	0.48	0.52
3.21×10^{-4}	2.89×10^{-4}	3.57×10^{-4}	54.81	1.92	1.93	0.47	0.50
2.61×10^{-4}	2.35×10^{-4}	2.90×10^{-4}	55.03	1.92	1.93	0.45	0.49
2.13×10^{-4}	1.92×10^{-4}	2.36×10^{-4}	55.25	1.93	1.94	0.43	0.47
1.73×10^{-4}	1.56×10^{-4}	1.92×10^{-4}	55.47	1.93	1.94	0.42	0.46
1.41×10^{-4}	1.27×10^{-4}	1.56×10^{-4}	55.68	1.94	1.95	0.41	0.45
1.15×10^{-4}	1.03×10^{-4}	1.27×10^{-4}	55.89	1.94	1.95	0.41	0.45
9.34×10^{-5}	8.41×10^{-5}	1.04×10^{-4}	56.10	1.95	1.96	0.42	0.46
7.60×10^{-5}	6.84×10^{-5}	8.44×10^{-5}	56.35	1.96	1.97	0.42	0.46
6.19×10^{-5}	5.57×10^{-5}	6.88×10^{-5}	56.57	1.97	1.98	0.43	0.47
5.04×10^{-5}	4.53×10^{-5}	5.60×10^{-5}	56.79	1.98	1.99	0.44	0.48
4.10×10^{-5}	3.68×10^{-5}	4.57×10^{-5}	57.02	1.99	2.00	0.46	0.50
3.34×10^{-5}	2.99×10^{-5}	3.72×10^{-5}	57.26	2.00	2.01	0.47	0.51
2.72×10^{-5}	2.43×10^{-5}	3.04×10^{-5}	57.51	2.01	2.02	0.47	0.51
2.21×10^{-5}	1.97×10^{-5}	2.48×10^{-5}	57.77	2.02	2.03	0.47	0.51
1.80×10^{-5}	1.60×10^{-5}	2.02×10^{-5}	58.01	2.03	2.04	0.47	0.51
1.46×10^{-5}	1.30×10^{-5}	1.65×10^{-5}	58.26	2.03	2.05	0.47	0.51
1.19×10^{-5}	1.06×10^{-5}	1.34×10^{-5}	58.51	2.04	2.05	0.46	0.51
9.70×10^{-6}	8.59×10^{-6}	1.10×10^{-5}	58.76	2.05	2.06	0.46	0.50
7.90×10^{-6}	6.97×10^{-6}	8.95×10^{-6}	59.02	2.06	2.07	0.46	0.50

APPENDIX D

FORWARD GAP ALGORITHM

The following C++ code implements the Forward Pseudorapidity Gap algorithm in the RIVET framework [114].

```
// -*- C++ -*-
/**
* @name ATLAS Diffractive Gaps Rivet Analysis
* @author Tim Martin, tim.martin@cern.ch
* @version 1.0
* @date 16/01/2012
* @see http://arxiv.org/abs/1201.2808
* @note pp, sqrt(s) = 7 TeV
* @note Rapidity gap finding algorithm designed to complement
* the ATLAS detector acceptance. Forward rapidity gap sizes
* are calculated for each event, considering all stable
* particles above pT cut values 200, 400, 600 and 800 MeV in
* turn. A forward rapidity gap is defined to be the largest
* continuous region stretching inward from either edge of the
* detector at eta = |4.9| which contains zero particles above
* pT Cut. Soft diffractive topologies are isolated at large
* gap sizes.
**/

#include "Rivet/Analysis.hh"
#include "Rivet/RivetAIDA.hh"
#include "Rivet/Tools/Logging.hh"
#include "Rivet/Projections/FinalState.hh"

namespace Rivet {

class ATLAS_2012_I1084540 : public Analysis {
public:

ATLAS_2012_I1084540() : Analysis("ATLAS_2012_I1084540"), _etaBins(49), _etaMax(4.9) {
  setNeedsCrossSection(true);
```

```
}

/// @name Analysis methods
//@{
/// Book histograms and initialise projections before the run
void init() {
  //All final states. Rapidity range = ATLAS calorimetry. Lowest pT cut = 200 MeV.
  const FinalState cnfs2(-_etaMax, _etaMax, 0.2 * GeV);
  const FinalState cnfs4(-_etaMax, _etaMax, 0.4 * GeV);
  const FinalState cnfs6(-_etaMax, _etaMax, 0.6 * GeV);
  const FinalState cnfs8(-_etaMax, _etaMax, 0.8 * GeV);
  addProjection(cnfs2, "CNFS2");
  addProjection(cnfs4, "CNFS4");
  addProjection(cnfs6, "CNFS6");
  addProjection(cnfs8, "CNFS8");

  _etaBinSize = (2. * _etaMax)/(double)_etaBins;

  //Book histogram
  _h_DeltaEtaF_200 = bookHistogram1D(1, 1, 1);
  _h_DeltaEtaF_400 = bookHistogram1D(2, 1, 1);
  _h_DeltaEtaF_600 = bookHistogram1D(3, 1, 1);
  _h_DeltaEtaF_800 = bookHistogram1D(4, 1, 1);
}

private:
void fillMap(const FinalState& fs, bool* energyMap, double pTcut) {
  // Fill true/false array by iterating over particles and compare their
  // pT with pTcut
  foreach (const Particle& p, fs.particlesByEta()) {
    int checkBin = -1;
```

```
    double checkEta = -_etaMax;
    while (1) {
      checkEta += _etaBinSize;
      ++checkBin;
      if (p.momentum().eta() < checkEta) {
        energyMap[checkBin] = (p.momentum().pT() > pTcut * GeV);
        break;
      }
    }
  }
}

public:
/// Perform the per-event analysis
void analyze(const Event& event) {
  static unsigned int event_count = 0;
  ++event_count;
  const double weight = event.weight();
  const FinalState& fs2 = applyProjection<FinalState>(event, "CNFS2");
  const FinalState& fs4 = applyProjection<FinalState>(event, "CNFS4");
  const FinalState& fs6 = applyProjection<FinalState>(event, "CNFS6");
  const FinalState& fs8 = applyProjection<FinalState>(event, "CNFS8");

  // Set up Yes/No arrays for energy in each eta bin at each pT cut
  bool* energyMap_200 = new bool[_etaBins];
  bool* energyMap_400 = new bool[_etaBins];
  bool* energyMap_600 = new bool[_etaBins];
  bool* energyMap_800 = new bool[_etaBins];
  for (int i = 0; i < _etaBins; ++i) {
    energyMap_200[i] = false;
    energyMap_400[i] = false;
```

```
  energyMap_600[i] = false;
  energyMap_800[i] = false;
}

// Veto bins based on final state particles > Cut (Where Cut = 200 - 800 MeV pT)
fillMap(fs2, energyMap_200, 0.2);
fillMap(fs4, energyMap_400, 0.4);
fillMap(fs6, energyMap_600, 0.6);
fillMap(fs8, energyMap_800, 0.8);

// Apply gap finding algorithm
// Detector layout follows...
// -Eta [Proton--DetectorCSide--DetectorBarrel--DetectorASide--Proton] +Eta
bool gapDirectionAt200 = false; //False is gap on C size, True is gap on A side.
double largestEdgeGap_200 = 0.;
double largestEdgeGap_400 = 0.;
double largestEdgeGap_600 = 0.;
double largestEdgeGap_800 = 0.;

for (int E = 200; E <= 800; E += 200) {
  double EdgeGapSizeA = -1, EdgeGapSizeC = -1;
  bool* energyMap = 0;
  switch (E) {
    case 200: energyMap = energyMap_200; break;
    case 400: energyMap = energyMap_400; break;
    case 600: energyMap = energyMap_600; break;
    case 800: energyMap = energyMap_800; break;
  }

  // Look left to right
  for (int a = 0; a < _etaBins; ++a) {
```

```
  if (energyMap[a] == true) {
    EdgeGapSizeA = (_etaBinSize * a);
    break;
  }
}

// And look right to left
for (int c = _etaBins-1; c >= 0; --c) {
  if (energyMap[c] == true) {
    EdgeGapSizeC = (2 * _etaMax) - (_etaBinSize * (c+1));
    if (fuzzyEquals(EdgeGapSizeC, 4.47035e-08)) EdgeGapSizeC = 0.0;
    break;
  }
}
// Put your hands on your hips

// Find the largest gap
double largestEdgeGap = 0.;
if (E == 200) {
  // If the 200 MeV pass, take the biggest of the two gaps. Make note of which side for higher pT cuts.
  largestEdgeGap = std::max(EdgeGapSizeA,EdgeGapSizeC);
  gapDirectionAt200 = (EdgeGapSizeA > EdgeGapSizeC);
} else {
  // Use the direction from 200 MeV pass, most accurate measure of which side gap is on.
  if (gapDirectionAt200) {
    largestEdgeGap = EdgeGapSizeA;
  }
  else largestEdgeGap = EdgeGapSizeC;
}

// Check case of empty detector
```

```
  if (largestEdgeGap < 0.0) largestEdgeGap = 2.0 * _etaMax;

  // Fill bin centre
  switch (E) {
    case 200: _h_DeltaEtaF_200->fill(largestEdgeGap + _etaBinSize/2., weight); break;
    case 400: _h_DeltaEtaF_400->fill(largestEdgeGap + _etaBinSize/2., weight); break;
    case 600: _h_DeltaEtaF_600->fill(largestEdgeGap + _etaBinSize/2., weight); break;
    case 800: _h_DeltaEtaF_800->fill(largestEdgeGap + _etaBinSize/2., weight); break;
  }

  if (E == 200) largestEdgeGap_200 = largestEdgeGap;
  if (E == 400) largestEdgeGap_400 = largestEdgeGap;
  if (E == 600) largestEdgeGap_600 = largestEdgeGap;
  if (E == 800) largestEdgeGap_800 = largestEdgeGap;
}

// Algorithm result every 1000 events
if (event_count % 1000 == 0) {
  for (int E = 200; E <= 800; E += 200) {
    bool* energyMap = 0;
    double largestEdgeGap = 0;
    switch (E) {
      case 200: energyMap = energyMap_200; largestEdgeGap = largestEdgeGap_200; break;
      case 400: energyMap = energyMap_400; largestEdgeGap = largestEdgeGap_400; break;
      case 600: energyMap = energyMap_600; largestEdgeGap = largestEdgeGap_600; break;
      case 800: energyMap = energyMap_800; largestEdgeGap = largestEdgeGap_800; break;
    }
    MSG_DEBUG("Largest Forward Gap at pT Cut " << E << " MeV=" << largestEdgeGap
      << " eta, NFinalState pT > 200 in ATLAS acceptance:" << fs2.particles().size());
    std::string hitPattern = "Detector HitPattern=-4.9[";
    for (int a = 0; a < _etaBins; ++a) {
```

```
        if (energyMap[a] == true) hitPattern += "X";
        else hitPattern += "_";
      }
      hitPattern += "]4.9";
      MSG_DEBUG(hitPattern);
      std::string gapArrow = "                          ";
      if (!gapDirectionAt200) {
        int drawSpaces = (int)(_etaBins - (largestEdgeGap/_etaBinSize) + 0.5);
        for (int i = 0; i < drawSpaces; ++i) gapArrow += " ";
      }
      int drawArrows = (int)((largestEdgeGap/_etaBinSize) + 0.5);
      for (int i = 0; i < drawArrows; ++i) gapArrow += "^";
      MSG_DEBUG(gapArrow);
    }
  }

  delete[] energyMap_200;
  delete[] energyMap_400;
  delete[] energyMap_600;
  delete[] energyMap_800;
}

/// Normalise histograms after the run, Scale to cross section
void finalize() {
  MSG_DEBUG("Cross Section=" << crossSection() / millibarn << "mb, SumOfWeights=" << sumOfWeights());
  scale(_h_DeltaEtaF_200, (crossSection() / millibarn)/sumOfWeights());
  scale(_h_DeltaEtaF_400, (crossSection() / millibarn)/sumOfWeights());
  scale(_h_DeltaEtaF_600, (crossSection() / millibarn)/sumOfWeights());
  scale(_h_DeltaEtaF_800, (crossSection() / millibarn)/sumOfWeights());
}
//@}
```

```
private:
/// @name Histograms
//@{
AIDA::IHistogram1D* _h_DeltaEtaF_200;
AIDA::IHistogram1D* _h_DeltaEtaF_400;
AIDA::IHistogram1D* _h_DeltaEtaF_600;
AIDA::IHistogram1D* _h_DeltaEtaF_800;
//@}
/// @name Private variables
//@{
int _etaBins;
double _etaMax;
double _etaBinSize;
//@}

};

// The hook for the plugin system
DECLARE_RIVET_PLUGIN(ATLAS_2012_I1084540);

}
```